Understanding the Mechanisms and Potential of Microbial Peroxide-Producing Cells (MPPCs)

by

Michelle Nichole Young

A Dissertation Presented in Partial Fulfillment
of the Requirements for the Degree
Doctor of Philosophy

Approved September 2018 by the
Graduate Supervisory Committee:

Bruce E. Rittmann, Chair
Andrew K. Marcus
César I. Torres

ARIZONA STATE UNIVERSITY

December 2018

ABSTRACT

Microbial electrochemical cells (MxCs) are a novel technology that use anode-respiring bacteria (ARB) to bioremediate wastewaters and respire an electrical current, which can then be used directly to produce value-added products like hydrogen peroxide (H_2O_2). Ninety-five percent of the world's H_2O_2 is currently produced using the anthraquinone process, whose production requires expensive and potentially carcinogenic catalysts and high amounts of electricity. However, the amount of H_2O_2 that can be produced from these microbial peroxide-producing cells (MPPCs) has not been thoroughly investigated. Predicting potential H_2O_2 production in MxCs is further complicated by a lack of mathematical models to predict performance utilizing complex waste streams like primary sludge (PS).

A reactor design methodology was developed for MPPCs to systematically optimize H_2O_2 production with minimal energy consumption. H_2O_2 stability was evaluated with different catholytes, membranes, and catalysts materials, and the findings used to design and operate long-term a dual-chamber, flat-plate MPPC using different catholytes, ferrochelating stabilizers, and hydraulic retention times (HRT). Up to 3.1 ± 0.37 g H_2O_2 L^{-1} was produced at a 4-h HRT in an MPPC with as little as 1.13 W-h g^{-1} H_2O_2 power input using NaCl catholytes. Attempts to improve H_2O_2 production by using weak acid buffers as catholytes or ferrochelating stabilizers failed for different reasons.

A non-steady-state mathematical model, MYAnode, was developed combinging existing wastewater treatment, anode biofilm, and chemical speciation models to predict MxC performance utilizing complex substrates. The model simulated the large-scale

trends observed when operating an MPPC with PS substrate. At HRTs ≥ 12-d, the model demonstrated up to 20% Coulombic recovery. At these conditions, ARB required additional alkalinity production by ≥ 100 mgVSS/L of acetoclastic methanogens to prevent pH inhibition when little influent alkalinity is available. At lower HRTs, methanogens are unable to produce the alkalinity required to prevent ARB inhibition due to washout and rapid acidification of the system during fermentation. At ≥ 100 mgVSS/L of methanogens, increasing the diffusion layer thickness from 500 to 1000 μm improved Coulombic efficiency by 13.9%, while increasing particulate COD hydrolysis rates to 0.25/d only improved Coulombic efficiency by 3.9%.

To my mum and sis – the strongest women in my life.

To Nat – you are my inspiration.

ACKNOWLEDGMENTS

To be entirely honest, I completed something like this for my Master thesis, and many of the same debts of gratitude still apply. Any list of acknowledgements must begin with my amazingly brilliant and patient advisor and my committee chair, Dr. Bruce Rittmann. He has been there as a sounding board at the right times, provides guidance when needed, and has a wonderfully wicked sense of humor. I wish to thank Dr. César Torres and Dr. Andrew Marcus for the support during my Ph.D. studies. Both provided invaluable guidance and wisdom – as well as many incredible conversations. These two gentlemen are the ones that provided the daily or as needed guidance during my dissertation. Working with these three, I realize what a unique situation we have in the Biodesign Swette Center for Environmental Biotechnology. These men are geniuses – and we are spoiled rotten working with such innovative talents! I also thank my peers on the SERDP project, Drs. Dongwon Ki and Rakesh Joshi, for pushing me to be my best and develop a deeper level of understanding of the topics. My desk/cube mates over the years – Dr. Alex Zevin, Dr. Aura Ontiveros-Valencia, Dr. Rachel Yoho, Dr. Yen-Jung "Sean" Lai, Steven Hart, and Megan Altizer – for the laughs and fun conversations. Thanks to Dr. Prathap Parameswaran and Dr. Sudeep Popat for their mentorship and help.

I also acknowledge the financial support have obtained in pursuit of this degree. Most of my research was funded by the Department of Defense's Strategic Environmental Research and Develop Program (SERDP) grant number ER-2239. I also received funding from the Biodesign Swette Center for Environmental Biotechnology,

ARCS Foundation, Phoenix/Scottsdale Groundwater Contamination Scholarship for Environmental Science, and Arizona State University Graduate College.

Finally, a big thanks to my friends and family for their support. You all played a critical role in getting me through this journey. I thank my husband, Jim, and parents, Melvin and Cindy, for loving me through the (very) difficult and easy times and appreciating my silly sense of humor. I thank my sister, Heather, for telling it like it is and her daughter, Natalie, for being my inspiration. My love to all my sweet bunnies for providing a wonderful distraction – Bingley (BIP), Louise, Sunshine, Digby (BIP), Moose, Topanga, Aspen, Fletcher, Sonata, and Malcolm. Finally, a big thanks to my friends Bridget Cavanaugh and Michelle Barry – I miss our lunches! – and Esra Ilhan for listening.

With that, let's get this show on the road…

TABLE OF CONTENTS

Page

LIST OF TABLES

LIST OF FIGURES

Figure Page

Figure Page

Figure Page

Figure Page

LIST OF ABBREVIATIONS

1D	One-dimensional
2D	Two-dimensional
3D	Three-dimensional
AD	Anaerobic digestion
ADM	Anaerobic Digestion Model
AEM	Anion exchange membrane
Ag/AgCl	Silver/silver chloride
AOB	Ammonium-oxidizing bacteria
ARB	Anode-respiring bacteria
ASM	Activated Sludge Model
BAP	Biomass-associated products
BOD	Biological oxygen demand
BOD_5	Biological oxygen demand at 5 days
BSM	Benchmark Simulation Model
CASADM	Combined Activated Sludge-Anaerobic Digestion Model
CCBATCH	Co-Contaminants in a Batch reactor
CCE	Cathodic coulombic efficiency
CEM	Cation exchange membrane
CFUs	Coliform forming units
CH_3COO^-	Acetate
CH_3COOH	Acetic acid
CH_4	Methane
Cl^-	Chloride ion
CO_2	Carbon dioxide
CO_3^{2-}	Carbonate
COD	Chemical oxygen demand
CV	Cyclic voltammetry
DI	Deionized
DL	Diffusion layer
e^-	Electrons
$E^{o'}$	Electrical potential at standard temperature, pressure, and pH
EDTA	Ethylenediaminetetraacetic acid
EET	Extracellular electron transfer
EIS	Electrochemical impedance spectroscopy
E_{KA}	Anode potential at one-half of the maximum current density
EPS	Extracellular polymeric substances
GC-FID	Gas chromatography with a flame ionization detector
H^+	Protons
H_2	Hydrogen gas
H_2O	Water
H_2O_2	Hydrogen peroxide
H_2CO_3	Carbonic acid
$H_2PO_4^-$	Dihydrogen phosphate

H_3PO_4	Phosphoric acid
HCO_3^-	Bicarbonate
HNO_2	Nitrous acid
HO_2^-	Peroxide anion
HPO_4^{2-}	Hydrogen phosphate
HRT	Hydraulic retention time
IC	Ion chromatography
k_{hyd}	PCOD hydrolysis rate
LSV	Linear sweep voltammetry
MEC	Microbial electrolysis cell
MFC	Microbial fuel cell
MPPC	Microbial peroxide-producing cell
MxC	Microbial electrochemical cell
N_2	Nitrogen gas
Na^+	Sodium ion
NH_3	Ammonia
NH_4^+	Ammonium
NO_2^-	Nitrite
NO_3^-	Nitrate
NOB	Nitrite-oxidizing bacteria
O_2	Oxygen
ODE	Ordinary differential equation
OH^-	Hydroxide ions
ORR	Oxygen reduction reaction
PBS	Phosphate buffer solution
PC	Proton condition
PCBIOFILM	Proton Condition in Biofilm
PCOD	Particulate COD
PO_4^{3-}	Phosphate
PS	Primary sludge
PTFE	Polytetrafluoroethylene
RRDE	Rotating-ring disk electron
SCE	Standard calomel electrode
SCOD	Soluble COD
SMP	Soluble microbial products
SRT	Solids retention time
SS	Suspended solids
TCOD	Total COD
$TCOD_{in}$	Influent total COD
TOC	Total organic carbon
TSS	Total suspended solids
UAP	Utilization-associated products
U.S.	United States
UV	Ultraviolet
VFA	Volatile fatty acid

VSS	Volatile suspended solids
WAS	Waste activated sludge
WWT	Wastewater treatment
WWTP	Wastewater treatment plants
X_m	Methanogens

LIST OF MATHEMATICAL VARIABLES

Symbol	Description	Units
β_i^c	The formation constant of complex i adjusted for the solution's ionic strength	Varies
ε_{H2O2}	Efficiency of current conversion to H_2O_2	%
λ_{hg}	The stoichiometric coefficient of species h in reaction g	--
ν_{ij}	The stoichiometric coefficient giving the number of moles of component j in complex i	--
C_{actual}	Actual H_2O_2 concentration	M/L^3
C^B	Actual bulk liquid concentration	M/L^3
C^{eff}	Concentration in the influent	M/L^3
C_h	The concentration of the chemical or biological species h	M/L^3
c_{H^+}	Concentration of uncomplexed H^+	M/L^3
C_{H^+}	Total analytical concentration of H^+	M/L^3
C^{inf}	Concentration in the influent	M/L^3
C^{Int}	Concentration at the DL/biofilm interface	M/L^3
c_j	Concentration of component j	M/L^3
C_j	The total analytical concentration of component j	M/L^3
$\hat{C}_j$	Chemical formula for component j	--
c_k	Concentration of ion k	M/L^3
C^{mig}	Amount of migration charge	$Charge/L^3$
C_{req}^{mig}	Charge required to migrate to maintain electroneutrality	$Charge/L^3$
C^{prod}	Theoretical concentration of product	M/L^3
C^{req}	Concentration of charges that migrated to maintain electroneutrality between the anode and cathode chambers over a set HRT	M/L^3
$C_i^{theoretical}$	Theoretical concentration of species i	M/L^3
C_{theory}	Theoretical concentration of H_2O_2	M/L^3
D	Diffusion coefficient	L^2/t
E	Fixed cell potential	V
E^*	Apparent electric field	1/L
$E^{o'}$	Electrical potential at standard temperature, pressure, and pH	V
E_{KA}	The potential at which half of the maximum specific growth rate is achieve	V
F	Faraday's constant	96485 C/mol
g	A chemical or biological reaction	
H_i	Henry's law constant of species i	M/L^3
I	Current	A
$I_{g,pH}$	pH inhibition term for reaction g	--
I_{pH}	pH inhibition term	--

Symbol	Description	Units
J	Mass flux	M/L^2-t
J_{ion}	Total flux of an ion	M/L^2-t
J_{diff}	Diffusive flux of an ion	M/L^2-t
J_{mig}	Flux due to migration	M/L^2-t
k	Ion of species k	--
$K_{h,inh}$	The inhibition factor (M/L^3) for species h	M/L^3
K_La	Mass transfer coefficient	1/t
L	Length or thickness of the diffusion layer	L
L_f	Length or thickness of the biofilm	L
n	Number of electrons transferred as part of electrochemical reactions	--
N_c	Number of components in a system	--
N_p	The total number of complexes associated with component j	--
N_x	Number of complexes	--
p_i	Concentration of complex i	M/L^3
$\widehat{P}_i$	Chemical formula for complex i	--
pH_{opt}	Optimal pH for bacteria	--
Q	Volumetric flow rate	L^3/T
$\hat{q}X_f$	Maximum specific growth rate in the biofilm	M/L^3-t
R	Ideal gas constant	8.314 J/mol K
r_h	Reaction rate for component h	M/L^3-t
SA	Anode surface area	L^2
$S_{g,inh}$	Substrate limitation function for component h in reaction g	--
$S_{h,inh}$	Substrate limitation function for component h	--
t	Time	t
T	Temperature	T
V	Volume	L^3
Vol	Volume	L^3
W	Range of functional pHs for bacteria	--
x	Spatial coordinate	L
z_k	Charge of ion k	--

CHAPTER 1

Introduction

1.1 Wastewater treatment and its critical impacts on society

Efficient and effective wastewater treatment is critical for sustainable human health and preservation of the environment. Every day in the United States, more than 14,000 wastewater treatment plants (WWTPs) treat 33.2 billion gallons per day of wastewater for 238 million people (U.S. EPA, 2016). Of those WWTPs, 84% of plants provide secondary treatment (i.e., removal of soluble and particulate chemical oxygen demand, or COD, using an activated sludge process and a secondary clarifier) or higher. Secondary treated wastewater must meet minimum discharge standards of less than 30 mg BOD_5/L and more than 85% removal of biochemical oxygen demand at day 5 (BOD_5) and total suspended solids (TSS) (U.S. EPA, 2016).

The quest for energy efficiency has become an industry-wide focus in wastewater treatment (WWT). WWTPs account for ~1% of the United States' (U.S.) electricity consumption (Carns, 2005; Reekie et al., 2013). Not surprisingly, aeration accounts for ~50-54% of energy consumption in a typical activated sludge WWTP (U.S. EPA, 2008; O'Callaghan, 2009). Energy usage continues to climb as technologies with higher energy consumption technologies, like ultraviolet (UV) disinfection and membrane filters, are implemented to help facilities meet more stringent treatment guidelines.

WWTPs are also increasingly focused on reducing biosolids. Approximately 8 million dry tons of sludge were produced by U.S. wastewater treatment facilities in 2005, with 51% being applied to land application, 28% being disposed of at landfills,

and 15% incinerated (Center for Sustainable Systems, 2016; U.S. EPA, 2016). While sludge produced during WWT is nutrient-rich, solids must undergo energy-intensive reconditioning to be used as soil nutrients, incineration is energy intensive and produces greenhouse gases, and biosolids transportation has significant greenhouse gas emissions and life cycle impacts (Center for Sustainable Systems, 2016).

Industry-wide, WWTPs seek more energy-efficient wastewater treatment and higher sludge stabilization to reduce operational costs (U.S. EPA, 2008; Rittmann, 2013; Li et al., 2014; Lowrie, 2015). While activated sludge processes are used in COD and nitrogen removal, aerobic bacteria have high biomass yields, producing substantial sludge for disposal (Rittmann and McCarty, 2001; Rittmann, 2013). Anaerobic digestion (AD) is increasingly utilized a method of stabilizing biosolids while simultaneously producing methane (CH_4) for on-site heat and power (Eastern Research Group, Inc. and Energy and Environmental Analysis, Inc., 2007; U.S. EPA Combined Heat and Power Partnership, 2008; Rittmann, 2013; Metcalf & Eddy, 2014). During AD, sludge is decomposed and converted to CH_4 by a three-step process: hydrolysis of solid and macromolecular organics, i.e., sludge stabilization; fermentation of the hydrolysis products to simple organic acids, alcohols, and hydrogen gas (H_2); and methanogenesis of the fermentation products to CH_4. Sludge stabilization reduces the mass of solids required for disposal (Center for Sustainable Systems, 2016; Rittmann, 2013; Metcalf & Eddy, 2014; Lowrie, 2015).

1.2 Hydrogen peroxide (H_2O_2) and its role in water and wastewater treatment

H_2O_2 is an industrial chemical with a wide range of uses including as a bleaching agent for textiles and paper, a propellant, and an oxidant in chemical manufacturing (Campos-Martin et al., 2006). Approximately 5% of the U.S.'s annual H_2O_2 usage is in the water and wastewater treatment (FMC Corp., 2012). H_2O_2 is used in low concentrations with the Fenton process or UV treatment for advanced oxidation of complex organic chemicals and emerging contaminants (Campos-Martin et al., 2006; De la Cruz et al., 2012; Yang et al., 2014) and for disinfection (Glaze et al., 1987; Wagner et al., 2002; Ksibi, 2006; Kruithof et al., 2007; Snyder et al., 2008). H_2O_2 also is used in advanced oxidation processes to remove biological products or contaminants that contribute to taste and odor issues (Ksibi, 2006; Acero and von Gunten, 2000; Drogui et al., 2001). H_2O_2 is utilized at WWTPs for hydrogen sulfide removal in scrubbing towers to reduce odor emissions (Charron et al., 2004; Metcalf & Eddy, 2014).

Approximately 95% of the world's annual H_2O_2 production is through the anthraquinone oxidation process (Campos-Martin et al., 2006). During the anthraquinone oxidation process, anthraquinone is hydrogenated with hydrogen gas (H_2) using palladium or nickel at catalysts to form anthrahydroquinone (Deed, 1998; Campos-Martin et al., 2006). After the metal catalysts are filtered from the solution, the anthrahydroquinone solution is aerated using large blowers to produce H_2O_2 and anthraquinone. The H_2O_2 is extracted in a distillation column at a 25-30 weight % solution, and the anthraquinone is recycled back to the hydrogenation step. Additional distillation steps are performed if higher H_2O_2 concentrations are desired. The anthraquinone oxidation process is estimated to use 2 to 10 W-h to produce one

gram of H_2O_2 (Althaus et al., 2007; Yang et al., 2014). Within the last 15 years, anthraquinone and its byproducts have been under scrutiny for being suspected carcinogens. In the mid-2000s, California added anthraquinone to its Proposition 65 list due to its carcinogenic effects in animal studies (Hart and Rudie, 2014). In 2013, the European Food Safety Authority limited anthraquinone residue levels to less than 10 ppb in H_2O_2-bleached pulp and paper board that contacts food due to its suspected carcinogenic effects (Hart and Rudie, 2014). Thus, a sustainable and efficient alternative for H_2O_2 production is required to satisfy the market's needs.

H_2O_2 is also produced by electrosynthesis in fuel cells. Electrolysis of H_2O_2 has been commercially available for more than 100 years but is economically disadvantageous versus the anthraquinone oxidation process due to large energy requirements (Campos-Martin et al., 2006). Over the last 20 years, research has focused on electrosynthesis of H_2O_2 in fuel cells. Ichiro Yamanaka's group has been at the forefront of this fuel cell research, exploring H_2O_2 production at different electrolyte pH, improved oxygen gas (O_2) delivery to the electrolyte, and cathode design (Otsuka and Yamanaka, 1990; Yamanaka et al., 2003; Yamanaka et al., 2011). Their research has achieved H_2O_2 concentrations up to 72 g/L in fuel cells operating at 60-93% cathodic efficiency and producing up to $3x10^{-4}$ W-h/g H_2O_2, but the cell requires a direct feed of H_2 gas to the anode and O_2 to the cathode leading to concerns regarding safe cell operations.

Chemical compatibility and storage of H_2O_2 are obstacles for any proposed H_2O_2 manufacturing process. As a strong oxidant, H_2O_2 is highly susceptible to degradation in presence of a myriad of reduced compounds, including metals and organic compounds. Commercially available H_2O_2 often includes either a metal

chelator to prevent its catalytic degradation or a sequestrant that produces protective colloids with H_2O_2 to minimize degradation. The most common chelating agents used in H_2O_2 solutions include sodium pyrophosphate, ethylenediaminetetraacetic acid (EDTA), and organophosphonates, which chelate metals (Knotter et al., 1999; Rämö and Sillanpää, 2001; Campos-Martin et al., 2006). Sodium stannate is the most common H_2O_2 sequestrant, but other sequestrants include sodium silicate and sodium nitrate (Colodette et al., 1989; Campos-Martin et al., 2006).

1.3 Microbial electrochemical cells and byproduct formation

1.3.1 Overview

Microbial electrochemical cell (MxC) technology is a fledgling, transformative technology investigated over the last decade for wastewater treatment. Figure 1.1 is an illustration of a typical dual-chamber MxC. In MxCs, anode-respiring bacteria (ARB) consume volatile fatty acids (VFAs) like acetate (CH_3COO^-) and propionate or H_2 as electron donor for energy and biomass synthesis (Kim et al., 2010; Lee et al., 2008; Kannaiah Goud and Venkata Mohan, 2011). Unlike most other bacteria, ARB respire electrons to a solid anode, which functions as the electron acceptor via a conductive biofilm matrix or a shuttling mediator through extracellular electron transfer (EET), producing an electrical current that flows to the cathode via an electrical circuit. MxCs are operated as single-chambered systems (i.e., the anode and cathode are located in the same chamber) or dual-chambered systems (i.e., a membrane separates the anode and cathode chambers.

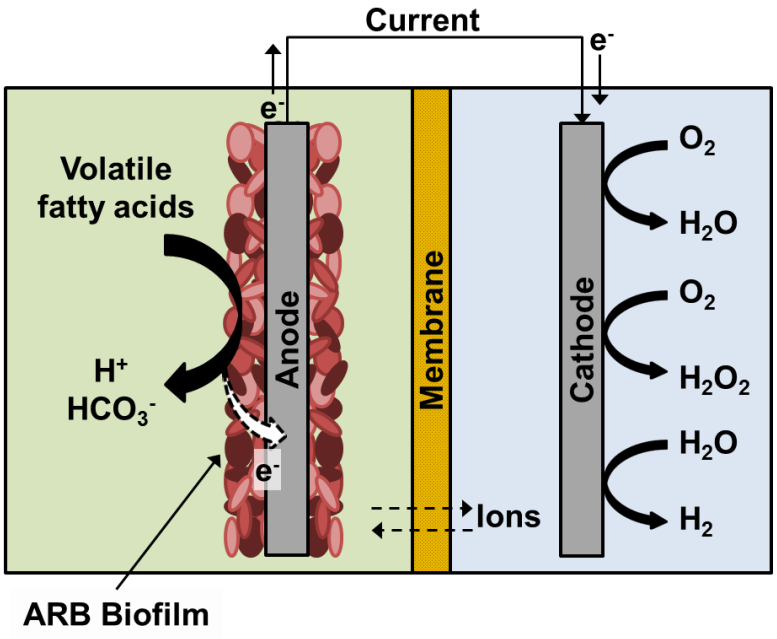

Figure 1.1. A schematic of the processes in a dual-chamber MxC.

ARB perform electrode respiration under anaerobic conditions and largely depend upon other microorganisms to biodegrade complex organic compounds to the simple substrates they can utilize (Rozendal et al., 2008; Parameswaran et al., 2009; Kiely et al., 2011; Parameswaran et al., 2011; Miceli et al., 2014). Their place in the anaerobic food web is shown in Figure 1.2. During hydrolysis, complex and particulate organic compounds undergo disintegration to carbohydrates, proteins, and lipids, which are further enzymatically hydrolyzed by fermenting bacteria to monosaccharides, amino acids, and long chain fatty acids (Vavilin et al., 2008). The hydrolysis products are fermented by acidogenic or acetogenic bacteria to VFAs, alcohols, keytones, and H_2 gas (Rittmann and McCarty, 2001; Bitton, 2005). This step is critical to providing substrate to most common ARB (Kiely et al., 2011; Parameswaran et al., 2011; Miceli et al., 2014). Acidogens metabolize fatty acids, amino acids, and sugars to VFAs like acetate, propionate, and butyrate, and to alcohols including ethanol, bicarbonate (HCO_3^-), and H_2. Acetogens convert hydrolysis and fermentation products to acetate, HCO_3^-, and H_2 and are classified into two different groups: H_2-producing acetogens and homoacetogens. H_2-producing acetogens ferment VFAs and ethanol to acetate, while homoacetogens produce acetate directly from consumption of HCO_3^- and H_2. Two sets of microorganisms compete for these fermentation products: acetoclastic or hydrogenotrophic methanogens consume acetate and H_2 and generate CH_4 while ARB consume VFAs and H_2 to respire electrons to an anode. Large-scale MxCs applications likely will utilize complex waste streams with diverse microbial consortia to produce the fermentation products consumed by ARB but will also require system design and operation to control or minimize methanogenic activity (Rozendal et al., 2008; Kiely et al., 2011; Li et al., 2014).

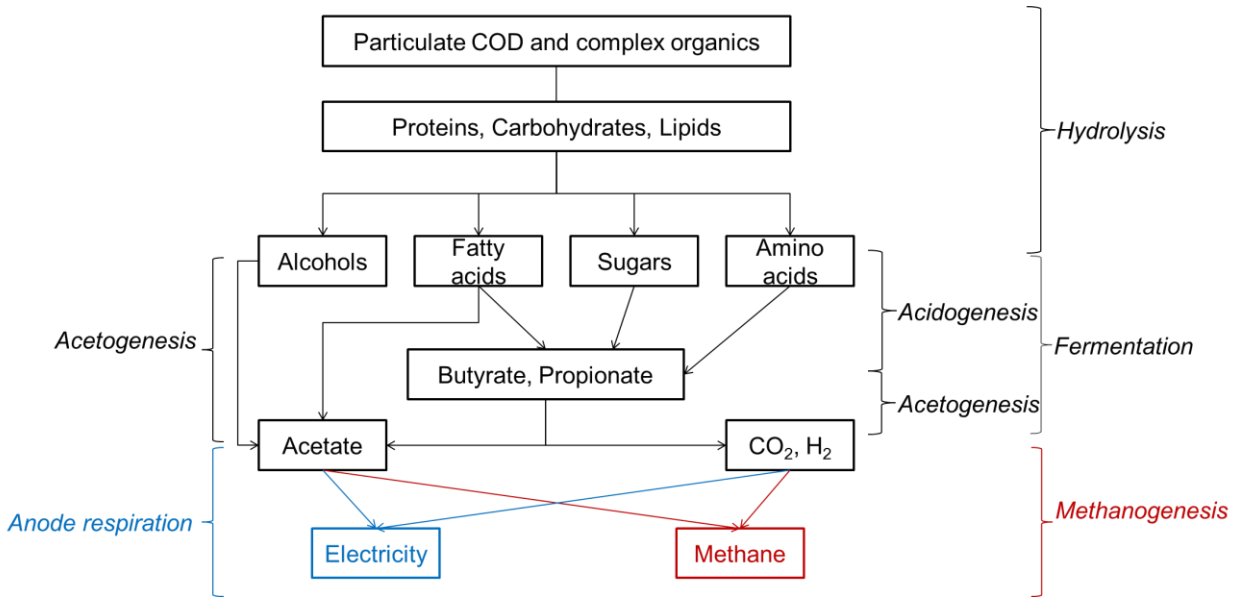

Figure 1.2. The anaerobic food web that includes methanogenesis and anode respiration.

Various products can be generated at the cathode through reduction reactions that use the electrons transmitted through the electrical circuit from the anode. In microbial fuel cells (MFCs), the objective is to produce electrical energy through the 4-electron reduction of O_2 to water (H_2O). Theoretically, a 4-electron reduction produces ~1.1 V when coupled with acetate oxidation at the anode (Logan et al., 2006). In reality, inefficiencies in cell performance reduce the recovered energy to 0.2-0.4 V (Rozendal et al., 2008; Li et al., 2014). Causes of these cell inefficiencies include electrode catalysts that fail to significantly reduce the activation energy required for the chemical reaction to proceed; increased Ohmic resistances due to migration of counter ions over long distances to sustain electroneutrality; and concentration overpotentials due to large pH differences between the anolyte and catholyte (Bard and Faulkner, 2001; Logan et al., 2006; Torres, 2014; Popat and Torres, 2016).

In microbial electrochemical cells (MECs), a small amount of energy is put into the system to produce a valuable byproduct at the cathode. One example of a valuable byproduct is H_2 gas: under anaerobic catholyte conditions, H_2O is reduced to form H_2 gas, which evolves from the liquid and is captured as the energy output. Theoretically, H_2 can be produced at the cathode with as little as 0.14 V of applied energy (Rabaey and Verstraete, 2005; Logan and Regan, 2006), but the same kinds of Ohmic and concentration energy losses exhibited in MFCs reduce operating efficiency, resulting in the addition of > 0.2 V energy to reduce H_2O to H_2 (Logan et al., 2008; Kadier et al., 2014). To mitigate cathode-related losses, MECs and MFCs use expensive catalysts like platinum or gold.

1.3.2 Microbial Peroxide Producing Cells (MPPCs)

One potentially energy-neutral application of MxC technology is cathodic electrosynthesis of H_2O_2 using microbial peroxide producing cells (MPPCs):

$$O_2 + 2H_2O + 2e^- \rightarrow H_2O_2 + 2OH^- \qquad (E^{o\prime} = +0.58\ V) \qquad \text{(Eqn. 1.1)}$$

High concentrations of H_2O_2 can be achieved using simple carbon catalysts. Researchers have had limited success producing H_2O_2 in batch MPPCs: Either high concentrations of H_2O_2 were generated by adding energy into a MPPC, or very low H_2O_2 concentrations were produced along with a small output of electrical energy. Rozendal et al. (2009) produced 3.9 g H_2O_2/L-d and concentrations as high as 1.3 g/L but required 0.93 W-h/g H_2O_2. Conversely, Fu et al. (2010) produced a low H_2O_2 concentration of 79 mg/L but generated 0.06 W-h/g H_2O_2. Modin and Fukushi (2013) produced 9 g/L H_2O_2 at a rate of 11.1 g/L-d while applying 3.0 W-h/g H_2O_2, demonstrating that high H_2O_2 concentrations can be achieved with significant energy input into the MPPC.

MPPC research has generally focused understanding the impact of one or two variables, rather than a systematic investigation of factors affecting the overall MPPC performance. Fu et al. (2010), Modin and Fukushi (2013), Arends et al. (2014), and Sim et al. (2015) used different wastewater sources at different anode and cathode hydraulic retention times (HRTs) to maximize H_2O_2 production. Modin and Fukushi (2012), Chen et al. (2014) and Li et al. (2016) explored different catalysts for improved H_2O_2 production.

Significant gaps exist in MPPC research. Only Li et al. (2016) demonstrated continuous production of H_2O_2 at the cathode chamber, and they achieved very low H_2O_2 concentrations of ($8x10^{-5}$ g H_2O_2/L). MPPCs have not been systematically investigated to minimize overpotentials, identify key material compatibility issues, characterize the efficiency of materials, and to design cells for long-term operations.

1.4 MxC Mathematical Modeling

Mathematical models provide an important tool for wastewater treatment professionals. Many models capture features typical of WWTPs, including mass transport, biological, and chemical phenomena. Standard industry models like the Anaerobic Digestion Model (ADM), Activated Sludge Model (ASM), and the Benchmark Simulation Model (BSM) compartmentalize biological and chemical mechanisms to vessels with specific functions (Henze et al., 2000; Batstone et al., 2002; Nopens et al., 2009). These models focus on carbon, nitrogen, hydrogen and oxygen-based electron donors and acceptors and processes common to wastewater treatment: aerobic oxidation, nitrification, denitrification, acidogenesis, acetogenesis, homoacetogenesis, and hydrogenotrophic and acetoclastic methanogenesis. The models include the biological processes of bacterial growth and respiration and cell decay and the chemical process of chemical speciation.

The Combined Activated Sludge-Anaerobic Digestion Model (CASADM) (Young et al., 2013b) provides the most comprehensive analysis of biological and chemical mechanisms without *a priori* assumptions of rate limiting steps as well as the inclusion of biomass-generated products like soluble microbial products (SMP) and extracellular polymeric substances (EPS).

Others have modified the above-mentioned models to varying degrees for specific scenarios, including dynamic variations in flows for controls simulations (Solon et al., 2017), nutrient recovery (particularly phosphorus recovery and struvite precipitation) (Flores-Alsina et al., 2015), greenhouse gas emissions (Ni and Yuan, 2015; Peng et al., 2016), and detailed bacterial growth and respiration pathways that

evaluate ATP and NADH in respiration (Jiang et al., 2011; Ni and Yuan, 2015; Peng et al., 2016).

1.4.1 Anode models

Many of the basic concepts applied in WWTP models are also applicable in MxCs. As described in a previous section, the anode chamber of an MxC and anaerobic digestion depend on several upstream metabolic processes, including hydrolysis and fermentation, that are included in anaerobic digester models. However, MxC models must incorporate EET as part of ARB respiration to an anode.

The earliest MxC models developed describe mediator-based transfer of electrons from ARB to an anode. Zhang and Halme (1995) introduced one of the first MxC models, which utilizes diffusion of an external mediator to transfer electrons between ARB and an anode. Substrate consumption and respiration are based on Monod kinetics and first order decay, respectively, while electrochemical reactions are described using the Nernst equation for open circuit potential, the Tafel equation to describe activation overpotential, and Ohm's law to describe resistance overpotentials in the MEC. Picioreanu et al. (2007, 2008, 2010) developed several two- and three-dimensional (2D, 3D) anode models describing the interactions between bulk liquid and biofilm. The models use Monod kinetics to describe biomass growth and respiration. The Butler-Volmer equation is used determine current density, taking into account Ohmic and activation losses within the cell. Picioreanu et al.'s (2010) work culminates in the incorporation of ADM1 to describe substrate competition between ARB and methanogenic bacteria in the anode chamber.

As research focus turned to mediator-less EET mechanisms, the works by Marcus et al. (2007, 2010, 2011) became the cornerstone of MxC anode and biofilm

modeling. Marcus et al. (2007) introduced the Nernst-Monod model to describe ARB performance. They utilized steady-state, dual-limitation kinetics using the Monod equation for biomass oxidation and respiration and the Nernst equation to describe electrical conduction of electrons to the electron acceptor, i.e., anode. ARB kinetics are combined with mass balances and diffusion based on Fick's law to describe current production in conductive biofilms. Marcus et al. (2011) introduced PCBIOFILM, a steady-state, one-dimensional (1D) model that incorporates the Nernst-Monod model and diffusion with pH dependence and electrical neutrality. Since ARB produce an imbalance of charge from H^+ at the anode, PCBIOFILM addresses the precarious balance between H^+ diffusion from the biofilm and alkalinity diffusion into the biofilm to maintain electrical neutrality. In PCBIOFILM, Marcus et al. utilize CCBATCH, a modeling platform that was developed to incorporate slow biological reactions with faster pH and chemical speciation reactions (VanBriesen and Rittmann, 1999). Since H^+ is the primary component produced at the anode, one advantage of utilizing the CCBATCH platform is its application of the proton condition (PC) to provide a mass balance on the change in H^+ within the system. Marcus et al. (2010) expanded PCBIOFILM further to include the impact of ionic migration from the electric field produced due to EET.

Over the last five years, a plethora of anode models were developed to describe anode phenomena ranging from the thermodynamic to the molecular to the mechanistic. Merkey and Chopp (2012) expanded Marcus et al.'s (2010) model to a 2D model to include a conductivity parameter for the biofilm, but neglected pH variation within the biofilm. Oliveira et al. (2013) utilized EET kinetics as described by Marcus et al. (2007) developed an MFC model that couples mass, heat, and charge transfer with biofilm formation. Oliveira et al. (2013) determined that heat dissipation

at the anode has little effect on anode chamber performance. Several researchers have developed more detailed models of extracellular electron transfer combined with biofilm formation. Pinto et al. (2010, 2011) developed several dynamic multispecies mathematical models of the anode chamber that include mass balances on intracellular electron transfer between redox mediators in ARB. However, Pinto et al.'s models neglect the impacts of pH. Renslow et al. (2013) developed a model that explored isolated and concurrent diffusion and conduction-based electron transfer mechanisms. Building on Marcus et al. (2010), Jayasinghe et al. (2014) combined the extracellular electron transfer mechanism with intracellular metabolic model based on flux balances through ARB cells. Korth et al. (2015) expand on Marcus et al. (2007) to describe intra- and extracellular electron transfer based on metallic-like conductivity through the biofilm.

Many existing models omit important phenomena which can significantly affect ARB performance. Excluding Marcus et al. (2010, 2011) and Picioreanu et al. (2007, 2008, 2010), models generally assume constant pH and neglect chemical speciation even though several works have demonstrated pH inhibition in ARB biofilms (Torres et al., 2008a, Franks et al., 2009). Most models only include simple substrates like acetate or glucose, which are unrealistic for wastewater treatment modeling. No prior model accounts for the formation of EPS and SMP, which can divert up to 24% of energy obtained from substrate utilization from the production of fermentation products fermenting bacteria (Noguera et al., 1994; Laspidou and Rittmann, 2002a; Ni et al., 2010; Xie et al., 2012).

1.4.2 Combined anode and cathode models

Models that describe the anode and cathode generally are based on a mediator-less EET. Oliveira et al. (2013) developed a steady-state, 1D model of dual-chamber MFCs largely based on previous work modeling direct methanol fuel cells. The Nernst-Monod equation is used to describe ARB respiration at the anode, which dictates oxygen reduction reaction (ORR) rates at the cathode since the cathode is considered non-rate-limiting. Esfandyari et al. (2017) developed a dual-chamber cell model to determine the amount of current produced in the cell based on an ORR of O_2 to H_2O. The anode is modeled using Marcus et al. (2007) to determine theoretical current production based on three different models for specific growth rate: the Monod, Blackman, and Tessier models. Esfandyari et al. evaluate cathodic coulombic efficiency performance and the required O_2 cathodic loading rate by subtracting anodic and cathodic Ohmic overpotential, activation, and concentration overpotentials from the theoretical cell potential based on the Nernst equation like Oliveira et al. (2013). Esfandyari et al. assumes constant pH at the anode and cathode chambers, neglecting pH variations and concentration overpotential at either electrode, and no diffusion limitation through the membrane.

Ou et al. (2016a, 2016b, 2017) have provided significant advances in holistic modeling for batch MFCs under non-advective conditions. Ou et al. (2016a) developed a steady state, 1D model of a batch single-chamber MFC primarily to study the interrelationships between a bioanode and a biocathode. The anode model was divided into three layers: a metal current collector, the anode electrode, and the ARB biofilm. The anode biofilm was modeled based on Marcus et al. (2010). The cathode was modeled as four layers: a polytetrafluoroethylene (PFTE)-coated gas diffusion layer, a carbon cloth cathode, a catalyst-coated layer on top of the carbon cloth, and a

multispecies biofilm. At the anode and cathode, the values of several critical parameters, like limiting current density and the charge transfer coefficient, were assumed rather than quantified. Unlike previous models, pH was assumed variable, affecting concentration overpotentials at the anode and cathode. The cathodic biofilm performance and efficiency was determined by Monod kinetics. Ou et al. (2016b) expanded on their earlier work to develop a transient model of biocathode formation with the assumption of steady-state conditions and pH at the anode. In Ou et al. (2017), the authors added pH dependence at the anode and cathode, which affects overall cell performance. A clear advancement over other models, Ou et al. (2016a, 2016b, 2017) consider concentration overpotential at the anode and cathode using the Nernst equation; however, critical parameters--like limiting current density--were assumed rather than experimentally quantified. In addition, representing the anode and cathode by a few discreet layers is speculative since a plethora of assumptions must be made for critical parameters.

1.5 Dissertation Objectives

The main objective of my work is to provide a holistic mathematical model of MxCs using complex waste streams to produce different byproducts at the cathode, specifically H_2O_2. This requires a comprehensive understanding of the impacts of catalyst, electrolytes, and cell performance on the production of H_2O_2 at the cathode chamber.

My dissertation is organized into the following chapters:

1. In Chapter 2, I discuss a methodology for designing MPPCs. I systematically evaluate H_2O_2 production capability and loading of different catalysts and H_2O_2 compatibility with different membranes and catholytes at varying pH. These learnings are combined into a flat-plate, continuously-fed cathode MPPC that produces H_2O_2 at high concentrations and low energy input over a long operational period. This chapter was published in *ChemSusChem*.
2. In Chapter 3, I optimize the performance of the flat-plate MPPC discussed in Chapter 2. I vary several operating conditions, including HRT, catholyte type and dose, and stabilizer concentration, to evaluate their influence on MPPC performance like H_2O_2 production rate, effluent H_2O_2 concentration, and power consumption. I provide a perspective on these results that demonstrates that a medium-sized WWTP can produce 5-10x more H_2O_2 than is required for disinfection when coupled with UV treatment. This chapter was published in *Journal of Power Sources*.
3. In Chapter 4, I expand PCBIOFILM to provide a holistic mathematical model of anode chamber using a new model, MYAnode, which combines typical biological processes found in WWTPs (based on CASADM), chemical speciation and pH

changes (based on CCBATCH), and ARB substrate utilization and respiration at the anode (based on PCBIOFILM) to describe the influence of complex waste streams concentration on ARB electricity production. Based on the work by Ki et al. (2017a), this chapter focuses on utilization of primary sludge for current production by ARB for one set of scenarios, i.e., a 12-d HRT for primary sludge in the anode chamber. I explore the important role of alkalinity production by methanogens in low alkalinity waste streams, which is important for maintaining the appropriate pH range in ARB biofilms for respiration.

4. In Chapter 5, I expand upon the work presented in Chapter 4 to determine the effect on MxC performance of varying diffusion layer (DL) thickness from 500 to 1000 μm and particulate COD (PCOD) hydrolysis rates from 0.12 to 0.5/d. I explore how DL thickness impacts acetate and HCO_3^- concentrations availability for the ARB biofilm. I also discover that faster hydrolysis rates do not necessarily translate into increased CH_4 or current production.
5. In Chapter 6, I expand upon the work presented in Chapters 4 and 5 to determine the impact of varying HRT from 6 to 15 d on MxC performance to explore the potential synergies between methanogens and ARB.
6. In Chapter 7, I summarize the key findings in my research. I also provide recommendations on future research for optimization and applications of MPPCs and holistic MxC modeling.

CHAPTER 2

Tailoring microbial electrochemical cells for production of hydrogen peroxide at high concentrations and efficiencies

This work was published in a modified version in ChemSusChem *by Young et al. (2016).*

2.1 Introduction

Hydrogen peroxide (H_2O_2) is an industrial chemical used in the water and wastewater industries in low concentrations coupled with the Fenton process or UV treatment for advanced oxidation of complex organic chemicals and emerging contaminants (Campos-Martin et al., 2006; De la Cruz et al., 2012; Yang et al., 2014) and for disinfection (Glaze et al., 1987; Wagner et al., 2002; Ksibi, 2006; Kruithof et al., 2007; Snyder et al., 2008). For example, Badawy and Ali (2006) demonstrated that 550 mg/L H_2O_2 was sufficient for 92% COD removal and 100% color removal from wastewater diluted to 1600 mg COD/L. H_2O_2 is also effective in advanced oxidation processes at removing biological products or contaminants contributing to taste and odor (Acero and von Gunten, 2000; Drogui et al., 2001; Ksibi, 2006). Rajala-Mustonen and Heinonen-Tanski (1995) achieved a 3 to 4 log-units reduction in coliphages when coupling H_2O_2 with UV radiation for disinfection. Yang et al. (2014)'s review found many organic micropollutants can be remediated 99+% using H_2O_2 doses in the 50-150 mg/L range and moderate to high UV radiation doses (< 5000 mJ/cm^2).

While H_2O_2 itself is considered environmentally friendly, 95% of the world's H_2O_2 is produced using the energy-intensive anthraquinone-oxidation process, which uses dangerous compounds as catalysts (Campos-Martin et al., 2006). One potential

technology for sustainable H_2O_2 production is microbial peroxide producing cells (MPPCs). In MPPCs, ARB consume volatile fatty acids produced during fermentation and respire electrons to an anode, producing electrical current. The electrons pass through an external circuit to a cathode, where they reduce different electron acceptors. In cathodic ORR, O_2 is completely reduced to hydroxide ions, OH^-, to produce electrical power

$$O_2 + 2H_2O + 4e^- \rightarrow 4OH^- \qquad (E^{o'} = +1.018\ V_{Ag/AgCl}) \qquad \text{(Eqn. 2.1)}$$

or partially reduced to produce H_2O_2.

$$O_2 + 2H_2O + 2e^- \rightarrow H_2O_2 + 2OH^- \qquad (E^{o'} = +0.424\ V_{Ag/AgCl}) \qquad \text{(Eqn. 2.2)}$$

Above the pK_a of 11.8, H_2O_2 is produced as HO_2^- via

$$O_2 + H_2O + 2e^- \rightarrow HO_2^- + OH^- \qquad \text{(Eqn. 2.3)}$$

H_2O_2 synthesis is advantageous since it requires only a simple carbon catalyst and, depending upon the required rate of H_2O_2 production, has the potential to be produced with little or no energy input.

Researchers have had limited success producing H_2O_2 in MPPCs using batch reactors, as summarized in Table 2.1. Generally, either high concentrations of H_2O_2 were generated by adding energy into the system, or low H_2O_2 concentrations were produced along with a small output of electrical energy. Rozendal et al. (2009) produced 3.9 g H_2O_2/L-d and concentrations as high as 1.3 g/L but required 0.93 W-h/g H_2O_2. Conversely, Fu et al. (2010) produced a low H_2O_2 concentration of 79 mg/L, but generated 0.06 W-h/g H_2O_2. In an attempt to maximize H_2O_2 production, Modin and Fukushi (2013) produced 9 g/L H_2O_2 at a rate of 11.1 g/L-d while applying 3.0 W-h/g H_2O_2, demonstrating that high H_2O_2 concentrations can be achieved when enough energy is added to the system.

Most MPPC research has focused more on optimization of one or two variables, rather than a systematic investigation of factors affecting H_2O_2 production, net energy demand, and reactor design. Fu et al. (2010), Modin and Fukushi (2013), Arends et al. (2014), and Sim et al. (2015) focused on maximizing H_2O_2 production from different wastewater sources at different anode and cathode HRTs. Modin and Fukushi (2012) and Chen et al. (2014) focused on designing cathode catalysts for H_2O_2 production. Li et al. (2016) had a continuous-flow cathode but focused primarily on optimizing abiotic catalyst performance.

Several abiotic studies have demonstrated that H_2O_2 rapidly decomposes to H_2O when exposed to platinum-carbon catalysts via (Otsuka and Yamanaka, 1990; Yamanaka et al., 2003; Rabaey and Rozendal, 2010)

$$H_2O_2 + 2e^- + 2H^+ \rightarrow 2H_2O \qquad (E = +1.508\ V_{Ag/AgCl}) \qquad \text{(Eqn. 2.4)}$$

While carbon-based electrodes can achieve high H_2O_2 concentrations and current efficiencies through Eqn. 2.1, carbon electrodes can degade the H_2O_2 to H_2O, particularly when the catalyst layer is thick (Otsuka and Yamanaka, 1990; Foller and Bombard, 1995; Yamada et al., 1999; Li et al., 2016). Paulus et al. (2001) used a rotating-ring disk electrode (RRDE) to understand catalyst reaction pathways at a variety of operating conditions and catalysts characteristics.

pH can be an important source of overpotential in MPPCs. When the pH in the cathode chamber increases one unit at standard temperature and pressure, the MPPC incurs a ~60 mV drop in voltage based on the Nernst equation (Bard and Faulkner, 2001). Because ARB media is at their optimal pH of 7.0 (Lee et al., 2008), a pH 12 cathode incurs ~300 mV of concentration overpotential between the cathode and anode. Cathodic pH control is confounded by OH- production during H_2O_2 synthesis via Eqn. 2.2 and 2.3, increasing catholyte pH and overpotential. Ki et al.

(2016) tested the effects of pH-reducing buffers at the cathode to reduce pH-related concentration overpotentials and or determined that the addition of bicarbonate buffer decreased catholyte pH from ~1 to ~7, reducing the applied voltage by 200 mV.

The strong oxidant property of H_2O_2 further complicates MPPC design. H_2O_2 and its ions and radicals present chemical incompatibility problems with the materials typically used in MECs, including catalysts, binders, and membranes. Furthermore, the reactions by which H_2O_2 attacks MPPC materials also lead to H_2O_2 decomposition. Until now, research has not been performed to determine the compatibility of typical MEC materials with H_2O_2 and at high pH.

In previous works, Ki et al. (2016) designed a flat-plate, two-chamber MEC to maximize current densities and voltage efficiency by applying a high-surface area anode with buffered catholytes to reduce pH. Applied potentials and current densities were greatly affected by two factors: reduced distance between the anode and cathode and the use of buffered catholyte to reduce the pH gradient between the anode and cathode chambers. Reducing the distance between anode and cathode to ~0.5 cm minimized Ohmic overpotentials between the electrodes. In addition to these results, Ki et al. (2016) found that membrane selection had the smallest effect on system overpotentials.

In this work, I outline a methodology for designing MECs for H_2O_2 production. I modify Ki et al. (2016)'s MEC design to construct an MPPC that achieves long-term, continuous H_2O_2 production. I first evaluated various membranes, cathode materials, and catholytes for H_2O_2 compatibility. I then apply my learnings to design and operate a continuous-flow cathode in a flat-plate MPPC to obtain a good balance of H_2O_2 concentration (>3.1 g/L H_2O_2) and a low power input (1.1 W-h/g H_2O_2).

Table 2.1. H_2O_2 production in MECs as reported in literature. All reactors were dual-chamber systems. Anion exchange membranes are abbreviated as AEM and cation exchange membranes as CEM.

Authors	Cathode setup	Membrane type	Cathode HRT (h)	Anolyte/ Buffer	Catholyte	Maximum H_2O_2 concentration (g/L)	H_2O_2 production rate (g/L-d)	Maximum current and power/voltage applied	Power input required (W-h/g H_2O_2)
Arends et al. (2014)	Batch	AEM	4	Domestic and hospital wastewaters	50 mM NaCl	0.34	2.0	10 A/m^2 at 0.6V	2.5
Chen et al. (2014)	Batch	3-D CEM	24	Domestic wastewater and 12 mM acetate media/50 mM PBS	50 mM $NaSO_4$	0.2	0.2	18.4 A/m^3 at 0.04V *produced*	0.09 *power output*
Fu et al. (2010)	Batch	CEM	3	Glucose media/50 mM PBS	50 mM $K_3Fe(CN)_6$ + PBS	0.08	0.6	0.2 A/m^2 at 0.4V *produced*	0.06 *power output*
Li et al. (2016)	Continuous	CEM	0.023	12 mM acetate media/50 mM PBS	50 mM $NaSO_4$	$8x10^{-5}$	0.1	6.1 A/m^2 at 0.6V	56
Modin & Fukushi (2012)	Batch	CEM	47	Acetate media	50 mM NaCl	5	2.6	2.5 A/m^2 at 3.8V	2.3
Modin & Fukushi (2012)	Batch	CEM	21	Domestic wastewater	50 mM NaCl	0.08	0.1	0.4 A/m^2 at 0.9V	1.8
Modin & Fukushi (2013)	Batch	CEM	21	6 mM acetate media/10 mM PBS	50 mM NaCl	9.7	11.1	1.7 A/m^2 at 11.8V	3.0
Rozendal et al. (2009)	Batch	CEM	8	12 mM acetate media/190 mM PBS	50 mM NaCl	1.3	3.9	5.3 A/m^2 at 0.5V	0.93
Sim et al. (2015)	Batch	CEM	2-24	5 mM acetate media/50 mM PBS	Deionized water	1.4	$7.9x10^{-4}$	7.7 A/m^2 at 1V	2.6
Sim et al. (2015)	Batch	CEM	2-10	Raw domestic wastewater	Deionized water	0.15	$8.5x10^{-5}$	0.56 A/m^2 at 6.3V	28
This chapter	**Continuous**	**AEM**	**4**	**Acetate media**	**200 mM NaCl**	**3.1**	18.6	**10.1 A/m^2 at 0.31V**	**1.1**

23

2.2 Materials and Methods

2.2.1 H_2O_2 measurements and stability tests

For membrane stability experiments, I measured H_2O_2 concentration using the National Diagnostics Hydrogen Peroxide Assay Kit. For all other experiments, I analyzed H_2O_2 using the method of Graf and Penniston (1980). Colorimetric measurements were performed using a Cary 50-Bio UV-Visible spectrophotometer (Varian, Palo Alto, CA). When compared, these two methods demonstrated equivalent results (not presented here).

I evaluated H_2O_2 stability with different electrolytes. I prepared 200-mL solutions of 10 g/L H_2O_2 in five different electrolytes: 200 mM pH 4.5 phosphate buffer solution (PBS), 200 mM pH 7.5 PBS, 200 mM NaCl at pH 6.5, 200 mM NaCl at pH 12, and 200 mM Na_2CO_3 at pH 11.5. Sixty-five mL of each electrolyte combination were placed in three 100-mL glass serum bottles and corked with butyl-rubber stoppers (Bellco Glass, NJ) and aluminum caps. I removed 2-mL samples using a needle and syringe from each bottle at 2, 4, 6, and 12 h and every 12 h subsequently for 120 h. Samples were analyzed for pH and H_2O_2 concentration.

2.2.2 Membrane stability tests

I characterized five ion exchange membranes to determine their compatibility with H_2O_2: three anion exchange membranes (AEMs) including AMI-7001 (Membranes International, Inc.), Excellion I-200 (SnowPure LLC), and fumasep® FAA (fumatech GmbH); and two cation exchange membranes (CEMs) including CMI-7000 (Membranes International, Inc.) and Nafion-117 (Dupont™). I tested unconditioned membrane

stability in solutions with H_2O_2 and pH 7 and 12. Membranes with surface areas of 9 cm^2 samples were cut, left at ambient lab conditions for 48 hours, and weighed. The membranes were placed in 25-mL serum bottles filled with 20 mL of 100 mM NaCl at pH 12, 100 mM NaCl with 10 g/L H_2O_2 at pH 12, or 100 mM NaCl with 10 g/L H_2O_2 at pH 7. I adjusted the electrolyte pH to 12, as it is the highest pH anticipated during MPPC operations. Bottles were prepared in triplicate, capped with butyl rubber stoppers and aluminium crimps, and degassed regularly. After 45 days, I emptied the bottles' contents and analyzed the solutions for H_2O_2 concentration and pH. Membranes were washed with deionized (DI) water and dried under ambient laboratory conditions prior to measuring the final mass.

2.2.3 Catalyst/binder characterization

I performed RRDE tests using a RRDE-3A rotating ring disk electrode apparatus (ALS-Japan) to determine potential H_2O_2 production efficiency from different catalyst/binder combinations. I used a Vulcan carbon catalyst-Nafion binder mixture to coat the catalyst layer on the disk electrode at catalyst loadings of 0.22, 0.44, 0.67, 0.89, and 1.12 mg/cm^2. The ring/disk electrode was rotated at 1200 rpm for ~30 minutes until the ink dried. Once dried, the ring was submerged in 100-mM NaCl sparged with O_2 for >30 minutes to saturate the solution. I measured the ring and disk current densities at a disk speed of 1600 rpm and ring potential of 0.08 $V_{Ag/AgCl}$, and the disk potential was varied from -0.60 to 0 $V_{Ag/AgCl}$ at a scan rate of 10 mV/s to determine the number of electrons transferred to O_2.

2.2.4 MPPC setup and operation

Figure 2.1 illustrates the two-chamber, flat-plate MPPC operated at 30°C. The anode, cathode, and membrane had geometrical areas of 49 cm^2. The anode chamber volume was 200 mL. The anode was composed of carbon fiber (24K Carbon Tow, Fibre Glast, OH, USA) woven through a titanium frame, as detailed in Ki et al. (2016). An AMI-7001 membrane was preconditioned in 2 M NaCl for one day prior to use. The cathode chamber consists of a 18-mL liquid serpentine flow cell and a serpentine air chamber supplied with 30 cm^3/min air (EcoPlus® Eco Air 3 commercial pump). The two cathode chambers are separated by the carbon cloth cathode (FuelCellsEtc GDL-CT). The liquid-exposed side of the cathode was coated with a slurry of 0.5 mg/cm^2 Vulcan carbon powder using a paint brush. The catalyst slurry consisted of 0.5 g Vulcan carbon powder, 3.5 mL 0.83 mL/cm^2 of 5% Nafion dispersion in alcohol (D521; FuelCellStore). The air-exposed microporous layer side is coated with 2 layers of 16 mg/cm^2 Teflon PTFE DISP 30 cured 15 minutes at 200°C and 1 hour at 280°C to improve cathode hydrophobicity. The distance separating the anode and cathode was ~0.5 cm. I used a Bioanalytical Systems, Inc. RE-5B Ag/AgCl reference electrode (+0.27 V_{SHE} in acetate media at 30°C) and a Bio-Logic VMP3 potentiostat to control anode potential at -0.30 $V_{Ag/AgCl}$ and monitored current production. I measured pH using Thermo Scientific, Inc.'s Orion 2 Star pH meter.

I inoculated the anode chamber with effluent from operating MECs in the Biodesign Swette Center for Environmental Biotechnology laboratory to develop current-producing biofilms. The MPPC's anode was poised at -0.3 $V_{Ag/AgCl}$ and operated in batch mode until biofilms were formed and then placed into continuous-flow mode fed with

100-mM acetate medium (~pH 7; detailed in Parameswaran et al., 2012) at a 0.5-h HRT. The cathode was operated in continuous-flow mode and fed 200 mM NaCl catholyte with a 4-h HRT to the liquid chamber and 20 cm^3/min air to the air chamber. The MPPC operated in the peroxide-producing mode for more than three weeks.

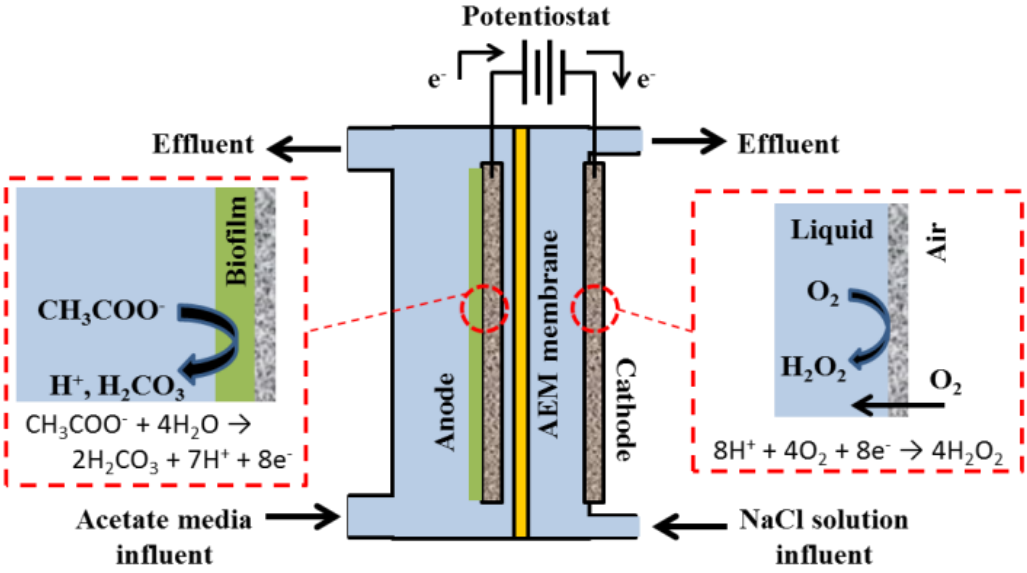

Figure 2.1. A schematic of the MPPC configuration used to produce H_2O_2 in the liquid cathode chamber.

2.3 Results and Discussion

2.3.1 H_2O_2 stability tests

Figure 2.2 illustrates that H_2O_2 was more stable at lower pH in 120-h stability tests. Phosphate buffers performed well, with pH 4.5 PBS resulting in no H_2O_2 detectable degradation in 24 h and 7% degradation over 120 h, while pH 7.5 PBS resulted in 6% degradation over 24 h and 21% degradation over 120 h, which is consistent with Yang et al. (2014). A NaCl solution at pH 6.5 also resulted in short-term stability of H_2O_2, as H_2O_2 degraded 13% in 24 h and 62% in 120 h. H_2O_2 became increasingly unstable as pH increased to alkaline conditions in the presence of Na_2CO_3 and NaCl. H_2O_2 in pH 11.5 Na_2CO_3 degraded 31% within the first 2 h and 99% within 24 h. Similarly, 49% of H_2O_2 degraded in pH 12 NaCl within 24 h. The susceptibility of H_2O_2 to degradation under alkaline conditions is consistent with Abbot and Brown (1990) and Qiang et al. (2002). Worsening stability with CO_3^{2-} may be attributed to increased H_2O_2 decomposition rates caused by the formation of metal-hydrogen-carbonate complexes in alkaline conditions (Nicoll and Smith, 1955; Csanyi and Galbacs, 1985; Navarro et al., 1984; Lee et al., 2000).

From a broader perspective, the decreasing stability of H_2O_2 at higher pH becomes a processing and storage issue. My stability tests confirm that alkaline-produced H_2O_2 cannot be stored long-term without significant degradation. Thus, maintaining a relatively low or neutral pH at the cathode is optimal for H_2O_2 production and stability.

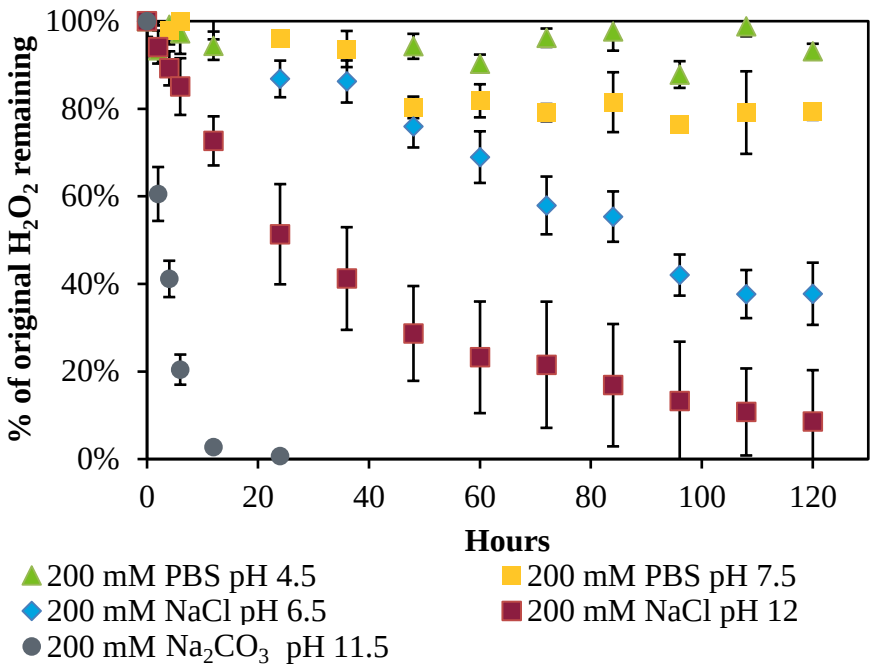

Figure 2.2. H_2O_2 stability in different electrolytes at different pHs.

2.3.2 Membrane materials selection

Several factors are considered important in membrane selection. Membrane compatibility with H_2O_2 is the most important factor as contaminants or functional groups on the membrane may potentially contribute to H_2O_2 degradation either catalytically or through a decomposition reaction with the membrane itself. H_2O_2 reacting with the membrane may destabilize the membrane's integrity, leading to membrane failures. Membrane compatibility at different pHs is also important since the OH^- produced during the ORR (Eqn. 2.2) has the potential to significantly increase the catholyte pH, and H_2O_2 deprotonates to the more reactive HO_2^- at the pK_a of 11.8. Therefore, I evaluated H_2O_2 degradation and membrane weight loss over a 45-day exposure period at pH 7 and 12. I used electrochemical impedance spectroscopy (EIS; detailed in the Appendix A) to evaluate membrane Ohmic overpotentials. Finally, the

choice of using an AEM or CEM results in operational trade-offs. HO_2^- produced at high pH can potentially diffuse across an AEM. However, a CEM provides preferential diffusion of cations other than H^+ to the cathode to maintain electroneutrality, potentially lowering the pH below an acceptable threshold for ARB.

AMI-7001, CMI-700, and FAA membranes were evaluated for stability in a 10 g/L H_2O_2 solution at pH 7. After 45 days of exposure, there was negligible H_2O_2 degradation at pH 7 (Appendix Figure A.1a), and the membranes experienced negligible mass loss (Appendix Figure A.1b). This stability was likely due to the membranes being well suited for use near neutral pH and increased H_2O_2 stability at pH 7.

Since OH^- production due to H_2O_2 formation at the cathode would likely increase catholyte pH during MPPC operations, membranes were evaluated for compatibility and H_2O_2 degradation at pH 12. Appendix Figure A.2 illustrates that H_2O_2 was most stable in the presence of the Nafion membrane: ~11% of the total H_2O_2 was degraded over 45 days while the electrolyte pH decreased from pH 12 at day zero to pH 2.5 at day 45. This degradation was significantly lower than the 91% degradation exhibited during H_2O_2 stability tests without the membrane (Figure 2.2). All other membranes exhibited >85% H_2O_2 degradation, values similar to the 91% degradation measured during H_2O_2/NaCl stability tests without a membrane without significant pH change between days 0 and 45. Thus, the lack of degradation with Nafion was likely due to acidification of the electrolyte.

H_2O_2 degradation did not necessarily correlate with membrane mass loss during the stability tests. Figure 2.3 illustrates that all membranes had weight loss at pH 12, regardless of the presence of H_2O_2. Except CMI-7000, all other membranes exposed to

H_2O_2 experienced higher weight loss than membranes exposed to electrolyte only. The CEM membranes demonstrated lower differences in weights (< 5% for both CEMs) than AEMs, since the CEMs' negatively charged active sites likely repelled HO_2^- ions from the membrane. For AEMs, the I-200 membrane had a 14% difference between the H_2O_2-exposed and electrolyte-only masses, making it the AEM with the smallest change in mass when exposed to H_2O_2. AMI-7001 and FAA lost 39% and 44% more mass, respectively, when exposed to H_2O_2 versus pH only.

While FAA is rated by the manufacturer as stable at pH 12, FAA's lower thickness (130 μm) may have contributed to a lower structural integrity, causing the membrane to disintegrate when exposed to H_2O_2 at pH 12 (Appendix Figure A.3). AMI-7001 experienced the lowest absolute mass loss (0.69 mg/cm^2 with and 0.96 mg/cm^2 without H_2O_2), which I speculate is due to either AMI-7001 being a less reactive material or its greater thickness (3.5x thicker than FAA), which hampered H_2O_2 permeation into and, therefore, decomposition of the membrane. Total organic carbon (TOC) analyses (detailed in Appendix A) revealed that membranes exposed to H_2O_2 and/or high pH consistently produced more TOC over the duration of the experiment, likely caused by the release of complex soluble organics into solution during polymer deterioration (Appendix Figure A.4).

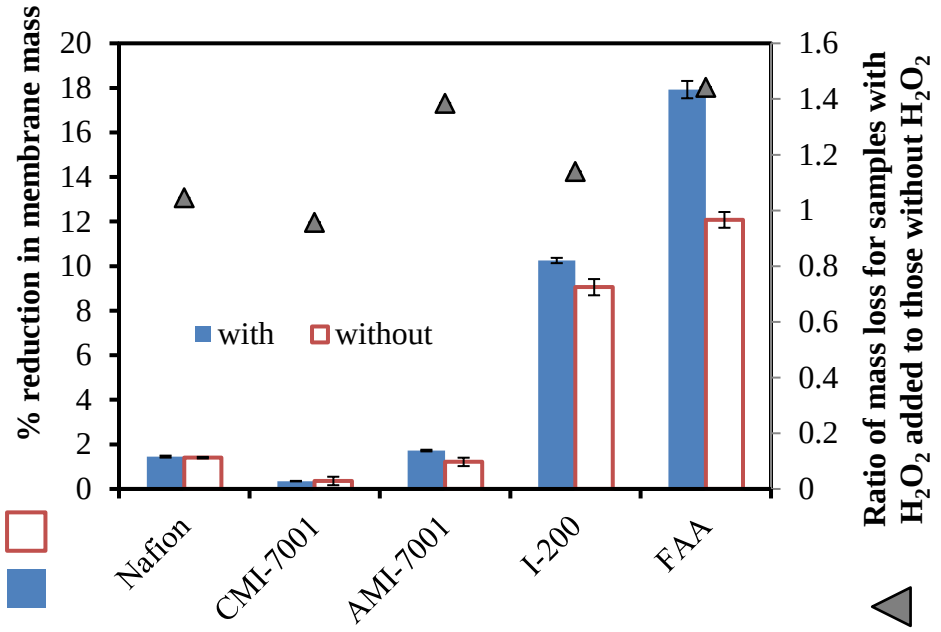

Figure 2.3. (left axis) Percent reduction in membrane mass during batch bottle tests for membrane stabilities with 10 g/L H_2O_2 at pH 12 and (right axis) ratio of mass loss for membranes exposed to H_2O_2 versus membranes exposed to pH 12 only. Values >1 indicate that membranes exposed to H_2O_2 lost more weight than membranes exposed to electrolyte only. Values <1 indicate that membranes exposed to electrolyte only lost more weight than membranes exposed to H_2O_2.

Nafion, AMI-7001, and FAA demonstrated greater H_2O_2 stability in the short term, making them the most viable candidates for an MPPC. In addition, all membranes exhibited low Ohmic losses <85 Ω-cm^2 (detailed in Appendix A). Based on this evaluation, I opted to use an AEM in the MPPC to provide easy regulation of anode pH. Based on its low reactivity with H_2O_2, I chose to utilize AMI-7001 for MPPC experiments. If pH rises at the cathode, catholyte choice could help regulate the pH near neutral to reduce concentration overpotentials.

2.3.3 Cathode materials characterization

I utilized linear sweep voltammetry in a half-cell with 100-mM sodium perchlorate to narrow my catalyst and binder choices to Vulcan carbon and Nafion, respectively (method detailed in the Appendix A). The Vulcan carbon had ~0.4V lower activation potential than graphite carbon using the same binder (Appendix Figure A.7).

I used RRDE testing to determine the optimal Vulcan carbon loading, as it distinguishes between 2-electron and 4-electron ORR. Consistent with Bonakdarpour et al. (2008) and Paulus et al. (2001), lower catalyst loadings routed a higher number of electrons to H_2O_2, instead of to H_2O. From Figure 2.4 and between -0.37 to -0.57 $V_{Ag/AgCl}$, loadings of 0.22 and 0.45 mg/cm^2 provided the lowest average catalyst loading, 0.22 mg/cm^2, yielded an average of 2.04 ± 0.03 electrons per O_2 reduced, or almost 100% delivery of electrons to the 2-electron reduction to H_2O_2. The highest catalyst loading (1.12 mg/cm^2) yielded an average of 2.72 ± 0.06 electrons per O_2 reduced, or about two-thirds of the electrons were routed to H_2O. At higher loadings, the produced H_2O_2 must be transported through a thick catalyst layer, providing additional catalyst-contact time that increases the likelihood H_2O_2 is reduced again through Eqn. 2.4 to H_2O. Figure 2.4 also demonstrates the disk potentials because the cell required current input regardless of operating potential in order to operate. At an E_{KA} (the anode potential at one-half of the maximum current density) of -0.42 $V_{Ag/AgCl}$ for *Geobacter sulfurreducens*, the MPPC will likely require some small power input to produce H_2O_2 (Torres et al., 2008a).

To summarize, the Vulcan carbon/Nafion binder combination produced the lowest cathodic overpotentials with an optimal Vulcan carbon loading of ~0.45 mg/cm^2 for the

highest H_2O_2 production over a wide range of cathode potentials. Based on these results, I applied ~0.5 mg/cm^2 Vulcan carbon to the cathode for MPPC operations.

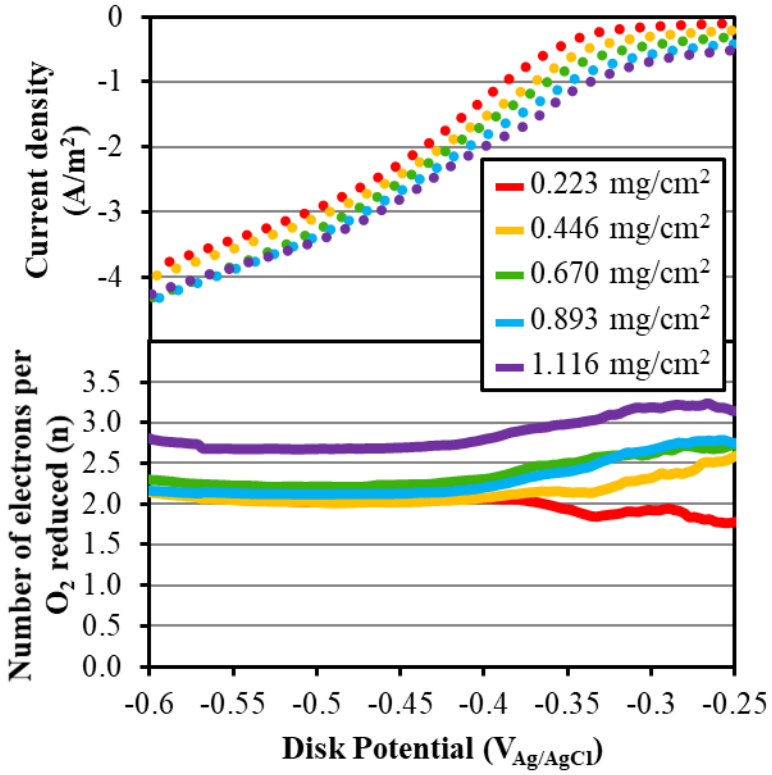

Figure 2.4. Ring current density (dotted lines) and the number of electrons per O_2 reduced (n; solid lines) as a function of disk potential for Vulcan carbon catalyst loadings ranging from 0.22 to 1.12 mg/cm^2.

2.3.4 MPPC operation

I assembled a MPPC using the optimal conditions from my previous testing: 200 mM NaCl at pH 7, which demonstrated good stability with H_2O_2 in the short term; the AMI-7001 AEM, which demonstrated low mass loss; and 0.5 mg/cm^2 of Vulcan carbon catalyst with Nafion binder, which maintained lowest cathodic overpotentials over the largest range while partitioning the highest number of electrons to H_2O_2. I operated the MPPC continuously for 18 days with a 4-h HRT in the liquid cathode chamber and air

flow rates of 10, 20, and 30 cm^3/min through the air cathode chamber. Prior to anode inoculation, I quantified the total cell abiotic Ohmic overpotential using EIS as 75.0 Ω-cm^2.

As demonstrated in Figure 2.5, the MPPC gave good performance with the optimized design variables. Varying the air supply rate had minimal effect on H_2O_2 concentration: the average effluent H_2O_2 ranged from 2.5 ± 0.4 to 3.1 ± 0.4 g/L, with the highest H_2O_2 concentration (3.8 g/L) achieved at 20 cm^3/min. These high concentrations were achieved even though the effluent catholyte pH ranged from 12.1 to 12.4. While the cathode potential decreased from -0.54 to -0.50 $V_{Ag/AgCl}$, the H_2O_2 concentration decrease from 20 to 30 cm^3/min likely was due to the 1 A/m^2 decrease in current density. For comparison, my cell used 18% more energy to produce 3 times the amount of H_2O_2 compared to Rozendal et al. (2009).

I used cyclic voltammetry (CV) to understand my MPPC's performance. The CVs illustrated that the MPPC achieved higher energy-neutral current densities (i.e., the current at which the reactor experiences 0 V cell potential) than other systems due to reduced overpotentials, and cathodic overpotentials are still the limiting factor in MPPC performance. Figure 2.6 shows a CV of my MPPC at a 1 mV/s scan rate. Correcting for Ohmic losses in the system, the open-circuit potential was 0.20 V for all scans, which is lower than the theoretical potential of 0.56 V. The ~0.3 V difference is associated with the equilibrium pH difference between the anode and cathode since there was a ~5 pH unit difference between the anode and cathode. Energy neutral operations occurred at 3.72 ± 0.29 A/m^2, which is significantly larger than that achieved by Rozendal et al. (2009), at 1.6 A/m^2, and Modin and Fukushi (2012), 0.54 A/m^2. The superior energy-

neutral performance indicates that H_2O_2 could be produced at up to 3.72 A/m^2 without requiring energy input, and the cell had significantly lower overpotentials versus previous studies. Based on the theoretical potentials at the anode and cathode and not corrected for Ohmic losses, Figure 2.5a demonstrates that, at energy neutral conditions, the anode overpotential was 0.149 V and cathode overpotential was 0.379 V. Concentration overpotential due to pH differences between the anode and cathode chambers account for 0.27 V or 51% of cathode overpotentials. Therefore, 0.029 V of Ohmic overpotential exists at energy neutral conditions, reiterating that my cell design significantly decreases Ohmic losses within the MPPC. While small, these Ohmic losses significantly affected cell performance: adjusted for Ohmic losses, Figure 2.5b shows that the anode and cathode overpotentials increase to 0.157 V and 0.403 V, respectively, and that the cell could operate at 4.58 A/m^2 before drawing additional energy to produce H_2O_2. At the operating current density of ~ 10 A/m^2 and pH 12.08-12.43, the cathode overpotential increased to 0.524 V, of which 58% was due to pH differences between the anode and cathode chambers. As discussed in Popat and Torres (2016), the production of OH^- ions during the oxygen reduction reaction increases pH at the cathode, making it more difficult to reduce the cathode operating pH and, consequently, concentration overpotential.

The superior performance of the MPPC I report here likely was due to a combination of several factors. The improvement in energy-neutral operations was largely driven by the decreased distance between anode and cathode: When the distance was decreased from 1 to 0.5 cm in the MPPC, the energy-neutral current density increased from 1.63 (± 0.03) to 3.72 A/m^2 (Appendix Figure A.5). Catalyst selection

tailored to H_2O_2 production resulted in low cathode potentials and good net cathodic efficiencies with little power input. The use of AMI-7001 membrane provided long term, stable performance while having minimal effect on H_2O_2 production versus other membranes, as shown in Appendix Figure A.5. Nevertheless, performance could be further improved by reducing the pH gradient between the anode and cathode chambers, consequently reducing the MPPC's concentration overpotential.

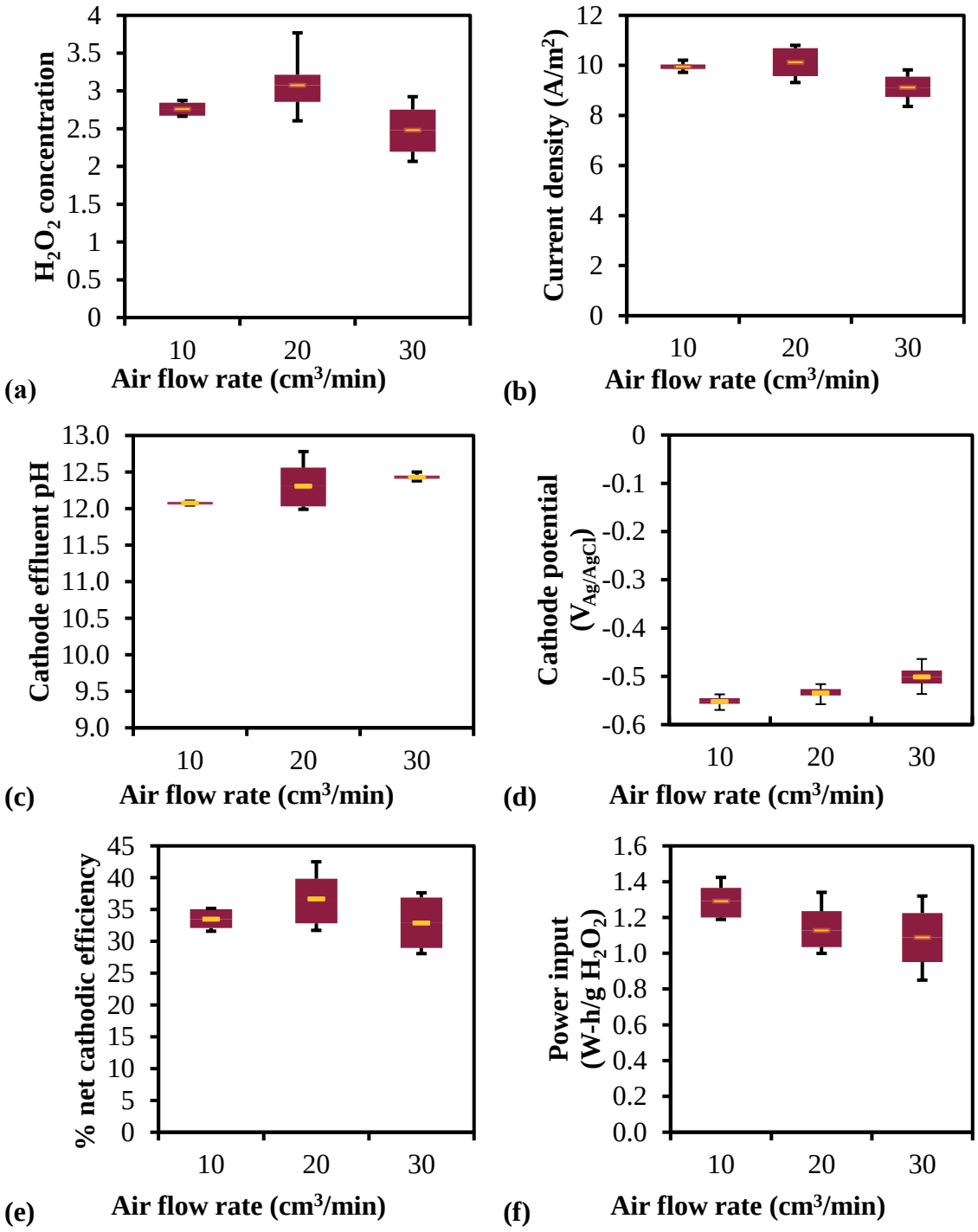

Figure 2.5. Performance during continuous operations with varying air flow rate: (a) H_2O_2 concentration, (b) current density, (c) pH, (d) cathode potential, (e) percent net cathodic efficiency (as H_2O_2), and (f) power input required to produce 1 g of H_2O_2.

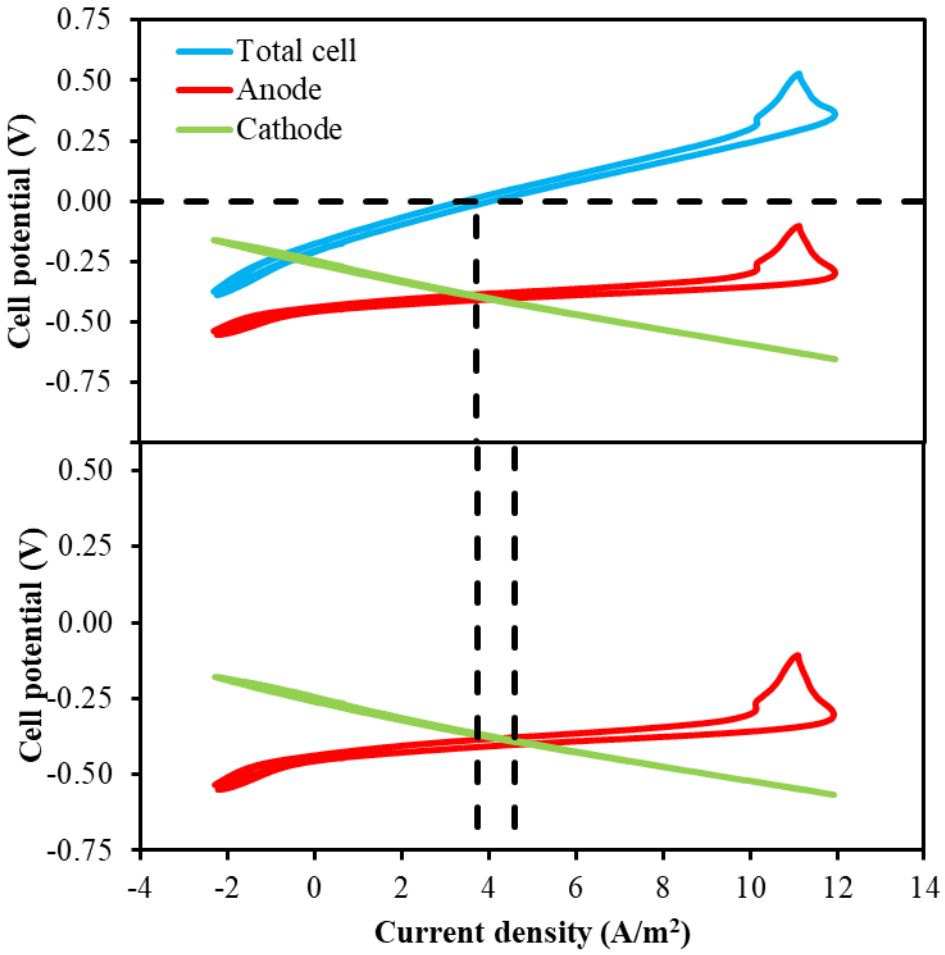

Figure 2.6. Cyclic voltammetry of the MPPC for (a) unadjusted cell and (b) Ohmic corrected potentials, with cell (blue), anode (red), and cathode (green) potentials. For the cell potentials, positive voltages represent power consumption and negative voltages represent power production.

2.4 Conclusions

In this work, I outlined a methodology for designing MECs for H_2O_2 production. I described the materials characterization required to design MECs to continuously produce H_2O_2. The Vulcan carbon/Nafion binder combination provided chemical stability with H_2O_2, while producing minimal activation overpotentials versus graphite catalyst. Using RRDE, I determined that the optimal catalyst loading to achieve the 2-electron ORR reaction was ~0.5 mg/cm^2. AEM membrane stability tests established AMI-7001 as the optimal membrane to resist H_2O_2 degradation and promote long-term MPPC performance due to its high structural integrity.

I combined these findings into a continuous flow flat-plate MPPC, which I operated using 200-mM NaCl catholyte at different air flow rates to optimize H_2O_2 concentration. Air flow rate did not drastically change MPPC performance: the MEC produced as high as 3.8 g/L H_2O_2 and an average of 2.5 ± 0.4 to 3.1 g/L H_2O_2 at the different air flow rates. MPPC's Ohmic overpotentials were small at 69.1 Ω-cm^2. During operation, anodic overpotentials were ~42% lower than cathodic overpotentials, and >58% of cathodic overpotential was caused by the pH gradient between the anode and cathode chambers. Thus, I assert that continuous H_2O_2 production in MECs is obtainable when materials are optimized for compatibility with and production of H_2O_2.

For perspective, my MPPC is capable of producing H_2O_2 at concentrations more than adequate for water and wastewater treatment. H_2O_2 concentrations of 2.5-3.0 g/L are 5- to10-fold higher than the doses required to remove 90+% COD from wastewater streams (Badawy and Ali, 2006; Ksibi, 2006), 20-fold greater than required for 99%+

removal of micropollutants and 10 to 100-fold higher than required for UV disinfection (Rajala-Mustonen and Heinonen-Tanski, 1995; Snyder et al., 2008; Yang et al., 2014).

CHAPTER 3

Understanding the Impact of Operational Conditions on Performance of Microbial Peroxide Producing Cells

This work was published in a modified version in Journal of Power Sources by Young et al. (2017).

3.1 Introduction

H_2O_2 is an industrial chemical widely used in the water and wastewater industries for advanced oxidation of complex organic chemicals and emerging contaminants (Campos-Martin et al., 2006; De la Cruz et al., 2012; Yang et al., 2014) and for disinfection (Glaze et al., 1987; Wagner et al., 2002; Ksibi, 2006; Kruithof et al., 2007). Currently, 95% of the world's H_2O_2 is produced using the anthraquinone-oxidation process, which is energy intensive and uses potentially carcinogenic compounds as catalysts (Campos-Martin et al., 2006; Hart and Rudie, 2014).

The MPPC is a technology for sustainable H_2O_2 production, particularly as part of wastewater treatment. In MPPCs, ARB consume volatile fatty acids from fermentation of organic wastes and respire electrons to an anode, producing an electrical current that travels to the cathode. At the cathode, oxygen (O_2) can be reduced by 4 or 2 electrons. The 4-electron ORR is:

$$O_2 + 2H_2O + 4e^- \rightarrow 4OH^- \qquad (E^{o\prime} = +0.81\ V_{SHE}) \qquad \text{(Eqn. 3.1)}$$

It is employed with power production as the goal. H_2O_2 is produced via the 2-electron ORR

$$O_2 + 2H_2O + 2e^- \rightarrow H_2O_2 + 2OH^- \qquad (E^{o\prime} = +0.28\ V_{SHE}) \qquad \text{(Eqn. 3.2)}$$

below H_2O_2's pKa ~11.8, or

$$O_2 + H_2O + 2e^- \rightarrow HO_2^- + OH^- \quad \text{(Eqn. 3.3)}$$

above the pKa. The 2-electron reduction has a smaller $E^{0'}$, making power production difficult, but synthesizing H_2O_2 is advantageous since it requires only a simple carbon catalyst and generates a useful chemical product. Ki et al. (2016) achieved H_2O_2 synthesis with a cathodic overpotential < 0.2 V, making it possible to generate H_2O_2 with little or no energy input. The MPPC technology is well suited for application in WWTPs, since the oxidation of biochemical oxygen demand (BOD) at the anode is accompanied by generation of H_2O_2 that can be used for disinfection later in the final stages of wastewater treatment, thereby reducing commodity costs.

Several researchers produced H_2O_2 using MPPCs with batch cathode chambers, and these studies demonstrated a clear tradeoff between H_2O_2 concentration and energy input. For example, Rozendal et al. (2009) demonstrated 1.3 g H_2O_2/L production with an 8-h retention time but required 0.93 Wh/g H_2O_2. Fu et al. (2010) produced 20 Wh/g H2O2 of energy but produced only 70 mg H_2O_2/L in 3 h of operation. Modin and Fukushi (2013) produced 9 g H_2O_2/L using acetate media in 21 h but applied 2.9 Wh/g H_2O_2. For comparison, the anthraquinone oxidation process uses 2 to 10 Wh to produce 1 g of H_2O_2 (Althaus et al., 2007; Goor et al., 2000; Eul et al., 2001), and electrochemical processes require 4-5Wh of energy to produce 1 g of H_2O_2 (Foller and Bombard, 1995; Goor et al., 2000; Eul et al., 2001).

Young et al. (2016) outlined a methodology for designing and operating a continuous MPPC to achieve high concentrations of H_2O_2 with low power input. They demonstrated that several potential electrolytes, including NaCl, phosphate buffer, and

bicarbonate buffer, provide good short-term stability of H_2O_2 (< 6-h). They tested a variety of catalysts, catalyst loadings, membranes, and catholytes in a flat-plate, continuous flow MPPC to determine their effects on H_2O_2 production. Their novel design included a serpentine flow cathode chamber to help minimize hot spots (i.e., areas where the localized voltage is much higher or lower than the rest of the electrode due to inconsistencies in catalyst coating, lack of advection, etc.) at the cathode and provide adequate mixing to achieve an average H_2O_2 concentration of 3.1 g/L at 37% cathodic coulombic efficiency using 200-mM NaCl as the catholyte. They also reduced the distance between the anode and cathode to ~0.5 cm to reduce Ohmic losses within the system.

Despite Young et al. (2016) achieving a balance between high H_2O_2 concentrations and lower power input, the catholyte pH was consistently > pH 12, meaning that H_2O_2 was present in its more reactive form (HO_2^-) and that the concentration overpotential between the anode and cathode chambers was large. By substituting Eqn. 3.2 into the Nernst equation, the potential of the reaction (E) is:

$$E = E^{0\prime} - \frac{RT}{nF}\log\left(\frac{[\text{Products}]}{[\text{Reactants}]}\right) = E^{0\prime} - \frac{RT}{2F}\log\left(\frac{[H_2O_2][OH^-]^2}{[O_2]}\right) = E^{0\prime} - \frac{RT}{F}\log\left(\frac{[H_2O_2][OH^-]}{[O_2]}\right) \quad \text{(Eqn. 3.4)}$$

where $E^{0\prime}$ is the standard reaction potential at 298 K, R is the ideal gas constant, T is temperature, F is Faraday's constant, and n is the number of electrons involved in the reaction. The term RT/F simplifies to ~60 mV; thus, a one-unit increase in the pH difference between the anode and cathode chambers results in concentration overpotential of ~60 mV (Bard and Faulkner, 2001; Popat and Torres, 2016). Since ARB anolyte

medium typically has pH ~7, a cathode pH ≥ 12 incurs ~300mV of concentration overpotential between the cathode and anode.

In this paper, I expand on the work presented in Young et al. (2016) to demonstrate long-term continuous production of H_2O_2 in an MPPC fed at the anode with acetate media to provide a comprehensive assessment of the effect of different operating conditions and parameters on MPPC performance, which comes from a balance between the rates of H_2O_2 production and auto-decay. The net decay rate is determined by the auto-decay rate and the catholyte hydraulic retention time. I begin by assessing performance with a typical electrolyte, NaCl, with varying HRT and concentration. Based on the opportunities identified in these trials, I expand my assessment to evaluate methods to increase H_2O_2 effluent concentration by using buffering electrolytes and an H_2O_2 stabilizer. I compare H_2O_2 production rates, coulombic efficiency, and required power input to determine the optimal conditions for long term MPPC operations. My results indicate that H_2O_2 concentrations >3.1 g/L can be sustained using NaCl, with less than 0.4 Wh/g H_2O_2 power input and as high as 78% net cathodic efficiency. At these production rates and using primary sludge (PS) or waste-activated sludge (WAS) as the substrate at the anode, a typical WWTP could provide 3- to 10-fold more H_2O_2 than required for UV coupled disinfection and micropollutant removal. I also document how anode and cathode phenomena confounded the benefits of buffering the pH and using an H_2O_2 stabilizer, EDTA, at the cathode.

3.2 Materials and Methods

3.2.1 Analytical techniques

H_2O_2 concentrations were determined using the blue starch-iodine colorimetric method summarized in Graf and Penniston (1980), with colorimetric measurements performed using a Cary 50-Bio UV-Visible spectrophotometer (Varian, Palo Alto, CA). COD was measured using high range HACH COD digestion vials (detection range 10-1500 mg/L). I measured pH using the Thermo Scientific, Inc. Orion 2 Star bench top pH meter.

To detect EDTA, anode samples were filtered through Acrodisc® 0.2-mm PVDF filters (Pall Life Sciences) and prepared for gas chromatography using Scandinavian Pulp, Paper and Board Test Committee's (2009) method based on derivatization of EDTA with boron trifluoride in methanol and chloroform. The solutions were analyzed using a Shimadzu GC-2010 with a flame ionization detector (GC-FID) (Columbia, Maryland) and a Restek Rxi®-1HT dimethyl polysiloxane column (30 m length, 0.25 mm ID, and 0.25 mm film thickness).

Chloride and phosphate concentrations were determined using the ICS-3000 Dionex ion chromatography (IC) system equipped with an IonPac® AS-20 anion exchange column, AG-20 guard column, and 150 mg/L injection loop. The column is capable of detecting F^-, Br^-, and NO_2^- at lower detection limits of 0.004 mM, Cl^- at 0.003 mM, and SO_4^{2-}, NO_3^-, and PO_4^{3-} at 0.002 mM. Although I tested for all anions, only Cl^- and PO_4^{3-} ions were detected in my samples.

Calculations for net cathodic coulombic efficiency and ionic current are discussed in Appendix B.

3.2.2 MEC design and operation

Following Young et al. (2016), I operated a two-chamber, flat-plate MPPC with anode, cathode, and membrane geometrical areas of 49 cm^2 at 30 ºC, shown in Figure 3.1. The anode chamber volume was 200-mL and composed of a carbon fiber (24 K Carbon Tow, Fibre Glast, OH, USA) anode woven through a titanium current collector frame. The anode chamber and 18-mL liquid cathode chamber were separated by an AMI-7001 (Membranes International, Inc.) AEM. The cathode chamber consisted of two serpentine flow cells separated by the cathode to form a liquid chamber located between the AEM and cathode and a serpentine air chamber supplied with pumped air (EcoPlus® Eco Air 3). The air cathode serpentine chamber provided extra stability to the cathode to prevent volume fluctuations from warping. Consequently, the catholyte and O_2 are exposed to 31.4 cm^2 of active surface area. The liquid cathode chamber was separated from the air cathode chamber by a carbon cloth cathode (FuelCellsEtc.com GDL-CT) coated on the air side with 2 layers of 16 mg/cm^2 of 30% PTFE dispersion (FuelCellStore) cured for 15 min at 200 ºC and 1-h at 280 ºC to improve cathode hydrophobicity and coated on the liquid-exposed side with 0.5 mg/cm^2 Vulcan carbon powder (FuelCellStore) with a Nafion binder (10% Nafion in alcohol, Sigma-Aldrich). The distance between the anode and cathode was ~0.5 cm. I used Bioanalytical Systems, Inc. RE-5B Ag/AgCl reference electrodes (+0.27 V_{SHE} in the MxC medium and NaCl catholyte at 30 ºC). The reference electrode was located in the anode chamber ~1 cm from the anode and ~1.5 cm from the cathode; thus, the anode functioned as the working electrode and the cathode as the counter electrode. All potentials are reported in reference to Ag/AgCl. I operated the MPPC using the Bio-Logic VMP3 potentiostat to control the

anode potential at -0.3 V and monitored current production, counter electrode potential, and cell potential. Data was collected using EC-Lab v.10.37 software.

To inoculate the MPPC, I used 100-mL of inoculum grown from operating MEC reactors fed with acetate medium and 100-mL of 1-M acetate MEC media at pH 7 (Parameswaran et al., 2012) to develop current-producing biofilms. Once the biofilms achieved > 10 A/m^2, I fed the anode continuously with 100-mM acetate medium with a 0.5-day HRT to provide additional mixing to improve current production. Throughout operations, the cathode was continuously fed with a catholyte solution. The air side of the cathode was supplied with air from an EcoPlus® Eco Air commercial pump and regulated using a Dwyer RMA-151-SSV 0-50 cm^3/min flow meter.

The reactor operated for more than 7 months to determine long-term functionality and performance. Appendix Figure B.1 summarizes the operating conditions and performance in terms of H_2O_2 concentration over the 7 months. Several catholytes were evaluated for H_2O_2 production using a 4-h HRT and no EDTA: 100e500-mM NaCl at pH 7; 100-mM H_3PO_4/KH_2PO_4 (PBS) at pH 2.5; 200-mM PBS at pH 2.5; 400-mM $NaHCO_3$ at pH 6.5; and 1-M $NaHCO_3$ at pH 8.5. I studied the effects of catholyte HRT from 1- to 6-h using 200-mM NaCl and no EDTA. I evaluated the use of EDTA as a stabilizer in 200-mM NaCl catholyte at concentrations ranging from 0- to 2-mM at a 4-h HRT. To obtain steady-state data, I waited at least 5 cathodic HRTs after each condition change prior to taking any H_2O_2 measurements. (Experiment duration by run conditions is summarized in Appendix Table B.1.) Reported cathode potentials were corrected for Ohmic resistance as established in Young et al. (2016).

I performed CV for different performance conditions to evaluate changes in cell overpotentials (Bard and Faulkner, 2001). CVs were performed at a 1 mV/s rate from -0.55 to -0.1 V with the anode as the working electrode.

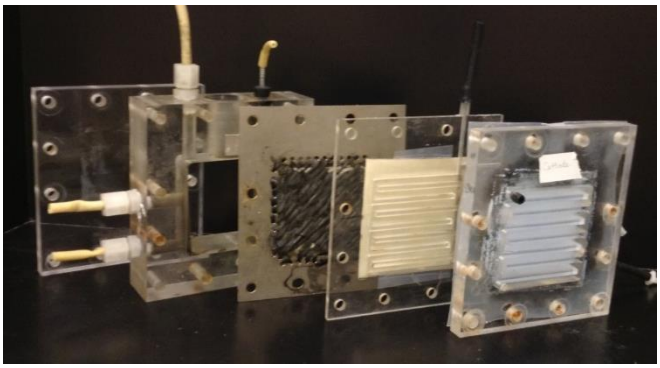

(a)

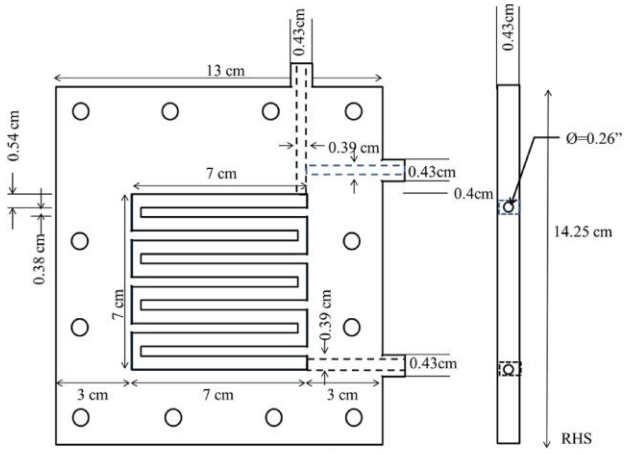

(b)

Figure 3.1. (a) The MPPC setup (from left to right): backing plate, anode chamber, anode, the liquid cathode chamber with AEM membrane attached between the anode and cathode, and the air cathode chamber with PTFE-coated cathode between the liquid and air cathode chambers. (b) A schematic of the serpentine cathode design.

3.3 Results and Discussion

3.3.1 Effects of varying cathode HRT

Based on the favorable results using NaCl as the catholyte in Young et al. (2016), I explored the impact of catholyte HRT with a fixed NaCl concentration of 200-mM on sustained performance. Figure 3.2a illustrates excellent H_2O_2 production: the concentration increased almost linearly from 1.0 to 3.1 g H_2O_2/L as the catholyte HRT increased from 1- to 4-h at similar current densities (Figure 3.2c). For perspective, these concentrations are more than adequate for disinfection (30-50 mg H_2O_2/L) and micropollutant removal (5-20 mg H_2O_2/L) when coupled with UV and Fenton processes (Rajala-Mustonen and Heinonen-Tanski, 1995; Yang et al., 2014). The increases in H_2O_2 concentration were coupled with pH increases from 11.8 to 12.3 (Appendix Figure B.5), since OH^- was produced during O_2 reduction and the catholyte was unbuffered. System overpotentials did not demonstrate any clear trends with HRT (Appendix Figure B.5). As expected, an optimal HRT existed due to a tradeoff between H_2O_2 production rate, which is highest at the lowest HRTs, and decay rate, which outpaces the production rate at longer HRTs. Figure 3.2e illustrates that the net production rate of H_2O_2 decreased from 1.02 to 0.76 g/$L_{cathode}$/d as HRT increases from 1- to 4-h. There was a corresponding decrease in Figure 3.2b shows the power required to produce H_2O_2 increased from 0.42 to 1.13 Wh/g H_2O_2 and cathodic Coulombic efficiency (CCE; detailed in Appendix B.2) from 78% to 21%. The decrease in net production rate with increasing HRT was a result of H_2O_2 decomposition that could have had several causes: (1) H_2O_2 dissociating to HO_2^- at high pH and diffusing across the AEM, (2) H_2O_2 reacting with the AMI membrane as illustrated in Young et al. (2016), and (3) H_2O_2 auto-

decaying to H_2O and O_2 due to prolonged exposure to the carbon catalyst or metals (Drogui et al., 2001):

$$H_2O_2 \rightarrow 2H_2O + O_2 \quad \text{(Eqn. 3.5)}$$

Above a 4-h HRT, the effluent H_2O_2 concentration decreased to 2.3 g H_2O_2 /L, leading to a pH decrease to 12.2 via Eqn. 3.3, even though the cathode potential was consistent with the other HRTs (-0.52 V; Appendix Figure B.5) and current density was similar to the 2- and 3-h HRTs (8.5 A/m^2). The deteriorating performance likely was due to the reduction of H_2O_2 to H_2O via the 2-electron ORR:

$$H_2O_2 + 2e^- \rightarrow 2OH^- \quad \text{(Eqn. 3.6)}$$

due to increased exposure to electrons at the cathode at the long HRT. I observed membrane failures only during the experiment operated at the 6-h HRT. The membrane failed twice in 6 days while operating at the 6-h HRT, and the total down time was 2% of the total operating time. I suspect that the long HRT may have also promoted H_2O_2 auto-decay by reacting with the membrane itself to form O_2 by Eqn. 3.5.

The MPPC design was efficient for sustained operation: the open-circuit potential was 0.18-0.20 V versus the theoretical value of 0.56 V, and the ~0.3 V difference was caused by the ~ 5-unit pH difference between the anode and cathode. Consistent with Young et al. (2016), the MPPC achieved high current density in energy-neutral situations (i.e., when the reactor experiences 0 V cell potential) ranging from 3.24 A/m^2 at 1-h and 2-h HRT and 3.73 A/m^2 at 4-h HRT.

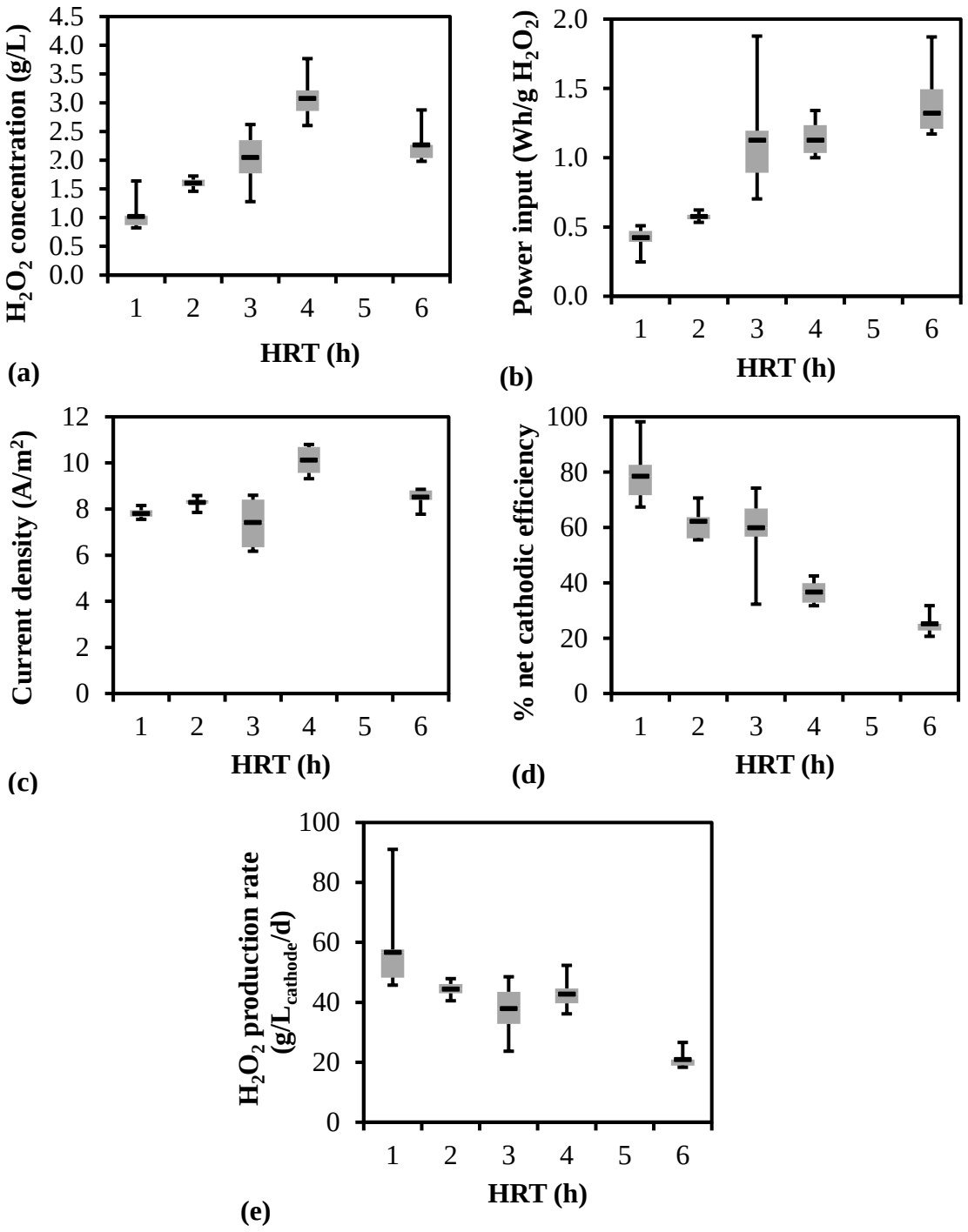

Figure 3.2. Results for the experiment with a range of HRT from 1- to 6-h using 200-mM NaCl catholyte: (a) H_2O_2 concentration, (b) power input, (c) current density, (d) net cathodic coulombic efficiency, and (e) H_2O_2 production. The light gray boxes represent the first and third quartiles, and the black point represents the average value. The whiskers represent the maximum and minimum data points.

3.3.2 Varying NaCl concentrations

As expected, increasing the electrolyte concentration improved MPPC power efficiency, although H_2O_2 production did not change. Figure 3.3a shows that NaCl concentration > 200-mM had little effect on H_2O_2 effluent concentration (2.4-3.1 g/L), but the required power input declined from 1.1 to 0.4 Wh/g H_2O_2 (Figure 3.3b). This improvement was observed even though there was a small decrease in current density from 10.1 to 9.1 A/m^2 (Figure 3.3c) and CCE stabilized between 37% and 43% (Figure 3.3d). 100-mM NaCl catholyte produced a lower average H_2O_2 concentration than ≥200-mM NaCl (~1.2 versus ~3.1 g/L), largely due to a limiting concentration of Cl^- ions to maintain electroneutrality; on an electron basis, 100-mM of NaCl supports the production of 1.7 g H_2O_2/L (50-mM). Above 100-mM, cathode potential improved as expected from -0.54 V at 200-mM to -0.33 V at 500-mM NaCl (Figure 3.3e) at similar current densities, indicating reduced Ohmic losses.

Figure 3.3f shows that, regardless of NaCl concentration, OH^- was the primary ion migrating from the cathode to the anode chamber, ranging from 56% to 60%. OH^- as the dominant anion also explains why all conditions achieved approximately the same pH (12.14-12.23): Cl^- migrated from the cathode chamber until the catholyte achieved a stable pH ~12.2-12.3, at which concentration the OH^- overcame the migration barrier to begin diffusing to the anode. Cl^- migration and/or diffusion increased 20-44% with increasing catholyte concentration and reduced ionic Ohmic overpotentials: Each 100-mM of NaCl present in the catholyte led to a linear increase of ~6% in Cl- anions migrating to the anode and ~50 mV decrease in cathode overpotential. The linear declines of Ohmic losses are consistent with the linear CVs in (Appendix Figure B.6b).

Consequently, reduced cathodic overpotentials led to a smaller power input for H_2O_2 production.

Since Cl^- and OH^- did not account for the total number of anions required to maintain electroneutrality in the cell, additional unidentified ions, identified as the "unknown" fraction in Figure 3.3f, must have diffused between the anion and cathode chambers. These unidentified ions represented 17% of the migrating ions at 100-mM NaCl, but they steadily decreased to 0% at higher NaCl catholyte concentrations. The unidentified ions could have been HO_2^-, present at the cathode due to the pH being greater than the H_2O_2's pKa, or counter diffusing cations like Na^+ from the anode chamber. It is more likely that HO_2^- anions were migrating to the anode, since the concentration of unidentified ions linearly decreased from 17% at 100-mM NaCl to 0% at 400-mM NaCl; if Na^+ had dominated the unidentified ions, then having more Na^+ in the anode chamber should have made them more important.

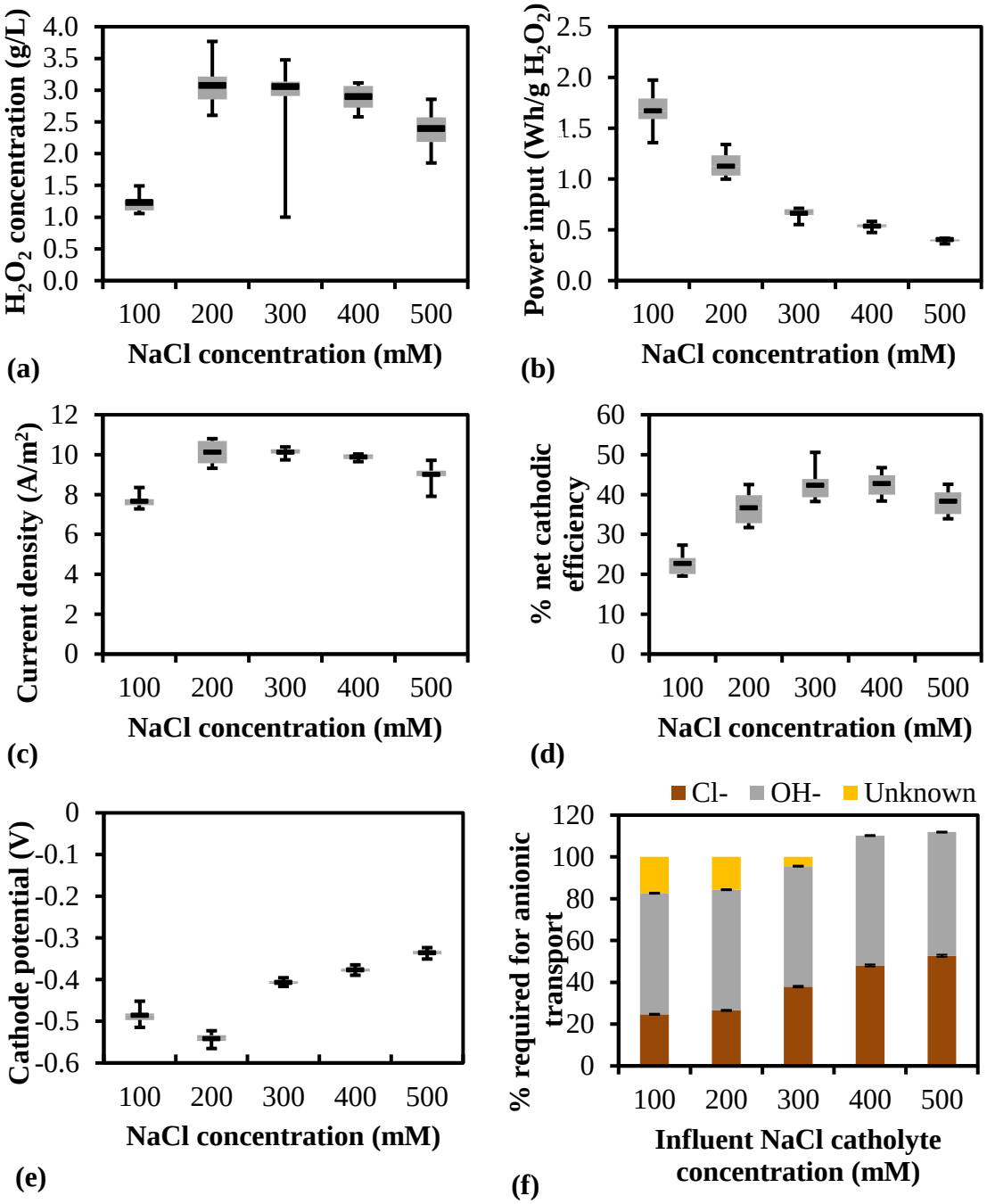

Figure 3.3. Results for varied NaCl concentrations from 100- to 500-mM: (a) H_2O_2 concentration, (b) power input, (c) current density, (d) net cathodic coulombic efficiency, (e) cathode potential, (f) and the percent of anionic transport from the cathode chamber to the anode chamber required to maintain electroneutrality. The light gray boxes represent the first and third quartiles, and the black point represents the average value. The whiskers represent the maximum and minimum data points.

3.3.3 Effects of applying EDTA as an H_2O_2 stabilizer

Metal chelators often are used to stabilize H_2O_2 solutions by preventing H_2O_2 from oxidizing metals (Campos-Martin et al., 2006). Based on stability testing in NaCl and PBS solutions in serum bottles (Young et al., 2016), EDTA increased H_2O_2 stability over a range of pH values in comparison with solutions without EDTA (Appendix Figure B.8). Therefore, I hypothesized that EDTA addition to the catholyte would further stabilize and improve H_2O_2 production.

Even though EDTA improved the CCE from 37 to 52% (Figure 3.4d), Figure 3.4a illustrates that the highest H_2O_2 concentrations were produced without EDTA: H_2O_2 concentration decreasing from 3.1 to 2.0 g/L with increasing EDTA concentration due in part to current densities decreasing from 10.1 to 4.6 A/m^2 (Figure 3.4c). Nonetheless, EDTA addition improved the energy efficiency of the MPPC from 1.13 to 0.54 Wh/g H_2O_2 (Figure 3.4b). The increased cathodic efficiency likely was due to EDTA slowing the decomposition of H_2O_2, improving CCE and power performance. This reiterates the trade off in operating MPPC: without EDTA, the MPPC achieved higher effluent concentrations, but adding EDTA reduced power requirements.

Decreased H_2O_2 concentrations were caused by EDTA diffusion to the anode, reducing current production. At the cathode, effluent pH was in the range of 11.8-12.3 (Appendix Figure B.8), meaning that EDTA was completely deprotonated and could diffuse through the AEM to the anode. Figure 3.4e shows that GC-FID analysis detected EDTA in the anode chamber at concentrations ranging from 0.030- to 0.043-mM when EDTA was present in the catholyte. In the anode chamber, EDTA likely chelated with Fe^{2+} supplied as a nutrient for ARB to facilitate extracellular electron transfer or with the

iron in the cells involved with EET (Estevez-Canales et al., 2015). The detected EDTA concentrations exceeded the 0.021-mM concentration required to chelate all Fe^{2+} present in the anode medium. In addition, Appendix Figure B4 illustrates little change in E_{KA} at any concentration of EDTA, further indicating that the decrease in current likely was not due to modification of the metabolic EET pathway. Iron has been identified as an important nutrient in the EET mechanism of a variety of ARB (Kato et al., 2013; Estevez-Canales et al., 2015; Shi et al., 2016). Estevez-Canales et al. (2015) demonstrated decreased current production due to a reduction in c-type cytochromes in ARB cells when iron-containing media was supplemented with the metal chelator 2,2'-bipyridine, and these cytochromes are critical for EET. Based on the CV results, it is likely that reduced current production was a result of ferrochelation rather than a change in metabolic pathway, as in Estevez-Canales et al. (2015). While EDTA can be effective when added to the catholyte after leaving the cathode chamber, it can harm MPPC performance if added in the catholyte. Future research should explore the utilization of non-metal-chelating stabilizers to improve H_2O_2 concentrations.

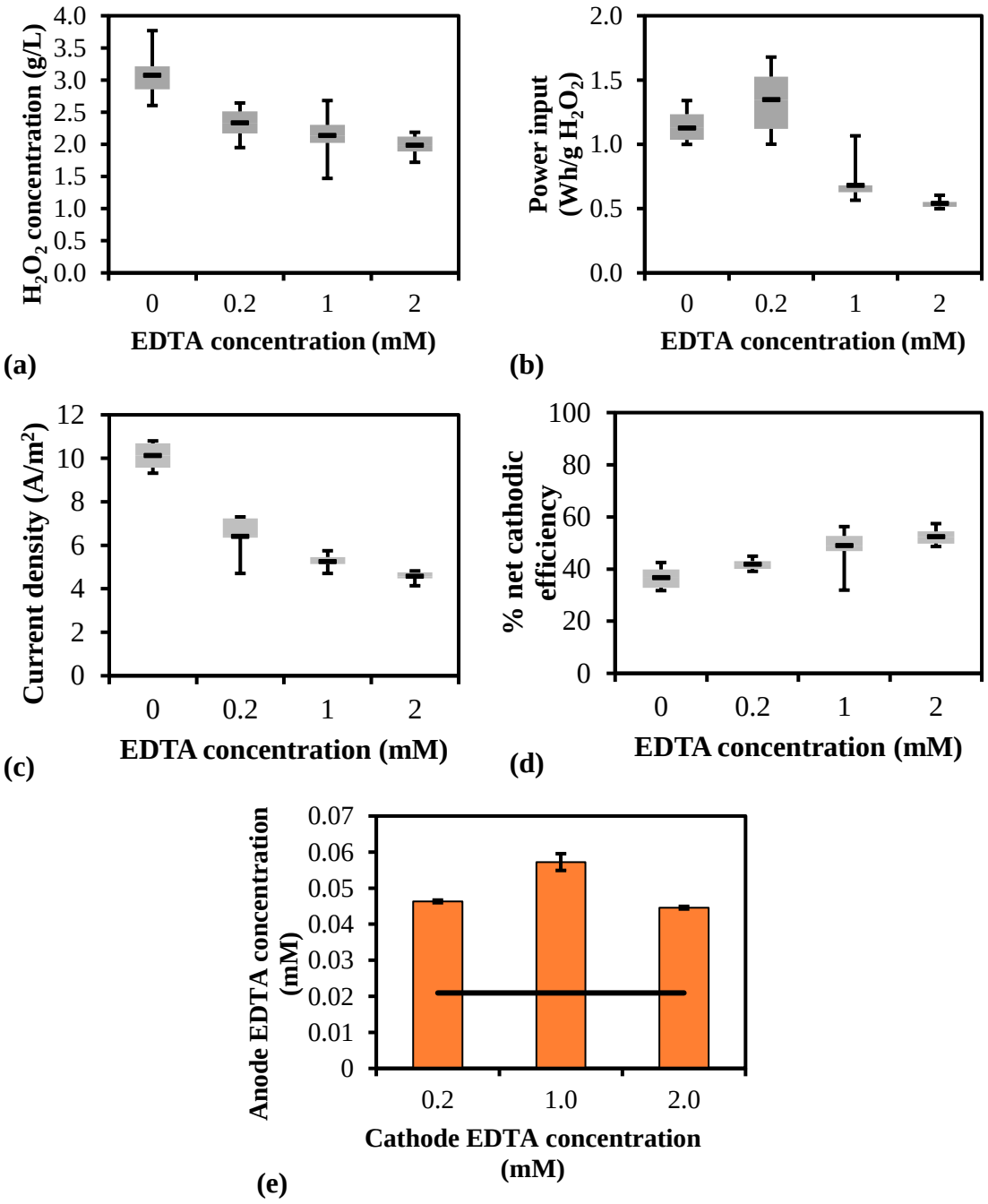

Figure 3.4. Results for the experiment varying EDTA concentrations from 0 to 2-mM: (a) H_2O_2 concentration, (b) power input, (c) current density, (d) net cathodic coulombic efficiency, and (e) EDTA concentrations in the catholyte and anolyte, where the black line represents the amount of EDTA required to chelate with all Fe^{2+} added in the anolyte. The light gray boxes represent the first and third quartiles, and the black point represents the average value. The whiskers represent the maximum and minimum data points.

3.3.4 Effects of buffering catholytes

As shown in Eqn. 3.4, reducing the pH difference between the anode and cathode chambers decreases pH concentration overpotentials and potentially leads to increased energy efficiency for H_2O_2 production. Based on this concept, I evaluated adding acid-base buffers to the catholyte to reduce concentration overpotentials. Although adding the buffers improved several performance variables – including pH, current density, and cathode potentials – acidic buffers failed to produce as much H_2O_2 as NaCl. Figure 3.5b shows that PBS catholyte lowered the pH to 12.13 and 10.36 with 100- and 200-mM PBS, respectively, and to 11.4 and 9.4 with 400-mM and 1-M $NaHCO_3$, respectively, which are lower than NaCl's pH of 12.3. Cathode potentials improved to -0.49 V with 200-mM PBS versus 200-mM NaCl (Figure 3.5c). Current densities were 2-3 A/m^2 higher with $NaHCO_3$ than NaCl (Appendix Figure B.7), since the $NaHCO_3$ diffused to the anode and improved mass transport through the anode biofilm. In addition, Figure 3.5f illustrates that more phosphate anions and OH^- anions were removed from the catholyte, versus with the NaCl electrolyte, which should have reduced Ohmic resistances in a method similar to that observed at the higher NaCl concentrations.

Regardless of these improvements, Figure 3.5a shows that using PBS and $NaHCO_3$ catholytes produced H_2O_2 concentrations ranging 0.3-2.5 g H_2O_2/L (p-value <0.003; detailed in the Appendix), values significantly less than 3.1 g H_2O_2/L with 200-mMNaCl. Since less H_2O_2 was produced, Figure 3.5d shows that the CCE decreased from 37% with 200-mM NaCl to 15% and 8% with 100- and 200-mM PBS and 26% and 4% with 400- and 1000-mM $NaHCO_3$. Correspondingly, power input was higher for all buffering catholytes versus NaCl (Figure 3.5e).

Because anode performance did not deteriorate (it even improved slightly), the poor performance for H_2O_2 production was caused by a net loss of H_2O_2 in the cathode chamber. With the buffering catholytes, the net loss probably was due to increased auto-decay of H_2O_2 to O_2 or the 2-electron ORR of H_2O_2 to H_2O at the influent end of the cathode chamber, where the pH was 2.5, even though the effluent pH exceeded 10. At the entrance, pH 2.5 PBS is thermodynamically more favorable for the 4-electon and 2-electron ORR reactions than at higher pHs. Consequently, the kinetics of these reactions are faster, likely resulting in the reduction of H_2O_2 to H_2O via Eqn. 3.6. With $NaHCO_3$, I hypothesize that H_2O_2 auto-decayed to O_2 in the presence of carbonate and bicarbonate, since both compounds have been shown to decrease H_2O_2 stability (Nicoll and Smith, 1955; Abbot and Brown, 1990; Qiang et al., 2002; Young et al., 2016). Auto-decay of H_2O_2 to O_2 is further supported by my observations of gas flowing out of the cathode chamber when $NaHCO_3$ was used as the catholyte.

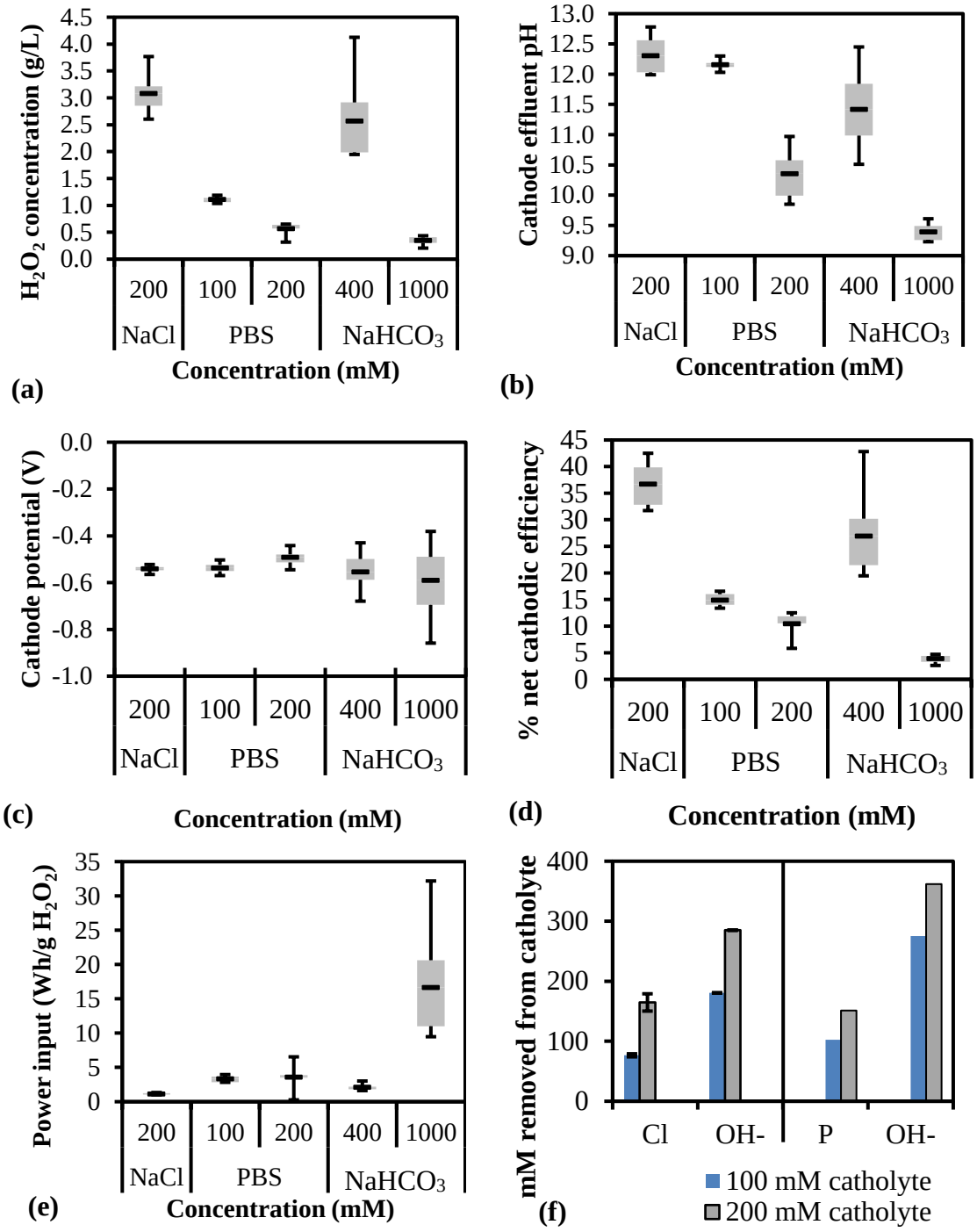

Figure 3.5. PBS and $NaHCO_3$ catholyte experiments results: (a) H_2O_2 concentration, (b) cathode effluent pH, (c) cathode potential, (d) net cathodic efficiency, (e) power input, and (f) the composition of anions that diffused from the cathode to the anode. The light gray boxes represent the first and third quartiles, and the black point represents the average value. The whiskers represent the maximum and minimum data points.

3.3.5 A perspective for the application of MPPCs in wastewater applications

MPPCs have the potential to provide cost savings to WWTPs that utilize H_2O_2 for disinfection. Since cathode performance is independent of the anode substrate content, I evaluated the potential for H_2O_2 production at WWTPs utilizing PS and WAS. I estimated the amount of H_2O_2 produced in a MPPC treating either PS or WAS in a 10 million L/d municipal WWTP based on the parameters summarized in Table 3.1. Detailed H_2O_2 calculations are included in the Appendix B. Depending upon the catholyte HRT, a WWTP could produce 890-1900 kg/d of H_2O_2 (or 89-191 mg/d/L influent wastewater) while consuming 1200 kg COD/d from PS. Similarly, a WWTP could produce 450-960 kg H_2O_2/d (or 45-96 mg/d/L of influent wastewater) while consuming 600 kg COD/d from WAS. Notably, the highest production is at the lowest catholyte HRTs. As expected, PS produces more H_2O_2, since it contains more COD that can be converted to current in a MPPC at higher current efficiencies. The production of H_2O_2 would require the WWTP to consume an additional 860-1150 kWh/d in supplemental electricity for H_2O_2 from PS or 430-540 kWh/d for H_2O_2 using WAS. By comparison, a 10 million L/d municipal WWTP with advanced treatment is estimated to consume 5000-9000 kWh/d (EPRI, 2002; de Haas and Dancey, 2015).

For perspective, the amount of H_2O_2 produced from PS is enough that it provides excellent options for a variety of tertiary treatments. Several researchers have demonstrated significant disinfection improvements using H_2O_2, including Drogui et al. (2001), who achieved 3-log reduction in coliform forming units, or CFUs, with 0.12 g/L of wastewater effluent using electrolysis-produced H_2O_2 for disinfection. Yang et al.'s (2014) review of organic micropollutant treatment found many micropollutants can

be remediated using H_2O_2 doses in the 5-15 mg/L range and moderate to high UV radiation doses (< 5000 mJ/cm^2). Primary sludge treatment also provides sufficient H_2O_2 for COD and color removal when coupled with UV radiation (Ksibi, 2006; Badawy and Ali, 2006; Arends et al., 2014) versus WAS treatment which provides about half of the required H_2O_2 dose. Thus, the amount of H_2O_2 produced, especially from PS is more than sufficient to provide most or all the H_2O_2 required for tertiary treatment for WWTPs. Foley et al.'s (2010) life cycle assessment, which concluded that on-site H_2O_2 production at similar conditions to those in this study, demonstrates significant environmental benefits through reduction of greenhouse gas emissions due to reduced transport of disinfectants for tertiary treatment at WWTPs. Foley et al. (2010) also concluded that the reduction in transportation outweighed the environmental impacts from the materials and construction of the WWTP.

Table 3.1. Parameters used to estimate H_2O_2 production in a typical WWTP

Parameter	1 h catholyte HRT	4 h catholyte HRT	Source
Plant influent flow rate (L d^{-1})	10^7		Metcalf & Eddy (2014)
Influent TCOD concentration (mg L^{-1})	500		Metcalf & Eddy (2014)
Cathodic coulombic efficiency	75%	35%	This paper
Power input (Wh g^{-1} H_2O_2)	0.45	1.2	This paper
For PS treatment in MPPC			
Percentage of influent TCOD in PS	60%		Metcalf & Eddy (2014)
Percentage of PS converted to current	40%		Ki et al. (2017a)
H_2O_2 production based on catholyte HRT (mg $L^{-1}_{\text{influent WW flow}}$ d^{-1})	190	89	This paper
Amount of COD converted to H_2O_2 (kg d^{-1})	1200		This paper
Energy required (kWh d^{-1})	860	1150	This paper
For WAS treatment in MPPC			
Percentage of influent TCOD in WAS	30%		Metcalf & Eddy (2014)
Percentage of WAS converted to current	35%		Kim et al. (2005); Zhang et al. (2012)
H_2O_2 production based on catholyte HRT (mg $L^{-1}_{\text{influent WW flow}}$ d^{-1})	96	45	This paper
Amount of COD converted to H_2O_2 (kg d^{-1})	600		This paper
Energy required (kWh d^{-1})	430	540	This paper

3.4 Conclusions

The flat-plate MPPC design demonstrated continuous H_2O_2 production at concentrations (3.1 g/L) sufficient for disinfection and micropollutant removal and with low power input (1.1 Wh/g H_2O_2). This H_2O_2 concentration is ~30-fold more than required for disinfection and micro-pollutant removal during water and wastewater treatment. The MPPC performed well using a simple NaCl catholyte with a 1- to 4-h HRT and no stabilizers. At a 1-h HRT, the H_2O_2 production rate provides more than 3 times the H_2O_2 required for disinfection and micro-pollutant removal at a power input 5- to 25-fold lower than required in the conventional anthraquinone process. The addition of the metal-chelating stabilizer EDTA inhibited current production at the anode by chelating Fe^{2+} at the anode, reducing the amount of current produced by ARB and, consequently, reducing the number of electrons available for H_2O_2 production at the cathode. In the current reactor configuration, weak acid buffers provided no performance benefit versus a NaCl catholyte, largely due to increasing H_2O_2 auto-decay either due to pH gradients along the cathode or the presence of compounds reducing H_2O_2 stability.

Ultimately, the best conditions for MPPC operation will depend upon the operational goals of the process. High HRTs generally favor higher effluent concentrations. However, the MPPC will require larger power inputs to achieve the necessary concentration and operate at lower net cathodic coulombic efficiencies. High production rates can be achieved at low HRTs with lower power inputs but produce lower effluent H_2O_2 concentrations. WWTPs would benefit from operating at lower HRTs to produce more H_2O_2 for use in advanced oxidation processes or sludge pretreatment.

Regardless, the high pH resulting from H_2O_2 production and high salt concentrations for the electrolyte will impact downstream equipment performance.

CHAPTER 4

A Model of a Microbial Electrochemical Cell Anode Chamber and Biofilm (MYAnode) Utilizing Complex Substrates

4.1 Introduction

MxCs are novel technologies that can bioremediate wastewater while simultaneously producing an electrical current. In MxCs, ARB consume volatile fatty acids and respire electrons extracellularly to an anode. The electrons travel through an external circuit to the cathode, producing an electrical current. MxC technology has advanced significantly over the last two decades (Torres, 2014; Jadhav et al., 2017; Santoro et al., 2017; Jain and He, 2018).

MxC research has increasingly focused on treating complex organic waste streams like brewery effluent, swine wastes, and primary and secondary municipal wastewater sludges (Zhuang et al., 2012; Pous et al., 2013; Sevda et al., 2013; Ki et al., 2015; Kim et al., 2016). These anaerobic, complex waste streams present a variety of obstacles in MxC technologies. While diverse communities are essential in providing the syntrophic functions required for production of VFAs for ARB consumption (Parameswaran et al., 2009), wastewater sludges host bacteria and *Archaea* that compete with ARB for acetate substrate, including heterotrophic bacteria performing denitrification using NO_3^- and NO_2^- as electron acceptors and acetoclastic methanogens (X_m) (Gray et al., 2002; Young et al., 2013a). However, acetoclastic methanogens may provide a benefit: the consumption of acetate, a relatively strong weak acid, which produces bicarbonate, which helps stabilize pH.

Alkalinity and pH can have profound impacts on the performance of biofilm anodes in MxCs, particularly for complex waste streams having low alkalinity, because ARB produce a large amount of protons (H^+):

$$CH_3COO^- + 3H_2O \rightarrow CO_2 + HCO_3^- + 8H^+ + 8e^- \quad \text{(Eqn. 4.1)}$$

To prevent ARB inhibition due to low pH in the biofilm, alkalinity must diffuse into the biofilm from the bulk liquid. Torres et al. (2008a) identified that alkalinity diffusion into the biofilm is important for enabling proton transport away from the anode, thereby allowing the ARB biofilm to maintain pHs favorable for respiration. When treating primary sludge in MFCs, Ge et al. (2013) reported limited current and CH_4 recovery due to low pH (< 5.6) at the end of each feeding cycle. When Ge et al. added additional bicarbonate and phosphate buffer to the primary sludge, the pH was consistently > 6.5, which led to a doubling of current and CH_4 production in the MFC. However, Ge et al. were unable to determine the concentration of methanogens in the system. Dhar and Lee (2014) documented that low alkalinity (200 mg as $CaCO_3$/L) was important for the utilization organic matter in domestic wastewater in MxCs. The breakdown of complex organic matter in anaerobic systems often releases NH_3, which can act as a base, although it also can inhibit biomass growth and metabolisms if at a too-high concentrations.

While some research has addressed complex substrates and fundamental processes, only a few mathematical models describe and predict MxC performance. Picioreanu et al. (2007, 2008, 2010) developed two- and three-dimensional (2D, 3D) models that incorporated using an external mediator for EET between the ARB and anode. Picioreanu et al. (2007, 2008, 2010) also utilized increasingly complex substrates as the starting resource as established in the ADM1 (Batstone et al., 2002). Picioreanu et

al. (2010), who reported results focused primarily on the impact on bulk conditions on the biofilm performance, assumed that acetoclastic methanogenesis and anode respiration using oxidized mediators were performed by the same biomass. Thus, the impact on performance could not be determined for independent microbial entities.

Mediator-less EET was represented by the models of Marcus et al. (2007, 2010, 2011) and became the standard for describing high-performance biofilm anodes. Marcus et al. (2007) introduced the Nernst-Monod model, which represents ARB kinetics and EET using a unique form of steady-state, dual-limitation kinetics. While the Nernst-Monod model includes the normal Monod equation for the donor concentration, it exploits the Nernst equation to represent the acceptor "concentration" via the anode potential, and it explicitly allows for electrical conduction of electrons to the anode surface. The Nernst-Monod model was combined with mass balances and diffusive transport to describe current production in conductive biofilms, and experimental studies confirmed the validity of the Nernst-Monod model for conductive biofilms dominated by *Geobacter sulfurreducens* (Torres et al., 2008b).

Marcus et al. (2010, 2011) developed PCBIOFILM, a conduction-based, steady-state, 1D biofilm model that couples the Nernst-Monod model and diffusion with pH calculations, electrical neutrality, and ionic migration. Within PCBIOFILM, Marcus et al. (2010) utilized CCBATCH, a modeling platform that incorporates kinetically-controlled biological reactions with much faster pH and chemical speciation reactions using the proton condition (PC) (VanBriesen and Rittmann, 1999). Utilizing the CCBATCH platform and the PC were beneficial for analyzing the large production rate of H^+ during the ARB's anode respiration.

Several models of the MFC anode chamber have expanded upon Marcus et al. (2007, 2010, 2011) to describe phenomena ranging from heat transfer due to EET (Oliveira et al., 2013) to the internal and external molecular mechanisms of EET (Pinto et al., 2010, 2011; Merkey and Chopp, 2012; Renslow et al., 2013; Jayasinghe et al., 2014; Korth et al., 2015). Excepting Marcus et al. (2010, 2011) and Picioreanu et al. (2007, 2008, 2010), the other models assume constant pH and neglect chemical speciation, even though several works have demonstrated pH inhibition in ARB biofilms (e.g., Torres et al., 2008a, Franks et al., 2009). Most models also only include simple substrates like acetate or glucose, which are not appropriate for applications that involve complex organics, or neglect the complex microbial communities required to hydrolyze and degrade complex organics. Furthermore, no prior model accounts for the formation of EPS and SMP, which can divert as much as 24% of the electron flow for energy and biomass synthesis (Noguera et al., 1994; Laspidou and Rittmann, 2002a; Ni et al., 2010; Xie et al., 2012).

In this work, I first develop a novel non-steady-state mathematical model, MYAnode, which integrates the chemical and biological processes in the bulk liquid with substrate utilization and current production by ARB in the biofilm anode. MYAnode combines CASADM, a comprehensive wastewater treatment modeling platform (Young et al., 2013b); CCBATCH, which combines rapid chemical speciation reactions with slower biological reactions (VanBriesen and Rittmann, 1999); and PCBIOFILM, which describes the chemical, biological, and transport mechanisms within the ARB biofilm affecting current production (Marcus et al., 2010; Marcus et al. 2011).

I then demonstrate the unique capabilities of MYAnode by exploring the interactions between ARB and acetoclastic methanogens. In particular, I vary the influent concentration of methanogens entering the MxC under alkalinity-limited conditions typical of primary sludge. I demonstrate that methanogens play an essential role by promoting bicarbonate that stabilizes pH in a range that is not inhibitory for ARB.

4.2 MYAnode formulation

4.2.1 Modeling system and assumptions

Table 4.1 summarizes the features of CASADM, PCIOBILM, and the PC incorporated into MYAnode. The modeling foundation of the bulk liquid is based on CASADM, a non-steady-state model that describes typical aerobic, anoxic, and anaerobic biological phenomena exhibited in continuous stirred tank reactors in WWTPs (Young et al., 2013b). CASADM assumes that all biological mechanisms can occur in parallel, rather than assuming *a priori* the rate-limiting steps. For this work, CASADM was upgraded by using the framework of CCBATCH (VanBriesen and Rittmann, 1999) to efficiently link fast chemical speciation reactions, including acid-base equilibrium and complexation reactions, with slower microbial reactions. Several critical assumptions are made in MYAnode. The chemical formulas for various components include domestic wastewater are: $C_{10}H_{19}O_3N$ for PCOD and soluble COD (SCOD); $C_5H_7O_2N$ for biomass, PCOD for biomass-associated products (BAP) and EPS; and $C_6H_{12}O_6$ for utilization-associated products (UAP) (Rittmann and McCarty, 2001; Metcalf & Eddy, 2014). During denitrification, the consumption of the electron acceptors NO_2^- and NO_3^- produces N_2 gas directly without the production of intermediates (de Silva and Rittmann, 2000; Henze et al., 2000).

The modeling foundation for the ARB biofilm is PCBIOFILM, which describes biological, chemical, and transport phenomena through an electricity-producing biofilm (Marcus et al., 2010; Marcus et al., 2011). The biofilm anode is modeled as two domains: an idealized one-dimensional biofilm with constant thickness and uniform biofilm density that consists of ARB only, and a liquid-only DL. These two domains are

located between the bulk liquid and anode surface. ARB oxidize donor substrate and respire electron only when in a biofilm that is conductive and connected to an anode. PCBIOFILM includes the following assumptions: the biofilm consists of ARB only; biomass synthesis is neglected, which allows the biofilm DL and biofilm thicknesses to be assumed as constant and modeled using ordinary differential equations (i.e., I neglect biofilm dynamics); no biological reactions occur within the DL; and EET occurs through a conductive matrix or direct contact with anode.

Table 4.1. A summary of model features that are incorporated into MYAnode

	CASADM	**CCBATCH**	**PCBIOFILM**
Types of reactions	• Biological mechanisms typical to WWTPs • Hydrolysis • EPS and SMP	• Fast chemical speciation of acids/bases	• Fast chemical speciation of acids/bases • ARB metabolism • Electrical migration
Transport phenomena	• Bulk liquid transport • Gas/liquid phase equilibrium	• No transport phenomena	• Diffusion through a biofilm
Biological mechanisms	• Aerobic oxidation by heterotrophic bacteria • Nitrification • Denitrification • Acetogenesis • Acetoclastic methanogenesis	• N/A	• Anode respiration

MYAnode is a multi-component, non-steady-state mathematical model that describes substrate utilization in the bulk anode chamber and in the biofilm, as illustrated

in Figure 4.1. The reactor consists of two systems to be modeled: the bulk liquid within the anode chamber and the biofilm on the anode. Liquid flows into and out of the bulk liquid chamber. MYAnode is presented as four parts: (1) acid/base and chemical speciation using the PC, (2) biological processes in the bulk liquid, (3) processes in the biofilm anode , and (4) the coupling of slow biological reactions with transport.

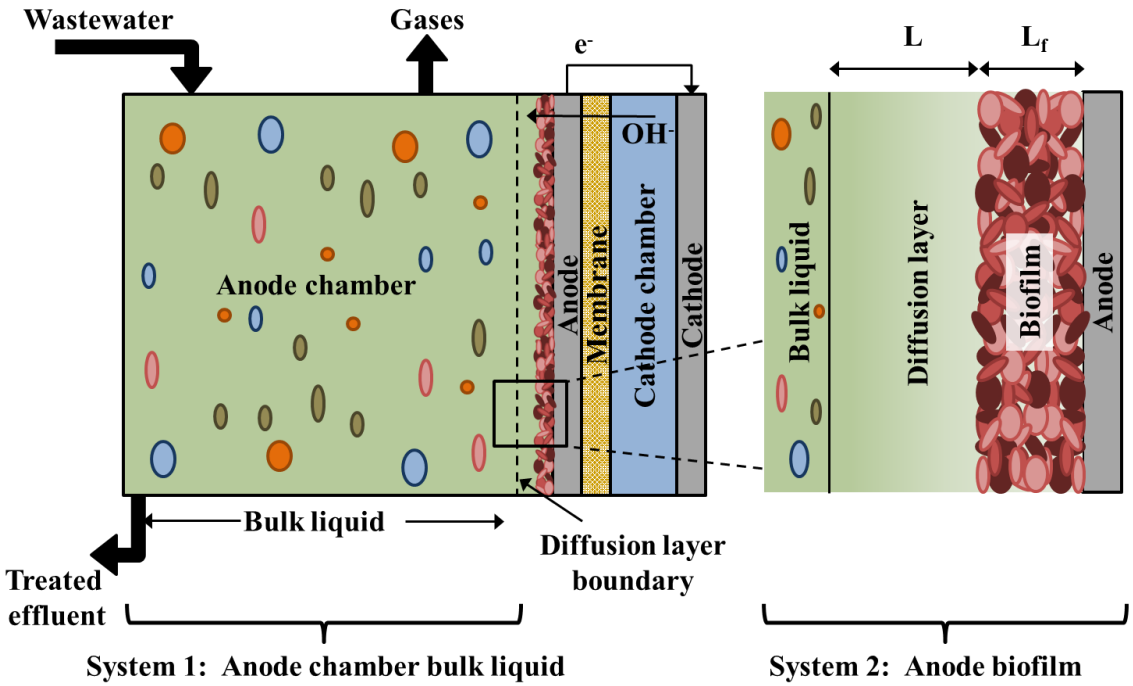

Figure 4.1. The reactors modelled, divided into two systems: the bulk liquid and the biofilm anode. L represents the length of the diffusion layer. L_f represents the length of the biofilm.

4.2.2 Chemical speciation using the proton condition

MYAnode calculates the concentrations of chemical species in the bulk liquid and biofilm anode using the PC. The PC describes changes in acidity by performing a special mass balance on protons generated or consumed, rather than basing a mass balance on charge. While not discussed in depth here, excellent references for utilizing the PC include Snoeyink and Jenkins (1980), VanBriesen and Rittmann (1999), and Benjamin

(2015). As described in VanBriesen and Rittmann (1999) and Marcus et al. (2010), the model divides chemical species into two groups: components and complexes. A proton mass balance is calculated in relation to a "reference-level" for the protons and are neutral with respect to acidity, even though they are not necessarily neutral with respect to charge; these "reference-level" chemicals are the components. Components are combined together to describe other chemical species, or complexes, in the system. For simplicity, I chose components and complexes that can dissociate under acid/base conditions or are present as charge carriers, which affect ionic migration through the biofilm anode.

For MYAnode, I expanded Marcus et al. (2011) to include all protonated forms of acetate (CH_3COO^-), phosphate, CO_3^{2-}, NO_2^-, and NH_4^+; I also included the charged species NO_3^-, Na^+, and Cl^-, which do not participate in acid-base reactions at relevant pH values. The following are the component species: H^+, CH_3COO^-, HPO_4^{2-}, HCO_3^-, NO_2^-, NH_4^+, NO_3^-, Na^+, and Cl^-. The chemical speciation formulas and acid dissociation constants are summarized in Table 4.2

A general form of the complexation reaction is defined in reference to the components:

$$\sum_{j=1}^{N_c} \nu_{ij} \hat{C}_j \leftrightarrow \hat{P}_i \qquad \text{(Eqn. 4.2)}$$

where ν_{ij} is the stoichiometric coefficient giving the number of moles of component j in complex i, $\hat{C}$ is the chemical formula for component j (listed in the first row of Table 4.2), and $\hat{P}$ is the chemical formula for complex i (listed in the first column of Table 4.2),

and N_c is the number of components in the system. For example, in row 1 of Table 4.2, one mole of H^+ and one mole CH_3COO^- produce one mole of CH_3COOH, or the reaction $H^+ + CH_3COO^- \leftrightarrow CH_3COOH$.

Table 4.2. Acid-base reactions and pK_a information

Reaction	pK_a [a]
$CH_3COOH \leftrightarrow CH_3COO^- + H^+$	4.76
$H_2CO_3 \leftrightarrow HCO_3^- + H^+$	6.35
$HCO_3^- \leftrightarrow CO_3^{2-} + H^+$	10.33
$H_3PO_4 \leftrightarrow H_2PO_4^- + H^+$	2.14
$H_2PO_4^- \leftrightarrow HPO_4^{2-} + H^+$	6.77
$HPO_4^{2-} \leftrightarrow PO_4^{3-} + H^+$	11.57
$NH_4^+ \leftrightarrow NH_3 + H^+$	9.25
$HNO_2 \leftrightarrow NO_2^- + H^+$	4.50[b]
$H_2O \leftrightarrow H^+ + OH^-$	14.00

[a] From Snoeyink and Jenkins (1980) unless otherwise stated
[b] From da Silva et al. (2006)

Since the complexation reactions generally achieve thermodynamic equilibrium very rapidly, the concentration of complexes and components satisfy the law of mass action:

$$p_i = \beta_i^c \prod_{j=1}^{N_c} \upsilon_{ij} c_j \qquad \text{(Eqn. 4.3)}$$

where p_i is the concentration of complex i (M/L^3), c_j is the concentration of component j (M/L^3), and β_i^c is formation constant of complex i adjusted for the solution's ionic strength (thus, the c coefficient). The units of β_i^c vary depending upon the reaction stoichiometry. Several textbooks, including Snoeyink and Jenkins (1980) and Benjamin (2015), discuss correcting formation constants for ionic strength.

The law of mass conservation requires that the total aqueous concentration of component j must equal the sum of component j and all complexes i in the system for all components in the system, or

$$C_j = c_j + \sum_{i=1}^{N_p} \upsilon_{ij} p_i \qquad j = 1, \ldots, N_c$$

(Eqn. 4.4)

where C_j is the total analytical concentration of component j and N_p is the total number of complexes associated with component j. For example, the mass conservation equation for bicarbonate is

$$C_{HCO_3^-} = p_{H_2CO_3} + c_{HCO_3^-} + p_{CO_3^{2-}}$$

(Eqn. 4.5)

The value of C_j is always positive.

The PC has a key advantage in biological systems in that the tracking of protons integrates well with oxidation-reduction reactions, which produce and consume H^+ ions. Variations in H^+ can be used to determine changes in pH. (Eqn. 4.4) is expanded to include protons

$$C_{H^+} = c_{H^+} + \sum_{i=1}^{N_p} \upsilon_{iH^+} p_i$$

(Eqn. 4.6)

where C_{H^+} is the total analytical concentration of H^+ defined in reference to the component species and c_{H^+} is the concentration of uncomplexed H^+ which is represented by the solution pH. Since $\upsilon_{iH^+} p_i$ represents the amounts of protons in reference to the component species i, C_{H^+} can be a positive or negative value. Since electrochemical reactions result in electrical charge taking different paths in the anode and cathode

chambers, the PC is useful in the biofilm anode for estimating ionic current production at the anode and ionic migration (i.e., the impacts of ion transport due to an electric field) calculations.

Because the total analytical concentration is sufficient for calculating the concentrations of all components and complexes, I follow the precedent of previous works and use the total aqueous concentrations of the components as the primary dependent variables for pH and transport, while treating the complexes as secondary variables and calculating their values for biological reactions as needed (Steefel and McQuarrie, 1996; Parkhurst and Appelo, 1999; VanBriesen and Rittmann, 1999). Chemical complexation reactions are generally much faster than biological reactions; thus, they are treated as instantaneous values rather than time dependent variables.

Table 4.3. The tableau illustrating the relationship between components and complexes for the proton condition. Blank cells are equal to zero.

Complexes	**Components**									**Charge**	**D (cm^2/d)** [a]
	H^+	CH_3COO^-	HPO_4^{2-}	HCO_3^-	NO_2^-	NH_4^+	NO_3^-	Na^+	Cl^-		
CH_3COOH	1	1								0	1.05
H_3PO_4	2		1							0	1.00[b]
$H_2PO_4^-$	1		1							-1	0.83
PO_4^{3-}	-1		1							-3	0.71
H_2CO_3	1			1						0	1.66
CO_3^{2-}	-1			1						-2	0.80
HNO_2	1				1					0	1.00[b]
NH_3	-1					1				0	1.00[b]
Charge	+1	-1	-2	-1	-1	+1	-1	+1	-1		
D (cm^2/d)[a]	N/A	0.94	0.66	1.02	1.65	1.69	1.64	1.15	1.76		

[a] From Haynes et al. (2011)

[b] Value not available -- assumed value

4.2.3 Bulk-liquid processes

ARB perform anode respiration in anaerobic conditions and depend upon other microorganisms that are common to anaerobic wastewater treatment to hydrolyze and ferment complex organic compounds to simple substrates for their consumption (Rozendal et al., 2008; Parameswaran et al., 2009; Kiely et al., 2011; Parameswaran et al., 2011; Miceli et al., 2014). During hydrolysis, complex and particulate organic compounds undergo disintegration to carbohydrates, proteins, and lipids, which are further enzymatically hydrolyzed by fermenting bacteria to monosaccharides, amino acids, and long chain fatty acids (Vavilin et al., 2008). The hydrolysis products are fermented by fermenting bacteria via acidogenesis or acetogenesis to VFAs, alcohols, keytones, and H_2 gas (Rittmann and McCarty, 2001; Bitton, 2005). This step is critical to providing substrate to most common ARB (Kiely et al., 2011; Parameswaran et al., 2011; Miceli et al., 2014). Acidogens metabolize fatty acids, amino acids, and sugars to VFAs like acetate, propionate, and butyrate, alcohols including ethanol, HCO_3^-, and H_2. Acetogens convert hydrolysis and fermentation products to acetate, HCO_3^-, and H_2 and are classified into two different groups: H_2-producing acetogens and homoacetogens. H_2- producing acetogens metabolize VFAs and ethanol to acetate, consequently repiring H_2. Homoacetogens produce acetate directly from consumption of HCO_3^- and H_2. Two sets of microorganisms compete for these fermentation products: acetate and H_2 are consumed by acetoclastic or hydrogenotrophic X_m to produce CH_4, and ARB can consume VFAs and H_2 to respire electrons to an anode. Large-scale MxCs applications will likely utilize complex waste streams with diverse microbial consortia to produce the fermentation products consumed by ARB but will also require system design and

operation to control or minimize methanogenic activity (Rozendal et al., 2008; Kiely et al., 2011; Li et al., 2014).

I assume that the microbiological processes in the bulk liquid of the MEC are similar to those in biological wastewater treatment, which form the foundation of CASADM, a non-steady-state mathematical model of biological kinetics typically found in wastewater treatment. CASADM is unique in that it assumes that all mechanisms can occur simultaneously rather than assuming *a priori* that any one rate is limiting and that it includes biomass-generated products like EPS and SMP, which are neglected in other models like ADM, ASM, and BSM (Henze et al., 2000; Batstone et al., 2002; Nopens et al., 2009). While specifically implemented for the system described later, the stoichiometry and kinetics matrices detailed in Appendix C are easily modified to describe a variety of activated sludge, AD, ARB systems and any combination thereof.

In MYAnode, I expand CASADM as summarized in Table 4.4. For solid materials, the model includes six components of active biomass – heterotrophic bacteria, ammonium-oxidizing bacteria (AOB), nitrite-oxidizing bacteria (NOB), fermenting bacteria, acetoclastic *Archaea*, and ARB – as well as EPS, inert (non-biodegradable) biomass, and PCOD. The soluble components include SCOD, CH_3COO^-, UAP, BAP, NH_4^+, NO_2^-, NO_3^-, O_2, HCO_3^-, Na^+, and Cl^-, as well as any complexes derived from them due to chemical speciation. COD is assumed to have a slightly negative charge due to the organic matter containing acidic functional groups (Metcalf & Eddy, 2014). Gas-phase materials include CO_2, O_2, N_2, NH_3, and CH_4. Although other models include H_2 production from fermentation (Batstone et al., 2002), I am consistent with others (Aquino and Stuckey, 2008), who omit H_2 production during fermentation and consumption by

hydrogenotrophic methanogens or ARB. This simplification was made for a variety of reasons. Kinetics for H_2 production during fermentation are not well understood and can vary significantly with pH; thus, models like ADM assume a set stoichiometry for volatile fatty acid and H_2 production from fermentation and relatively stable pH (Batstone et al., 2002; Siegrist et al., 2002). As observed by Ki et al. (2017a), pH varied as much as 1.5 pH units in the semi-continuous reactors fed daily, making it difficult to predict the production or utilization of H_2. Even with H_2 formation, homoacetogens would quickly outcompete H_2-utilizing ARB for H_2, utilizing H_2 to form acetate (Parameswaran et al., 2009; Parameswaran et al., 2011). The kinetics for H_2 production from SMP utilization are poorly understood. The relatively long solid retention times utilized in the anaerobic digestion and MEC systems allow acetoclastic methanogenesis to dominate in anaerobic systems versus hydrogenotrophic methanogens (Rittmann and McCarty, 2001). Thus, I assume that the respiration product of fermentation is only acetate.

As described in Young et al. (2013b) and with the exception of ARB, all biomass undergoes biomass synthesis based on Monod kinetics, first-order endogenous decay, and generation of EPS and UAP, as outlined in Laspidou and Rittmann (2002a, 2002b), but with two modifications: (1) UAP and BAP can be utilized as substrate by fermenters and heterotrophs, and (2) UAP and BAP utilization can result in the formation of additional EPS and BAP. Hydrolysis of PCOD and EPS to SCOD and BAP, respectively, can occur in any environment and follow first-order kinetics. When applicable, substrate utilization adheres to dual-limitation Monod kinetics dictated by electron donor and electron acceptor kinetics. I utilized the pH inhibition function developed by Park et al. (2007), in

which the substrate utilization rate is multiplied by a factor, $I_{pH,}$ (unitless), according to the following conditions

$$I_{pH} = 0 \quad \text{for } pH < pH_{opt} - W \qquad \text{(Eqn. 4.7)}$$

$$I_{pH} = 0.5*(1+\cos(\pi(pH-pH_{opt})/W)) \quad \text{for } pH_{opt} - W < pH < pH_{opt} + W \qquad \text{(Eqn. 4.8)}$$

$$I_{pH} = 0 \quad \text{for } pH > pH_{opt} + W \qquad \text{(Eqn. 4.9)}$$

where pH_{opt} is the optimal pH for the bacteria and W is one-half the value of the difference between the upper and lower pH limits. I also utilize substrate limitation functions for reactions that can occur only when specific chemical components are not present, e.g., denitrification under anoxic conditions and fermentation and methanogenesis under anaerobic conditions. The substrate limitation function, $S_{h,inh}$, component h is described as

$$S_{h,inh} = \frac{K_{h,inh}}{K_{h,inh} + C_h} \qquad \text{(Eqn. 4.10)}$$

where h is a chemical or biological components, $K_{h,inh}$ is the inhibition factor (M/L^3), and C is concentration (M/L^3).

Since the biological reactions are slower than the chemical-speciation reactions, the change in concentration over time is described as

$$\frac{dC_h}{dt} = \sum_{g=1}^{g=N} \lambda_{hg} r_h \, I_{g,pH} S_{g,inh} \qquad \text{(Eqn. 4.11)}$$

where g is a chemical or biological reaction, C_h is concentration (M/L^3) of the solid or soluble components h, λ_{hg} is the stoichiometric coefficient of component h in reaction g, r

is reaction rate (M/L^3-t), $I_{g,ph}$ is pH inhibition term for reaction g, and $S_{g,inh}$ is the substrate limitation factor.

Table 4.4. Materials (including all components and complexes) in MYAnode. **Bolded** entries delineate components for chemical-speciation calculations.

Solid phase	Heterotrophic bacteria
	Ammonium-oxidizing bacteria (AOB)
	Nitrite-oxidizing bacteria (NOB)
	Fermenters
	Acetoclastic methanogens
	Anode-respiring bacteria (ARB)
	EPS
	Inert biomass
	Particulate COD (PCOD)
Liquid phase components and complexes	Soluble COD (SCOD)
	UAP
	BAP
	Acetate/Acetic acid
	NH_4^+/ NH_3
	NO_2^-/ HNO_2
	NO_3^-
	H_2CO_3/**HCO_3^-**/ CO_3^{2-}
	H_3PO_4/$H_2PO_4^-$/**HPO_4^{2-}**/PO_4^{3-}
	Na^+
	Cl^-
	H^+
	O_2
	N_2
	CH_4
Gas phase	O_2
	CH_4
	CO_2
	N_2
	NH_3

4.2.4 Biofilm-anode processes

Processes in the biofilm anode are based on PCBIOFILM (Marcus et al., 2010; Marcus et al., 2011), with minor modifications to the ionic components (i.e., adding NO_2^-, NO_3^-, and NH_4^+) that can diffuse into the biofilm to maintain electrical neutrality. For

ARB, all stoichiometry and kinetics are consistent with PCBIOFILM. Since the biofilm thickness is assumed, ARB performance is dictated by Monod kinetics with acetate being the lone electron donor for ARB. The effects of pH inhibition are corrected for using the inhibition functions described above. To correct for the effect of fixed potentials (E; V) on substrate utilization, the maximum specific growth rate in the biofilm ($\hat{q}X_f$; M/L^3-t) was adjusted using the Nernst-Monod equation (Marcus et al., 2007; Torres et al., 2008b)

$$(\hat{q}X_f)|_E = \left[(\hat{q}X_f)|_{E_{KA}}\right]\frac{1}{1+\exp(-\frac{F}{RT}(E-E_{KA}))} \quad \text{(Eqn. 4. 12)}$$

where F is Faraday's constant (96,485 C/mol), R is the idea gas constant (8.314 J/mol K), T is temperature (K), and E_{KA} (V) is the potential at which half of the maximum specific growth rate is achieved.

Within an ARB biofilm, two phenomena dictate the transport of ions: mass transport via diffusion and migration due to the induced electric field. The total flux of an ion, J_{ion} (M/L^2-t), within the system is described as

$$J_{ion,k} = J_{diff,k} + J_{mig,k} \quad \text{(Eqn. 4.13)}$$

where k is the ion (component or complex), J_{diff} is the diffusion flux (M/L^2-t), and J_{mig} is the migration flux (M/L^2-t). Diffusive flux of components j and complexes i through the biofilm is described by Fick's law

$$-J_{diff,j} = D_j\frac{\partial c_j}{\partial x} + \sum_{i=1}^{Nx}\left(D_i\frac{\partial p_i}{\partial x}\right) \quad \text{(Eqn. 4.14)}$$

where $J_{diff,j}$ is the total flux of component j (M/L^2-t), D is the diffusion coefficient (L^2/t), x is the spatial coordinate (L), and N_x is the number of complexes. Since there can be large variations, I assign independent diffusivities for each complex and component. Derived in Marcus et al. (2010), migration of ions is due to changes in the electrostatic potential through the biofilm and is described as

$$J_{mig,k} = z_k c_k D_k E^*$$

(Eqn. 4.15)

where z is the charge of ion k, c is the concentration (M/L^3), and E^* is the apparent electric field (1/L). E* can be calculated from

$$E^* = \frac{F}{RT} E$$

(Eqn. 4.16)

where E is the electric field (V/L).

4.2.5 The coupling of kinetically controlled reactions and transport

A differential mass balance containing transport and reaction terms describes the total analytical concentration of each component within the system

$$Vol \frac{\partial C_h}{\partial t} = Q_{in} C_{h,in} - Q_{out} C_{h,out} + (SA)\, J_{ion,h} + Vol \sum_{g=1}^{Ng} \lambda_{hg} r_h\, I_{g,pH} S_{g,inh}$$

(Eqn. 4.17)

where Vol is the anode chamber volume (L^3), Q is the volumetric flow rate (L^3/T), r_h is the reaction rate for component h (M/L^3-t), and SA is the surface area of the anode (L^2). Within the DL and biofilm, a component's total analytical concentration is subject to changes due to chemical speciation, biological reactions and diffusion. Thus, (Eqn. 4.17 within the biofilm and DL simplifies to

$$\frac{\partial C_h}{\partial t} = \frac{(SA)J_{ion,h}}{Vol} + \sum_{g=1}^{Ng} \lambda_{hg} r_h \, I_{g,pH} S_g$$

(Eqn. 4.18)

Assuming that length $x = L + L_f$ is the boundary between the bulk and DL, $x = L_f$ is the boundary between the DL and biofilm anode, and the anode surface is at $x = 0$, the following boundary conditions exist:

(1) Continuity of flux between the bulk liquid, the DL, and biofilm anode:

$$-J_{bulk,h}\big|_{x=L+L_f} = -J_{ion,h}\big|_{x=L} = J_{ion,h}\big|_{x=L_f}$$

(Eqn. 4.19)

(2) No flux at the anode surface:

$$J_{ion,h} = 0$$

(Eqn. 4.20)

Within the bulk liquid, advection, chemical speciation, and biological reactions affect a component's concentration, simplifying (Eqn. 4.17 to

$$\frac{\partial C_h}{\partial t} = \frac{1}{Vol}\left(Q_{in} C_{h,in} - Q_{out} C_{h,out}\right) + \sum_{g=1}^{Ng} \lambda_{hg} r_h \, I_{g,pH} S_g$$

(Eqn. 4.21)

Gas-liquid phase equilibrium is described as

$$\frac{dC_i^L}{dt} = \frac{dC_i^G}{dt} = \frac{Vol_i^L}{Vol_i^G} K_L a_i \left(C_i^L - C_i^L H_i RT\right)$$

(Eqn. 4.22)

where L represents the liquid phase, G represents the gas phase, C_i is the concentration of species i, K_La is the mass transfer coefficient of species i (1/t), and H is species i's Henry's law constant (M/L^3). Since the Henry's law constant for other species are relatively large, this model assumes that only the following species partition between gas

and liquid phases: CH_4, CO_2, H_2, N_2, NH_3, and O_2. To simplify the model, I also assume no formation of gas within the DL to the biofilm or in the biofilm.

4.3 Modeling approach and implementation

MYAnode consists of three main programs, as illustrated in Figure 4.2: CASADM, PCBIOFILM, and a chemical speciation routine employed by CASADM and PCBIOFILM. CASADM has 37 nonlinear ordinary differential equations (ODEs) that describe the flow through the anode chamber using the chemical and biological components and complexes described in Table 4.4. The ODEs are solved using Euler's method using initial value conditions equal to the influent composition and time steps ≤ 1 min until the system obtains steady state (i.e., a relative difference between data points < 10^{-4}). Mass balance checks are performed as part of each step's execution for each element within the model, with < 10^{-8} relative error for any element.

For the initial time point, the free-component and complex concentrations are calculated to determine the amount of H^+ (also referred to as the "ACID" concentration) in the PC. The PC solves 16 nonlinear equations simultaneously using a modified Newton-Raphson method (Marcus et al., 2011) for the components acetate, phosphate, carbonate, nitrite, ammonium, and H^+. The total analytical component concentrations were used to calculate the bulk liquid concentrations for each free component and complex in the bulk. The bulk concentrations were used to evaluate the flux at the boundary layer between the bulk liquid and biofilm and concentrations of components with the biofilm using PCBIOFILM. The model was executed until steady-state was reached.

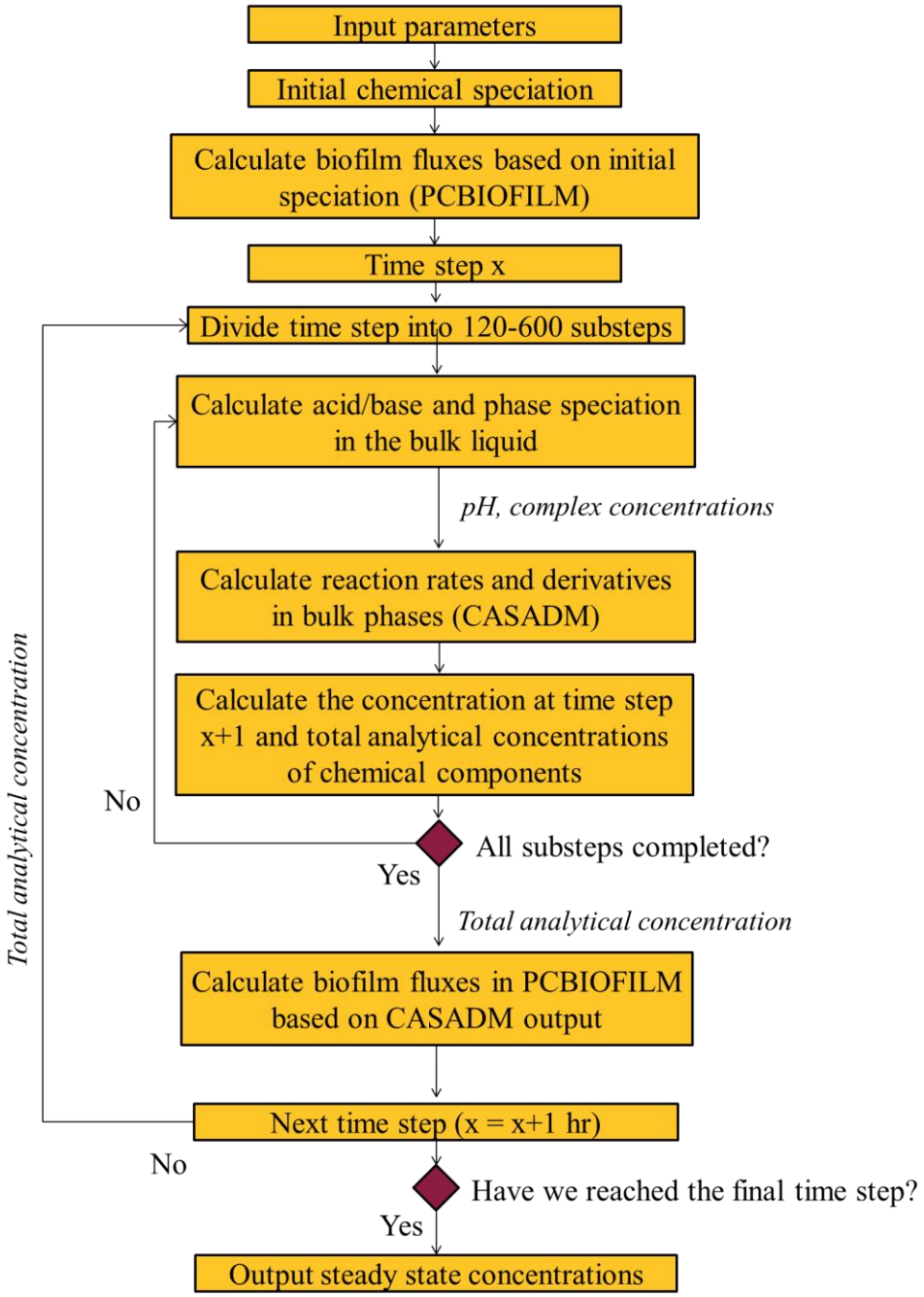

Figure 4.2. Flow chart of the solution procedure for MYAnode.

PCBIOFILM's solver routine, described in depth in Marcus et al. (2011), sequentially solves the mass action equations and mass conservation equations based on the boundary conditions. The DL is represented as 10 nodes and the biofilm as 20 nodes,

although the number of nodes can be changed if required. The bulk components are speciated based on the bulk pH, and the initial amount of H^+ at the boundary is determined using the proton condition and bulk liquid concentrations. A finite-differences method is used to transform the set of boundary conditions and mass conservation equations into a set of algebraic equations. A modified Newton-Raphson method is used to find which component and complex concentrations will set the objective functions equal to zero, with the initial conditions from the bulk as the starting point. Complex and component values are iterated on until the objective functions converge on the value of flux from the DL to the bulk is equal to the flux obtained from CASADM with a relative error of 10^{-6} in the objective functions. The concentration values are then fed back to CASADM.

To test the predictive ability of the model for realistic conditions, I utilized waste stream parameters outlined in Young et al. (2013b), Metcalf & Eddy (2014), and Ki (2017); the parameters are summarized in Table 4.5. Ki et al. (2017a) operated a 0.5-L, dual-chamber MEC with two anodes and cathodes separated by anion exchange membranes. In Ki et al. (2017a), the reactor was fed daily with focused pulse-treated primary sludge. The anode geometric surface area was 200 cm^2. For the first part of the experiments, pH was adjusted daily with 5M NaOH to maintain the anode chamber bulk liquid pH at > 6.7. Once all experiments were complete, Ki et al. (2017a) noted the final biofilm anode thickness ranged from 0.25 to 0.6 cm.

To evaluate the simulation capacity of MYAnode, I modeled a scenario reported by Ki et al. (2017a). For this, I assumed a uniform biofilm thickness of 250 μm, as it should be a sufficient thickness for that the acetate to become limited (i.e., a deep

biofilm) assuming with sufficient alkalinity present. It is my assertion that this thickness is not critical to the analysis of the system, as the biofilm is probably so deep that all acetate gets consumed well before the anode surface. Since Ki et al. (2017a) experienced intermittent poor mixing, I assumed a relatively thick DL of 1000 μm versus other models (Marcus et al., 2010; Marcus et al., 2011). To illustrate a dramatic interpretation obtained using MYAnode, I varied influent X_m concentration from 0 to 100 mg VSS/L while keep DL at 1000 μm and the hydrolysis rate at 0.25/d (consistent with Ki et al., 2017a).

Table 4.5. Influent model parameters.

Parameter	Units	Value
Influent wastewater		
HRT*	d	12
Anode chamber volume*	L	0.5
Influent pH*		6.9
Daily pH target*		7.5
SCOD*	mgCOD/L	550
PCOD*	mgVSS/L	4350
Inert biomass*	mgTSS/L	750
NH_4^{+} **,†	mgN/L	50
NO_2^{-} *	mgN/L	0
NO_3^{-} *	mgN/L	0.2
Dissolved oxygen†	mgO_2/L	0.2
HCO_3^{-} *	$mgHCO_3/L$	360
Cl^{-}‡	$mgCl^{-}/L$	142
Heterotrophic biomass**,°	mgVSS/L	300
AOB**,°	mgVSS/L	1
NOB**,°	mgVSS/L	1
Fermenting bacteria**,°	mgVSS/L	165
Acetoclastic methanogens**,°,°°	mgVSS/L	0-200
PCOD hydrolysis rate	1/d	0.25
Anode and biofilm		
Anode surface area*	cm^2	200
Anode potential*	V_{SHE}	-0.03
Substrate utilization rate‡	mmol Ace/(cm^3 d)	17.5
Half-maximum rate concentration‡	mmol Ace/cm^3	0.002
Biofilm thickness*,‡	μm	250
Diffusion layer thickness‡	μm	1000
pH optimal‡		7.5
pH inhibition range for ARB‡		2.1

*Ki et al. (2017a), **Young et al. (2013a,2013b), †Metcalf & Eddy (2014), ‡Marcus et al. (2010), °Nopens et al. (2009), °°Gray et al. (2002).

4.4 Results and discussion

4.4.1 Model evaluation

MYAnode simulated the large-scale trends seen by Ki et al. (2017a) for current and CH_4 production when the X_m value was well poised. Figure 4.3 presents the experimental and model-generated electron-equivalent mass balances (as COD) and TSS, volatile suspended solids (VSS), and SCOD effluent concentrations at a 12-d HRT, k_{hyd} of 0.25/d, a DL thickness of 1000 μm, and a range of influent X_m concentrations (0-200 mg X_m as VSS/L). (Graphs of effluent concentrations and current densities are included in Appendix C.) The most important insight from the modeling analysis is that the best fit occurred for X_m of at least 100 mg VSS/L. For this X_m, the model captured the large-scale data trends for the 12-d HRT: The electron equivalents were distributed among effluent COD > CH_4 > Coulombs, and effluent COD was dominated by VSS. Lower X_m values achieved far too low CH_4 and current recovery. X_m concentrations in PS in literature range from 0.1 to 10 mg VSS/L (Batstone et al., 2002; Nopens et al., 2009); if this range is relevant for Ki et al. (2017a), the additional X_m are probably present in the anode's biofilm, which is not included in the single-species biofilm model presented here.

Fig. 4.3a shows that MYAnode predicted a Coulombic recovery of 20% with X_m of 100 mg/L (compared to the experimental Coulombic recovery of 28%), and 94% of the current production occurred within 150 μm of the biofilm surface (Fig. 4.3b). Therefore, the assumption of a deep biofilm was reasonable. As expected, more electrons were recovered as CH_4 when the influent X_m concentration increased: the experimental CH_4 recovery was 32%, versus MYAnode results of 20% at X_m of 100 mg/L. Model-

predicted effluent COD was higher with the model (61 to 94%) than experimental observations (39%).

For the effluent COD distribution, Figure 4.3c shows that active VSS was by far the largest component, but MYAnode slightly over-estimated active VSS in the model at X_m values greater than 100 mgVSS/L: MYAnode predicted 72% of effluent COD as VSS, versus experimental results of 69%. SCOD from the model was 2% at X_m of 100 mg/L, lower than the experimental observation of 8%. MYAnode over-estimated the amount of inert suspended solids (SS) produced in the MxC by ~1%.

The output with the 1000-μm DL thickness fits the experimental data well, but 1000 μm is much large than typical DL thicknesses (Rittmann and McCarty, 2001; Wanner et al., 2006; Picioreanu et al., 2007; Picioreanu et al., 2008; Picioreanu et al., 2010; Marcus et al., 2010; Marcus et al., 2011); thus, the physical meaning of the DL must be considered. As observed by Ki et al. (2017a), the biofilm was thick and included a nonuniform layer of hydrolysable materials and other microorganisms near the boundary between the DL and biofilm. This layer likely reduced the diffusivity of all chemicals, and the diffusion coefficient in such a composite DL is likely to lie between the diffusion coefficient in a DL outside the biofilm and the diffusion coefficient within the ARB biofilm. Because MYAnode used the bulk-liquid diffusion coefficient, the DL thickness was relatively large to compensate.

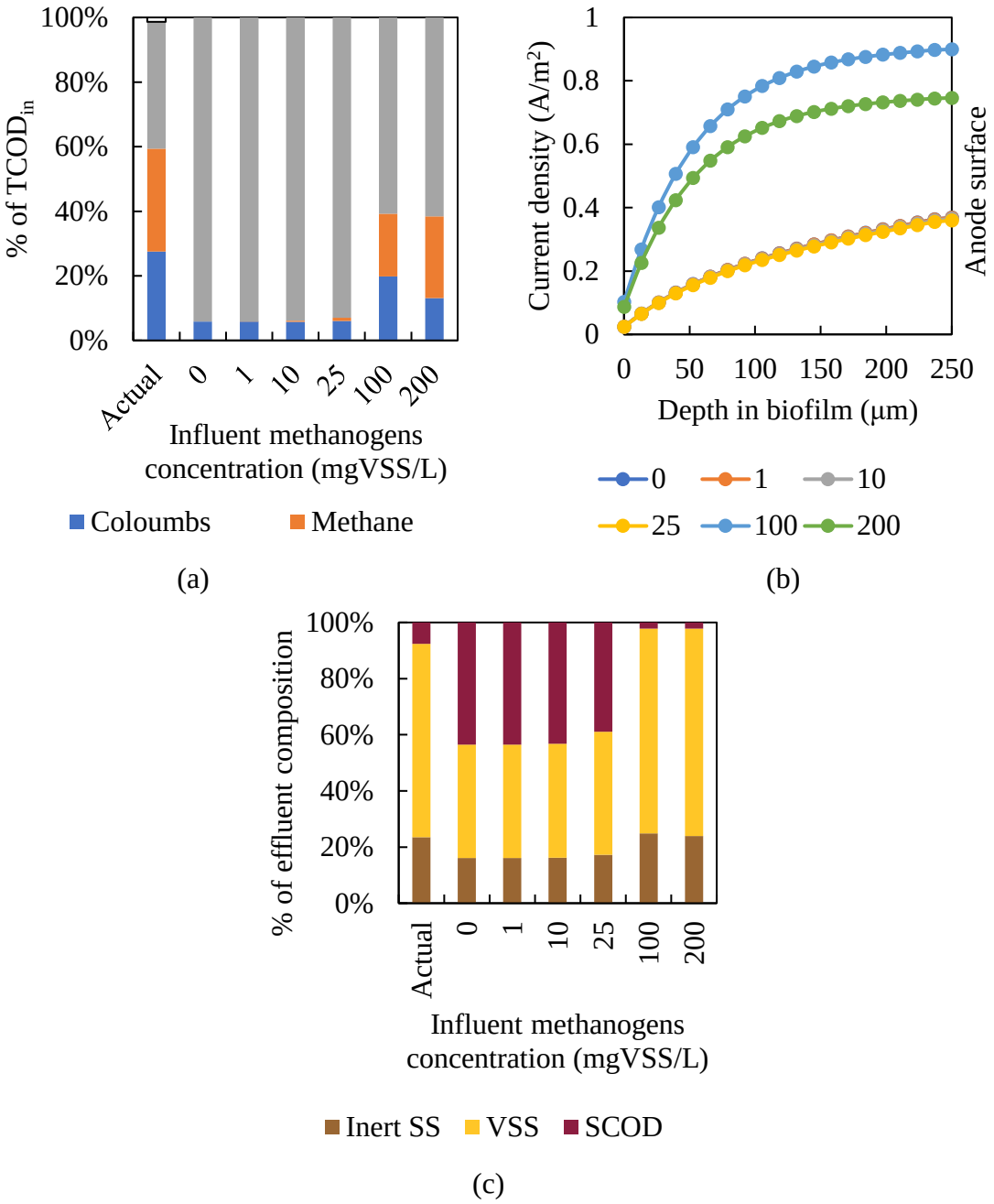

Figure 4.3. (a) Electron balances on respiration products based on $TCOD_{in}$ at a 12-d HRT, k_{hyd} = 0.25/d, DL = 1000μm, and influent methanogens concentration of 1 to 100 mg X_m as VSS/L. "Actual" refers to the experimental data. "Other" is unaccounted TCOD as reported in Ki et al. (2017a). (b) The current density profile through the biofilm. Effluent represents SCOD and TSS concentrations removed from the reactor. (c) The percentage of effluent COD as inert suspended solids (SS), VSS, and SCOD concentrations.

4.4.2 Current production depended upon bicarbonate alkalinity supplied by methanogens

The influent X_m concentration controlled the HCO_3^- alkalinity and pH. For the scenarios presented, adequate alkalinity and, therefore, current production, were achieved only at $X_m \geq 100$ mgVSS/L. For $X_m \leq 25$ mgVSS/L, Figure 4.4a shows a high acetate concentration at the biofilm surface at ~42 mM, but the high concentration did not result in high current production. In fact, little acetate was oxidized in the biofilm. $X_m \geq 100$ mg/L gave much higher current (Figure 4.4a), even though the acetate concentration was lower in the biofilm. HCO_3^-- and CO_3^{2-}-related alkalinity production in the bulk liquid was minimal, less than 1 mg$CaCO_3$/d, for $X_m \leq 25$ mg/L. Coupled with less than 13 mg$CaCO_3$/d supplied in the influent stream and low alkalinity production from NH_4^+ release by hydrolysis, alkalinity delivered to the biofilm was small, and the pH declined to 5.44 in the bulk liquid and 5.42 in the anode (Figure 4.4a). This net flow of alkalinity into the biofilm is illustrated by the gradients in Figure 4.4c.

The presence of $X_m \geq 100$ mg/L provided greater pH stability by decreasing the amount of acetate, a relatively strong weak acid, in the bulk liquid, while simultaneously producing HCO_3^-, a weaker weak acid and alkalinity; however, too great X_m competed for acetate with ARB. The bulk HCO_3^- from methanogenesis (Figure 4.4b) increased from negligible at 1 mg X_m/L to 1230-1500 mg $CaCO_3$/d at 100-200 mg X_m/L, and this stabilized the pH of the bulk liquid to the 6.3-7.3 range (Figure 4.5a). Specifically, HCO_3^- alkalinity diffused into the DL and biofilm at 215-317 mg $CaCO_3$/d, stabilizing the biofilm pH to a less inhibitory range of pH 6.31 to 6.43 (Figure 4.5b) prior to the daily reactor feeding.

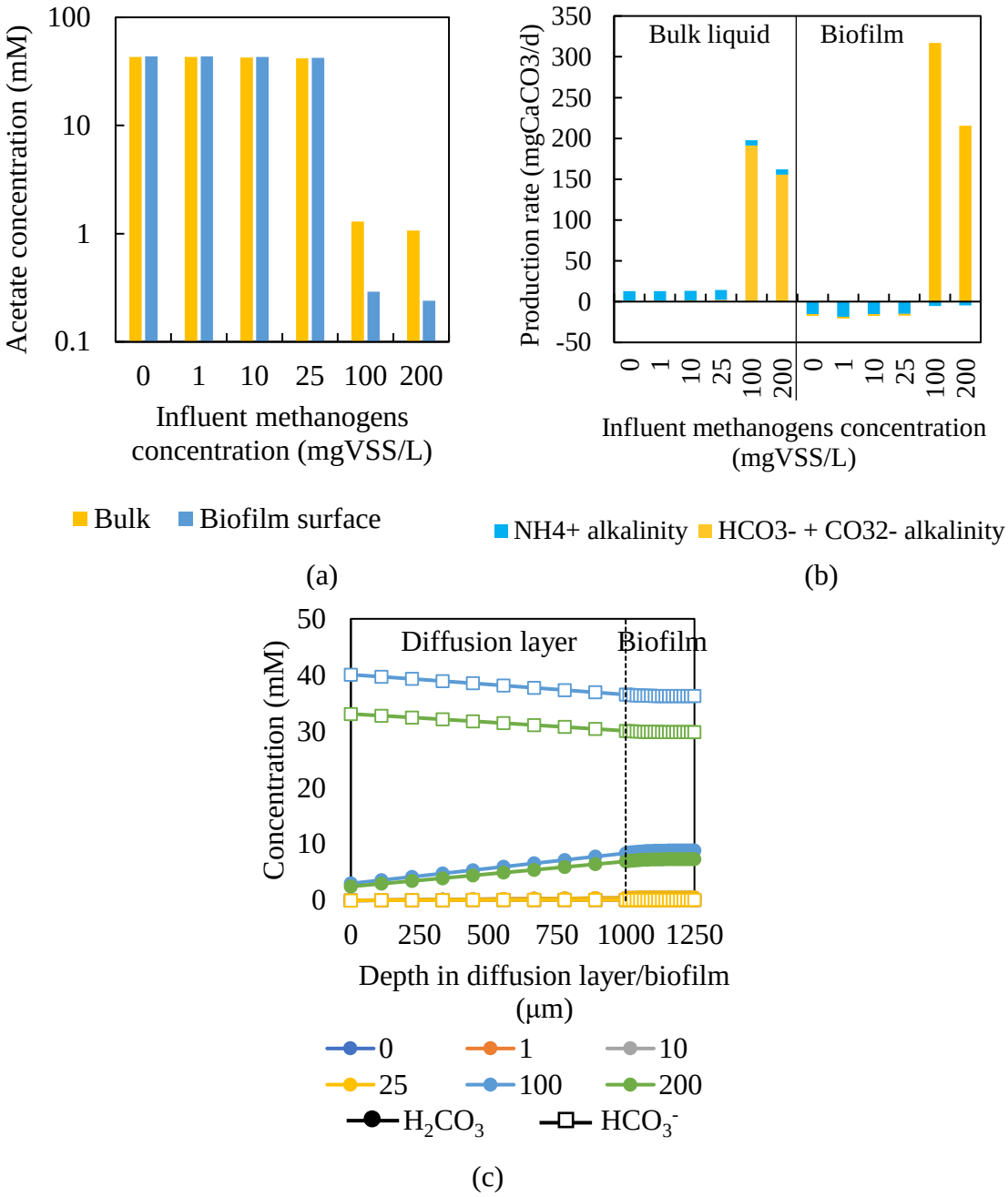

Figure 4.4. As a function of influent methanogens concentration (X_m, in mg VSS/L): (a) the acetate profile from the bulk liquid to the anode surface immediately after the daily reactor feeding; (b) the production rate of HCO_3^- + CO_3^{2-} and NH_4^+ alkalinity in the bulk liquid and the mass flow into the biofilm, with positive numbers representing flow into the biofilm and negative numbers representing flow out of the biofilm; and (c) H_2CO_3 and HCO_3^- concentrations in the diffusion layer and biofilm.

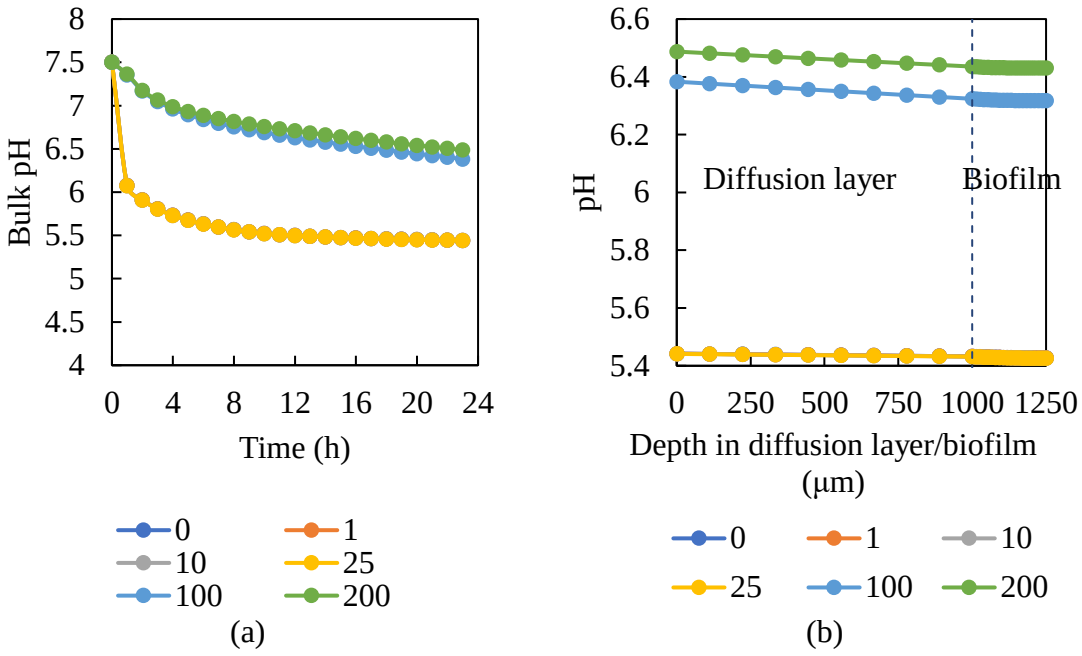

Figure 4.5. As a function of influent methanogens concentration (X_m, in mg VSS/L): (a) The bulk liquid pH over the course of 1 d; and (b) pH in the diffusion layer and biofilm prior to the daily feeding, where the black dashed line represents the biofilm surface.

Having high X_m was not a panacea for MxC treatment of low-alkalinity streams, since acetoclastic methanogens compete with the ARB for acetate. Even though the pH was maintained relatively high with X_m of 200 mg/L (Figure 4.5), an influent X_m of 200 mg/L caused a decline in current that was commensurate with an increase in methanogenesis (Figures 4.3a and b). Having more input methanogens decreased the flux of HCO_3^- into the biofilm (Figures 4.4b and c), because the lower current production required less alkalinity to counterbalance H^+ production from ARB oxidation of acetate.

4.5 Conclusion

MYAnode is a novel mathematical model that combines chemical and biological wastewater treatment processes in the bulk liquid with substrate utilization and current production in electrically active biofilms. In this work, MYAnode was applied to the anode of an MxC utilizing primary sludge. The model accurately simulated the large-scale trends in effluent concentrations, CH_4 production, and Coulombic efficiency, as long as the influent concentration of acetoclastic methanogens (X_m) was properly poised at ~100 mg/L. MYAnode explained the that influent X_m performed a critical role in providing alkalinity to prevent the pH from dropping to inhibitory levels for ARB and methanogens. However, X_m also competed with ARB for acetate. Thus, controlling the X_m input is key to providing adequate bicarbonate alkalinity to buffer the biofilm anode while minimizing CH_4 production when the influent stream has naturally low alkalinity.

CHAPTER 5

Understanding the Role of Diffusion Layer Thickness and Hydrolysis Rates in MxC Performance using MYAnode

5.1 Introduction

MxCs research constantly strives for improved current production and COD removal for successful scale up of the technology. To this end, MxC research topics have ranged from reactor configuration to cathode-performance improvement to increased substrate bioavailability through substrate pretreatment. For example, researchers have focused on improving MxC performance through faster hydrolysis rates in the MxC (Velasquez-Orta et al., 2011; Dhar et al., 2013; Li et al., 2013; Gao et al., 2014; Ki et al., 2017a) or via prefermentation of complex waste streams (Oh and Logan, 2005; Zuo et al., 2006; Kannaiah Goud and Venkata Mohan, 2011; Mahmoud et al,. 2014; Ki et al., 2015). MxCs have been suggested as a potential monitoring device for hydrolysis rates in anaerobic digesters, since ARB and methanogens consume acetate substrate and have similar pH limitations (Liu et al., 2011; Liu et al., 2014; Young et al., 2015).

Most experiments have been performed under well-buffered conditions, including Rezaei et al. (2008) and Velasquez-Orta et al. (2011) with cellulose hydrolysis, Young et al. (2015) using alkaline- and thermally-pretreated waste activated sludge centrates, and Choi and Ahn (2014) using high rate anaerobic prefermentation of primary sludge. While few studies have studied hydrolysis rates of complex waste streams in low-alkalinity conditions (Li et al., 2013; Ki et al., 2017a; Ki et al., 2017b; Colombo et al., 2017), each of these studies mentioned significant variations in bulk liquid pH, which

dampened or inhibited current production. Until now, modeling researchers have not focused on the impact of varied hydrolysis rates on MxC performance.

Like hydrolysis rates, DL thickness is an important parameter dictating substrate availability to the biofilm. While the benefits of decreasing the DL thickness continues to be thoroughly researched for the cathode, the effects of DL thickness have not been a focus in MxC-anode research. Fick's law states that the mass flux, J_{diff}, through a medium is linear:

$$J_{diff} = -D\frac{\partial C}{\partial x} \approx -\frac{D}{L}(C^{B} - C^{Int}) \quad \text{(Eqn. 5.1)}$$

where C^{B} is the concentration in the bulk liquid, C^{Int} is the concentration at the DL and biofilm interface, D is the diffusion coefficient in the bulk liquid, and L is the DL thickness. Therefore, the mass flux will be highest at the biofilm when the DL thickness is at its shortest. Torres et al. (2008a,2008b) established that diffusion of buffer into and out of the biofilm is important to maximize current production in the biofilm. Other works focused on measuring diffusion through the biofilm (ter Heijne et al., 2008; Renslow et al., 2013), understanding the impact of DL thickness on estimation of ARB kinetic parameters (Lee et al., 2009), and using forced flow through or away from the anode biofilm to change diffusion layer thicknesses (Sleutels et al., 2009; Sleutels et al., 2011).

Some mathematical models of the biofilm anode include DL and biofilm thicknesses as input parameters, but researchers have not modeled how DL thickness affects performance using complex waste streams. Modelers have generally varied substrate concentration (Katuri and Scott, 2009) or buffer concentration (Picioreanu et al.,

2008; Picioreanu et al., 2010; Marcus et al., 2010; Marcus et al., 2011) to improve diffusion and ion transport through the biofilm. Merkey and Chopp (2012) used 2D modeling to explore the impact of diffusion layer thickness on current production from multiple rod anodes using acetate substrate, but neglected the microbial complexity, syntrophy, and competition that occurs in the complex waste streams like municipal or industrial wastewater.

Developed by Marcus et al. (2010, 2011), PCBIOFILM defines two regions involving diffusion and migration: a DL and a biofilm layer composed of active ARB. Although DL is usually used to represent mass transfer resistance external to a biofilm, a DL can be defined as any medium in which microbial reactions of interest are not occurring. In my model, the microbial reaction of interest is the ARB reaction. As observed by Ki et al. (2017a), the external layers of the anode biofilm can consist of a variety of hydrolysable materials and other microorganisms that likely reduce the diffusivity of all chemicals that must transport from the bulk liquid to the ARB near the anode surface. Similar to Sabba et al. (2017), I define a "composite" DL that consists of a non-reactive layer of liquid next to a large layer of non-reactive biomass and PCOD. Different chemical species must diffuse through the composite layer to reach the anode biofilm. For simplicity, I define one diffusion constant for the composite layer, with a value that probably lies between the diffusion coefficient in the DL outside the biofilm and the diffusion coefficient within the ARB biofilm. Assuming that the value of D in Eqn. 5.1 is held constant, a composite DL requires that L increase to maintain the C^{B} and C^{Int} boundary conditions. For example, Katuri and Scott (2009) accurately predicted the anode potential by utilizing a lumped mass-transfer coefficient for the combination of DL

and biofilm. Varying the DL thickness for a composite biofilm allows a model to explore the impact of heterotrophic bacteria or methanogens on the metabolic activity of ARB.

In this work, I utilize MYAnode, the mathematical model developed in Chapter 4, to examine the role of two operational parameters, DL thickness and substrate bioavailability from hydrolysis, on MxC performance. Specifically, I vary the DL thickness and hydrolysis rates (k_{hyd}) for a MxC operated in alkalinity-limited conditions typical of primary sludge. I demonstrate that DL thickness plays an important role in providing adequate substrate and alkalinity required to maintain ARB respiration and current production in the biofilm. In contrast, acetate availability from hydrolysis plays a less important role in improving MxC performance.

5.2 Methods and modeling approach

I evaluated the effects of DL thickness and hydrolysis rate using MYAnode, which is discussed in depth in Chapter 4. MYAnode is a novel non-steady-state mathematical model that integrates the chemical and biological processes common in wastewater treatment and ARB oxidation of acetate. The model pulls three mathematical model foundations into one platform: CASADM, a non-steady-state model that describes typical aerobic, anoxic, and anaerobic biological phenomena exhibited in continuous stirred tank reactors in WWTPs; CCBATCH, a steady-state model that links fast chemical speciation reactions, including acid-base equilibrium and complexation reactions, with slower microbial reactions; and PCBIOFILM, a non-steady-state model that describes transport from a bulk liquid and acetate utilization by an anode biofilm. The model system is the same as described in Figure 4.1: a chemostat-like bulk-liquid chamber fed primary sludge, an anode populated with an ARB biofilm, and a membrane that separates the anode from the cathode chamber and allows for counter-diffusion of OH^- molecules into the anode chamber to maintain electroneutrality due to electrons leaving the system as current.

MYAnode was implemented in MATLAB using the solution procedure outlined in Figure 4.2. The ODEs were solved using Euler's method, initial value conditions equal to the influent composition, and time steps ≤ 1 min until the system obtained steady state (i.e., a relative difference between data points < 10^{-8}). The chemical components and complexes are summarized in Table 4.4, and the same physical and operational parameters are summarized in Table 4.5 with a few modifications. For models varying DL thickness, the DL thickness was varied from 500 to 4000 μm with an X_m

concentration of 100 mgVSS/L and a PCOD-hydrolysis rate of 0.25/d (optimal values from Chapter 4). These DL thicknesses are larger than the typical values in various sources (Rittmann and McCarty, 2001; Wanner et al., 2006; Picioreanu et al., 2007; Picioreanu et al., 2008; Picioreanu et al., 2010; Marcus et al., 2010; Marcus et al., 2011), because the DL thickness represents a composite of an external diffusion layer and non-ARB in the biofilm; the best-fit value of 1000 μm was obtained from performance observations in Ki et al. (2017a). For models varying the hydrolysis rate, k_{hyd} was varied from 0.12 to 0.5/d at an X_m concentration of 100 mgVSS/L and DL thickness of 1000 μm. In all cases, the modeled reactor was fed daily with primary sludge with a 12-d HRT and simultaneously adjusted to pH 7.5 using NaOH in the anode chamber. The anode geometric surface area was 200 cm^2, and the biofilm thickness was assumed to be 250 μm, which Chapter 4 demonstrated was essentially a deep biofilm when pH was not inhibitory.

5.3 Results and discussion

5.3.1 Varying diffusion-layer thickness

While decreasing DL thickness provided more acetate at the biofilm surface, the smallest DL tested did not provide the best performance due to pH inhibition in the rest of the system. Figure 5.1a shows that the highest combined production CH_4 and Coulombs, 40% of influent total COD (TCOD), was achieved at a 1000-μm DL thickness, versus the lowest, 7.8% of influent TCOD, at the 500-μm DL thickness. Increasing the DL thickness from 1000 to 4000 μm decreased Coulombic recovery from 19.4 to 7.6%, which was counter-balanced by an increase in CH_4 generation from 21 to 30.6%. The decline of current production with increasing DL thickness above 1000 μm was due to coupled decreases the concentrations of acetate and HCO_3^- alkalinity at the biofilm surface. The higher concentration of acetate at the biofilm surface at DL of 1000 μm led to higher acetate consumption within the almost-deep biofilm, as illustrated in Figure 5.1b. However, acetate consumption was possible only with concurrent availability of HCO_3^- (Figure 5.1c): At DL 1000 μm and larger, adequate HCO_3^- was available to prevent to buffer H^+ production and a decreased of biofilm pH below 6.0, which incurs low-pH inhibition for ARB (Torres et al., 2008a; Franks et al., 2009).

The 500-μm DL thickness produced lower methane and Coulombs than the larger DL thicknesses, even though the bulk liquid had an acetate concentration 30-fold and 200-fold higher at the anode and biofilm surfaces, respectively. Figure 5.1d shows that the poor performance at the 500-μm DL thickness was due to the bulk pH decreasing from 7.5 to 5.93 within the one hour of reactor feeding and to 5.42 within 24 h; the latter pH value is inhibitory for X_m consumption of acetate (McCarty, 1964; Parkin and Owen,

1986; Appels et al., 2008). Consequently, insufficient oxidation of acetate to HCO_3^- by X_m lowered the amount of HCO_3^- at the anode surface to only 0.25% of that present with 1000-μm DL thickness; the ARB were severely inhibited by the low pH.

The most common method to reduce the diffusion layer thickness is to increase the mixing intensity, which reduces the DL thickness. However, it is difficult to predict the impact of reducing the DL thickness on the biofilm. On the one hand, reducing the DL thickness will increase the shear stress and turbulence at the outer boundary of the biofilm, which can increase biofilm detachment and decrease the composite DL thickness (Stoodley et al., 2002; Laspidou and Ritmann, 2004; Flemming and Wingender, 2010; Merkey and Chopp, 2012). In a complex waste stream like primary sludge where heterotrophic bacteria and methanogens dominating the outer layer composition (Ki et al., 2017a), increased detachment effectively removes the ARB's competitors for acetate substrate, allowing more substrate to diffusion to the ARB and improve current production. On the other hand, increasing shear stress in some biofilms leads to increased entanglement of biopolymers in the biofilm, causing either a consolidation of the biofilm or increased matrix stability, making it more difficult to remove the non-ARB microorganisms from the outer biofilm layer (Stoodley et al., 2002; Laspidou and Rittmann, 2004; Flemming and Wingender, 2010) and, consequently, a larger effective DL thickness.

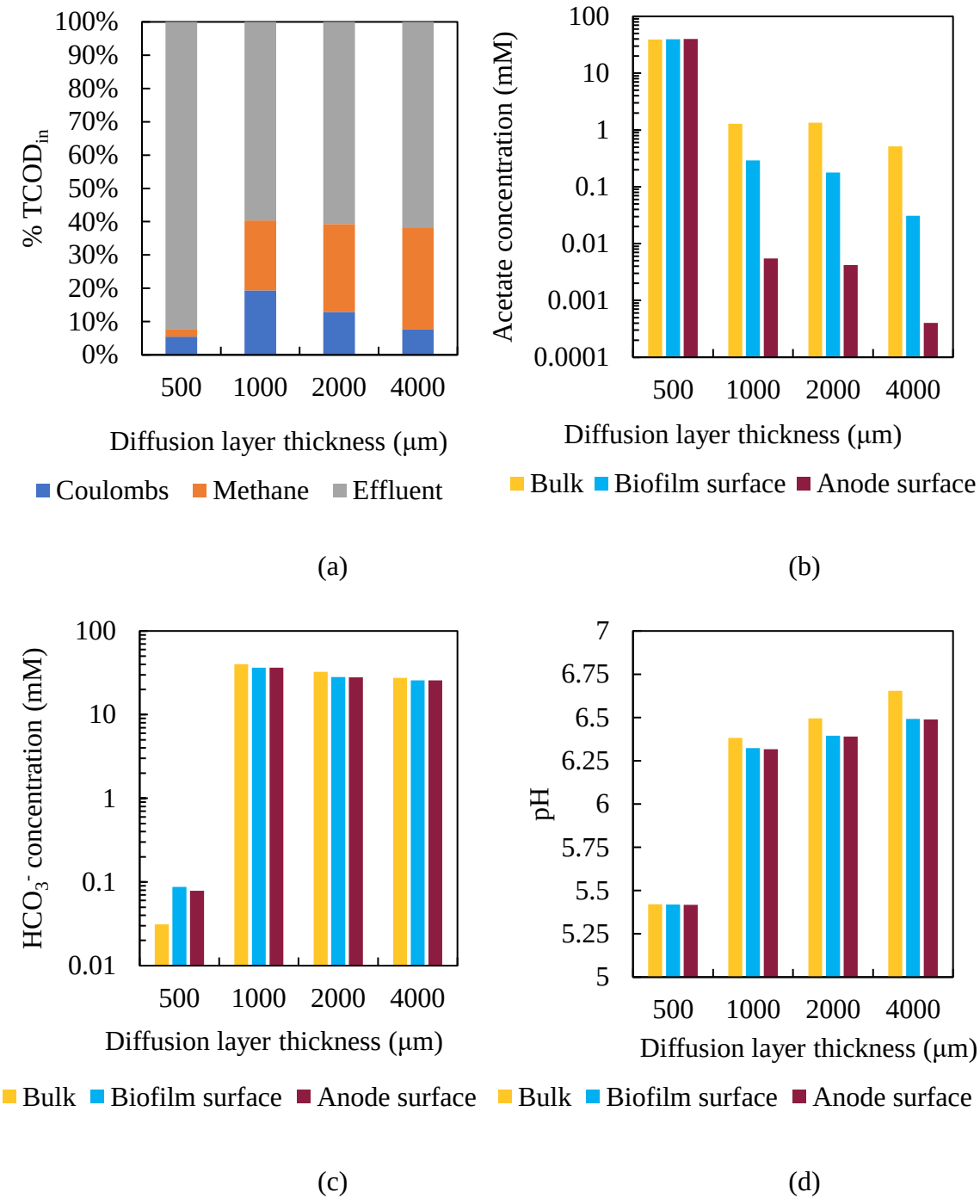

Figure 5.1. With a 12-d HRT and a hydrolysis rate of 0.25/d, the impact of DL thickness on (a) electron balances of respiration products normalized to the $TCOD_{in}$ concentration. In the bulk liquid, at the biofilm surface, and at the anode surface, (b) acetate concentration after daily reactor feeding, (c) HCO_3^- concentration after daily reactor feeding, and (d) pH prior to the daily reactor feeding.

5.3.2 Varying PCOD hydrolysis rates

While a faster hydrolysis rate increased the concentration of acetate available in the bulk liquid, it did not necessarily translate into significant improvements in current production and even hindered MxC performance at higher hydrolysis rates. Figure 5.2a illustrates that a PCOD hydrolysis rate of 0.25/d had the highest CH_4 production and Coulombs recovery -- 21.0 and 19.4%, respectively -- which were slightly larger than the CH_4 and Coulombs recoveries at 0.12/d (17.1% and 16.7%, respectively). CH_4 production and Coulombs recovery percentages were significantly lower at a 0.5/d hydrolysis rate, which converted 5.6% of influent TCOD to current and 4.1% to CH_4.

Similar to the results obtained by varying X_m and DL thickness, the performance trends when varying the hydrolysis rate largely depended on the concentrations of acetate and HCO_3^-. Although more acetate was available with the higher lower hydrolysis rate of 0.5/d (seen in Figure 5.2b), the oxidation of acetate by X_m produced more HCO_3^- at hydrolysis rates of 0.12 and 0.25/d, 165 to 191 mg $CaCO_3$/d of HCO_3^-, respectively, compared with only 8 mg $CaCO_3$/d produced at 0.5/d. The higher HCO_3^- concentrations in the bulk liquid (Figure 5.2c) led to more than 230-fold more HCO_3^- buffer at the biofilm surface and throughout the biofilm for the two lower hydrolysis rates. Subsequently, Figure 5.2d shows that the bulk and biofilm pH were maintained above 6.30 for the two lower hydrolysis rates, while the pH for the 0.5/d hydrolysis rate dropped from 7.5 to 6.1 within the first hour of feeding and to 5.43 within 24 h. Low pH inhibited anode respiration and methanogenesis.

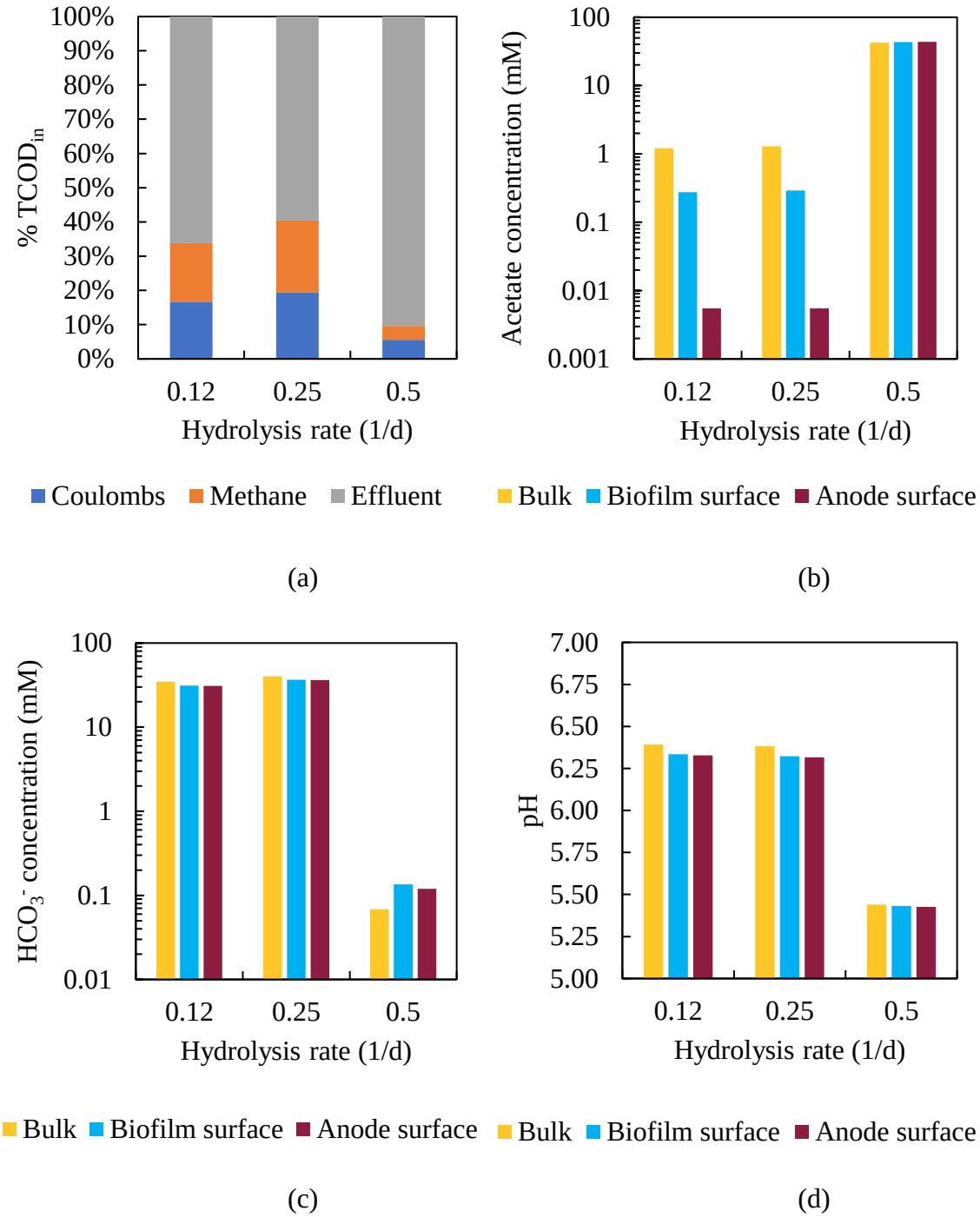

Figure 5.2. At 12-d HRT and DL thickness of 1000 μm, the impact of hydrolysis rate on (a) electron balances on respiration products based on $TCOD_{in}$ concentrations. In the bulk liquid, at the biofilm surface, and at the anode surface, (b) acetate concentration after daily reactor feeding, (c) HCO_3^- concentration after daily reactor feeding, and (d) pH prior to the daily reactor feeding.

5.4 Conclusion

Using MYAnode, I defined optimal conditions for DL thickness and hydrolysis rate. DL had a much larger effect. Increasing the hydrolysis rates from 0.12 to 0.25/d in the reactor only marginally improved Coulombic efficiency and methane production, by 2.6 and 3.9%, respectively. Increasing the DL thickness from 500 to 1000 μm improved Coulombic efficiency and methane production by 13.9 and 18.6%, respectively. Performance improvements for the best DL and hydrolysis rates depended the production of HCO_3^- alkalinity by X_m. However, a too-high DL thicknesses (> 1000 μm) led to an increase in CH_4 production, because less acetate was available at the biofilm surface due to external mass-transport resistance. A too-high hydrolysis rates (> 0.25/d) produced too much acetate, causing the bulk pH to drop to inhibitory levels for X_m in the bulk liquid. Without acetate oxidation by X_m, insufficient HCO_3^- was available to prevent pH depression and inhibition of ARB throughout the biofilm. Thus, reactor design should prioritize decreasing the DL over increasing hydrolysis rates as a method of improving current production from MxCs. DL probably can be made smaller by introducing more intense mixing in the anode chamber, but this trend is hypothesized, not proven. In all cases, providing more alkalinity will improve performance.

CHAPTER 6

Using MYAnode to Understand the Impact of Hydraulic Retention Time on a Microbial Electrochemical Cell Fed Primary Sludge

6.1 Introduction

MxCs provide a novel method of converting organic waste directly to electricity or other valuable outputs. MxC research has increasingly focused on treating complex organic waste streams like brewery effluent, swine wastes, and primary and secondary municipal wastewater sludges (Zhuang et al., 2012; Pous et al., 2013; Sevda et al., 2013; Ki et al., 2015; Kim et al., 2016). Complex waste streams present a variety of obstacles in MxC technologies. First and foremost, complex waste streams require hydrolysis to hydrolyze the waste to soluble forms than can then be fermented to acetate or H_2 for ARB consumption (Eastman and Ferguson, 1981; Vavilin et al., 2008; Parameswaran et al., 2009). Depending upon the hydrolysis rate, most VFAs produced from hydrolysis of primary sludge or waste-activated sludge are produced within 10-20 days (Rittmann and McCarty, 2001; Vavilin et al., 2008; Velasquez-Orta et al., 2011). This HRT time range invites competition from diverse microorganism populations like facultative heterotrophic bacteria and methanogens (X_m) for the acetate and H_2 produced during fermentation (Gray et al., 2002; Young et al., 2013a). However, diverse communities are essential in providing the syntrophic functions required for production of VFAs) for ARB consumption (Parameswaran et al., 2009; Lee et al., 2009; Lee and Rittmann, 2009; Pant et al., 2010; Gao et al., 2014).

To address some of these issues, several researchers have explored operating MxCs at HRTs ranging from hours to 15 d. One method to minimize competition

between ARB and acetoclastic methanogens is to operate MxCs closer to the washout SRT for acetoclastic methanogens, ~ 4 d (Rittmann and McCarty, 2001; Gao et al., 2014; Ki et al., 2017a; Ki et al., 2017b). Many authors found higher current densities, but lower coulombic recovery and COD removal with decreasing HRT (Liu et al., 2004; Choi and Ahn, 2014; Gao et al., 2014; Fazli et al., 2018). Hours-long HRTs (< 12 h) encouraged H_2-scavenging by homoacetogens and hydrogenotrophic methanogens, improving current production by ARB (Lee et al., 2009; Lee and Rittmann, 2010; Parameswaran et al., 2011; Parameswaran et al., 2012). However, these HRTs are inadequate for effective hydrolysis of primary sludge or WAS (Vavilin et al., 2008).

Few models have explored the effect of HRT on MxC performance. Several MxC mathematical models have explored the impact of limited microbial diversity in the bulk liquid (Picioreanu et al., 2010; Pinto et al., 2010, 2011). Li and He (2016) and Zhao et al. (2016) explored modeling MxC performance at HRTs < 24 h HRTs under non-competitive conditions using acetate media. To date, no model has explored the impacts of varying HRT using complex communities and substrates.

In this Chapter, I expand upon the analyzes in Chapters 4 and 5 by applying MYAnode for utilization of primary sludge at different anode HRTs. I vary the influent X_m concentration between 0 and 200 mg VSS/L and the hydrolysis rate from 0.12 to 0.5/d. I demonstrate that, like in Chapter 4, the influent concentration of X_m plays an important role in anode performance by providing additional buffering capacity in the system. Like in Chapter 5, hydrolysis rate plays a lesser role in improving MxC performance, and higher hydrolysis rates may be inhibitory for current production, as too

few X_m or ARB are present to prevent the acetate produced from lowering the bulk and biofilm pH values.

6.2 Methods and modeling approach

Consistent with Chapters 4 and 5, I evaluated the effects of HRT using MYAnode. As discussed previously, MYAnode is a novel non-steady-state mathematical model that combines the chemical and biological processes common to wastewater treatment (from CASADM) with ARB oxidation of acetate to produce current on an anode (from PCBIOFILM). Based on CCBATCH, MYAnode also includes a steady-state model that couples fast chemical speciation reactions, like acid-base equilibrium, with slower microbial reactions. The model system is the same as described in Figure 4.1: an anode bulk chamber fed primary sludge, an anode populated with an ARB biofilm, and a membrane that separates the anode and cathode chambers and allows for counter-diffusion of OH^- molecules into the anode bulk liquid to maintain electroneutrality.

Like in the previous modeling chapters, MYAnode was implemented in MATLAB using Euler's method and 1-min. time steps until steady-state values were obtained (~150-200 d simulated; i.e., a relative difference between data points < 10^{-8}). The biofilm fluxes were recalculated hourly. The chemical components and complexes are summarized in Table 4.4. The physical and operational parameters are the same as listed in Table 4.5, except that the HRT was varied from 6 to 15d and hydrolysis rates from 0.12 to 0.5/d at each HRT. The DL thickness was 1000 μm, the optimal value obtained from Chapter 5. Since the parameters evaluated here vary from the physical conditions documented by Ki et al. (2017a) at HRTs 6, 9, and 15, the data will not be directly compared but will be evaluated for the general trends.

6.3 Results and discussion

6.3.1 Model validation and the effect of varying influent methanogens concentration

MYAnode simulated the large-scale trends demonstrated by Ki et al. (2016) at HRTs ≥ 12 d when the X_m value was well chosen. The best modeling fits occurred at HRTs ≥ 12 d and at an influent X_m concentration of 100 mg VSS/L. Like Ki et al. (2016), Figure 6.1a illustrates that, at a hydrolysis rate of 0.25/d, MYAnode predicted increasing CH_4 production with increasing HRT, and the electron equivalents were distributed among effluent COD > CH_4 > Coulombs. (Data for other X_m values are presented in Appendix E.) At all conditions, the model predicted higher concentrations of effluent COD than the experimental results.

The model predicted major trends accurately at ≥ 12 d HRT. At a 12-d HRT, the modeling results and experimental data predicted roughly the same ratio of electrons end up as CH_4 and Coulombs: 16.7-17.1% for each product in the modeling results vs. 28%-31% with the experimental data. The model and experimental data were consistent in predicting that more CH_4 would be produced at ≥ 12 d versus the shorter HRTs. For the effluent COD distribution, Figure 6.1b shows that active VSS was by far the largest component, but MYAnode slightly over-estimated active VSS in the model at X_m values greater than 100 mgVSS/L: MYAnode predicted 72-73% of effluent COD as VSS, versus experimental results of 69%. SCOD from the model was 2% at X_m of 100 mg/L, lower than the experimental observation of 6-7%. MYAnode over-estimated the amount of SS produced in the MxC by ~1-2%.

At HRTs ≤ 9 d, the model significantly underestimated methane and current production. For all influent X_m concentrations evaluated, the model predicted that, at a 6

d HRT, < 1% of influent TCOD converted to current or CH_4, versus the experimentally determined 29% of influent TCOD converted to Coulombs and 12% to CH_4. At the 9 d HRT, the model predicted 5% of influent TCOD converted to current and < 1% to CH_4 versus the experimentally obtained 34% of influent TCOD converted to Coulombs and 20% to CH_4. The effluent COD distribution illustrates that the model overestimated SCOD as 42-47% of effluent COD, versus 12-13% with the experimental data, and underestimated VSS as 38-42% of effluent COD. versus 67-70% in the experimental data.

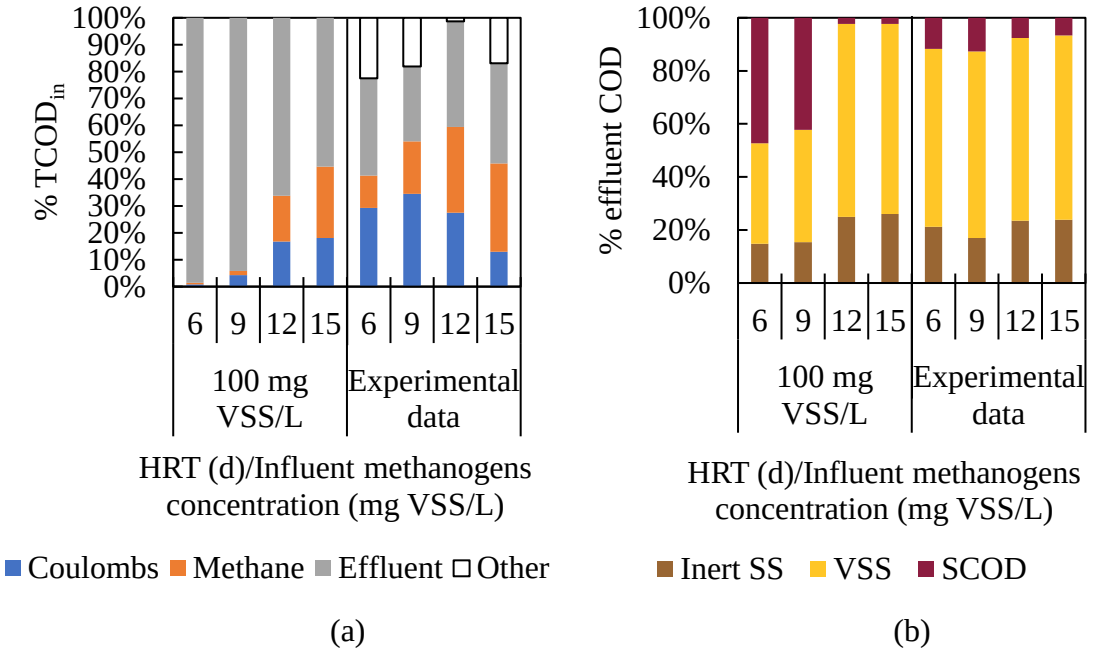

Figure 6.1. (a) Electron balances on respiration products based on $TCOD_{in}$ at an influent methanogens concentration of 100 mg X_m as VSS/L and a 0.25/d hydrolysis rate. "Other" is unaccounted TCOD, as reported in Ki et al. (2016). (b) The percentage of effluent COD as inert suspended solids (SS), VSS, and SCOD concentrations.

6.3.2 High PCOD loading leads to pH inhibition at low HRTs and moderate X_m concentrations

The model predicted low current and CH_4 production at 6- and 9-d HRTs, primarily due to low bulk and biofilm pH values, regardless of hydrolysis rate and with $X_m \leq 200$ mgVSS/L. At the 6- and 9-d HRTs, the bulk-liquid pH decreased from 7.5 to less than 6.0 within an hour of the daily reactor feeding and pH adjustment and to less than 5.45 by the end of 24 h (Figure 6.2a), resulting in most of the day being at an inhibitory pH for ARB and X_m (McCarty, 1964; Parkin and Owen, 1986; Appels et al., 2008; Torres et al., 2008a; Franks et al., 2009). Approximately 520 and 340 mg COD/L/d, respectively, of PCOD were hydrolyzed to SCOD at 6- and 9-d HRTs, versus 260 and 200 mg COD/L/d at 12- and 15-d HRT. As discussed in depth in Chapter 4, pH inhibition was due to a combination of high acetate concentrations lowering the pH towards the pKa of 4.76 (Figure 6.2b) and either an insufficient population of X_m to maintain a population above washout or enough ARB (and anode surface area) to oxidize acetate to current and a relatively weaker acid HCO_3^- (Figure 6.2c).

The 6- and 9-d HRTs maintained acetate concentrations in the bulk liquid greater than 13 and 34 mM from the bulk liquid to the anode surface. For comparison, acetate concentrations were less than 1.3 mM at the 12- and 15-d HRTs. At the same time, the X_m concentrations in the bulk liquid were 100-101 mg VSS/L, which indicated little biomass growth and, thus, HCO_3^- respiration by acetoclastic methanogens (< 1 mM HCO_3^-). Conversely, at the 12- and 15-d HRTs, X_m bulk concentrations range from 153 to 156 mg VSS/L, respectively, indicating active respiration of 25-27 mmol/d HCO_3^- from acetoclastic methanogenesis.

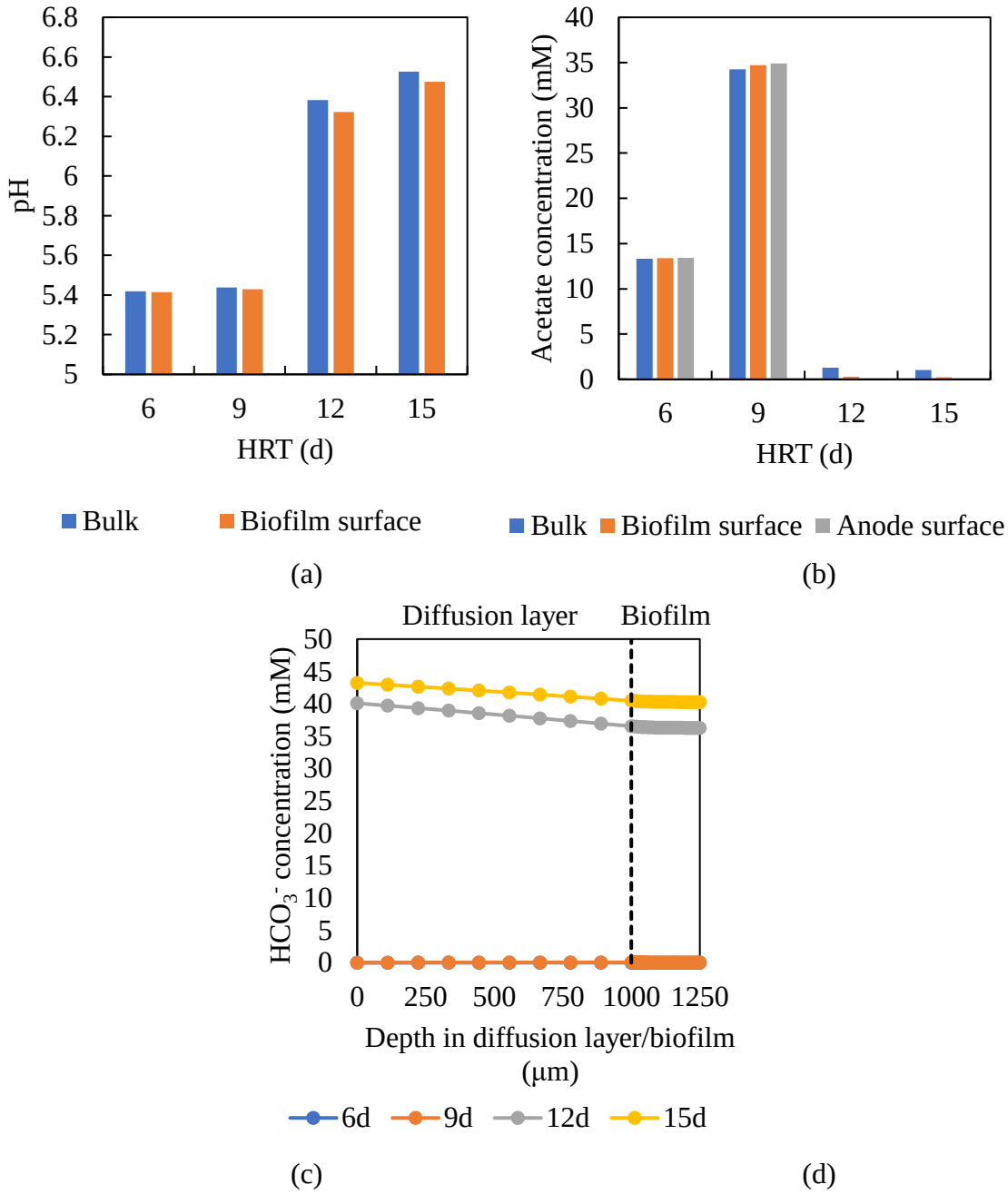

Figure 6.2. (a) pH and (b) acetate concentration in the bulk, biofilm surface, and anode surface prior to daily feeding at 100 mg/L influent X_m. (c) HCO_3^- concentration in the diffusion layer and biofilm prior to daily feeding.

Based on the results obtained at 12- and 15-d HRTs, it is likely that increasing X_m concentrations in the bulk liquid beyond the concentrations examined in this work would

eventually result in adequate HCO_3^- production to prevent pH inhibition of X_m and ARB. However, higher of X_m concentrations would likely result in significantly higher CH_4 production that would quickly outpace current production. Thus, increasing alkalinity to maintain a more hospitable pH for ARB is a better control strategy for current production at the low HRTs.

6.3.3 Increased hydrolysis rate can be detrimental to current production

Current and CH_4 production were hindered at all hydrolysis rates for the 6- and 9-d HRTs. Figure 6.3 shows that performance was consistent for all hydrolysis rates and influent X_m concentrations evaluated at 6- and 9-d HRTs. At a 6-d HRT, only 1-2% of electrons from influent TCOD were used to produce current and 0.1 to 0.6% to CH_4 with increasing hydrolysis rate regardless of X_m concentration. At a 9-d HRT, 3.5-5.1% of electrons from influent TCOD were used to current while CH_4 production increased 0.4 to 0.5% at 25 mg VSS/L influent X_m and 1.3 to 1.8% at 100 mg VSS/L influent X_m with increasing hydrolysis rate. As previously discussed, the system was inhibited due to the bulk and biofilm pH decreasing to ~5.45 at even the slowest hydrolysis rates (Figure 6.4a) due to combination of high acetate concentrations (13-15 mM at 6-d and 29-42 mM at 9-d HRTs) in the bulk (Figure 6.4b) and < 0.1 mM HCO_3^- alkalinity conditions (Figure 6.4c).

In contrast with the lower HRTs, the 12- to 15-d HRTs demonstrated improved performance with increasing hydrolysis rate at higher influent X_m concentrations. Consistent with the 6- and 9-d HRTs, 25 mg VSS/L influent X_m concentrations demonstrated little performance difference at different hydrolysis rates: CH_4 and Coulombs products accounted for 1-2% and 5-7% respectively, of the electrons present

from the influent TCOD (Figure 6.1), largely due to the pH limitation as discussed previously.

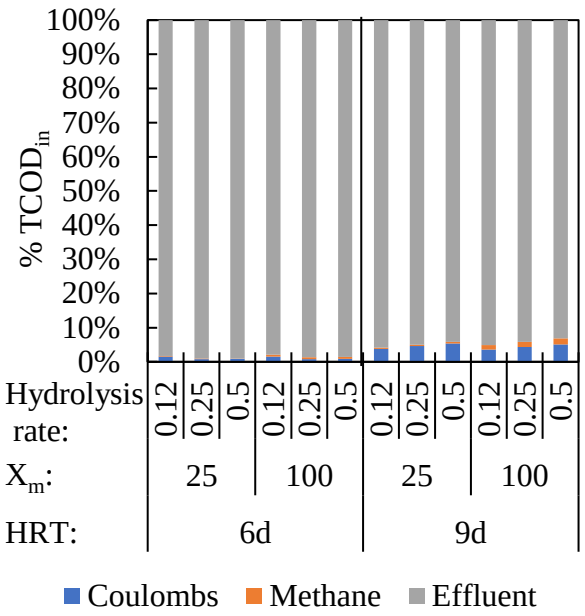

Figure 6.3. Electron balances on respiration products normalized to the influent TCOD concentration at 25 and 100 mg VSS/L influent X_m concentrations and HRTs of 6 and 9 d.

MxC performance at the 12- and 15-d HRTs surmounted the pH and alkalinity limitations at an influent X_m of 100 mg VSS/L. As was discussed in Chapter 5 and shown in Figure 5.2, the 0.25/d hydrolysis rate was optimal at a 12-d HRT due to 191 mg $CaCO_3$/d of HCO_3^- being able to adequately buffer the acetate produced versus the 8 mg $CaCO_3$/d at 0.5/d hydrolysis rate. The higher concentrations of HCO_3^- in the bulk diffused through the biofilm to the anode surface, allowing the biofilm to maintain a pH > 6.30.

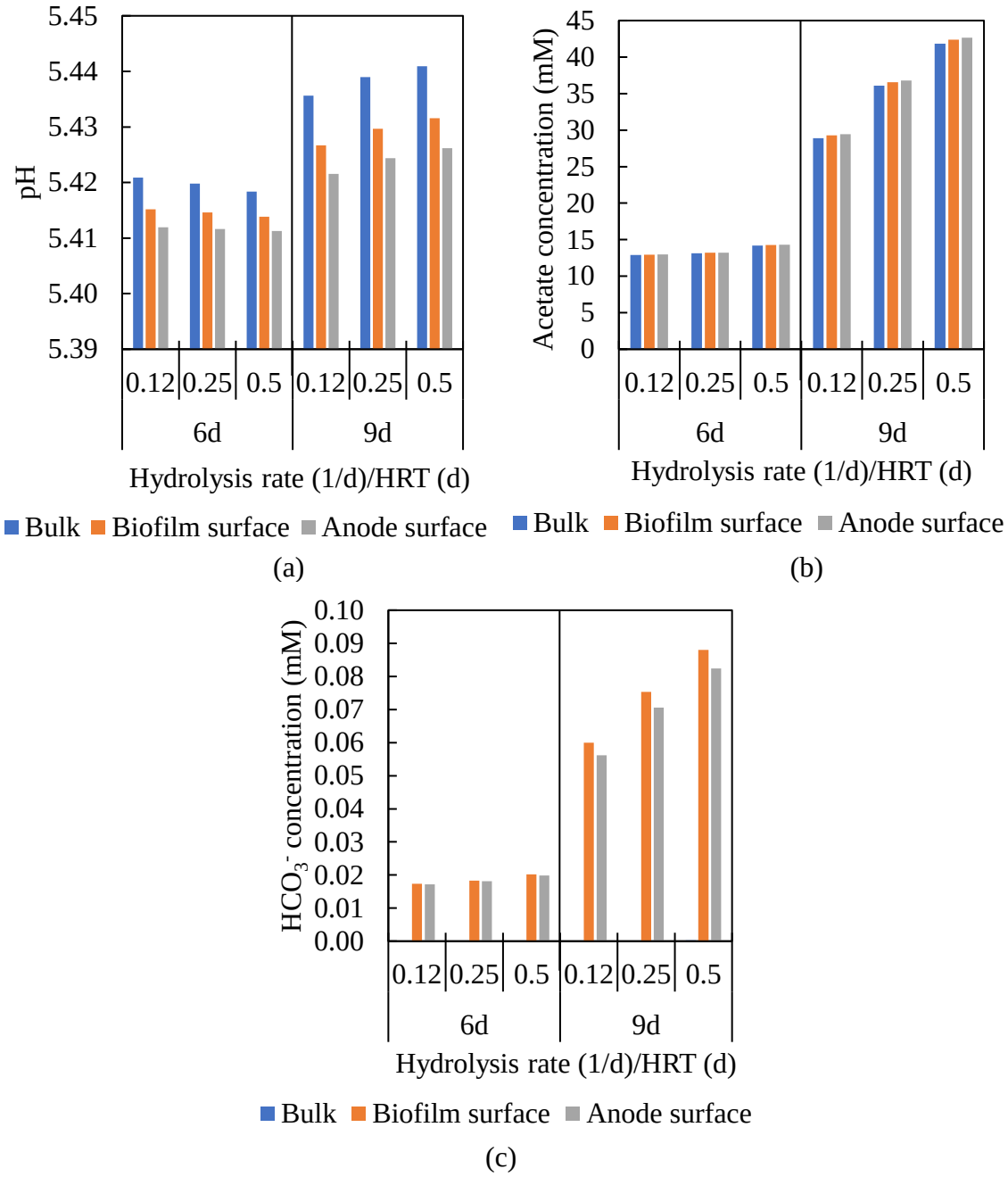

Figure 6.4. At 25 mg VSS/L influent X_m concentrations and HRTs of 6 and 9 d, (a) pH at the bulk liquid, biofilm surface, and anode surface; and (b) acetate and (c) HCO_3^- concentrations at the bulk liquid, biofilm surface, and anode surface. 100 mg VSS/L influent X_m concentrations values are shown in Figure 6.2.

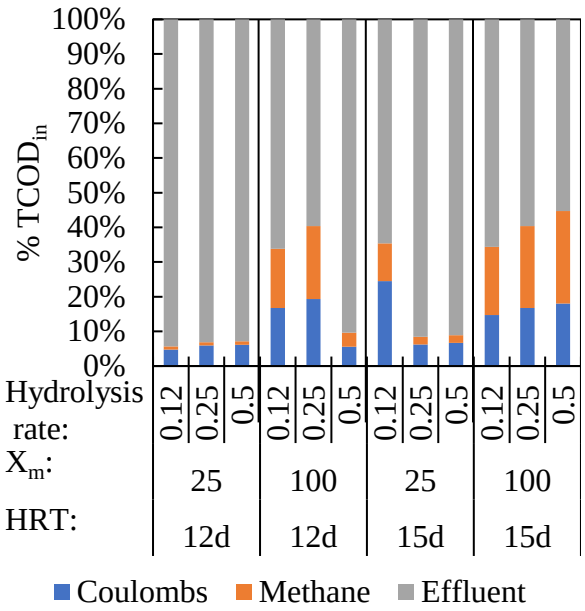

Figure 6.5. Electron balances on respiration products normalized to the influent TCOD concentration at 25 and 100 mg VSS/L influent X_m concentrations and HRTs of 12- and 15-d.

At the 15-d HRT and an influent X_m concentration of 25 mgVSS/L, 24.5% and 11% of electrons are respired to Coulombs and CH_4, respectively, at the 0.12/d hydrolysis rate, while the faster hydrolysis rates produced ~ 7% Coulombs and 2% CH_4 from available COD. Although the 0.12 and .025/d hydrolysis rates had similar acetate production rates (30-32 mmol/d), the acetate production rate at the 0.12/d hydrolysis rate was 65-75% of the production rate in the first 4 hours of the day versus the 0.25/d hydrolysis rate (Figure 6.6a). Consequently, the pH decreased more rapidly to inhibitory levels at the 0.25/d conditions, causing almost immediate X_m inhibition. X_m inhibition prevented needed HCO_3^- production to assist bulk liquid buffering, resulting in a domino effect of pH inhibition in the ARB biofilm (Figure 6.6b). As hydrolysis rate increases at 100 mg/L influent X_m and a 15-d HRT, more influent TCOD is converted to Coulombs (15-18%) and CH_4 (20-27%), as Figure 6.6c illustrates that X_m produced sufficient

HCO_3^- alkalinity to prevent pH from decreasing below 6.5 even with the high acetate production rate (62 mM/d at 0.12/d hydrolysis rate and 77 mM/d at 0.25/d hydrolysis rate).

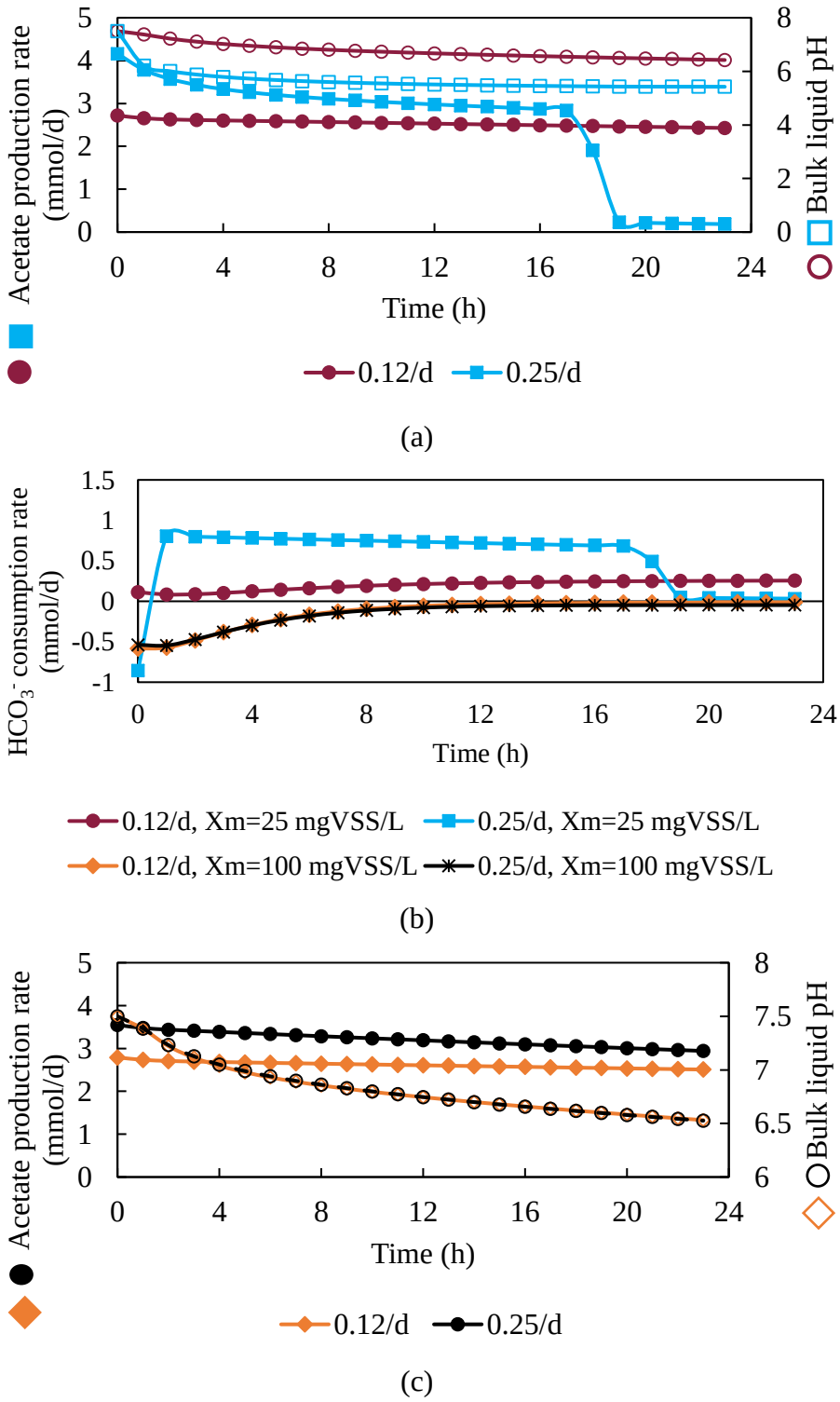

Figure 6.6. At a 15-d HRT, (a) acetate production rate and bulk liquid pH at 25 mg VSS/L influent methanogens concentration; (b) HCO_3^- consumption rate; and (c) acetate production rate and bulk liquid pH at 100 mg VSS/L influent methanogens concentration.

6.4 Conclusions

Using MYAnode, I determined trends in operating efficiency for relevant ranges of HRT, hydrolysis rate, and influent X_m concentration. The model demonstrated accurate trends at ≥ 12-d HRT but failed to predict Coulombic recovery at lower HRTs regardless of influent X_m concentrations. Performance at lower HRTs was largely inhibited by insufficient alkalinity, which means that pH inhibition of ARB and methanogens was important. The latter inhibition was especially critical, because methanogenesis of acetate produces the bicarbonate alkalinity needed to prevent a large pH drop. Increasing hydrolysis rates improved Coulombic and CH_4 recovery at 12- and 15-d HRTs, largely due to the long HRTs allowing for more growth of methanogens and the increased methanogenesis needed to generate sufficient HCO_3^- alkalinity to prevent pH from dropping below 6.2 within the first hours of feeding. These first hours were particularly important for pH buffering, because that was when the highest rates of acetate production occurred (up to 20-times higher production than prior to the daily feeding).

CHAPTER 7

Conclusions and Recommendations for Future Work

7.1 Summary and conclusions

Water and wastewater treatment are energy-intensive services critical for healthy societies (Carns, 2005; Reekie et al., 2013; Rittmann, 2013). Wastewater is ripe with embedded energy that currently is partially converted to either heat or power in medium to large WWTPs that utilize anaerobic digestion (U.S. Environmental Protection Agency Combined Heat and Power Partnership, 2008; Rittmann, 2013). As they implement more energy-intensive, advanced technologies to improve effluent quality, water treatment plants and WWTPs seek more energy and cost-efficient methods to improve energy recovery from wastewater, reduce biosolids for landfilling, and efficiently perform advanced treatment prior to effluent discharge (Reekie et al., 2013; Rittmann, 2013; Center for Sustainable Systems, 2016)

H_2O_2 is an industrial chemical has a large potential role in water and wastewater treatment to improve sludge stabilization, disinfection, micropollutant removal, and hydrogen sulfide removal for odor emissions control (Charron et al., 2004; Eskicioglu et al., 2008; Snyder et al., 2008; Dhar et al., 2011; Abelleira et al., 2012; Yang et al., 2014). H_2O_2 can be produced via electrosynthesis using fuel cells with high energy input. One option for capturing energy from wastewater is the MxC. In an MxC, ARB oxidize organics and respire the electrons to an anode; the current can be used to produce H_2O_2 at the cathode. While previous researchers demonstrated modest H_2O_2 production in batch MxC reactors (Rozendal et al., 2009; Fu et al., 2010; Modin and Fukushi, 2013), a

systematic analysis of what is required to continuously produce H_2O_2 had not been attempted prior to this work. This work provides a methodology for tailoring MPPCs for optimal H_2O_2 production and mathematical models to provide clarity to the underlying mechanisms effecting current recovery and H_2O_2 production in MPPCs.

Chapter 2 provided a comprehensive methodology for the design of MPPCs. The chapter focused on understanding the impacts of H_2O_2 on catholyte and membrane stability and optimizing H_2O_2 production at the cathode. Since H_2O_2 is a strong oxidant, the choices of catholyte and materials are important factors in improving H_2O_2 recovery from the MPPC and long-term operation. Without stabilizers present, H_2O_2 stability in different catholyte solutions decreased with increasing pH and time due to deprotonation of H_2O_2 above the pKa of 11.8. All membrane materials experienced membrane degradation at pH 12, but percent degradation increased with H_2O_2 present. Evaluating three different catalyst-binder combinations for demonstration, the chapter outlines how to utilize j-V curves and RRDE experiments to determine that the Vulcan carbon-Nafion binder combination provided lower Ohmic losses than other combinations and the optimal catalyst loading was ~0.5 mg/cm^2 of Vulcan carbon for maximum H_2O_2 production.

These finding were utilized to demonstrate continuous H_2O_2 production for the first time using of a continuous-flow, flat-plate MPPC. The MPPC was operated using a catholyte having 200 mM NaCl and air flow rates ranging from 10 to 30 cm^3/min. The MPPC achieved long-term operation (18 days) without any downtime. Varying air flow rates had minimal effect on MPPC performance: H_2O_2 effluent concentrations ranged from 2.5±0.4 to 3.1±0.4 g/L, and effluent pH ranged from 12.1 to 12.4. Cathodic

overpotentials were 1.7 times higher than anodic overpotentials, with > 58% of cathodic overpotential associated with concentration overpotentials due to the high pH gradient between the anode and cathode chambers.

The work in Chapter 3 expanded on Chapter 2 to further optimize the performance of a continuous-flow, flat-plate MPPC. Several operational conditions were varied, including catholyte HRT, catholyte concentration, different catholytes, and the use of EDTA as a metal-chelating stabilizer for H_2O_2. The MPPC produced its highest H_2O_2 concentrations -- 3.1±0.4 g/L -- using NaCl catholytes. Energy input increased and net cathodic efficiency decreased with increasing cathodic HRT due to H_2O_2 decay, likely through a reaction with the membrane or other contaminants in the system. Similarly, an increase in NaCl concentration in the cathode reduced Ohmic losses due to better ion transport, which improved the MPPC's net cathodic efficiency, although it failed to produce higher H_2O_2 concentrations. Attempts to improve performance by using weak acid buffers catholytes to reduce pH gradients failed to produce higher H_2O_2 concentrations, since the pH gradient either favored the formation of H_2O instead of H_2O_2 at the entrance to the cathode or the catholytes favored formation of O_2 from H_2O_2 auto-decay. The addition of EDTA to the catholyte failed to increase H_2O_2 effluent concentration, because the ferrochelator diffused to the anode and reduced the ARB's current production, either by inhibiting uptake of the nutrient iron or disrupting electron transfer by ARB to the anode surface.

Chapters 4-6 introduced MYAnode, a new mathematical model for anode chamber performance, and used it to evaluate MxC performance for a range of operational parameters. In Chapter 4, the model combined three existing platforms –

CASADM, PCBIOFILM, and CCBATCH – to describe chemical and biological processes occurring in a bulk liquid modeled as typical wastewater and at an anode biofilm. The model was evaluated against data obtained by Ki et al. (2017a), which treated primary sludge at a 12-d HRT in an MxC. The model demonstrated a reasonable fit to experimental data when the acetoclastic methanogens concentration was well poised at 100 mg VSS/L influent X_m concentration: The model predicted 20% Coulombic recovery and 20% CH_4 recovery versus the experimental results of 28% and 32%, respectively. Using MYAnode, I demonstrated little Coulombic or CH_4 recovery at lower influent X_m concentrations ($\leq$ 25 mg VSS/L) due to the pH decreasing to inhibitory levels. The decrease in pH was caused by the formation of too much acetate, a relatively strong weak acid; a too low concentration of X_m, which were needed to produce HCO_3^- from acetate oxidation; and too little acetate oxidation by ARB due to the limited surface area. A too-high of influent X_m concentration ($\geq$ 200 mg VSS/L) resulted in X_m outcompeting ARB for acetate, with the MxC producing more CH_4 than Coulombs.

In Chapter 5, I explored the role of DL thickness and hydrolysis rate on MxC performance at a 12-d HRT and 100 mg VSS/L influent X_m concentration. Reducing the DL thickness had greater impact on improving MxC performance than increasing the hydrolysis rate: Increasing the DL thickness from 500 to 1000 μm improved Coulombic efficiency and CH_4 production by 13.9 and 18.6%, respectively, versus the 2.6 and 3.9% improvement, respectively, as hydrolysis rates from 0.12 to 0.25/d. Like I the previous chapter, performance improvements largely depended upon HCO_3^- production by X_m to help maintain pH above the inhibitory levels for ARB and X_m. Too-high of DL thicknesses (> 1000 μm) led to increased CH_4 production, because mass transport limited

the acetate concentration at the biofilm surface. A too-high hydrolysis rates (> 0.25/d) produced too much acetate too quickly, causing the bulk pH to drop to inhibitory levels for X_m in the bulk liquid.

Chapter 6 explored MxC performance at 6- to 15-d HRTs for different X_m concentrations and hydrolysis rates. The model trends were consistent with experimental data at ≥ 12-d HRT, although they failed to match Coulombic and CH_4 recoveries at lower HRTs. For example, the model predicted less than 1% Coulombic and CH_4 recoveries, respectively, at 6-d HRT, compared with the experimental data, which demonstrated 29 and 12% recoveries, respectively. The model predicted that performance at lower HRTs was largely inhibited by insufficient HCO_3^- production by X_m from acetate oxidation; too-little HCO_3^- allowed the pH to decrease to inhibitory levels. Increasing hydrolysis rates improved Coulombic and CH_4 recovery at 12- and 15-d HRTs. X_m benefitted from the long HRTs, which provided adequate time for their growth and allowed them to produce sufficient HCO_3^- alkalinity to prevent the pH from dropping below 6.2 within the first hours of feeding. These first hours were particularly important to buffer, as it was when the highest rates of acetate production occurred (up to 20-times higher production than prior to the daily feeding).

7.2 Recommendations for future work

In this section, I provide recommendations for futures studies into MPPCs and MxC modeling. I begin by outlining studies to reduce cathodic Ohmic and concentration overpotentials. I explore experiments that couple MPPCs with wastewater treatment for sludge stabilization, disinfection, and micropollutant removal. Finally, I discuss incorporating MYAnode into a holistic MxC model.

7.2.1 Reduce concentration overpotentials in MPPCs

Chapters 2 and 3 concluded that concentration overpotentials and pH gradients between the cathode surface and cathode bulk liquid and between the cathode and anode chambers led to significant voltages losses within the MPPC. Attempts in this work to reduce cathode effluent pH by utilizing weak acid buffers as the catholyte were ineffective due to the creation of localized high pH gradients, which favored the production of H_2O versus H_2O_2 or auto-decay of H_2O_2 with the buffer to O_2. Other researchers utilized strong acids like H_2SO_4 and HCl to reduce the pH variation over the cathode (Yamanaka et al., 2002; Kolyagin and Kornienko, 2003; Kolyagin et al., 2011), but practical problem preclude using strong acids at large scale: strong acid catholytes provides safety issues in large-scale applications, must be neutralized prior to discharge, and are not compatible with most AEMs, which are not rated for use at a pH < 2.

One method to reduce the pH gradient along the serpentine flow channel is to implement high-rate recirculation of the catholyte, which should provide more complete mixing and moderate the pH change in the system. Preliminary results reported by Rumsey and Torres (2017) demonstrated that a 20-fold recirculation rate using 200 mM,

pH 2.5 PBS increased H_2O_2 effluent concentration 2-fold versus without recycle and reduced the effluent pH from 10.4 to 7.5. However, high recirculation rates could have negative impacts on MPPC performance, including potentially increasing the pressure on the cathode, which may increase the likelihood of catholyte leaking through the cathode. Also, recirculation incurs pumping costs that offset the added value of the H_2O_2. Therefore, any modifications would require long-term evaluation to assess the system's robustness.

7.2.2 Develop MPPC systems for sludge stabilization, wastewater disinfection, and micropollutant removal

H_2O_2 has been explored for a variety of WWT applications, including as an additive to reduce hydrogen sulfide emissions (Charron et al., 2004; Dhar et al., 2011; Metcalf & Eddy, 2014), as a sludge pretreatment technology (Eskicioglu et al., 2008; Kim et al., 2009; Abelleira et al., 2012), and to improve disinfectant and micropollutant removal (Glaze et al., 1987; Wagner et al., 2002; Ksibi, 2006; Kruithof et al., 2007; Snyder et al., 2008; De la Cruz et al., 2012; Yang et al., 2014). One potential application of MPPCs is to directly feed H_2O_2-rich catholyte to the anode chamber or produce cathodic H_2O_2 in a single chamber reactor to increase sludge stabilization, which also may reduce fecal coliforms and micropollutant concentrations. Similarly, a catholyte stream containing H_2O_2 can be combined with the anolyte solution and passed through a tubular reactor surrounded by a UV lamp. For further efficacy, iron ions can be added to the catholyte stream prior to addition to the UV reactor to promote Fenton oxidation of organic contaminants. While the addition of iron may seem counterintuitive, since Fenton processes are inhibited at high pH, it may synergize well with municipal

wastewater treatment, in which iron-based coagulants are used in primary and secondary wastewater settling. The effluent anolyte could also be supplemented with specific contaminants of concern, like pharmaceuticals and personal care products and pesticides (Klamerth et al., 2010; Kruithof et al., 2007), to determine the reactor's removal efficacy.

7.2.3 Gain greater understanding of the pH limitations modeled in MYAnode to better fit experimental data

Several improvements must be made to MYAnode to obtain better overall fits to the experimental data, especially at the 6- and 9-d HRTs. Ki et al. (2017a) demonstrated significant current production and sludge stabilization at the 6- and 9-d HRTs, but MYAnode failed to reflect them because MYAnode predicted a significant pH drop due to limited alkalinity in the system. Since the modeling fitting was worse for lower HRTs, one potential improvement is to add hydrogenotrophic methanogenesis and fermentation of propionate and butyrate to acetate and H_2, which can consume CO_2 in the former case and produce CO_2 in the latter. Another approach is to examine the largest biological consumer of alkalinity: fermentation. Approximately 2.5 mol of HCO_3^- are consumed (mostly for EPS and UAP formation) during domestic wastewater fermentation to acetate, EPS, and UAP. Changing the EPS and UAP kinetics or chemical formulas may result in less consumption of alkalinity, which Chapter 6 indicated in part leads to rapid inhibition of methanogens due to a rapid pH drop from acetate formation.

7.2.4 Establish holistic mathematical models of MxCs

The modeling foundation in this dissertation provides separate anode and cathode models, but not a holistic MxC model. While several holistic MxC models exist, as

reviewed in Chapter 1, many of these models do not evaluate the impact of pH and chemical speciation, complex waste streams, diffusion and migration at the anode and cathode, and diffusion through the membrane on MxC performance. Developing a holistic MxC model with all these features requires extensive abiotic characterization of the membrane to determine ion diffusivity and conductivity. Any abiotic experiments must evaluate common catholyte ions and OH^- diffusion to the anode chamber, and common wastewater ions -- like acetate, bicarbonate, phosphate, and ammonium -- must be evaluated for diffusion from the anode to the cathode. These ions can be detected using high performance liquid chromatography and IC, and the experiments are so straightforward they would provide an excellent research opportunity for an undergraduate researcher. The diffusion of both anions and cations through the selected membrane must be evaluated – laboratory observations have demonstrated ammonium diffusing through the AMI-7001 AEM. Ions should be evaluated at open circuit and with current applied to determine the effect of ionic migration on diffusivity.

Once the data are obtained, MYAnode could be incorporated into a larger model consisting of 5 compartments, as illustrated in Figure 7.1: the bulk anode liquid, the anode and biofilm, the membrane, the bulk catholyte, and the cathode. My opinion is that a cathode model should be designed to predict cathode overpotential, electrolysis products, and pH based on the current supplied from the anode. In this case, PCBIOFILM cannot be directly applied because the program and, more importantly, numerical methods are centered on determining the current density versus overpotential, which requires the addition of activation and concentration overpotentials for H_2O_2 and HO_2^- in the system that would require nested Newton-Raphson solver routines to obtain

the desired output variables. Boundary conditions will need to be established. The bulk liquid/diffusion layer interface boundary conditions are to those implemented in PCBIOFILM, with the flux between equal in magnitude on each sides of the boundary. The boundary condition at the cathode surface and diffusion layer will need to be modified to be equivalent to concentrations of H_2O_2 and HO_2^- as dictated by activation and concentration overpotentials and the current supplied from the anode. Ohmic and activation overpotential parameters for the cathode and catalyst were obtained as part of the experiments in Chapters 2 and 3, including exchange current density and the alpha fitting parameter from the Butler-Volmer equation.

A membrane model could be formulated similarly to the proposed cathode model using Fick's law and ionic migration to produce profiles of ionic transport through the membrane. However, all membrane parameters would still need to be quantified, including diffusion through the membrane of salt, OH^-, H_2O_2, and HO_2^-, at open circuit and different operating potentials.

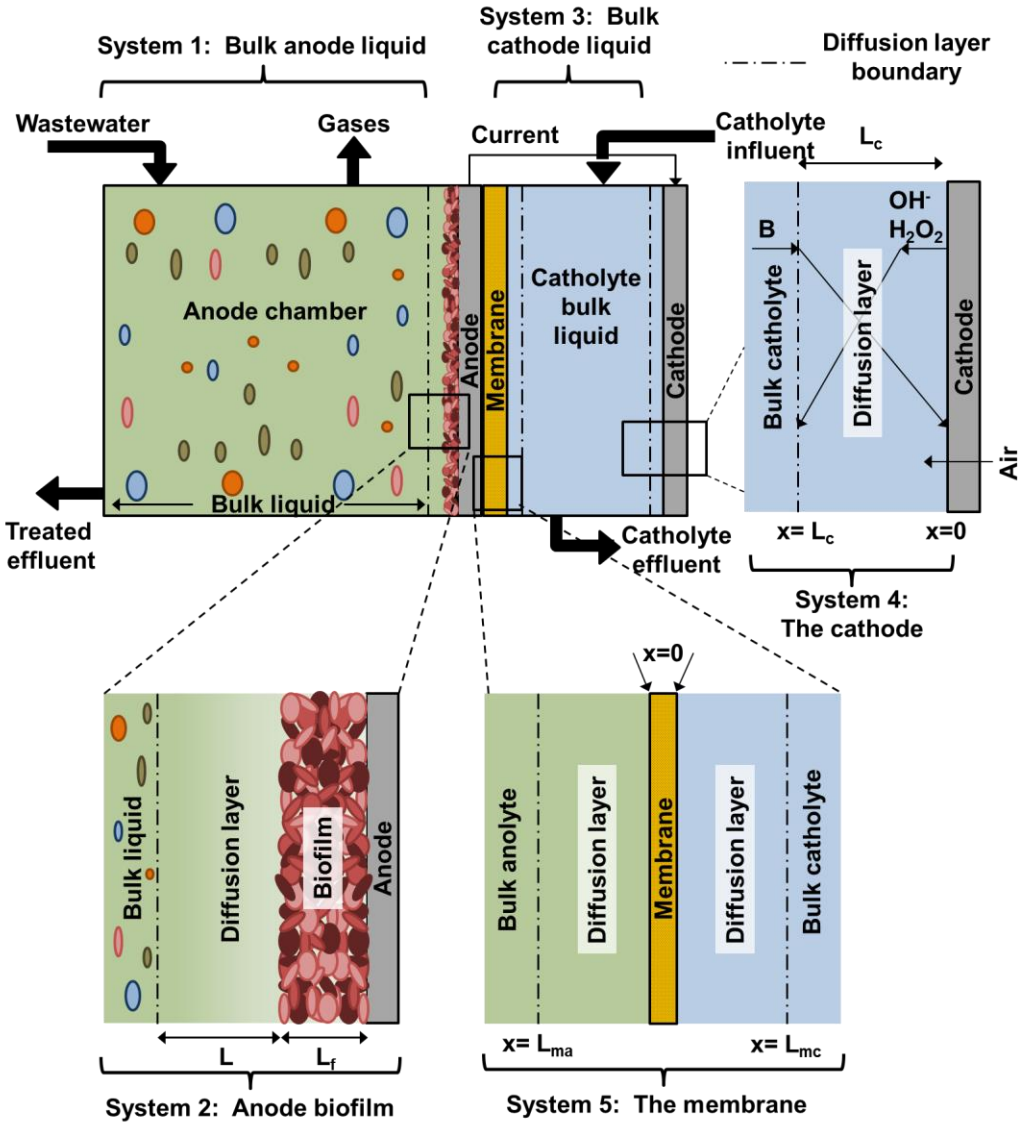

Figure 7.1. The reaction in five systems to be modeled: the bulk anolyte chamber, the anode and biofilm, the bulk catholyte chamber, the cathode, and the membrane.

REFERENCES

1. Abbot, J., Brown, D.G., 1990. Kinetics of Iron-catalyzed decomposition of hydrogen peroxide in alkaline solution, International Journal of Chemical Kinetics. 22, 963-974.

2. Abelleira, J., Pérez-Elvira, S., Sánchez-Oneto, J., Portela, J., Nebot, E., 2012. Advanced thermal hydrolysis of secondary sewage sludge: a novel process combining thermal hydrolysis and hydrogen peroxide addition, Resour. Conserv. Recycling. 59, 52-57.

3. Acero, J.L., von Gunten, U., 2000. Influence of Carbonate on the Ozone/Hydrogen Peroxide Based Advanced Oxidation Process for Drinking Water Treatment, Ozone: Sci. Eng. 22, 305-328.

4. Althaus, H., Chudacoff, M., Hischier, R., Jungbluth, N., Osses, M., Primas, A., 2007. Life cycle inventories of chemicals.

5. Appels, L., Baeyens, J., Degrève, J., Dewil, R., 2008. Principles and potential of the anaerobic digestion of waste-activated sludge, Progress in energy and combustion science. 34, 755-781.

6. Aquino, S.F., Stuckey, D.C., 2008. Integrated model of the production of soluble microbial products (SMP) and extracellular polymeric substances (EPS) in anaerobic chemostats during transient conditions, Biochem. Eng. J. 38, 138-146.

7. Arends, J.B.A., Van Denhouwe, S., Verstraete, W., Boon, N., Rabaey, K., 2014. Enhanced disinfection of wastewater by combining wetland treatment with bioelectrochemical H_2O_2 production, Bioresour. Technol. 155, 352-358.

8. Badawy, M.I., Ali, M.E.M., 2006. Fenton's peroxidation and coagulation processes for the treatment of combined industrial and domestic wastewater, J. Hazard. Mater. 136, 961-966.

9. Bard, A.J., Faulkner, L.R., 2001. Electrochemical Methods: Fundamentals and Applications.

10. Batstone, D., Keller, J., Angelidaki, I., Kalyuzhnyi, S., Pavlostathis, S., Rozzi, A., Sanders, W., Siegrist, H., Vavilin, V., 2002. The IWA Anaerobic Digestion Model No 1 (ADM1), Water Science and Technology. 45, 65-73.

11. Benjamin, M.M., 2015. Water Chemistry, 2nd ed. Waveland Press, Inc., Long Grove, Ill.

12. Bitton, G., 2005. Wastewater microbiology. John Wiley & Sons.

13. Bonakdarpour, A., Lefevre, M., Yang, R., Jaouen, F., Dahn, T., Dodelet, J., Dahn, J., 2008. Impact of loading in RRDE experiments on Fe–N–C catalysts: two-or

four-electron oxygen reduction? Electrochemical and Solid-State Letters. 11, B105-B108.

14. Campos-Martin, J.M., Blanco-Brieva, G., Fierro, J.L.G., 2006. Hydrogen Peroxide Synthesis: An Outlook beyond the Anthraquinone Process, Angewandte Chemie International Edition. 45, 6962-6984.

15. Carns, K., 2005. Bringing Energy Efficiency to the Water and Wastewater Industry: How Do We Get There?

16. Center for Sustainable Systems, 2016. U.S. Wastewater Treatment Fact Sheet, CSS04-14.

17. Charron, I., Feliers, C., Couvert, A., Laplanche, A., Patria, L., Requieme, B., 2004. Use of hydrogen peroxide in scrubbing towers for odor removal in wastewater treatment plants, Water Science and Technology. 50, 267-274.

18. Chen, J., Li, N., Zhao, L., 2014. Three-dimensional electrode microbial fuel cell for hydrogen peroxide synthesis coupled to wastewater treatment, J. Power Sources. 254, 316-322.

19. Choi, J., Ahn, Y., 2014. Increased power generation from primary sludge in microbial fuel cells coupled with prefermentation, Bioprocess and biosystems engineering. 37, 2549-2557.

20. Colodette, J., Rothenberg, S., Dence, C., 1989. Factors affecting hydrogen peroxide stability in the brightening of mechanical and chemimechanical pulps. II: Hydrogen peroxide stability in the presence of sodium silicate, J. Pulp Paper Sci. 15, J3-J10.

21. Colombo, A., Schievano, A., Trasatti, S.P., Morrone, R., D'Antona, N., Cristiani, P., 2017. Signal trends of microbial fuel cells fed with different food-industry residues, International journal of hydrogen energy. 42, 1841-1852.

22. Csányi, L.J., Galbács, Z.M., 1985. Carbon dioxide-mediated decomposition of hydrogen peroxide in alkaline solutions, Journal of the Chemical Society, Faraday Transactions 1: Physical Chemistry in Condensed Phases. 81, 113-116.

23. da Silva, G., Kennedy, E.M., Dlugogorski, B.Z., 2006. Ab Initio Procedure for Aqueous-Phase p K a Calculation: The Acidity of Nitrous Acid, The Journal of Physical Chemistry A. 110, 11371-11376.

24. de Haas, D., Dancey, M., 2015. Wastewater Treatment Energy Efficiency, Water: Journal of the Australian Water Association. 42, 53-58.

25. De la Cruz, N., Giménez, J., Esplugas, S., Grandjean, D., De Alencastro, L., Pulgarin, C., 2012. Degradation of 32 emergent contaminants by UV and neutral photo-fenton in domestic wastewater effluent previously treated by activated sludge, Water Res. 46, 1947-1957.

26. de Silva, D., Rittmann, B., 2000. Nonsteady-state modeling of multispecies activated-sludge processes, Water Environ. Res. 72, 554-565.

27. Deed, T., 1998. The Manufacture of Hydrogen Peroxide.

28. Dhar, B.R., Youssef, E., Nakhla, G., Ray, M.B., 2011. Pretreatment of municipal waste activated sludge for volatile sulfur compounds control in anaerobic digestion, Bioresour. Technol. 102, 3776-3782.

29. Dhar, B.R., Gao, Y., Yeo, H., Lee, H., 2013. Separation of competitive microorganisms using anaerobic membrane bioreactors as pretreatment to microbial electrochemical cells, Bioresource Technology. 148, 208-214.

30. Dhar, B.R., Lee, H., 2014. Evaluation of limiting factors for current density in microbial electrochemical cells (MXCs) treating domestic wastewater, Biotechnology Reports. 4, 80-85.

31. Drogui, P., Elmaleh, S., Rumeau, M., Bernard, C., Rambaud, A., 2001. Oxidising and disinfecting by hydrogen peroxide produced in a two-electrode cell, Water Res. 35, 3235-3241.

32. Eastern Research Group, Inc., Energy and Environmental Analysis, Inc., 2007. Opportunities for and Benefits of Combined Heat and Power at Wastewater Treatment Facilities.

33. Eastman, J., Ferguson, J., 1981. Solubilization of Particulate Organic-Carbon during the Acid Phase of Anaerobic-Digestion, Journal Water Pollution Control Federation. 53, 352-366.

34. Electric Power Research Institute, Inc., 2002. Water & Sustainability (Volume 4): U.S. Electricity Consumption for Water Supply & Treatment - The Next Half Century, 1006787.

35. Esfandyari, M., Fanaei, M.A., Gheshlaghi, R., Mahdavi, M.A., 2017. Mathematical modeling of two-chamber batch microbial fuel cell with pure culture of Shewanella, Chem. Eng. Res. Design. 117, 34-42.

36. Eskicioglu, C., Prorot, A., Marin, J., Droste, R.L., Kennedy, K.J., 2008. Synergetic pretreatment of sewage sludge by microwave irradiation in presence of H 2 O 2 for enhanced anaerobic digestion, Water Res. 42, 4674-4682.

37. Estevez-Canales, M., Kuzume, A., Borjas, Z., Füeg, M., Lovley, D., Wandlowski, T., Esteve-Núñez, A., 2015. A severe reduction in the cytochrome C content of Geobacter sulfurreducens eliminates its capacity for extracellular electron transfer, Environmental microbiology reports. 7, 219-226.

38. Eul, W., Moeller, A., Steiner, N., 2001. Hydrogen peroxide, Kirk-Othmer encyclopedia of chemical technology.

39. Fazli, N., Mutamim, N.S.A., Jafri, N.M.A., Ramli, N.A.M., 2018. Microbial Fuel Cell (MFC) in treating spent caustic wastewater: Varies in Hydraulic Retention Time (HRT) and Mixed Liquor Suspended Solid (MLSS), Journal of Environmental Chemical Engineering. 6, 4339-4346.

40. Flemming, H., Wingender, J., 2010. The biofilm matrix, Nature reviews. 8, 623-633.

41. Flores-Alsina, X., Kazadi Mbamba, C., Solon, K., Vrecko, D., Tait, S., Batstone, D.J., Jeppsson, U., Gernaey, K.V., 2015. A plant-wide aqueous phase chemistry module describing pH variations and ion speciation/pairing in wastewater treatment process models, Water Res. 85, 255-265.

42. FMC Corporation, 2012. Vision 2015, 2016.

43. Foley, J.M., Rozendal, R.A., Hertle, C.K., Lant, P.A., Rabaey, K., 2010. Life Cycle Assessment of High-Rate Anaerobic Treatment, Microbial Fuel Cells, and Microbial Electrolysis Cells, Environ. Sci. Technol. 44, 3629-3637.

44. Foller, P., Bombard, R., 1995. Processes for the production of mixtures of caustic soda and hydrogen peroxide via the reduction of oxygen, J. Appl. Electrochem. 25, 613-627.

45. Franks, A.E., Nevin, K.P., Jia, H., Izallalen, M., Woodard, T.L., Lovley, D.R., 2009. Novel strategy for three-dimensional real-time imaging of microbial fuel cell communities: monitoring the inhibitory effects of proton accumulation within the anode biofilm, Energy & Environmental Science. 2, 113-119.

46. Fu, L., You, S., Yang, F., Gao, M., Fang, X., Zhang, G., 2010. Synthesis of hydrogen peroxide in microbial fuel cell, Journal of Chemical Technology & Biotechnology. 85, 715-719.

47. Gao, Y., Ryu, H., Santo Domingo, J.,W., Lee, H., 2014. Syntrophic interactions between H_2-scavenging and anode-respiring bacteria can improve current density in microbial electrochemical cells, Bioresource technology. 153, 245-253.

48. Ge, Z., Zhang, F., Grimaud, J., Hurst, J., He, Z., 2013. Long-term investigation of microbial fuel cells treating primary sludge or digested sludge, Bioresource Technology. 136, 509-514.

49. Glaze, W.H., Kang, J., Chapin, D.H., 1987. The Chemistry of Water Treatment Processes Involving Ozone, Hydrogen Peroxide and Ultraviolet Radiation, Ozone: Sci. Eng. 9, 335-352.

50. Goor, G., Glenneberg, J., Jacobi, S., 2000. Hydrogen Peroxide, Anonymous Ullmann's Encyclopedia of Industrial Chemistry. Wiley-VCH, Weinheim, Germany, pp. 393-427.

51. Graf, E., Penniston, J.T., 1980. Method for determination of hydrogen peroxide, with its application illustrated by glucose assay, Clin. Chem. 26, 658-660.

52. Gray, N.D., Miskin, I.P., Kornilova, O., Curtis, T.P., Head, I.M., 2002. Occurrence and activity of Archaea in aerated activated sludge wastewater treatment plants, Environ. Microbiol. 4, 158-168.

53. Hart, P.W., Rudie, A.W., 2014. Anthraquinone-A review of the rise and fall of a pulping catalyst, Tappi Journal. 13, 23-31.

54. Haynes, W.M. ed., 2011. CRC Handbook of Chemistry and Physics, 92 ed..

55. Henze, M., Gujer, W., Mino, T., Van Loosdrecht, M., 2000. Activated sludge models ASM1, ASM2, ASM2d and ASM3. IWA publishing.

56. Jadhav, D.A., Ghosh Ray, S., Ghangrekar, M.M., 2017. Third generation in bio-electrochemical system research – A systematic review on mechanisms for recovery of valuable by-products from wastewater, Renewable and Sustainable Energy Reviews. 76, 1022-1031.

57. Jain, A., He, Z., 2018. "NEW" resource recovery from wastewater using bioelectrochemical systems: Moving forward with functions, Frontiers of environmental science & engineering. 12, 1.

58. Jayasinghe, N., Franks, A., Nevin, K.P., Mahadevan, R., 2014. Metabolic modeling of spatial heterogeneity of biofilms in microbial fuel cells reveals substrate limitations in electrical current generation, Biotechnology journal. 9, 1350-1361.

59. Jiang, Y., Hebly, M., Kleerebezem, R., Muyzer, G., van Loosdrecht, M.C.M., 2011. Metabolic modeling of mixed substrate uptake for polyhydroxyalkanoate (PHA) production, Water Res. 45, 1309-1321.

60. Kadier, A., Simayi, Y., Kalil, M.S., Abdeshahian, P., Hamid, A.A., 2014. A review of the substrates used in microbial electrolysis cells (MECs) for producing sustainable and clean hydrogen gas, Renewable Energy. 71, 466-472.

61. Kannaiah Goud, R., Venkata Mohan, S., 2011. Pre-fermentation of waste as a strategy to enhance the performance of single chambered microbial fuel cell (MFC), Int J Hydrogen Energy. 36, 13753-13762.

62. Kato, S., Hashimoto, K., Watanabe, K., 2013. Iron-oxide minerals affect extracellular electron-transfer paths of Geobacter spp. Microbes and Environments. 28, 141-148.

63. Katuri, K.P., Scott, K., 2011. On the dynamic response of the anode in microbial fuel cells, Enzyme and Microbial Technology. 48, 351-358.

64. Ki, D., Popat, S.C., Torres, C.I., 2016. Reduced overpotentials in microbial electrolysis cells through improved design, operation, and electrochemical characterization, Chem. Eng. J. 287, 181-188.

65. Ki, D., Parameswaran, P., Popat, S.C., Rittmann, B.E., Torres, C.I., 2017a. Maximizing Coulombic recovery and solids reduction from primary sludge by controlling retention time and pH in a flat-plate microbial electrolysis cell, Environmental Science: Water Research & Technology. 3, 333-339.

66. Ki, D., Popat, S.C., Rittmann, B.E., Torres, C.I., 2017b. H_2O_2 production in microbial electrochemical cells fed with primary sludge, Environ. Sci. Technol.

67. Ki, D., Parameswaran, P., Popat, S.C., Rittmann, B.E., Torres, C.I., 2015. Effects of pre-fermentation and pulsed-electric-field treatment of primary sludge in microbial electrochemical cells, Bioresour. Technol. 195, 83-88.

68. Kiely, P.D., Regan, J.M., Logan, B.E., 2011. The electric picnic: synergistic requirements for exoelectrogenic microbial communities, Curr. Opin. Biotechnol. 22, 378-385.

69. Kim, J.R., Min, B., Logan, B.E., 2005. Evaluation of procedures to acclimate a microbial fuel cell for electricity production, Appl. Microbiol. Biotechnol. 68, 23-30.

70. Kim, J.R., Premier, G.C., Hawkes, F.R., Rodríguez, J., Dinsdale, R.M., Guwy, A.J., 2010. Modular tubular microbial fuel cells for energy recovery during sucrose wastewater treatment at low organic loading rate, Bioresour. Technol. 101, 1190-1198.

71. Kim, K., Yang, W., Evans, P.J., Logan, B.E., 2016. Continuous treatment of high strength wastewaters using air-cathode microbial fuel cells, Bioresour. Technol. 221, 96-101.

72. Kim, T., Lee, S., Nam, Y., Yang, J., Park, C., Lee, M., 2009. Disintegration of excess activated sludge by hydrogen peroxide oxidation, Desalination. 246, 275-284.

73. Klamerth, N., Malato, S., Maldonado, M., Aguera, A., Fernández-Alba, A., 2010. Application of photo-fenton as a tertiary treatment of emerging contaminants in municipal wastewater. Environ. Sci. Technol. 44, 1792-1798.

74. Knotter, D.M., De Gendt, S., Baeyens, M., Mertens, P.W., Heyns, M.M., 1999. Hydrogen peroxide decomposition in ammonia solutions, J. Electrochem. Soc. 146, 3476-3481.

75. Kolyagin, G., Kornienko, V., 2003. Kinetics of hydrogen peroxide accumulation in electrosynthesis from oxygen in gas-diffusion electrode in acidic and alkaline solutions, Russian journal of applied chemistry. 76, 1070-1075.

76. Kolyagin, G., Vasil'eva, I., Kornienko, V., 2011. Effects of the composition of acid solutions and the presence of organic acids on oxygen electroreduction to hydrogen peroxide in a carbon black gas-diffusion electrode, Russian J. Electrochem. 47, 282-287.

77. Korth, B., Rosa, L.F., Harnisch, F., Picioreanu, C., 2015. A framework for modeling electroactive microbial biofilms performing direct electron transfer, Bioelectrochemistry. 106, 194-206.

78. Kruithof, J.C., Kamp, P.C., Martijn, B.J., 2007. UV/ H_2O_2 Treatment: A Practical Solution for Organic Contaminant Control and Primary Disinfection, Ozone: Sci. Eng. 29, 273-280.

79. Ksibi, M., 2006. Chemical oxidation with hydrogen peroxide for domestic wastewater treatment, Chem. Eng. J. 119, 161-165.

80. Laspidou, C., Rittmann, B., 2002a. Non-steady state modeling of extracellular polymeric substances, soluble microbial products, and active and inert biomass, Water Res. 36, 1983-1992.

81. Laspidou, C., Rittmann, B., 2002b. A unified theory for extracellular polymeric substances, soluble microbial products, and active and inert biomass, Water Res. 36, 2711-2720.

82. Laspidou, C.S., Rittmann, B.E., 2004. Evaluating trends in biofilm density using the UMCCA model, Water research :. 38, 3362-3372.

83. Lee, H.H., Park, A., Oloman, C., 2000. Stability of hydrogen peroxide in sodium carbonate solutions, TAPPI J.

84. Lee, H., Rittmann, B.E., 2009. Significance of biological hydrogen oxidation in a continuous single-chamber microbial electrolysis cell, Environ. Sci. Technol. 44, 948-954.

85. Lee, H., Torres, C.I., Parameswaran, P., Rittmann, B.E., 2009. Fate of H_2 in an upflow single-chamber microbial electrolysis cell using a metal-catalyst-free cathode, Environ. Sci. Technol. 43, 7971-7976.

86. Li, J., He, Z., 2016a. Development of a dynamic mathematical model for membrane bioelectrochemical reactors with different configurations, Environmental Science and Pollution Research. 23, 3897-3906.

87. Li, N., An, J., Zhou, L., Li, T., Li, J., Feng, C., Wang, X., 2016b. A novel carbon black graphite hybrid air-cathode for efficient hydrogen peroxide production in bioelectrochemical systems, J. Power Sources. 306, 495-502.

88. Li, W., Yu, H., He, Z., 2014. Towards sustainable wastewater treatment by using microbial fuel cells-centered technologies, Energy & Environmental Science. 7, 911-924.

89. Li, X.M., Cheng, K.Y., Selvam, A., Wong, J.W.C., 2013. Bioelectricity production from acidic food waste leachate using microbial fuel cells: Effect of microbial inocula, Process biochemistry. 48, 283-288.

90. Liu, H., Ramnarayanan, R., Logan, B.E., 2004. Production of electricity during wastewater treatment using a single chamber microbial fuel cell, Environ. Sci. Technol. 38, 2281-2285.

91. Liu, Z., Liu, J., Zhang, S., Xing, X., Su, Z., 2011. Microbial fuel cell based biosensor for in situ monitoring of anaerobic digestion process, Bioresource technology. 102, 10221-10229.

92. Logan, B.E., Hamelers, B., Rozendal, R., Schröder, U., Keller, J., Freguia, S., Aelterman, P., Verstraete, W., Rabaey, K., 2006. Microbial fuel cells: methodology and technology, Environ. Sci. Technol. 40, 5181-5192.

93. Logan, B.E., Regan, J.M., 2006. Electricity-producing bacterial communities in microbial fuel cells, Trends Microbiol. 14, 512-518.

94. Lowrie, R., 2015. Wastewater treatment facilities turning to anaerobic digestion for energy uses, Biofuels Digest.

95. Mahmoud, M., Parameswaran, P., Torres, C.I., Rittmann, B.E., 2014. Fermentation pre-treatment of landfill leachate for enhanced electron recovery in a microbial electrolysis cell, Bioresource Technology. 151, 151-158.

96. Marcus, A.K., Torres, C.I., Rittmann, B.E., 2007. Conduction-based modeling of the biofilm anode of a microbial fuel cell, Biotechnol. Bioeng. 98, 1171-1182.

97. Marcus, A.K., Torres, C.I., Rittmann, B.E., 2010. Evaluating the impacts of migration in the biofilm anode using the model PCBIOFILM, Electrochim. Acta. 55, 6964-6972.

98. Marcus, A.K., Torres, C.I., Rittmann, B.E., 2011. Analysis of a microbial electrochemical cell using the proton condition in biofilm (PCBIOFILM) model, Bioresour. Technol. 102, 253-262.

99. McCarty, P.L., 1964. Anaerobic waste treatment fundamentals, Public Works. 95, 107-112.

100. Merkey, B.V., Chopp, D.L., 2012. The performance of a microbial fuel cell depends strongly on anode geometry: a multidimensional modeling study, Bull. Math. Biol. 74, 834-857.

101. Metcalf & Eddy, I., 2014. Wastewater Engineering: Treatment and Reuse, Anonymous McGraw-Hill Education, New York.

102. Miceli III, J.F., Garcia-Peña, I., Parameswaran, P., Torres, C.I., Krajmalnik-Brown, R., 2014. Combining microbial cultures for efficient production of

electricity from butyrate in a microbial electrochemical cell, Bioresour. Technol. 169, 169-174.

103. Modin, O., Fukushi, K., 2012. Development and testing of bioelectrochemical reactors converting wastewater organics into hydrogen peroxide, Water Science and Technology. 66, 831-836.

104. Modin, O., Fukushi, K., 2013. Production of high concentrations of H_2O_2 in a bioelectrochemical reactor fed with real municipal wastewater, Environ. Technol. 34, 2737-2742.

105. Navarro, J.A., Miguel, A., Roncel, M., Francisco, F., 1984. Carbon dioxide-mediated decomposition of hydrogen peroxide in alkaline solutions, Journal of the Chemical Society, Faraday Transactions 1: Physical Chemistry in Condensed Phases. 80, 249-253.

106. Ni, B., Yuan, Z., 2015. Recent advances in mathematical modeling of nitrous oxides emissions from wastewater treatment processes, Water Res. 87, 336-346.

107. Ni, B., Zeng, R.J., Fang, F., Xie, W., Sheng, G., Yu, H., 2010. Fractionating soluble microbial products in the activated sludge process, Water Res. 44, 2292-2302.

108. Nicoll, W., Smith, A., 1955. Stability of dilute alkaline solutions of hydrogen peroxide, Industrial & Engineering Chemistry. 47, 2548-2554.

109. Noguera, D.R., Araki, N., Rittmann, B.E., 1994. Soluble microbial products (SMP) in anaerobic chemostats, Biotechnol. Bioeng. 44, 1040-1047.

110. Nopens, I., Batstone, D.J., Copp, J.B., Jeppsson, U., Volcke, E., Alex, J., Vanrolleghem, P.A., 2009. An ASM/ADM model interface for dynamic plant-wide simulation, Water Res. 43, 1913-1923.

111. O'Callaghan, P., 2009. Water and Energy: A Presentation for the Water Innovations Alliance.

112. Oh, S., Logan, B.E., 2005. Hydrogen and electricity production from a food processing wastewater using fermentation and microbial fuel cell technologies, Water Res. 39, 4673-4682.

113. Oliveira, V.B., Simões, M., Melo, L.F., Pinto, A.M.F.R., 2013. A 1D mathematical model for a microbial fuel cell, Energy. 61, 463-471.

114. Otsuka, K., Yamanaka, I., 1990. One step synthesis of hydrogen peroxide through fuel cell reaction, Electrochim. Acta. 35, 319-322.

115. Ou, S., Kashima, H., Aaron, D.S., Regan, J.M., Mench, M.M., 2016a. Multi-variable mathematical models for the air-cathode microbial fuel cell system, J. Power Sources. 314, 49-57.

116. Ou, S., Zhao, Y., Aaron, D.S., Regan, J.M., Mench, M.M., 2016b. Modeling and validation of single-chamber microbial fuel cell cathode biofilm growth and response to oxidant gas composition, J. Power Sources. 328, 385-396.

117. Ou, S., Kashima, H., Aaron, D.S., Regan, J.M., Mench, M.M., 2017. Full cell simulation and the evaluation of the buffer system on air-cathode microbial fuel cell, J. Power Sources. 347, 159-169.

118. Pant, D., Van Bogaert, G., Diels, L., Vanbroekhoven, K., 2010. A review of the substrates used in microbial fuel cells (MFCs) for sustainable energy production, Bioresource Technology. 101, 1533-1543.

119. Parameswaran, P., Torres, C.I., D.-W. Kang, Rittmann, B.E., Krajmalnik-Brown, R., 2012. The role of homoacetogenic bacteria as efficient hydrogen scavengers in microbial electrochemical cells (MXCs), Water Science & Technology. 65, 1-6.

120. Parameswaran, P., Torres, C.I., Lee, H., Krajmalnik-Brown, R., Rittmann, B.E., 2009. Syntrophic interactions among anode respiring bacteria (ARB) and Non-ARB in a biofilm anode: electron balances, Biotechnol. Bioeng. 103, 513-523.

121. Parameswaran, P., Torres, C.I., Lee, H., Rittmann, B.E., Krajmalnik-Brown, R., 2011. Hydrogen consumption in microbial electrochemical systems (MXCs): the role of homo-acetogenic bacteria, Bioresour. Technol. 102, 263-271.

122. Park, S., Bae, W., Chung, J., Baek, S., 2007. Empirical model of the pH dependence of the maximum specific nitrification rate, Process Biochemistry. 42, 1671-1676.

123. Parkhurst, D.L., Appelo, C., 1999. User's guide to PHREEQC (Version 2): A computer program for speciation, batch-reaction, one-dimensional transport, and inverse geochemical calculations,.

124. Parkin, G.F., Owen, W.F., 1986. Fundamentals of Anaerobic-Digestion of Waste-Water Sludges, Journal of Environmental Engineering-Asce. 112, 867-920.

125. Paulus, U., Schmidt, T., Gasteiger, H., Behm, R., 2001. Oxygen reduction on a high-surface area Pt/Vulcan carbon catalyst: a thin-film rotating ring-disk electrode study, J Electroanal Chem. 495, 134-145.

126. Peng, L., Ni, B., Law, Y., Yuan, Z., 2016. Modeling N2O production by ammonia oxidizing bacteria at varying inorganic carbon concentrations by coupling the catabolic and anabolic processes, Chemical Engineering Science. 144, 386-394.

127. Picioreanu, C., Head, I.M., Katuri, K.P., van Loosdrecht, M.C., Scott, K., 2007. A computational model for biofilm-based microbial fuel cells, Water Res. 41, 2921-2940.

128. Picioreanu, C., Katuri, K., Head, I., van Loosdrecht, M.C., Scott, K., 2008. Mathematical model for microbial fuel cells with anodic biofilms and anaerobic digestion, Water science and technology. 57, 965-971.

129. Picioreanu, C., van Loosdrecht, M., Curtis, T.P., Scott, K., 2010. Model based evaluation of the effect of pH and electrode geometry on microbial fuel cell performance, Bioelectrochemistry. 78, 8-24.

130. Pinto, R., Srinivasan, B., Escapa, A., Tartakovsky, B., 2011. Multi-population model of a microbial electrolysis cell, Environ. Sci. Technol. 45, 5039-5046.

131. Pinto, R.P., Srinivasan, B., Manuel, M.-., Tartakovsky, B., 2010. A two-population bio-electrochemical model of a microbial fuel cell, Bioresour. Technol. 101, 5256-5265.

132. Popat, S.C., Torres, C.I., 2016. Critical transport rates that limit the performance of microbial electrochemistry technologies, Bioresour. Technol. 215, 265-273.

133. Pous, N., Puig, S., Coma, M., Balaguer, M.D., Colprim, J., 2013. Bioremediation of nitrate-polluted groundwater in a microbial fuel cell, Journal of Chemical Technology & Biotechnology. 88, 1690-1696.

134. Qiang, Z., Chang, J., Huang, C., 2002. Electrochemical generation of hydrogen peroxide from dissolved oxygen in acidic solutions, Water Res. 36, 85-94.

135. Rabaey, K., Rozendal, R.A., 2010. Microbial electrosynthesis—revisiting the electrical route for microbial production, Nature Reviews Microbiology. 8, 706-716.

136. Rabaey, K., Verstraete, W., 2005. Microbial fuel cells: novel biotechnology for energy generation, Trends Biotechnol. 23, 291-298.

137. Rajala-Mustonen, R.L., Heinonen-Tanski, H., 1995. Effect of advanced oxidation processes on inactivation of coliphages, Water Science and Technology. 31, 131-134.

138. Rämö, J., Sillanpää, M., 2001. Degradation of EDTA by hydrogen peroxide in alkaline conditions, J. Clean. Prod. 9, 191-195.

139. Reekie, L., Pabi, S., Amarnath, A., Goldstein, R., 2013. Electricity use and management in the municipal water supply and wastewater industries. Water Research Foundation.

140. Renslow, R.S., Babauta, J.T., Majors, P.D., Beyenal, H., 2013. Diffusion in biofilms respiring on electrodes, Energy & environmental science. 6, 595-607.

141. Rezaei, F., Richard, T.L., Logan, B.E., 2008. Enzymatic hydrolysis of cellulose coupled with electricity generation in a microbial fuel cell, Biotechnol. Bioeng. 101, 1163-1169.

142. Rittmann, B.E., 2013. The energy issue in urban water management, Source separation and decentralization for wastewater management.Edited by TA Larsen, K.Udert, and J.Lienert.IWA Publishing, London, UK. 13-27.

143. Rittmann, B.E., McCarty, P.L., 2001. Environmental biotechnology :principles and applications. McGraw-Hill, Boston.

144. Rozendal, R.A., Hamelers, H.V.M., Rabaey, K., Keller, J., Buisman, C.J.N., 2008. Towards practical implementation of bioelectrochemical wastewater treatment, Trends Biotechnol. 26, 450-459.

145. Rozendal, R.A., Leone, E., Keller, J., Rabaey, K., 2009. Efficient hydrogen peroxide generation from organic matter in a bioelectrochemical system, Electrochem. Commun. 11, 1752-1755.

146. Rumsey, T., Torres, C., 2017. Optimization of H_2O_2 Producing Cell. FURI Symposium, Arizona State University.

147. Sabba, F., Picioreanu, C., Boltz, J.P., Nerenberg, R., 2017. Predicting N2O emissions from nitrifying and denitrifying biofilms: a modeling study, Water Science and Technology. 75, 530-538.

148. Santoro, C., Arbizzani, C., Erable, B., Ieropoulos, I., 2017. Microbial fuel cells: From fundamentals to applications. A review, Journal of power sources. 356, 225-244.

149. Scandinavian Pulp, Paper and Board Testing Committee, 2009. Determination of EDTA and DTPA, SCAN-W 11:03.

150. Sevda, S., Dominguez-Benetton, X., Vanbroekhoven, K., De Wever, H., Sreekrishnan, T.R., Pant, D., 2013. High strength wastewater treatment accompanied by power generation using air cathode microbial fuel cell, Appl. Energy. 105, 194-206.

151. Shi, L., Dong, H., Reguera, G., Beyenal, H., Lu, A., Liu, J., Yu, H., Fredrickson, J.K., 2016. Extracellular electron transfer mechanisms between microorganisms and minerals, Nature Reviews Microbiology. 14, 651–662.

152. Siegrist, H., Vogt, D., Garcia-Heras, J.L., Gujer, W., 2002. Mathematical model for meso-and thermophilic anaerobic sewage sludge digestion, Environ. Sci. Technol. 36, 1113-1123.

153. Sim, J., An, J., Elbeshbishy, E., Ryu, H., Lee, H., 2015. Characterization and optimization of cathodic conditions for H_2O_2 synthesis in microbial electrochemical cells, Bioresour. Technol. 195, 31-36.

154. Sleutels, T.H., Lodder, R., Hamelers, H.V., Buisman, C.J., 2009. Improved performance of porous bio-anodes in microbial electrolysis cells by enhancing mass and charge transport, Int J Hydrogen Energy. 34, 9655-9661.

155. Sleutels, T.H.J.A., Hamelers, H.V.M., Buisman, C.J.N., 2011. Effect of mass and charge transport speed and direction in porous anodes on microbial electrolysis cell performance, Bioresource Technology. 102, 399-403.

156. Snoeyink, V.L., Jenkins, D., 1980. Water Chemistry. John Wiley & Sons, Inc., New York.

157. Snyder, S., Lei, H., Wert, E., Westerhoff, P., Yoon, Y., 2008. Removal of EDCs and Pharmaceuticals in Drinking Water. Water Environment Research Foundation.

158. Solon, K., Flores-Alsina, X., Mbamba, C.K., Ikumi, D., Volcke, E., Vaneeckhaute, C., Ekama, G., Vanrolleghem, P., Batstone, D.J., Gernaey, K., 2017. Plant-wide modelling of phosphorus transformations in wastewater treatment systems: Impacts of control and operational strategies, Water Res. 113, 97-110.

159. Steefel, C.I., MacQuarrie, K.T., 1996. Approaches to modeling of reactive transport in porous media, Reviews in Mineralogy and Geochemistry. 34, 85-129.

160. Stoodley, P., Cargo, R., Rupp, C.J., Wilson, S., Klapper, I., 2002. Biofilm material properties as related to shear-induced deformation and detachment phenomena, Journal of industrial microbiology & biotechnology. 29, 361-367.

161. ter Heijne, A., Hamelers, H.V.M., Saakes, M., Buisman, C.J.N., 2008. Performance of non-porous graphite and titanium-based anodes in microbial fuel cells, Electrochim. Acta. 53, 5697-5703.

162. Torres, C.I., Kato Marcus, A., Rittmann, B.E., 2008a. Proton transport inside the biofilm limits electrical current generation by anode-respiring bacteria, Biotechnol. Bioeng. 100, 872-881.

163. Torres, C.I., Marcus, A.K., Parameswaran, P., Rittmann, B.E., 2008b. Kinetic experiments for evaluating the Nernst− Monod model for anode-respiring bacteria (ARB) in a biofilm anode, Environ. Sci. Technol. 42, 6593-6597.

164. Torres, C.I., 2014. On the importance of identifying, characterizing, and predicting fundamental phenomena towards microbial electrochemistry applications, Curr. Opin. Biotechnol. 27, 107-114.

165. U.S. EPA. Clean Watersheds Needs Survey 2012: Report to Congress, 2016. 2016 ASI 9204-7.

166. U.S. EPA Combined Heat and Power Partnership, 2008. Catalog of CHP Technologies.

167. U.S. EPA, Global Environment & Technology Foundation, 2008. Ensuring a sustainable future.

168. VanBriesen, J.M., Rittmann, B.E., 1999. Modeling speciation effects on biodegradation in mixed metal/chelate systems, Biodegradation. 10, 315-330.

169. Vavilin, V.A., Fernandez, B., Palatsi, J., Flotats, X., 2008. Hydrolysis kinetics in anaerobic degradation of particulate organic material: An overview, Waste Manage. 28, 939-951.

170. Velasquez-Orta, S.B., Yu, E., Katuri, K.P., Head, I.M., Curtis, T.P., Scott, K., 2011. Evaluation of hydrolysis and fermentation rates in microbial fuel cells, Appl. Microbiol. Biotechnol. 90, 789-798.

171. Wagner, M., Brumelis, D., Gehr, R., 2002. Disinfection of wastewater by hydrogen peroxide or peracetic acid: development of procedures for measurement of residual disinfectant and application to a physicochemically treated municipal effluent, Water Environ. Res. 33-50.

172. Wanner, O., Ebert, H.J., Morgenroth, E., Noguera, D., Picioreanu, C., Rittmann, B.E., Van Loosdrecht, M.C.M., 2006. Mathematical Modeling of Biofilms. IWA Scientific and Technical Report No. 18 IWA Task Group on Biofilm Modeling.

173. Xie, W., Ni, B., Seviour, T., Sheng, G., Yu, H., 2012. Characterization of autotrophic and heterotrophic soluble microbial product (SMP) fractions from activated sludge, Water Res. 46, 6210-6217.

174. Yamada, N., Yaguchi, T., Otsuka, H., Sudoh, M., 1999. Development of Trickle-Bed Electrolyzer for On-Site Electrochemical Production of Hydrogen Peroxide, J. Electrochem. Soc. 146, 2587-2591.

175. Yamanaka, I., Hashimoto, T., Otsuka, K., 2002. Direct Synthesis of Hydrogen Peroxide (> 1 wt%) over the Cathode Prepared from Active Carbon and Vapor-Grown-Carbon-Fiber by a New H2–O2 Fuel Cell System, Chem. Lett. 31, 852-853.

176. Yamanaka, I., Onisawa, T., Hashimoto, T., Murayama, T., 2011. A Fuel-Cell Reactor for the Direct Synthesis of Hydrogen Peroxide Alkaline Solutions from H2 and O2, ChemSusChem. 4, 494-501.

177. Yamanaka, I., Onizawa, T., Takenaka, S., Otsuka, K., 2003. Direct and Continuous Production of Hydrogen Peroxide with 93 % Selectivity Using a Fuel-Cell System, Angewandte Chemie International Edition. 42, 3653-3655.

178. Yang, W., Zhou, H., Cicek, N., 2014. Treatment of organic micropollutants in water and wastewater by UV-based processes: a literature review, Crit. Rev. Environ. Sci. Technol. 44, 1443-1476.

179. Young, M.N., Chowdhury, N., Garver, E., Evans, P.J., Popat, S.C., Rittmann, B.E., Torres, C.I., 2017. Understanding the impact of operational conditions on

performance of microbial peroxide producing cells, J. Power Sources. 356, 448-458.

180. Young, M.N., Krajmalnik-Brown, R., Liu, W., Doyle, M.L., Rittmann, B.E., 2013a. The role of anaerobic sludge recycle in improving anaerobic digester performance, Bioresour. Technol. 128, 731-737.

181. Young, M.N., Marcus, A.K., Rittmann, B.E., 2013b. A Combined Activated Sludge Anaerobic Digestion Model (CASADM) to understand the role of anaerobic sludge recycling in wastewater treatment plant performance, Bioresour. Technol. 136, 196-204.

182. Young, M.N., Parameswaran, P., Torres, C., Rittmann, B.E., 2015. Application of Microbial Electrochemical Cells (MXCs) as Real-Time Sensors of Bioavailability from Sludge Pretreatment Technologies, Proceedings of the Water Environment Federation. 2015, 1-12.

183. Young, M.N., Links, M.J., Popat, S.C., Rittmann, B.E., Torres, C.I., 2016. Tailoring Microbial Electrochemical Cells for Production of Hydrogen Peroxide at High Concentrations and Efficiencies, ChemSusChem. 9, 3345-3352.

184. Zhang, G., Zhao, Q., Jiao, Y., Wang, K., Lee, D., Ren, N., 2012. Efficient electricity generation from sewage sludge using biocathode microbial fuel cell, Water Res. 46, 43-52.

185. Zhang, X., Halme, A., 1995. Modelling of a microbial fuel cell process, Biotechnol. Lett. 17, 809-814.

186. Zhao, L., Li, J., Battaglia, F., He, Z., 2016. Investigation of multiphysics in tubular microbial fuel cells by coupled computational fluid dynamics with multi-order Butler–Volmer reactions, Chemical Engineering Journal. 296, 377-385.

187. Zhuang, L., Yuan, Y., Wang, Y., Zhou, S., 2012. Long-term evaluation of a 10-liter serpentine-type microbial fuel cell stack treating brewery wastewater, Bioresour. Technol. 123, 406-412.

188. Zuo, Y., Maness, P., Logan, B.E., 2006. Electricity production from steam-exploded corn stover biomass, Energy Fuels. 20, 1716-1721.

APPENDIX A

SUPPLEMENTAL INFORMATION FOR CHAPTER 2

A.1 Supplemental graphs

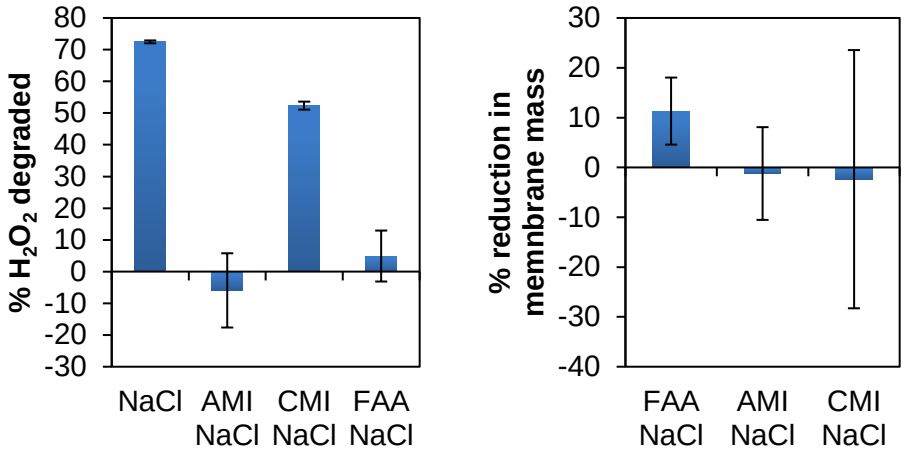

(a) (b)

Figure A.1. (a) Percent H_2O_2 degraded and (b) membrane weight loss for FAA, AMI, and CMI membranes at pH 7 and 10 g/L H_2O_2.

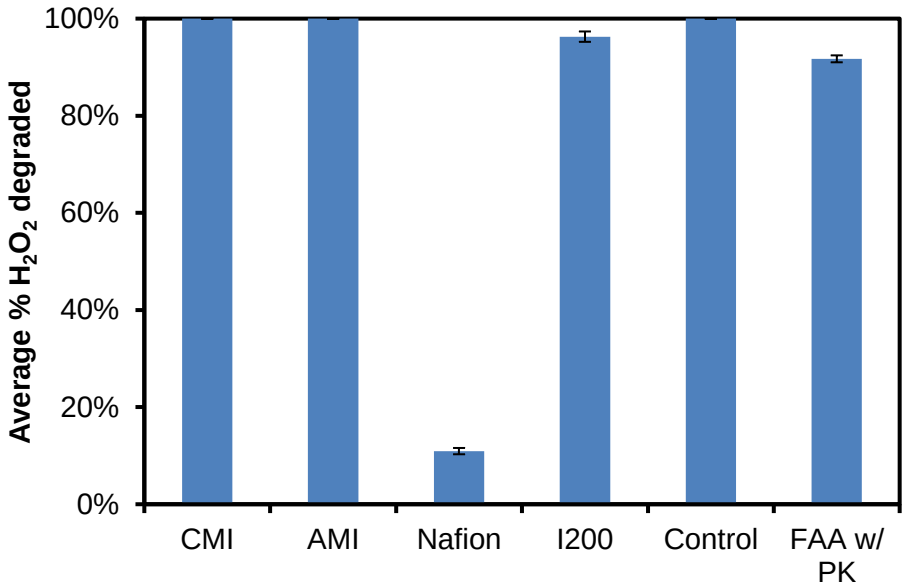

Figure A.2. H_2O_2 degraded during batch bottle tests for membrane stabilities at pH 12.

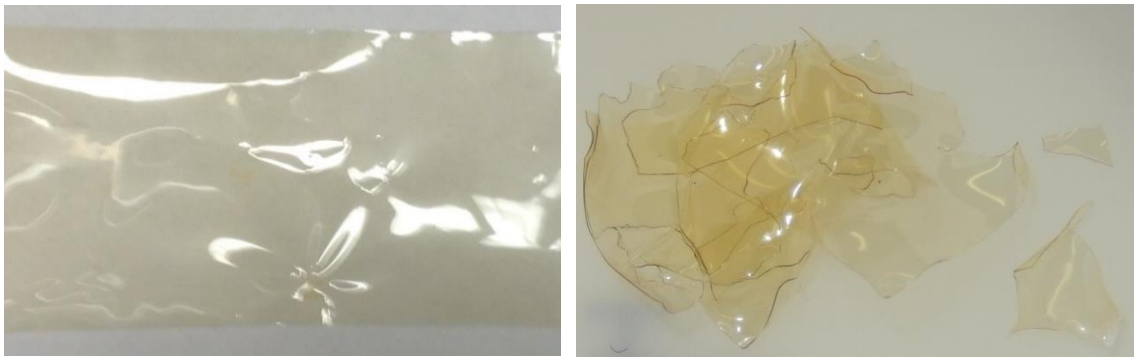

(a) (b)

Figure A.3. FAA (a) before and (b) after pH 12 100-mM NaCl and 10 g/L H_2O_2 stability tests. The stability tests used a 3 cm x 3 cm square that deteriorated to pieces by the end of the 45-day test.

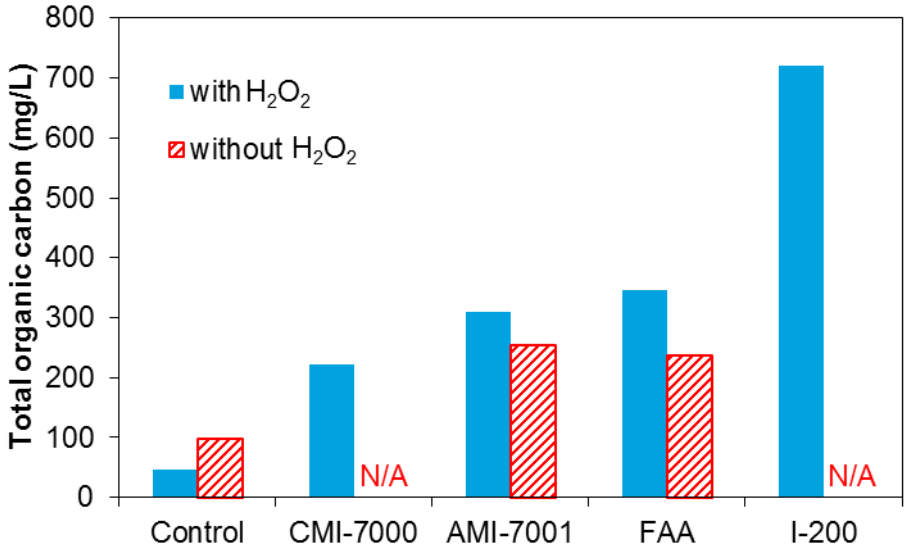

Figure A.4. Total organic carbon (TOC) from batch bottle tests of membrane stabilities with and without 10 g/L H_2O_2 present in the solution at pH 12. TOC measurements were obtained using a Shimadzu TOC-V CSH Total Organic Carbon analyzer. Tests were not performed on CMI-7000 and I-200 at pH 12 only.

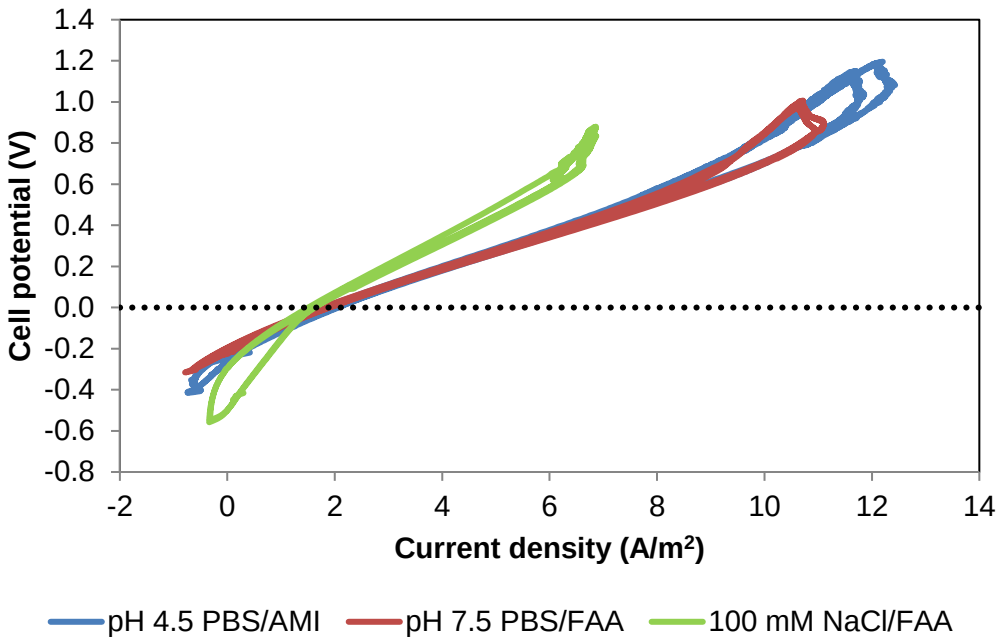

Figure A.5. CVs of preliminary reactor design. The MPPC CVs were performed with two different membranes (FAA and AMI-7001) and three different catholytes: 100 mM NaCl, pH 4.5 PBS, and pH 7.5 PBS. The MPPC was operated at a 4 hr HRT and 30 cm^3/min air flow rate. The reactor design was the same as the reactor presented in this paper, except there was 1 cm distance between the anode and cathode. The FAA membrane is ~1/3 the thickness of the AMI membrane and has a lower resistance.

A.2 EIS characterization of membrane resistances

I tested the membranes in a 100-mM $NaHCO_3$ solution using EIS to determine their ionic transport resistances. EIS was performed at 100 kHz and 10 mV amplitude with the anode as the working electrode and the cathode as the counter electrode. As illustrated in Figure A.6, heterogeneous membranes exhibited 45-85 ohm-cm^2 in resistance. Homogeneous membranes demonstrated resistances < 20 ohm-cm^2. For perspective, at 10 A/m^2, the homogeneous membranes have Ohmic overpotential < 20 mV and heterogeneous membranes between 50-85 mV.

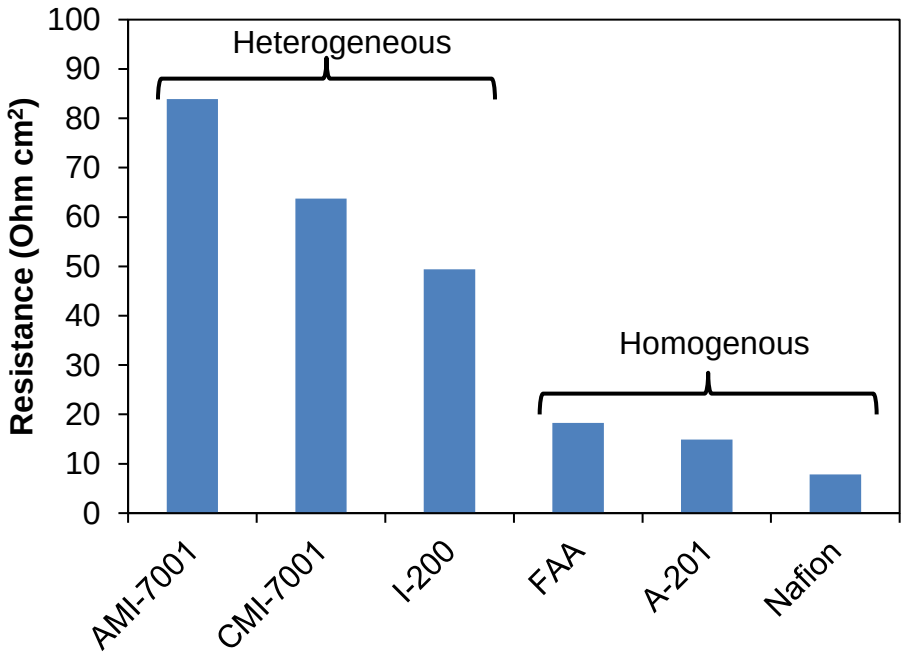

Figure A.6. Area-specific resistances determined using electrochemical impedance spectroscopy for seven different heterogeneous and homogenous membranes in 100 mM $NaHCO_3$.

A.3 Linear sweep voltammetry to determine activation overpotentials in catalyst/binder combinations

I used gas-diffusion half-cells to evaluate differences between catalyst and binder performance. I evaluated three catalyst/binder combinations: 50 g/L Vulcan carbon (FuelCellStore.com) in a 5% cationomer Nafion solution (10% Nafion in alcohol, Sigma-Aldrich); 62.5 g/L of Vulcan carbon in an 3.13% anionmer AS-4 solution (5% AS-4 in alcohol, Tokuyama Corp.); and 87.7 g/L of graphite (Sigma-Aldrich) in a 8.77% Nafion solution. The catalyst/binder was coated on a 9-cm^2 hydrophobic carbon cloth (FuelCell.com) at a loading of 0.5 mg/cm^2 and dried for 24 h. The cathode and a 316-stainless steel rod anode were placed in a 27 mL half-cell filled with 100-mM sodium perchlorate solution (Popat et al., 2014). A standard calomel electrode (SCE, CH Instruments, Inc.) was used as the reference (+0.21 V_{SHE}). For experiments utilizing NaOH or H_2O_2 in solution at the start, I used a Nafion-117 membrane to separate the cathode and anode chambers. The catalysts/binders were evaluated using linear sweep voltammetry (LSV) between -0.19 and 0.61 V_{SHE} at 1 or 2 mV/s scan rate and 30°C.

As illustrated in Appendix Figure A.6, the negatively-charged OH^- and HO_2^- produced at high pHs are more effectively transported from the cathode surface using the anionic AS-4 binder, resulting in lower concentration overpotential versus the cationic Nafion binder. Membrane-stability tests (not presented here) demonstrated that anionic polymers like AS-4 are not stable with H_2O_2, especially at high pH, eliminating it as a potential binder.

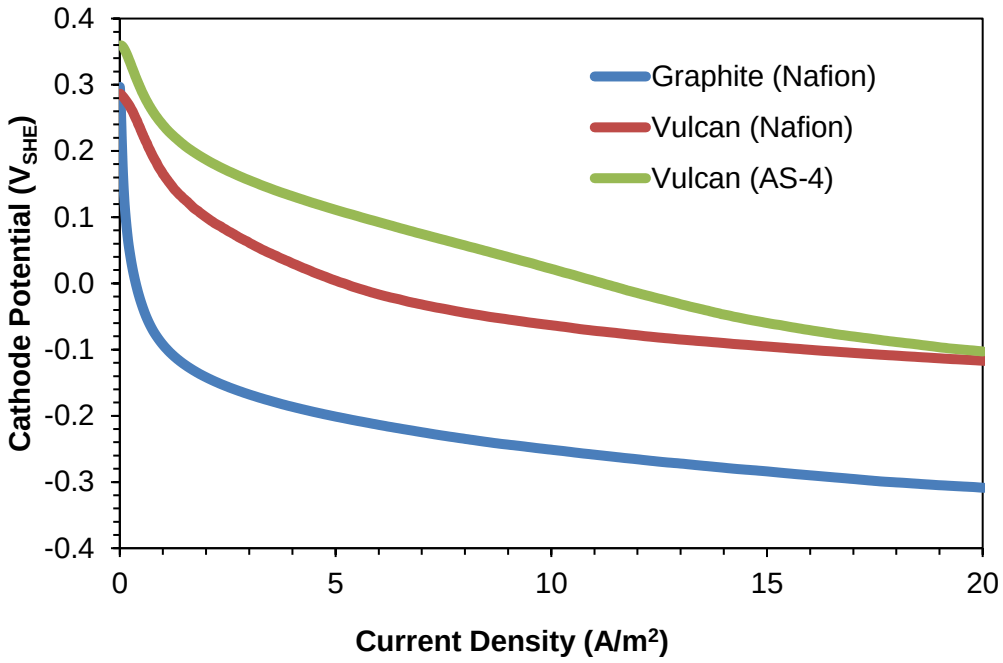

Figure A.7. Cathode potentials (up to 20 A m^{-2}) established using linear sweep voltammetry with three catalyst/binder combinations: 50 g/L Vulcan carbon in a 5% Nafion solution (labeled Vulcan (Nafion)); 62.5 g/L of Vulcan carbon in an 3.13% AS-4 solution (labeled Vulcan (AS-4)); and 87.7 g/L of graphite in a 8.77% Nafion solution (labeled Graphite (Nafion)).

APPENDIX B

SUPPLEMENTAL INFORMATION FOR CHAPTER 3

B.1 Supplemental graphs

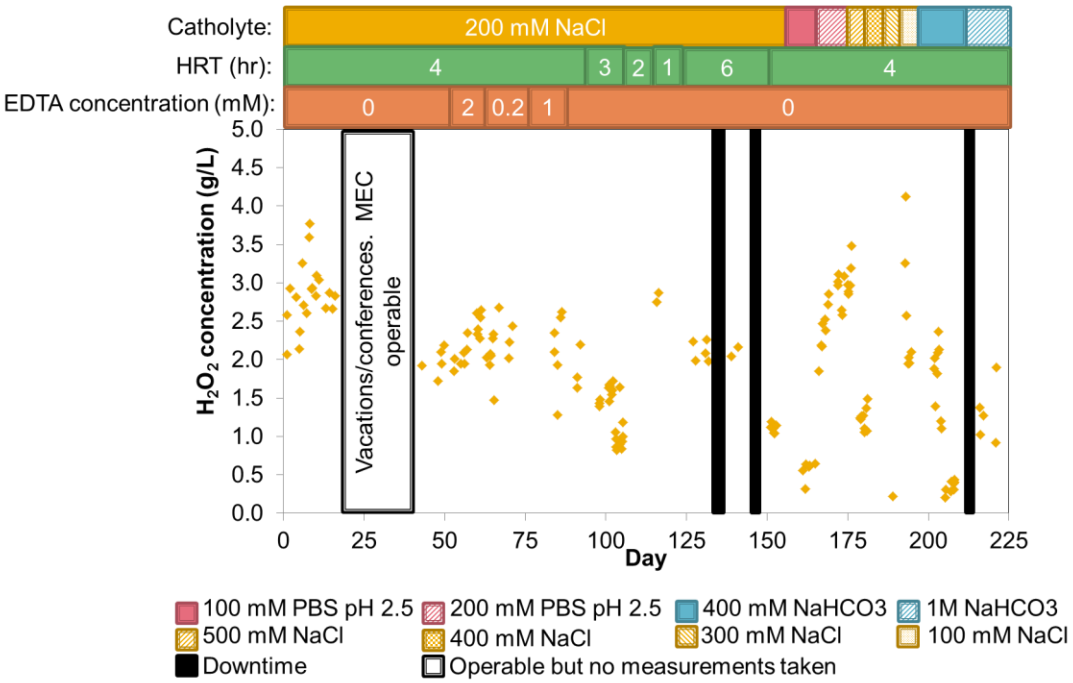

Figure B.1. Graph summarizing the conditions during long-term MPPC operation. The first two downtime events were associated with membrane failures. The last downtime event was due to the catholyte chamber pump failing.

Table B.1. Run time information for data obtained at each experimental setup.

	Duration prior to first measurement		Duration of measurements		Downtime (d)	Total experiment duration (d)	Number of samples taken
	Number of HRTs	Time (d)	Number of HRTs	Time (d)			
Varying HRT							
1-h HRT	6.1	0.3	69.4	2.9	0.0	3.1	10
2-h HRT	24.7	2.1	55.4	4.6	0.0	6.7	9
3-h HRT	6.8	0.9	89.3	11.2	0.0	12.0	9
4-h HRT	18.0	3.0	30.3	5.0	0.0	8.0	10
6-h HRT	14.7	3.7	61.7	15.4	2.1	23.8	9
Varying NaCl concentration							
100-mM	17.1	2.8	23.7	3.9	0.0	6.8	9
200-mM	18.0	3.0	30.3	5.0	0.0	8.0	10
300-mM	5.2	0.9	6.4	1.1	0.0	1.9	6
400-mM	16.4	2.7	18.4	3.1	0.0	5.0	6
500-mM	5.8	1.0	24.2	4.0	0.0	4.0	8
Varying EDTA concentration							
0-mM	18.0	3.0	30.3	5.0	0.0	8.0	10
0.2-mM	16.4	2.7	35.8	6.0	0.0	8.7	10
1-mM	6.5	1.1	84.0	14.0	0.0	15.1	11
2-mM	48.4	8.1	61.1	10.2	0.0	18.3	6
Varying electrolyte concentration							
200-mM NaCl	18.0	3.0	30.3	5.0	0.0	8.0	10
100-mM PBS	60.5	10.1	4.0	24.3	0.0	14.1	6
200-mM PBS	35.8	6.0	4.0	24.2	0.0	10.0	6
400-mM $NaHCO_3$	29.7	5.0	69.0	11.5	0.0	16.5	7
1000-mM $NaHCO_3$	5.2	0.9	18.1	3.0	0.0	3.9	8

Figure B.2. Membrane cracking observed during operation with a 6-hr HRT and using a 200-mM NaCl catholyte and 20 cm^3 min^{-1} air flow rate.

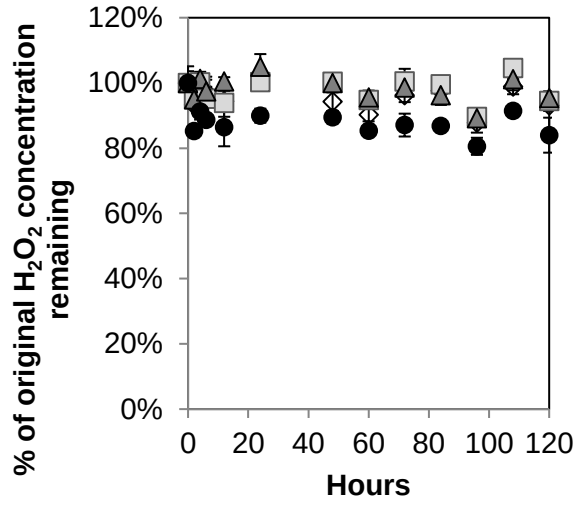
120%
100%
80%
60%
40%
20%
0%
% of original H_2O_2 concentration remaining
0
20
40
60
80
100
120
Hours
pH 4.5 PBS + no EDTA
pH 4.5 PBS + 2mM EDTA
pH 4.5 PBS + 4mM EDTA
pH 4.5 PBS + 6mM EDTA

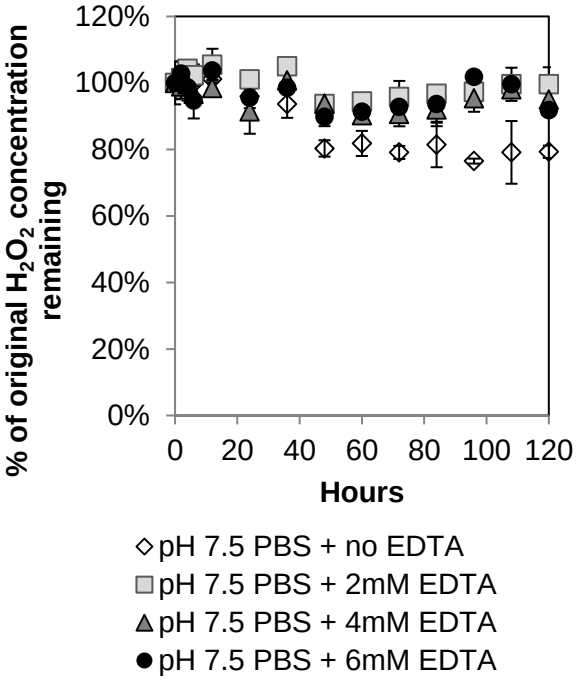
120%
100%
80%
60%
40%
20%
0%
% of original H_2O_2 concentration remaining
0
20
40
60
80
100
120
Hours
pH 7.5 PBS + no EDTA
pH 7.5 PBS + 2mM EDTA
pH 7.5 PBS + 4mM EDTA
pH 7.5 PBS + 6mM EDTA

(a) (b)

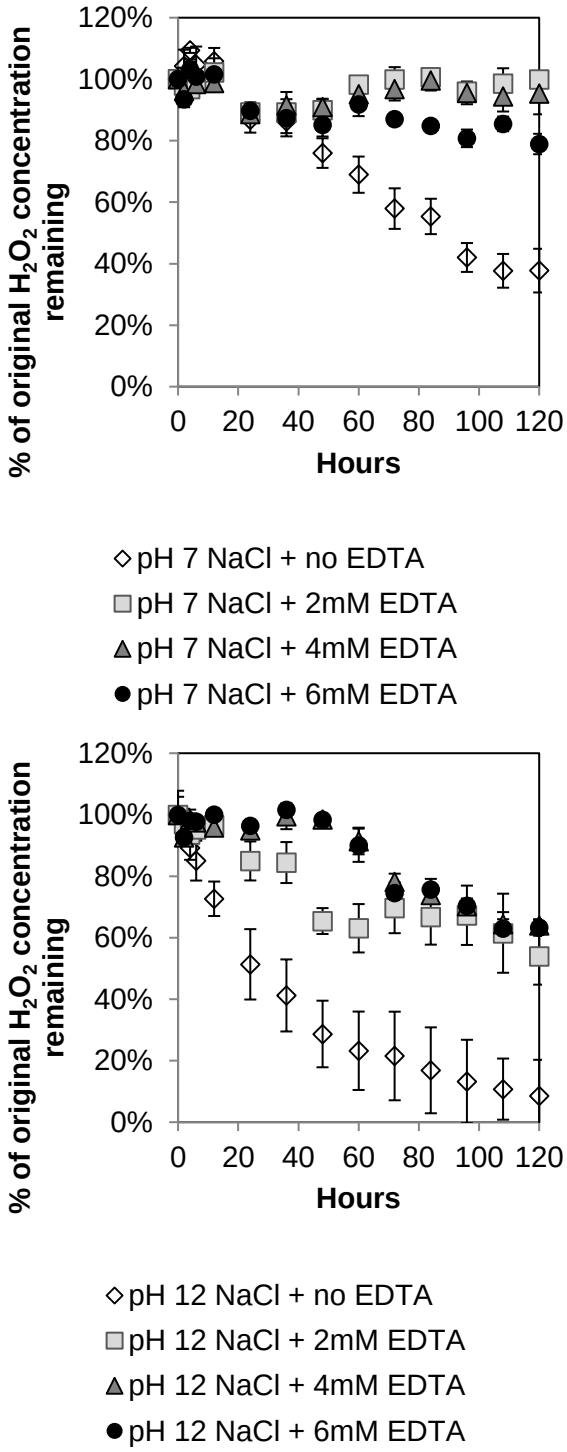

Figure B.3. H_2O_2 stability in different electrolytes and with 0- to 6-mM EDTA over 5 days: (a) pH 4.5 PBS, (b) pH 7.5 PBS, (c) pH 7 200-mM NaCl, and (d) pH 12 200-mM NaCl.

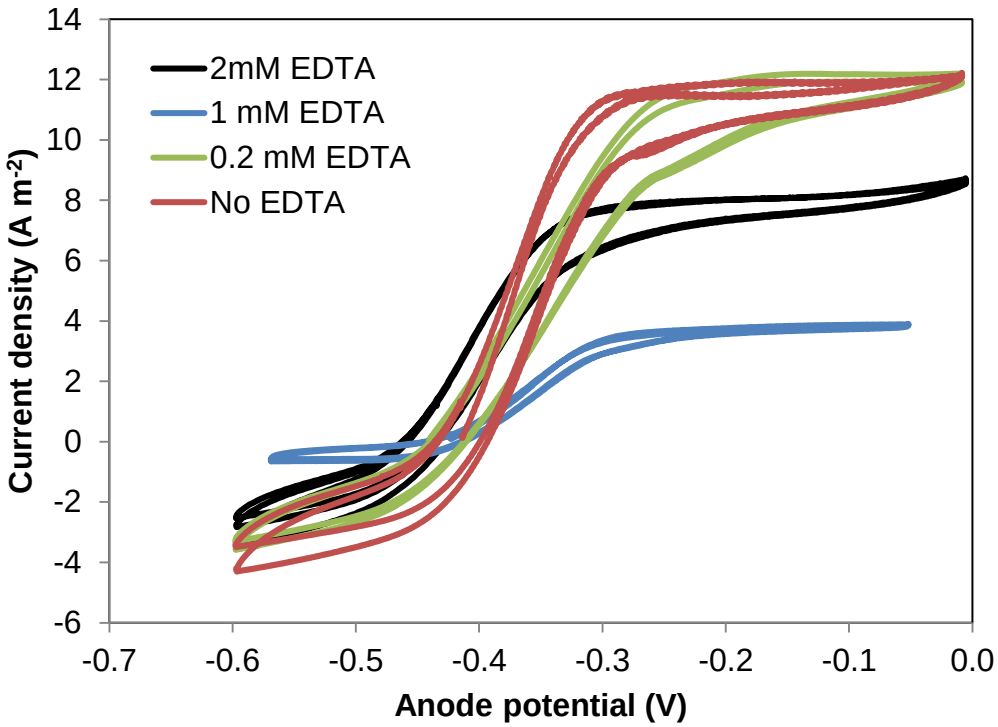

Figure B.4. Cyclic voltammetry of anode performance as a function of EDTA concentration.

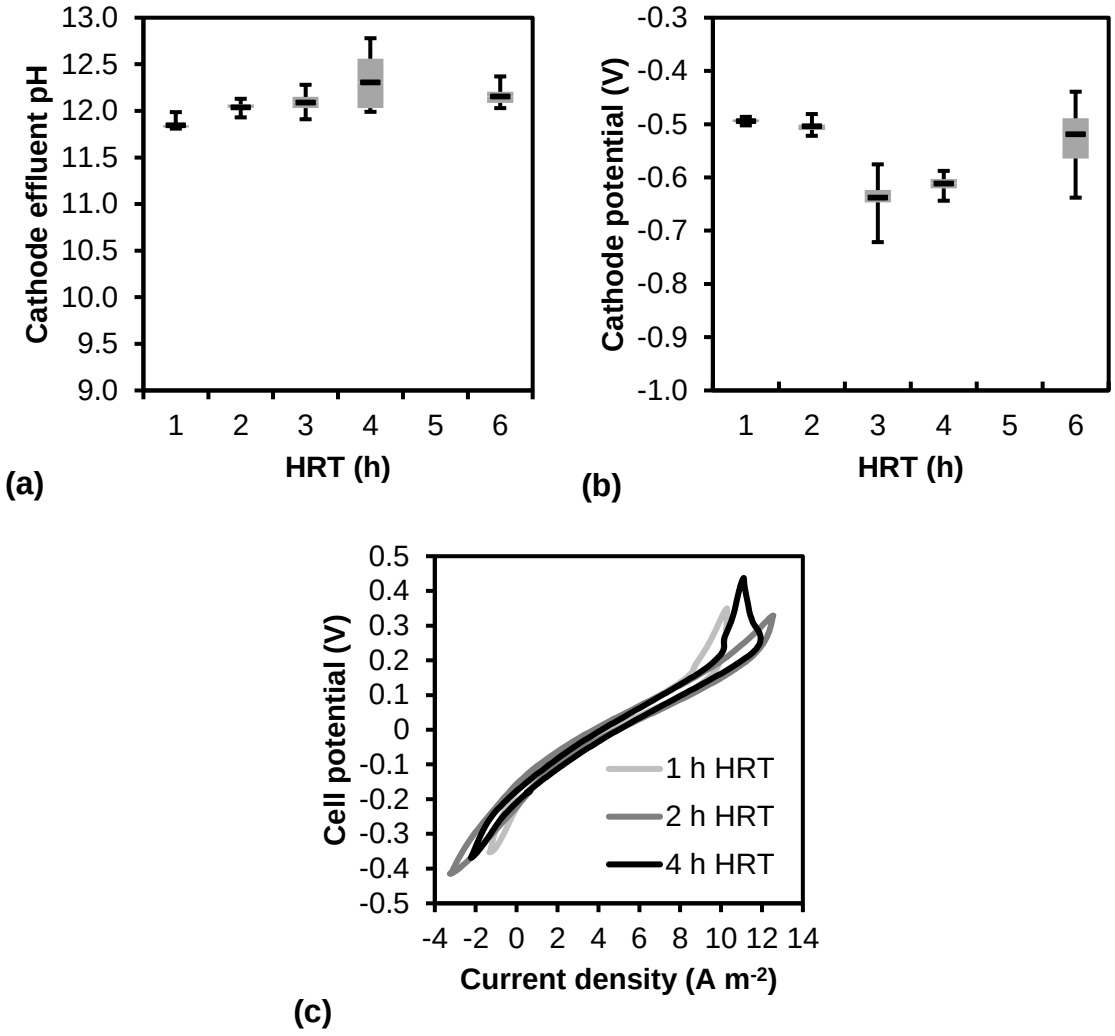

Figure B.5. Results for the experiment with a range of HRT from 1- to 6-h using 200-mM NaCl catholyte: (a) cathode effluent pH, (b) cathode potential, (c) net cathodic efficiency, and (d) cyclic voltammetry of cell performance. The light gray boxes represent the first and third quartiles, and the black point represents the average value. The whiskers represent the maximum and minimum data points.

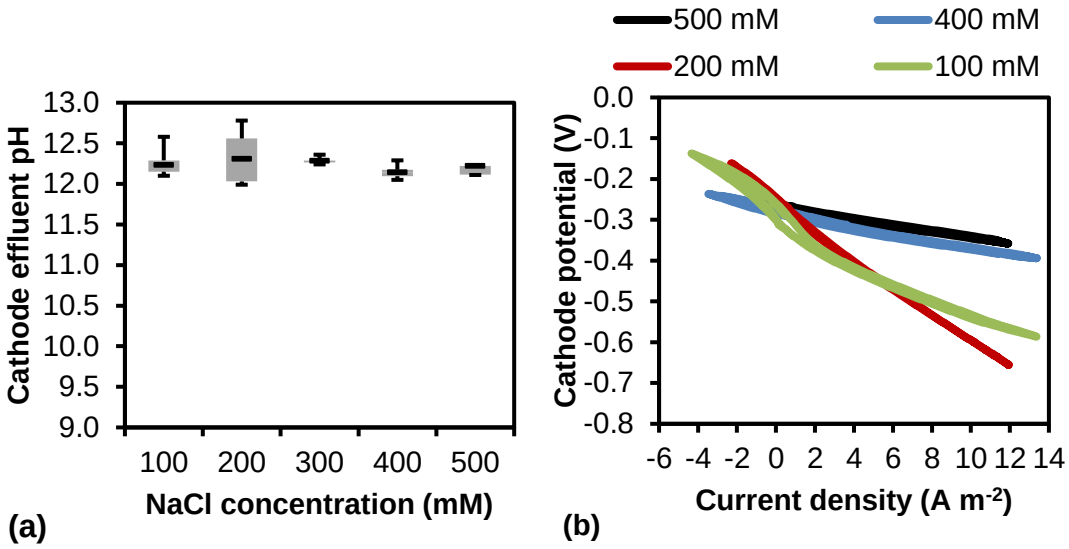

Figure B.6. Results for varied NaCl concentrations from 100- to 500-mM: (a) cathode effluent pH and (b) the cathode CV. The light gray boxes represent the first and third quartiles, and the black point represents the average value. The whiskers represent the maximum and minimum data points.

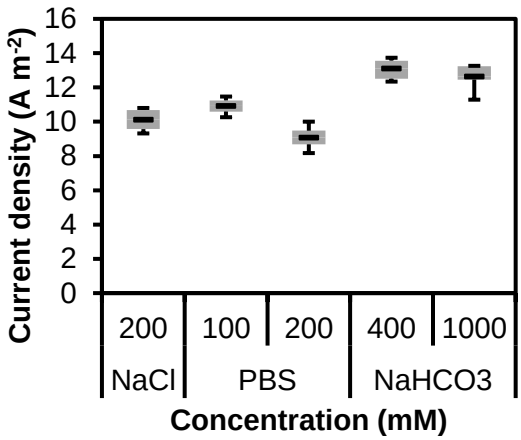

Figure B.7. Current density for varied buffering electrolyte concentrations. The light gray boxes represent the first and third quartiles, and the black point represents the average value. The whiskers represent the maximum and minimum data points.

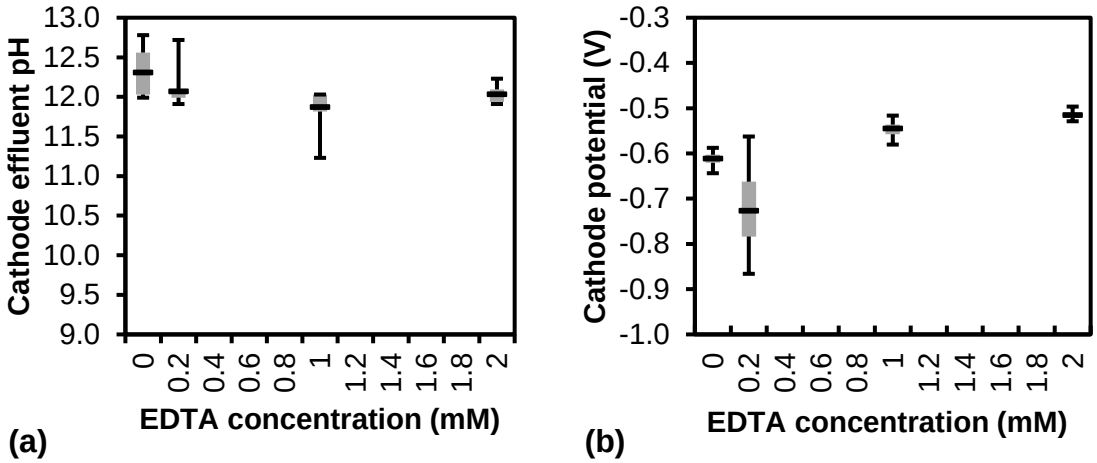

Figure B.8. Results for the experiment varying EDTA concentrations from 0- to 2-mM: (a) cathode effluent pH and (b) cathode potential. The light gray boxes represent the first and third quartiles, and the black point represents the average value. The whiskers represent the maximum and minimum data points.

B.2 Experimental calculations

Net cathodic coulombic efficiency (CCE) is defined as the efficiency at which current produced by the MPPC is converted to H_2O_2 molecules. First, I calculated the theoretical H_2O_2 concentration, C_{theory} (g/L), i.e., the amount of H_2O_2 produced if all current is converted to H_2O_2:

$$C_{theory} = \frac{I}{F} * \frac{HRT}{V} * \frac{3600\ s}{h} * \frac{mol\ H_2O_2}{2\ e^-} * \frac{34\ g\ H_2O_2}{mol\ H_2O_2} \quad \text{(Eqn. B.1)}$$

where I is current (mA), F is Faraday's constant (96485 C mol e-$^{-1}$), and V is cathode volume (mL). I then calculated percent current efficient, ε_{H2O2}, as the ratio of actual H_2O_2 concentration, C_{actual} (g L^{-1}), to C_{theory}.

$$\varepsilon_{H2O2} = C_{actual} / C_{theory} * 100\% \quad \text{(Eqn. B.2)}$$

Similarly, power input follows the inverse trend of coulombic efficiency, since power input is inversely proportional to C_{actual}:

$$P = \frac{E * I}{C_{actual} * V} \quad \text{(Eqn. B.3)}$$

where E is the cell potential (V).

Ionic current was determined based on IC and pH measurements for varying NaCl concentrations. The concentration of charges that migrated to maintain electroneutrality between the anode and cathode chambers over a set HRT (s), C^{req} (mol charge L^{-1}), is dictated by the amount of current produced:

$$C^{req} = \frac{I * HRT}{F * V} \quad \text{(Eqn. B.4)}$$

I assumed that OH^- and Cl^- anions could migrate across the AEM; therefore, the charge required to migrate to maintain electroneutrality, C_{req}^{mig} (mol charge L^{-1}), was

$$C_{req}^{mig} = C_{Cl-}^{mig} + C_{OH-}^{mig} \quad \text{(Eqn. B.5)}$$

The concentration of Cl^- charge that migrated to the anode was

$$C_{Cl-}^{mig} = |z_{Cl-}|\left(C_{Cl-}^{inf} - C_{Cl-}^{eff}\right) \quad \text{(Eqn. B.6)}$$

where C^{mig} is the concentration of charges that migrated (mol charge L^{-3}), z is the charge of anion (-1 for Cl^-), and C^{inf} and C^{eff} are the influent and effluent charge concentrations (M L^{-3}), respectively. The charge migration associated with OH^- is based both on the charge present in the system and production via Eqn. 3.2 and 3.3 in the main text; however, H_2O_2 is subject to degradation at the cathode. Assuming 100% of current is converted to H_2O_2 or HO_2^-, the theoretical amount of OH^- produced is

$$C_{OH-}^{prod} = 2 * C_{H2O2}^{theoretical} + C_{HO2-}^{theoretical} = \frac{C^{req}}{2} + \frac{C^{req}}{1 + \frac{10^{-pKa}}{10^{-pH}}} \quad \text{(Eqn. B.7)}$$

where pK_a is the 11.8 for H_2O_2 and pH is the effluent pH. Since the influent OH^- concentration is negligible as pH < 8 for all catholytes, the OH^- charge migrated to the anode, C_{OH-}^{mig}, is

$$C_{OH-}^{mig} = C_{OH-}^{prod} - C_{OH-}^{eff} \quad \text{(Eqn. B.8)}$$

where C_{OH-}^{eff} is the effluent OH^- charge concentration (M).

To determine statistical significance, I performed two-sample two tail t-test using the Data Analysis add-on in Microsoft Excel 2010. The t-test was performed assuming

equal and unequal variances to assess the impact of this assumption. I applied an alpha equal to 0.05 (95% confidence level) and hypothesized mean difference equal to zero.

B.3 Determining H_2O_2 production from a typical wastewater treatment plant (WWTP)

I determined the amount of H_2O_2 that would be produced from a MEC applied at a municipal WWTP based on two different wastewater sources: sludge from a primary settler and waste-activated sludge from a secondary clarifier. Table 3.1 outlines the assumed values for this analysis.

I assume a MEC is applied at a medium-sized WWTP treating 10 million L d^{-1} (or 2.64 MGD). The influent composition COD composition (500 mg L^{-1}) is based on average influent value for a medium-strength municipal wastewater (Metcalf & Eddy, 2014). I assume that 60% of influent TCOD is captured as primary sludge (Metcalf & Eddy, 2014), and 40% of the primary sludge's TCOD can be converted to current (Ki et al., 2017a). Thus, the amount of primary sludge COD converted to current per day is calculated as

$$\left(500\,\frac{\text{mgCOD}}{\text{L}}\right)\left(10^7\,\frac{\text{L}}{\text{d}}\right)(60\%\text{ of influent TCOD})(40\%\text{ efficiency})\left(\frac{\text{kg}}{10^6\text{mg}}\right) = 1200\,\frac{\text{kg}}{\text{d}}\text{COD} \quad \text{(Eqn. B.9)}$$

If the cathode exhibits 30% coulombic efficiency for H_2O_2 production, the amount of H_2O_2 produced from primary sludge treatment is

$$\left(1200\,\frac{\text{kg}}{\text{d}}\text{COD}\right)\left(\frac{1000\text{g}}{\text{kg}}\right)\left(\frac{1\text{ e}-\text{eq}}{8\text{g COD}}\right)\left(\frac{1\text{ mol }H_2O_2}{2\text{ e}-\text{eq}}\right)\left(\frac{34\text{ g }H_2O_2}{1\text{ mol }H_2O_2}\right)(30\%\text{ efficiency}) = 765\,\frac{\text{kg }H_2O_2}{\text{d}} \quad \text{(Eqn. B.10)}$$

Since 60% of the influent COD is being captured in primary sludge, the remaining 40% is undergoes secondary treatment and eventually subjected to further treatment in the MEC (i.e., waste-activated sludge or WAS). If I assume that 25% of the available COD during secondary treatment is lost due to biomass uptake, then 30% of the influent COD (i.e., 40%*75%) can be utilized by an MEC. For primary sludge, I assume that 35% of WAS TCOD is converted to current (Kim et al., 2005; Jiang et al., 2009; Zhang et al., 2012). The amount of secondary treatment COD converted to current is

$$\left(500\frac{\text{mgCOD}}{\text{L}}\right)\left(10^7\frac{\text{L}}{\text{d}}\right)(30\%\text{ of influent TCOD})(40\%\text{ efficiency})\left(\frac{\text{kg}}{10^6\text{mg}}\right) = 760\frac{\text{kg}}{\text{L}}\text{COD}$$

(Eqn. B.11)

If the cathode exhibits 30% coulombic efficiency for H_2O_2 production, the amount of H_2O_2 produced from WAS treatment is

$$\left(1200\frac{\text{kg}}{\text{L}}\text{COD}\right)\left(\frac{1000\text{g}}{\text{kg}}\right)\left(\frac{1\text{ e}-\text{eq}}{8\text{g COD}}\right)\left(\frac{1\text{ mol }H_2O_2}{2\text{ e}-\text{eq}}\right)\left(\frac{34\text{ g }H_2O_2}{1\text{ mol }H_2O_2}\right)(30\%\text{ efficiency}) = 383\ \frac{\text{kg }H_2O_2}{\text{d}}$$

(Eqn. B.12)

APPENDIX C

SUPPLEMENTAL INFORMATION FOR CHAPTER 4

C.1 Supplemental Graphs

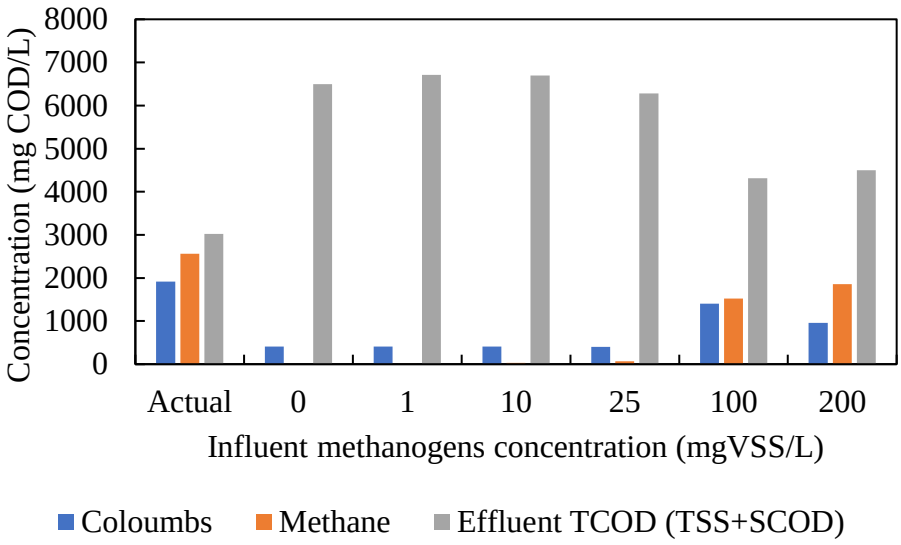

Figure C.1. Effluent composition at a 12-d anode chamber HRT, 0.25/d PCOD hydrolysis rate, and 1000 μm diffusion layer thickness. Experimental data was obtained from Ki et al. (2017a).

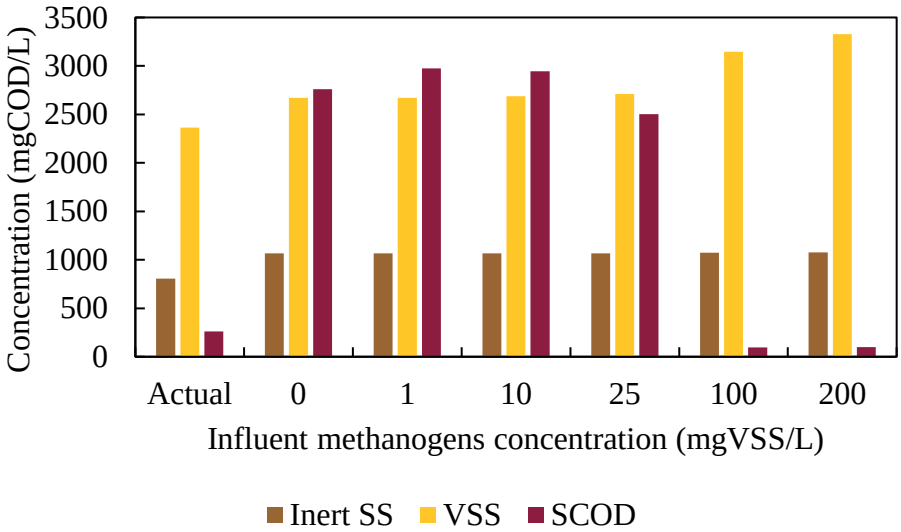

Figure C.2. Effluent TCOD composition at a 12-d anode chamber HRT, 0.25/d PCOD hydrolysis rate, and 1000 μm diffusion layer thickness. Experimental data was obtained from Ki et al. (2017a).

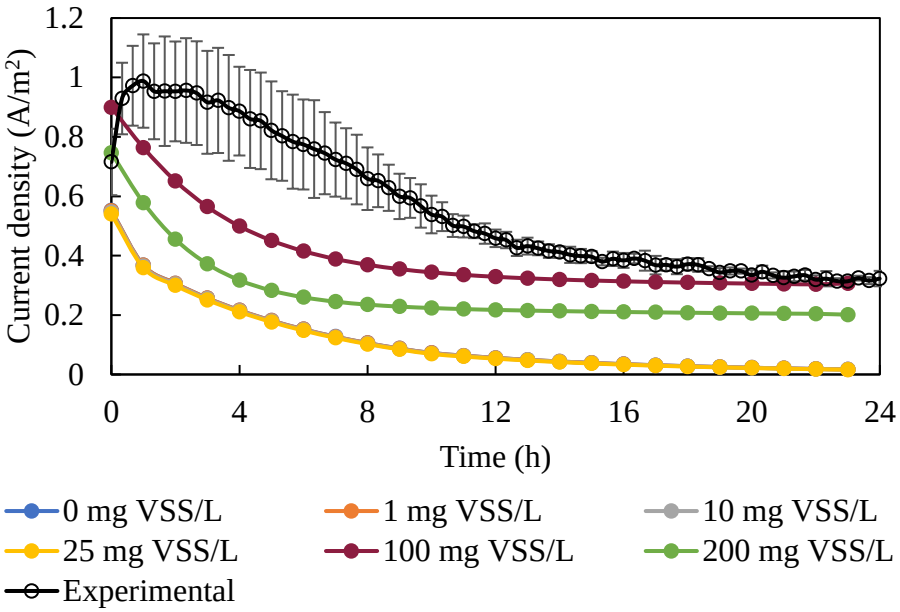

Figure C.3. Daily current densities at a 12-d anode chamber HRT, 0.25/d PCOD hydrolysis rate, and 1000 μm diffusion layer thickness for influent methanogens concentrations of 0-200 mg VSS/L. Experimental data was obtained from Ki et al. (2017a).

C.2 Modeling parameters

Table C.1. Kinetic parameters for the microorganisms. Unless otherwise stated, all values were obtained from Rittmann and McCarty (2001).

Kinetic Parameters		Symbol	Units	Heterotrophs	AOB	NOB	Fermenters	Methanogens[#]
Maximum utilization rate	Substrate	$\hat{q}$	mgCOD/mgVSS-d	10	3.1	13	10	--
	UAP[*]		mgCOD/mgVSS-d	1.8	--	--	1.8	--
	BAP[*]		mgCOD/mgVSS-d	0.5	--	--	0.5	--
	Acetate		mgAce/mgVSS-d	8.1	--	--	--	7
Half-maximum rate concentration	Substrate	K	mgCOD/L	10	1.5	2.7	10	--
	Acetate		mgAce/L	168	--	--	--	30
	DO		mgDO/L	0.2	0.5	0.68	--	--
	UAP[*]		mgCOD/L	100	--	--	100	--
	BAP[*]		mgCOD/L	85	--	--	85	--
	NO_2^-, NO_3^-		mgN/L	0.2	1.5	2.7	--	--
True fraction of electrons to cell synthesis	Substrate	f_s^0	mgCOD/L	0.6	--	--	0.18	--
	Acetate		mgAce/L	0.6	--	--	--	0.05
	UAP[*]		mgCOD/L	0.71	--	--	0.71	--
	BAP[*]		mgCOD/L	0.6	--	--	0.18	--
	NH_4^+		mgN/L	--	0.14	--	--	--
	NO_2^-		mgN/L	0.5	--	0.1	--	--
Biomass decay rate		b	1/d	0.3	0.15	0.15	0.04	0.03
Formation rate of UAP[*]		k_{UAP}	mgCOD/mgCOD	0.05				
Formation rate of EPS[*]		k_{EPS}	mgCOD/mgCOD	0.18				
Hydrolysis rate	EPS[*]	k_{hydEPS}	1/d	0.17				
	PCOD	k_{yd}	1/d	Model dependent				

Table C.1 continued. Kinetic parameters for the microorganisms. Unless otherwise stated, all values were obtained from Rittmann and McCarty (2001).

Kinetic Parameters		Symbol	Units	Heterotrophs	AOB	NOB	Fermenters	Methanogens[#]
Fraction of biodegradable biomass		f_d	-			0.8		
Optimal pH range			-	-	-	-	4.0-9.0	6.2-8.0[**]
Switch or inhibition concentration	O_2	K^{switch} or K^{inh}	mgO_2/L			0.2		
	NO_2^-		mgN/L			0.2		
	NO_3^-		mgN/L			0.2		
	HCO_3^-		mg HCO_3^-/L			0.005[^]		

[*] Laspidou and Rittmann (2002a, 2002b)

[**] McCarty (1964); Parkin and Owen (1986); Appels et al. (2008)

[#] Rittmann and McCarty (2001), Aquino and Stuckey (2008)

[^] Assumed

180

Table C.2. Gas/liquid phase partitioning constants. Unless otherwise stated, all values were obtained from Batstone et al. (2002). The ratio of liquid volume to gas headspace volume is assumed to be 1.

	Henry's law constant (mol/L-bar)	Partial pressure of gas (atm)	Volumetric mass transfer rate coefficient (K_La, 1/d)
CH_4	0.0014	--	50 **
CO_2	0.035	--	
H_2O	--	0.0411	
N_2	6.1×10^{-4} *	--	
NH_3	56 *	--	

* Haynes (2011)

** Rittmann and McCarty (2001)

C.3 Modeling methodology and stoichiometric relationships

C.3.1 Switch and Inhibition Equations and Constants

Nitrite switch:

$$NO_2^{sw} = \frac{K_{NO_2}^{switch}}{K_{NO_2}^{switch} + C_{NO_2}} \quad \text{(Eqn. C.1)}$$

Nitrate switch:

$$NO_3^{sw} = \frac{K_{NO_3}^{switch}}{K_{NO_3}^{switch} + C_{NO_3}} \quad \text{(Eqn. C.2)}$$

NO_x switch:

$$NO_x^{sw} = NO_2^{switch} + NO_3^{switch} \quad \text{(Eqn. C.3)}$$

Dissolved oxygen (DO) switch:

$$DO^{sw} = \frac{K_{DO}^{switch}}{K_{DO}^{switch} + C_{O_2}} \quad \text{(Eqn. C.4)}$$

HCO_3^- inhibition:

$$CO_2^{inh} = \frac{C_{HCO3-}}{K_{HCO3-}^{inh} + C_{HCO3-}} \quad \text{(Eqn. C.5)}$$

NH_4^+ inhibition:

$$NH_4^{+\ inh} = \frac{C_{NH4+}}{K_{NH4+}^{inh} + C_{NH4+}} \quad \text{(Eqn. C.6)}$$

C.3.2 Determining the half-reactions and full reactions for electron donor and acceptors

Because of the intricacies of the different biomass-electron donor-electron acceptor relationships in this model, I established a basic set of half reaction equations to be combined together to determine the overall reaction stoichiometry based on the method described in Rittmann and McCarty (2001). I first determined the half-reaction stoichiometry for the compound $C_aH_bO_cN_d^f$ (where f is the charge of the molecule) based on the assumption that H_2O, HCO_3^-, H^+, and electrons (e^-) as well as a nitrogen source

(NH_4^+, NO_3^-, or NO_2^-) can be combined stoichiometrically to form any electron donor or acceptor. For NH_4^+ as the nitrogen source, the half-reaction is

$$\frac{1}{\beta}C_aH_bO_cN_d^f \rightarrow \frac{a}{\beta}HCO_3^- + \frac{d}{\beta}NH_4^+ + \frac{\lambda}{\beta}H_2O + \frac{\alpha}{\beta}H^+ + e^- \quad \text{(Eqn. C.7)}$$

where

$$\lambda = c - 3a \quad \text{(Eqn. C.8)}$$

$$\alpha = b - 2\lambda - a - 4d \quad \text{(Eqn. C.9)}$$

$$\beta = d + \alpha - a - f \quad \text{(Eqn. C.10)}$$

For NO_2^- as the nitrogen source, the half-reaction becomes

$$\frac{1}{\beta}C_aH_bO_cN_d^f \rightarrow \frac{a}{\beta}HCO_3^- + \frac{d}{\beta}NO_2^- + \frac{\lambda}{\beta}H_2O + \frac{\alpha}{\beta}H^+ + e^- \quad \text{(Eqn. C.11)}$$

$$\lambda = c - 3a - 2d \quad \text{(Eqn. C.12)}$$

$$\alpha = b - 2\lambda - a \quad \text{(Eqn. C.13)}$$

$$\beta = \alpha - a - d - f \quad \text{(Eqn. C.14)}$$

For NO_3^- as the nitrogen source, the half-reaction becomes

$$\frac{1}{\beta}C_aH_bO_cN_d^f \rightarrow \frac{a}{\beta}HCO_3^- + \frac{d}{\beta}NO_3^- + \frac{\lambda}{\beta}H_2O + \frac{\alpha}{\beta}H^+ + e^- \quad \text{(Eqn. C.15)}$$

$$\lambda = c - 3a - 3d \quad \text{(Eqn. C.16)}$$

$$\alpha = b - 2\lambda - a \quad \text{(Eqn. C.17)}$$

$$\beta = \alpha - a - d - f \quad \text{(Eqn. C.18)}$$

The half-reactions are combined together to describe an overall reaction rate for growth, R^t, using the general equation

$$R^t = f_e R_a + f_s R_c - R_d \quad \text{(Eqn. C.19)}$$

where f_s and f_e are the fraction of electrons from the donor that are used for cell synthesis and cell energy, respectively, R_a is the electron acceptor half-reaction, R_c is the cell synthesis half-reaction, and R_d is the electron donor half-reaction. The fraction of electrons must add to one, i.e.,

$$1 = f_e + f_s \quad \text{(Eqn. C.20)}$$

For example, using domestic wastewater ($C_{10}H_{19}O_3N$) as the electron donor for fermentation of domestic wastewater to acetate and the f_s values from Table C.1, the overall reaction is

f_eR_a: $$f_e\left[\frac{2}{8}HCO_3^- + \frac{9}{8}H^+ + e^- \rightarrow \frac{1}{8}CH_3COO^- + \frac{4}{8}H_2O\right] \quad \text{(Eqn. C.21)}$$

$+f_sR_c$: $$f_s\left[\frac{5}{20}HCO_3^- + \frac{1}{20}NH_4^+ + \frac{24}{20}H^+ + e^- \rightarrow \frac{1}{20}C_5H_7O_2N + \frac{13}{20}H_2O\right] \quad \text{(Eqn. C.22)}$$

$-R_d$: $$\frac{1}{50}C_{10}H_{19}O_3N + \frac{27}{50}H_2O \rightarrow \frac{10}{50}HCO_3^- + \frac{1}{50}NH_4^+ + \frac{59}{50}H^+ + e^- \quad \text{(Eqn. C.23)}$$

R^t: $$0.02C_{10}H_{19}O_3N + 0.05HCO_3^- + 0.013H_2O \rightarrow 0.1025CH_3COO^- + 0.011NH_4^+ + 0.0415H^+ \quad \text{(Eqn. C.24)}$$

Similarly, the amount of electron donor that is used for primary respiration, EPS, and UAP formation can be expressed as:

$$R^t_{total} = (1-k_{UAP}-k_{EPS})R^t_{primary} + k_{EPS}R^t_{EPS} + k_{UAP}R^t_{UAP} \quad \text{(Eqn. C.25)}$$

Using the modeling parameters summarized in this chapter, Table C.3 describes the overall reaction stoichiometry for each utilization rate equation.

Table C.3. Stoichiometry matrix for MYAnode bulk liquid reactions

	Heterotrophs	AOB	NOB	Fermenters	Acetoclastic methanogens	Utilization rate equation
Chemical formula	$C_5H_7O_2N$	$C_5H_7O_2N$	$C_5H_7O_2N$	$C_5H_7O_2N$	$C_5H_7O_2N$	
Symbol	X_h	X_{AOB}	X_{NOB}	X_f	X_m	r_{ut}
1	1.1550					Heterotrophic aerobic utilization of domestic wastewater with NH_4^+: $\hat{q}_S^h X_h \left(\frac{C_S}{C_S + K_S^h}\right)\left(\frac{C_{DO}}{C_{DO} + K_{DO}^h}\right)\left(\mathrm{NH_4^{+inh}}\right)$
2	0.7692					Heterotrophic aerobic utilization of domestic wastewater with NO_3^-: $\hat{q}_S^h X_h \left(\frac{C_S}{C_S + K_S^h}\right)\left(\frac{C_{NO3}}{C_{NO3} + K_{NO3}^h}\right)(\mathrm{DO^{sw}})$
3	0.8070					Heterotrophic aerobic utilization of domestic wastewater with NO_2^-: $\hat{q}_S^h X_h \left(\frac{C_S}{C_S + K_S^h}\right)\left(\frac{C_{NO2}}{C_{NO2} + K_{NO2}^h}\right)(\mathrm{DO^{sw}})$
4	-0.0500					Heterotrophic biomass hydrolysis: $k_{hyd} X_h (\mathrm{DO^{sw}})(NO_x^{sw})$
5				0.3465		Fermenters utilization of domestic wastewater with NH_4^+: $\hat{q}_S^f X_f \left(\frac{C_S}{C_S + K_S^f}\right)(\mathrm{DO^{sw}})(NO_x^{sw})\left(\mathrm{CO_2^{inh}}\right) I_f^{pH}$

Table C.3 continued. Stoichiometry matrix for MYAnode bulk liquid reactions

	Heterotrophs	AOB	NOB	Fermenters	Acetoclastic methanogens	Utilization rate equation
Chemical formula	$C_5H_7O_2N$	$C_5H_7O_2N$	$C_5H_7O_2N$	$C_5H_7O_2N$	$C_5H_7O_2N$	
Symbol	X_h	X_{AOB}	X_{NOB}	X_f	X_m	r_{ut}
6			0.0059			NOB utilization of NO_2^-: $\hat{q}^{NOB} X_{NOB} \left(\frac{C_{NO2}}{C_{NO2} + K_{NO2}^{NOB}}\right)\left(\frac{C_{DO}}{C_{DO} + K_{DO}^{NOB}}\right) \mathrm{CO}_2^{\mathrm{inh}}$
7		0.0298				AOB utilization of NH_4^+: $\hat{q}^{AOB} X_{AOB} \left(\frac{C_{NH4}}{C_{NH4} + K_{NH4}^{NOB}}\right)\left(\frac{C_{DO}}{C_{DO} + K_{DO}^{AOB}}\right) \mathrm{CO}_2^{\mathrm{inh}}$
8	0.1848					Heterotrophic aerobic utilization of acetate with NH_4^+: $\hat{q}_{ace}^{h} X_h \left(\frac{C_{ace}}{C_{ace} + K_{ace}^{h}}\right)\left(\frac{C_{DO}}{C_{DO} + K_{DO}^{h}}\right) \left(\mathrm{NH}_4^{+\mathrm{inh}}\right)$
9	0.1100					Heterotrophic aerobic utilization of domestic wastewater with NO_3^-: $\hat{q}_{ace}^{h} X_h \left(\frac{C_{ace}}{C_{ace} + K_{ace}^{h}}\right)\left(\frac{C_{NO3}}{C_{NO3} + K_{NO3}^{h}}\right) (\mathrm{DO}^{\mathrm{sw}})$
10	0.1185					Heterotrophic aerobic utilization of domestic wastewater with NO_2^-: $\hat{q}_{ace}^{h} X_h \left(\frac{C_{ace}}{C_{ace} + K_{ace}^{h}}\right)\left(\frac{C_{NO2}}{C_{NO2} + K_{NO2}^{h}}\right) (\mathrm{DO}^{\mathrm{sw}})$

186

Table C.3 continued. Stoichiometry matrix for MYAnode bulk liquid reactions

	Heterotrophs	AOB	NOB	Fermenters	Acetoclastic methanogens	Utilization rate equation
Chemical formula	$C_5H_7O_2N$	$C_5H_7O_2N$	$C_5H_7O_2N$	$C_5H_7O_2N$	$C_5H_7O_2N$	
Symbol	X_h	X_{AOB}	X_{NOB}	X_f	X_m	r_{ut}
11					0.0154	Methanogens utilization of acetate: $\hat{q}^m X_m \left(\frac{C_{ace}}{C_{ace}+K^m}\right)(\mathrm{DO^{sw}})(NO_x^{sw})\left(\mathrm{NH_4^{+inh}}\right)I_m^{pH}$
12	0.6886					Heterotrophic aerobic utilization of UAP with NH_4^+: $\hat{q}_{UAP}^h X_h \left(\frac{C_{UAP}}{C_{UAP}+K_{UAP}^h}\right)\left(\frac{C_{DO}}{C_{DO}+K_{DO}^h}\right)\left(\mathrm{NH_4^{+inh}}\right)$
13	0.4918					Heterotrophic aerobic utilization of UAP with NO_3^-: $\hat{q}_{UAP}^h X_h \left(\frac{C_{UAP}}{C_{UAP}+K_{UAP}^h}\right)\left(\frac{C_{NO3}}{C_{NO3}+K_{NO3}^h}\right)(\mathrm{DO^{sw}})$
14	0.5300					Heterotrophic aerobic utilization of UAP with NO_2^-: $\hat{q}_{UAP}^h X_h \left(\frac{C_{UAP}}{C_{UAP}+K_{UAP}^h}\right)\left(\frac{C_{NO2}}{C_{NO2}+K_{NO2}^h}\right)(\mathrm{DO^{sw}})$
15				0.6889		Fermenters utilization of UAP with NH_4^+: $\hat{q}_{UAP}^f X_f \left(\frac{C_{UAP}}{C_{UAP}+K_{UAP}^f}\right)(\mathrm{DO^{sw}})(NO_x^{sw})\left(\mathrm{CO_2^{inh}}\right)I_f^{pH}$

187

Table C.3 continued. Stoichiometry matrix for MYAnode bulk liquid reactions

	Heterotrophs	AOB	NOB	Fermenters	Acetoclastic methanogens	Utilization rate equation
Chemical formula	$C_5H_7O_2N$	$C_5H_7O_2N$	$C_5H_7O_2N$	$C_5H_7O_2N$	$C_5H_7O_2N$	
Symbol	X_h	X_{AOB}	X_{NOB}	X_f	X_m	r_{ut}
16	0.4620					Heterotrophic aerobic utilization of BAP with NH_4^+: $\hat{q}^h_{BAP} X_h \left(\frac{C_{BAP}}{C_{BAP} + K^h_{UAP}}\right)\left(\frac{C_{DO}}{C_{DO} + K^h_{DO}}\right)\left(\mathrm{NH_4^{+inh}}\right)$
17	0.3526					Heterotrophic aerobic utilization of BAP with NO_3^-: $\hat{q}^h_{BAP} X_h \left(\frac{C_{BAP}}{C_{BAP} + K^h_{UAP}}\right)\left(\frac{C_{NO3}}{C_{NO3} + K^h_{NO3}}\right)(\mathrm{DO^{sw}})$
18	0.3601					Heterotrophic aerobic utilization of BAP with NO_2^-: $\hat{q}^h_{BAP} X_h \left(\frac{C_{BAP}}{C_{BAP} + K^h_{UAP}}\right)\left(\frac{C_{NO2}}{C_{NO2} + K^h_{NO2}}\right)(\mathrm{DO^{sw}})$
19				0.1386		Fermenters utilization of BAP with NH_4^+: $\hat{q}^f_{BAP} X_f \left(\frac{C_{BAP}}{C_{BAP} + K^f_{BAP}}\right)(\mathrm{DO^{sw}})(NO_x^{sw})\left(\mathrm{CO_2^{inh}}\right) I_f^p$
20						PCOD hydrolysis: $k_{hyd} X_{PCOD}$
21	-0.0500					Heterotrophic aerobic endogenous decay: $b_h X_h \left(\frac{C_{DO}}{C_{DO} + K^h_{DO}}\right)$

188

Table C.3 continued. Stoichiometry matrix for MYAnode bulk liquid reactions

	Heterotrophs	AOB	NOB	Fermenters	Acetoclastic methanogens	Utilization rate equation
Chemical formula	$C_5H_7O_2N$	$C_5H_7O_2N$	$C_5H_7O_2N$	$C_5H_7O_2N$	$C_5H_7O_2N$	
Symbol	X_h	X_{AOB}	X_{NOB}	X_f	X_m	r_{ut}
22	-0.0500					Heterotrophic anoxic endogenous decay with NO_3^-: $b_h X_h \left(\frac{C_{NO3}}{C_{NO3} + K_{NO3}^h}\right)$
23	-0.0500					Heterotrophic anoxic endogenous decay with NO_2^-: $b_h X_h \left(\frac{C_{NO2}}{C_{NO2} + K_{NO2}^h}\right)$
24		-0.0500				AOB endogenous decay: $b_{AOB} X_{AOB} \left(\frac{C_{DO}}{C_{DO} + K_{DO}^h}\right)$
25			-0.0500			NOB endogenous decay: $b_{NOB} X_{NOB} \left(\frac{C_{DO}}{C_{DO} + K_{DO}^h}\right)$
26				-0.0500		Fermenters endogenous decay: $b_f X_f (\mathrm{DO}^{\mathrm{sw}})(NO_x^{sw})(\mathrm{CO}_2^{\mathrm{inh}})$
27					-0.0500	Methanogens endogenous decay: $b_m X_m (\mathrm{DO}^{\mathrm{sw}})(NO_x^{sw})$
28						EPS hydrolysis: $k_{hydEPS} X_{EPS}$

189

Table C.3 continued. Stoichiometry matrix for MYAnode bulk liquid reactions

	Heterotrophs	AOB	NOB	Fermenters	Acetoclastic methanogens	Utilization rate equation
Chemical formula	$C_5H_7O_2N$	$C_5H_7O_2N$	$C_5H_7O_2N$	$C_5H_7O_2N$	$C_5H_7O_2N$	
Symbol	X_h	X_{AOB}	X_{NOB}	X_f	X_m	r_{ut}
34		-0.05				AOB biomass hydrolysis: $k_{hyd}X_{AOB}(\mathrm{DO^{sw}})(NO_x^{sw})$
35			-0.05			NOB biomass hydrolysis: $k_{hyd}X_{NOB}(\mathrm{DO^{sw}})(NO_x^{sw})$
36						Gas/liquid phase partitioning of CH_4: $\left(\frac{V_l}{V_g}\right)K_La\left(C_{CH4}-H_{CH4}C_{CH4}^{g}RT\right)$
37						Gas/liquid phase partitioning of CO_2: $\left(\frac{V_l}{V_g}\right)K_La\left(C_{H2CO3}-H_{CO2}C_{CO2}^{g}RT\right)$
38						Gas/liquid phase partitioning of NH_3: $\left(\frac{V_l}{V_g}\right)K_La\left(C_{NH3}-H_{NH3}C_{NH3}^{g}RT\right)$
39						Gas/liquid phase partitioning of N_2: $\left(\frac{V_l}{V_g}\right)K_La\left(C_{N2}-H_{N2}C_{N2}^{g}RT\right)$

Species only present in chemical speciation calculations are omitted (i.e., $CO3_2^-$, HNO_2).

190

Table C.3 continued. Stoichiometry matrix for MYAnode bulk liquid reactions

	EPS	Inerts	PCOD	Domestic wastewater	Utilization rate equation
Chemical formula	$C_5H_7O_2N$	$C_5H_7O_2N$	$C_{10}H_{19}O_3N$	$C_{10}H_{19}O_3N$	
Symbol	X_{EPS}	X_I	X_{PCOD}	C_S	r_{ut}
1	0.45			-1	Heterotrophic aerobic utilization of domestic wastewater with NH_4^+: $\hat{q}_S^h X_h \left(\frac{C_S}{C_S + K_S^h}\right)\left(\frac{C_{DO}}{C_{DO} + K_{DO}^h}\right)\left(\mathrm{NH_4^{+inh}}\right)$
2	0.5035			-1	Heterotrophic aerobic utilization of domestic wastewater with NO_3^-: $\hat{q}_S^h X_h \left(\frac{C_S}{C_S + K_S^h}\right)\left(\frac{C_{NO3}}{C_{NO3} + K_{NO3}^h}\right)(\mathrm{DO^{sw}})$
3	0.4905			-1	Heterotrophic aerobic utilization of domestic wastewater with NO_2^-: $\hat{q}_S^h X_h \left(\frac{C_S}{C_S + K_S^h}\right)\left(\frac{C_{NO2}}{C_{NO2} + K_{NO2}^h}\right)(\mathrm{DO^{sw}})$
4				0.0200	Heterotrophic biomass hydrolysis: $k_{hyd} X_h (\mathrm{DO^{sw}})(NO_x^{sw})$
5	0.4500			-1	Fermenters utilization of domestic wastewater with NH_4^+: $\hat{q}_S^f X_f \left(\frac{C_S}{C_S + K_S^f}\right)(\mathrm{DO^{sw}})(NO_x^{sw})\left(\mathrm{CO_2^{inh}}\right) I_f^{pH}$
6	0.0179				NOB utilization of NO_2^-: $\hat{q}^{NOB} X_{NOB} \left(\frac{C_{NO2}}{C_{NO2} + K_{NO2}^{NOB}}\right)\left(\frac{C_{DO}}{C_{DO} + K_{DO}^{NOB}}\right)\mathrm{CO_2^{inh}}$

191

Table C.3 continued. Stoichiometry matrix for MYAnode bulk liquid reactions

	EPS	Inerts	PCOD	Domestic wastewater	Utilization rate equation
Chemical formula	$C_5H_7O_2N$	$C_5H_7O_2N$	$C_{10}H_{19}O_3N$	$C_{10}H_{19}O_3N$	
Symbol	X_{EPS}	X_I	X_{PCOD}	C_S	r_{ut}
7	0.0497				AOB utilization of NH_4^+: $\hat{q}^{AOB} X_{AOB} \left(\frac{C_{NH4}}{C_{NH4} + K_{NH4}^{NOB}}\right)\left(\frac{C_{DO}}{C_{DO} + K_{DO}^{AOB}}\right) \mathrm{CO}_2^{\mathrm{inh}}$
8	0.0720				Heterotrophic aerobic utilization of acetate with NH_4^+: $\hat{q}_{ace}^{h} X_h \left(\frac{C_{ace}}{C_{ace} + K_{ace}^{h}}\right)\left(\frac{C_{DO}}{C_{DO} + K_{DO}^{h}}\right)\left(\mathrm{NH}_4^{+\mathrm{inh}}\right)$
9	0.0720				Heterotrophic aerobic utilization of domestic wastewater with NO_3^-: $\hat{q}_{ace}^{h} X_h \left(\frac{C_{ace}}{C_{ace} + K_{ace}^{h}}\right)\left(\frac{C_{NO3}}{C_{NO3} + K_{NO3}^{h}}\right)(\mathrm{DO}^{\mathrm{sw}})$
10	0.0720				Heterotrophic aerobic utilization of domestic wastewater with NO_2^-: $\hat{q}_{ace}^{h} X_h \left(\frac{C_{ace}}{C_{ace} + K_{ace}^{h}}\right)\left(\frac{C_{NO2}}{C_{NO2} + K_{NO2}^{h}}\right)(\mathrm{DO}^{\mathrm{sw}})$
11	0.0720				Methanogens utilization of acetate: $\hat{q}^{m} X_m \left(\frac{C_{ace}}{C_{ace} + K^{m}}\right)(\mathrm{DO}^{\mathrm{sw}})(NO_x^{sw})\left(\mathrm{NH}_4^{+\mathrm{inh}}\right) I_m^{pH}$
12	0.2274				Heterotrophic aerobic utilization of UAP with NH_4^+: $\hat{q}_{UAP}^{h} X_h \left(\frac{C_{UAP}}{C_{UAP} + K_{UAP}^{h}}\right)\left(\frac{C_{DO}}{C_{DO} + K_{DO}^{h}}\right)\left(\mathrm{NH}_4^{+\mathrm{inh}}\right)$

192

Table C.3 continued. Stoichiometry matrix for MYAnode bulk liquid reactions

	EPS	Inerts	PCOD	Domestic wastewater	Utilization rate equation
Chemical formula	$C_5H_7O_2N$	$C_5H_7O_2N$	$C_{10}H_{19}O_3N$	$C_{10}H_{19}O_3N$	
Symbol	X_{EPS}	X_I	X_{PCOD}	C_S	r_{ut}
13	0.2274				Heterotrophic aerobic utilization of UAP with NO_3^-: $\hat{q}^h_{UAP} X_h \left(\frac{C_{UAP}}{C_{UAP}+K^h_{UAP}}\right)\left(\frac{C_{NO3}}{C_{NO3}+K^h_{NO3}}\right)(\mathrm{DO^{sw}})$
14	0.2274				Heterotrophic aerobic utilization of UAP with NO_2^-: $\hat{q}^h_{UAP} X_h \left(\frac{C_{UAP}}{C_{UAP}+K^h_{UAP}}\right)\left(\frac{C_{NO2}}{C_{NO2}+K^h_{NO2}}\right)(\mathrm{DO^{sw}})$
15	0.2274				Fermenters utilization of UAP with NH_4^+: $\hat{q}^f_{UAP} X_f \left(\frac{C_{UAP}}{C_{UAP}+K^f_{UAP}}\right)(\mathrm{DO^{sw}})(NO_x^{sw})\left(\mathrm{CO_2^{inh}}\right) I_f^{pH}$
16	0.1800				Heterotrophic aerobic utilization of BAP with NH_4^+: $\hat{q}^h_{BAP} X_h \left(\frac{C_{BAP}}{C_{BAP}+K^h_{UAP}}\right)\left(\frac{C_{DO}}{C_{DO}+K^h_{DO}}\right)\left(\mathrm{NH_4^{+inh}}\right)$
17	0.2308				Heterotrophic aerobic utilization of BAP with NO_3^-: $\hat{q}^h_{BAP} X_h \left(\frac{C_{BAP}}{C_{BAP}+K^h_{UAP}}\right)\left(\frac{C_{NO3}}{C_{NO3}+K^h_{NO3}}\right)(\mathrm{DO^{sw}})$
18	0.2189				Heterotrophic aerobic utilization of BAP with NO_2^-: $\hat{q}^h_{BAP} X_h \left(\frac{C_{BAP}}{C_{BAP}+K^h_{UAP}}\right)\left(\frac{C_{NO2}}{C_{NO2}+K^h_{NO2}}\right)(\mathrm{DO^{sw}})$
19	0.1800				Fermenters utilization of BAP with NH_4^+: $\hat{q}^f_{BAP} X_f \left(\frac{C_{BAP}}{C_{BAP}+K^f_{BAP}}\right)(\mathrm{DO^{sw}})(NO_x^{sw})\left(\mathrm{CO_2^{inh}}\right) I_f^{pH}$

193

Table C.3 continued. Stoichiometry matrix for MYAnode bulk liquid reactions

	EPS	Inerts	PCOD	Domestic wastewater	Utilization rate equation
Chemical formula	$C_5H_7O_2N$	$C_5H_7O_2N$	$C_{10}H_{19}O_3N$	$C_{10}H_{19}O_3N$	
Symbol	X_{EPS}	X_I	X_{PCOD}	C_S	r_{ut}
20			-1	1	PCOD hydrolysis: $k_{hyd}X_{PCOD}$
21		0.0100			Heterotrophic aerobic endogenous decay: $b_hX_h\left(\frac{C_{DO}}{C_{DO}+K_{DO}^h}\right)$
22		0.0100			Heterotrophic anoxic endogenous decay with NO_3^-: $b_hX_h\left(\frac{C_{NO3}}{C_{NO3}+K_{NO3}^h}\right)$
23		0.0100			Heterotrophic anoxic endogenous decay with NO_2^-: $b_hX_h\left(\frac{C_{NO2}}{C_{NO2}+K_{NO2}^h}\right)$
24		0.0100			AOB endogenous decay: $b_{AOB}X_{AOB}\left(\frac{C_{DO}}{C_{DO}+K_{DO}^h}\right)$
25		0.0100			NOB endogenous decay: $b_{NOB}X_{NOB}\left(\frac{C_{DO}}{C_{DO}+K_{DO}^h}\right)$
26		0.0100			Fermenters endogenous decay: $b_fX_f(\mathrm{DO^{sw}})(NO_x^{sw})(\mathrm{CO_2^{inh}})$
27		0.0100			Methanogens endogenous decay: $b_mX_m(\mathrm{DO^{sw}})(NO_x^{sw})$

194

Table C.3 continued. Stoichiometry matrix for MYAnode bulk liquid reactions

	EPS	Inerts	PCOD	Domestic wastewater	Utilization rate equation
Chemical formula	$C_5H_7O_2N$	$C_5H_7O_2N$	$C_{10}H_{19}O_3N$	$C_{10}H_{19}O_3N$	
Symbol	X_{EPS}	X_I	X_{PCOD}	C_S	r_{ut}
28	-1				EPS hydrolysis: $k_{hydEPS}X_{EPS}$
29				0.0200	AOB biomass hydrolysis: $k_{hyd}X_{AOB}(\mathrm{DO^{sw}})(NO_x^{sw})$
30				0.0200	NOB biomass hydrolysis: $k_{hyd}X_{NOB}(\mathrm{DO^{sw}})(NO_x^{sw})$
31					Gas/liquid phase partitioning of CH_4: $\left(\frac{V_l}{V_g}\right)K_La\left(C_{CH4}-H_{CH4}C_{CH4}^{g}RT\right)$
32					Gas/liquid phase partitioning of CO_2: $\left(\frac{V_l}{V_g}\right)K_La\left(C_{H2CO3}-H_{CO2}C_{CO2}^{g}RT\right)$
33					Gas/liquid phase partitioning of NH_3: $\left(\frac{V_l}{V_g}\right)K_La\left(C_{NH3}-H_{NH3}C_{NH3}^{g}RT\right)$
34					Gas/liquid phase partitioning of N_2: $\left(\frac{V_l}{V_g}\right)K_La\left(C_{N2}-H_{N2}C_{N2}^{g}RT\right)$

Species only present in chemical speciation calculations are omitted (i.e., $CO3_2^-$, HNO_2).

195

Table C.3 continued. Stoichiometry matrix for MYAnode bulk liquid reactions.

	UAP	BAP	Acetate	Acetic acid	Carbonic acid	Utilization rate equation
Chemical formula	$C_6H_{12}O_6$	$C_5H_7O_2N$	CH_3COO^-	CH_3COOH	H_2CO_3	
Symbol	C_{UAP}	C_{BAP}	C_{ace}	C_{Hace}	C_{H2CO3}	r_{ut}
1	0.1042	0	0	0	0	Heterotrophic aerobic utilization of domestic wastewater with NH_4^+: $\hat{q}_S^h X_h \left(\frac{C_S}{C_S + K_S^h}\right)\left(\frac{C_{DO}}{C_{DO} + K_{DO}^h}\right)\left(\mathrm{NH_4^{+inh}}\right)$
2	0.1165	0	0	0	0	Heterotrophic aerobic utilization of domestic wastewater with NO_3^-: $\hat{q}_S^h X_h \left(\frac{C_S}{C_S + K_S^h}\right)\left(\frac{C_{NO3}}{C_{NO3} + K_{NO3}^h}\right)(\mathrm{DO^{sw}})$
3	0.1135	0	0	0	0	Heterotrophic aerobic utilization of domestic wastewater with NO_2^-: $\hat{q}_S^h X_h \left(\frac{C_S}{C_S + K_S^h}\right)\left(\frac{C_{NO2}}{C_{NO2} + K_{NO2}^h}\right)(\mathrm{DO^{sw}})$
4	0	0	0	0	0	Heterotrophic biomass hydrolysis: $k_{hyd} X_h (\mathrm{DO^{sw}})(NO_x^{sw})$
5	0.1042	0	3.946	0	0	Fermenters utilization of domestic wastewater with NH_4^+: $\hat{q}_S^f X_f \left(\frac{C_S}{C_S + K_S^f}\right)(\mathrm{DO^{sw}})(NO_x^{sw})\left(\mathrm{CO_2^{inh}}\right) I_f^{pH}$
6	0.0041	0	0	0	0	NOB utilization of NO_2^-: $\hat{q}^{NOB} X_{NOB} \left(\frac{C_{NO2}}{C_{NO2} + K_{NO2}^{NOB}}\right)\left(\frac{C_{DO}}{C_{DO} + K_{DO}^{NOB}}\right)\mathrm{CO_2^{inh}}$

196

Table C.3 continued. Stoichiometry matrix for MYAnode bulk liquid reactions.

	UAP	BAP	Acetate	Acetic acid	Carbonic acid	Utilization rate equation
Chemical formula	$C_6H_{12}O_6$	$C_5H_7O_2N$	CH_3COO^-	CH_3COOH	H_2CO_3	
Symbol	C_{UAP}	C_{BAP}	C_{ace}	C_{Hace}	C_{H2CO3}	r_{ut}
7	0.0115	0	0	0	0	AOB utilization of NH_4^+: $\hat{q}^{AOB} X_{AOB} \left(\frac{C_{NH4}}{C_{NH4} + K_{NH4}^{NOB}}\right)\left(\frac{C_{DO}}{C_{DO} + K_{DO}^{AOB}}\right) \mathrm{CO}_2^{\mathrm{inh}}$
8	0.0167	0	-1	0	0	Heterotrophic aerobic utilization of acetate with NH_4^+: $\hat{q}_{ace}^{h} X_h \left(\frac{C_{ace}}{C_{ace} + K_{ace}^{h}}\right)\left(\frac{C_{DO}}{C_{DO} + K_{DO}^{h}}\right)\left(\mathrm{NH}_4^{+\mathrm{inh}}\right)$
9	0.0167	0	-1	0	0	Heterotrophic aerobic utilization of domestic wastewater with NO_3^-: $\hat{q}_{ace}^{h} X_h \left(\frac{C_{ace}}{C_{ace} + K_{ace}^{h}}\right)\left(\frac{C_{NO3}}{C_{NO3} + K_{NO3}^{h}}\right)(\mathrm{DO}^{\mathrm{sw}})$
10	0.0167	0	-1	0	0	Heterotrophic aerobic utilization of domestic wastewater with NO_2^-: $\hat{q}_{ace}^{h} X_h \left(\frac{C_{ace}}{C_{ace} + K_{ace}^{h}}\right)\left(\frac{C_{NO2}}{C_{NO2} + K_{NO2}^{h}}\right)(\mathrm{DO}^{\mathrm{sw}})$
11	0.0167	0	-1	0	0	Methanogens utilization of acetate: $\hat{q}^{m} X_m \left(\frac{C_{ace}}{C_{ace} + K^{m}}\right)(\mathrm{DO}^{\mathrm{sw}})(NO_x^{sw})\left(\mathrm{NH}_4^{+\mathrm{inh}}\right) I_m^{pH}$
12	-1	0	0	0	0	Heterotrophic aerobic utilization of UAP with NH_4^+: $\hat{q}_{UAP}^{h} X_h \left(\frac{C_{UAP}}{C_{UAP} + K_{UAP}^{h}}\right)\left(\frac{C_{DO}}{C_{DO} + K_{DO}^{h}}\right)\left(\mathrm{NH}_4^{+\mathrm{inh}}\right)$

197

Table C.3 continued. Stoichiometry matrix for MYAnode bulk liquid reactions.

	UAP	BAP	Acetate	Acetic acid	Carbonic acid	Utilization rate equation
Chemical formula	$C_6H_{12}O_6$	$C_5H_7O_2N$	CH_3COO^-	CH_3COOH	H_2CO_3	
Symbol	C_{UAP}	C_{BAP}	C_{ace}	C_{Hace}	C_{H2CO3}	r_{ut}
13	-1					Heterotrophic aerobic utilization of UAP with NO_3^-: $\hat{q}^h_{UAP} X_h \left(\frac{C_{UAP}}{C_{UAP}+K^h_{UAP}}\right)\left(\frac{C_{NO3}}{C_{NO3}+K^h_{NO3}}\right)(\mathrm{DO^{sw}})$
14	-1					Heterotrophic aerobic utilization of UAP with NO_2^-: $\hat{q}^h_{UAP} X_h \left(\frac{C_{UAP}}{C_{UAP}+K^h_{UAP}}\right)\left(\frac{C_{NO2}}{C_{NO2}+K^h_{NO2}}\right)(\mathrm{DO^{sw}})$
15	-1		0.7101			Fermenters utilization of UAP with NH_4^+: $\hat{q}^f_{UAP} X_f \left(\frac{C_{UAP}}{C_{UAP}+K^f_{UAP}}\right)(\mathrm{DO^{sw}})(NO_x^{sw})\left(\mathrm{CO_2^{inh}}\right) I_f^{pH}$
16	0.0417	-1				Heterotrophic aerobic utilization of BAP with NH_4^+: $\hat{q}^h_{BAP} X_h \left(\frac{C_{BAP}}{C_{BAP}+K^h_{UAP}}\right)\left(\frac{C_{DO}}{C_{DO}+K^h_{DO}}\right)\left(\mathrm{NH_4^{+inh}}\right)$
17	0.0534	-1				Heterotrophic aerobic utilization of BAP with NO_3^-: $\hat{q}^h_{BAP} X_h \left(\frac{C_{BAP}}{C_{BAP}+K^h_{UAP}}\right)\left(\frac{C_{NO3}}{C_{NO3}+K^h_{NO3}}\right)(\mathrm{DO^{sw}})$
18	0.0507	-1				Heterotrophic aerobic utilization of BAP with NO_2^-: $\hat{q}^h_{BAP} X_h \left(\frac{C_{BAP}}{C_{BAP}+K^h_{UAP}}\right)\left(\frac{C_{NO2}}{C_{NO2}+K^h_{NO2}}\right)(\mathrm{DO^{sw}})$
19	0.0417	-1	1.5785			Fermenters utilization of BAP with NH_4^+: $\hat{q}^f_{BAP} X_f \left(\frac{C_{BAP}}{C_{BAP}+K^f_{BAP}}\right)(\mathrm{DO^{sw}})(NO_x^{sw})\left(\mathrm{CO_2^{inh}}\right) I_f^{pH}$

198

Table C.3 continued. Stoichiometry matrix for MYAnode bulk liquid reactions.

	UAP	BAP	Acetate	Acetic acid	Carbonic acid	Utilization rate equation
Chemical formula	$C_6H_{12}O_6$	$C_5H_7O_2N$	CH_3COO^-	CH_3COOH	H_2CO_3	
Symbol	C_{UAP}	C_{BAP}	C_{ace}	C_{Hace}	C_{H2CO3}	r_{ut}
20						PCOD hydrolysis: $k_{hyd}X_{PCOD}$
21						Heterotrophic aerobic endogenous decay: $b_hX_h\left(\frac{C_{DO}}{C_{DO}+K_{DO}^h}\right)$
22						Heterotrophic anoxic endogenous decay with NO_3^-: $b_hX_h\left(\frac{C_{NO3}}{C_{NO3}+K_{NO3}^h}\right)$
23						Heterotrophic anoxic endogenous decay with NO_2^-: $b_hX_h\left(\frac{C_{NO2}}{C_{NO2}+K_{NO2}^h}\right)$
24						AOB endogenous decay: $b_{AOB}X_{AOB}\left(\frac{C_{DO}}{C_{DO}+K_{DO}^h}\right)$
25						NOB endogenous decay: $b_{NOB}X_{NOB}\left(\frac{C_{DO}}{C_{DO}+K_{DO}^h}\right)$
26			0.1			Fermenters endogenous decay: $b_fX_f(\mathrm{DO^{sw}})(NO_x^{sw})(\mathrm{CO_2^{inh}})$
27						Methanogens endogenous decay: $b_mX_m(\mathrm{DO^{sw}})(NO_x^{sw})$

199

Table C.3 continued. Stoichiometry matrix for MYAnode bulk liquid reactions.

	UAP	BAP	Acetate	Acetic acid	Carbonic acid	Utilization rate equation
Chemical formula	$C_6H_{12}O_6$	$C_5H_7O_2N$	CH_3COO^-	CH_3COOH	H_2CO_3	
Symbol	C_{UAP}	C_{BAP}	C_{ace}	C_{Hace}	C_{H2CO3}	r_{ut}
28		1				EPS hydrolysis: $k_{hydEPS}X_{EPS}$
29						AOB biomass hydrolysis: $k_{hyd}X_{AOB}(\mathrm{DO^{sw}})(NO_x^{sw})$
30						NOB biomass hydrolysis: $k_{hyd}X_{NOB}(\mathrm{DO^{sw}})(NO_x^{sw})$
31						Gas/liquid phase partitioning of CH_4: $\left(\frac{V_l}{V_g}\right)K_La\left(C_{CH4}-H_{CH4}C_{CH4}^{g}RT\right)$
32					-1	Gas/liquid phase partitioning of CO_2: $\left(\frac{V_l}{V_g}\right)K_La\left(C_{H2CO3}-H_{CO2}C_{CO2}^{g}RT\right)$
33						Gas/liquid phase partitioning of NH_3: $\left(\frac{V_l}{V_g}\right)K_La\left(C_{NH3}-H_{NH3}C_{NH3}^{g}RT\right)$
34						Gas/liquid phase partitioning of N_2: $\left(\frac{V_l}{V_g}\right)K_La\left(C_{N2}-H_{N2}C_{N2}^{g}RT\right)$

200

Table C.3 continued. Stoichiometry matrix for MYAnode bulk liquid reactions.

	Bicarbonate	Nitrite	Nitrate	Ammonium	Ammonia (liquid)	Utilization rate equation
Chemical formula	HCO_3^-	NO_2^-	NO_3^-	NH_4^+	NH_3	
Symbol	C_{HCO3}	C_{NO2}	C_{NO3}	C_{NH4}	C_{NH3}	r_{ut}
1	1.35			-0.6050		Heterotrophic aerobic utilization of domestic wastewater with NH_4^+: $\hat{q}_S^h X_h \left(\frac{C_S}{C_S + K_S^h}\right)\left(\frac{C_{DO}}{C_{DO} + K_{DO}^h}\right)\left(\mathrm{NH_4^{+inh}}\right)$
2	2.9374		-4.3340	-0.2461		Heterotrophic aerobic utilization of domestic wastewater with NO_3^-: $\hat{q}_S^h X_h \left(\frac{C_S}{C_S + K_S^h}\right)\left(\frac{C_{NO3}}{C_{NO3} + K_{NO3}^h}\right)(\mathrm{DO^{sw}})$
3	2.8317	-7.0513		-0.2398		Heterotrophic aerobic utilization of domestic wastewater with NO_2^-: $\hat{q}_S^h X_h \left(\frac{C_S}{C_S + K_S^h}\right)\left(\frac{C_{NO2}}{C_{NO2} + K_{NO2}^h}\right)(\mathrm{DO^{sw}})$
4	0.0500			0.03		Heterotrophic biomass hydrolysis: $k_{hyd} X_h (\mathrm{DO^{sw}})(NO_x^{sw})$
5	-2.5000			0.2035		Fermenters utilization of domestic wastewater with NH_4^+: $\hat{q}_S^f X_f \left(\frac{C_S}{C_S + K_S^f}\right)(\mathrm{DO^{sw}})(NO_x^{sw})\left(\mathrm{CO_2^{inh}}\right) I_f^{pH}$
6	-0.1438	-1	0.9941	-0.0179		NOB utilization of NO_2^-: $\hat{q}^{NOB} X_{NOB} \left(\frac{C_{NO2}}{C_{NO2} + K_{NO2}^{NOB}}\right)\left(\frac{C_{DO}}{C_{DO} + K_{DO}^{NOB}}\right)\mathrm{CO_2^{inh}}$

201

Table C.3 continued. Stoichiometry matrix for MYAnode bulk liquid reactions.

	Bicarbonate	Nitrite	Nitrate	Ammonium	Ammonia (liquid)	Utilization rate equation
Chemical formula	HCO_3^-	NO_2^-	NO_3^-	NH_4^+	NH_3	
Symbol	C_{HCO3}	C_{NO2}	C_{NO3}	C_{NH4}	C_{NH3}	r_{ut}
7	-0.4664	0.9205		-1		AOB utilization of NH_4^+: $\hat{q}^{AOB} X_{AOB} \left(\frac{C_{NH4}}{C_{NH4} + K_{NH4}^{NOB}}\right)\left(\frac{C_{DO}}{C_{DO} + K_{DO}^{AOB}}\right) \mathrm{CO}_2^{\mathrm{inh}}$
8	0.6160			-0.2568		Heterotrophic aerobic utilization of acetate with NH_4^+: $\hat{q}_{ace}^{h} X_h \left(\frac{C_{ace}}{C_{ace} + K_{ace}^{h}}\right)\left(\frac{C_{DO}}{C_{DO} + K_{DO}^{h}}\right)\left(\mathrm{NH}_4^{+\mathrm{inh}}\right)$
9	0.9900		-0.726	-0.0720		Heterotrophic aerobic utilization of domestic wastewater with NO_3^-: $\hat{q}_{ace}^{h} X_h \left(\frac{C_{ace}}{C_{ace} + K_{ace}^{h}}\right)\left(\frac{C_{NO3}}{C_{NO3} + K_{NO3}^{h}}\right)(\mathrm{DO}^{\mathrm{sw}})$
10	0.9477	-1.1451		-0.0720		Heterotrophic aerobic utilization of domestic wastewater with NO_2^-: $\hat{q}_{ace}^{h} X_h \left(\frac{C_{ace}}{C_{ace} + K_{ace}^{h}}\right)\left(\frac{C_{NO2}}{C_{NO2} + K_{NO2}^{h}}\right)(\mathrm{DO}^{\mathrm{sw}})$
11	0.7315			-0.0874		Methanogens utilization of acetate: $\hat{q}^{m} X_m \left(\frac{C_{ace}}{C_{ace} + K^{m}}\right)(\mathrm{DO}^{\mathrm{sw}})(NO_x^{sw})\left(\mathrm{NH}_4^{+\mathrm{inh}}\right) I_m^{pH}$
12	1.4202			-0.9160		Heterotrophic aerobic utilization of UAP with NH_4^+: $\hat{q}_{UAP}^{h} X_h \left(\frac{C_{UAP}}{C_{UAP} + K_{UAP}^{h}}\right)\left(\frac{C_{DO}}{C_{DO} + K_{DO}^{h}}\right)\left(\mathrm{NH}_4^{+\mathrm{inh}}\right)$

202

Table C.3 continued. Stoichiometry matrix for MYAnode bulk liquid reactions.

	Bicarbonate	Nitrite	Nitrate	Ammonium	Ammonia (liquid)	Utilization rate equation
Chemical formula	HCO_3^-	NO_2^-	NO_3^-	NH_4^+	NH_3	
Symbol	C_{HCO3}	C_{NO2}	C_{NO3}	C_{NH4}	C_{NH3}	r_{ut}
13	2.4039		-1.6280	-0.2274		Heterotrophic aerobic utilization of UAP with NO_3^-: $\hat{q}^h_{UAP} X_h \left(\frac{C_{UAP}}{C_{UAP}+K^h_{UAP}}\right)\left(\frac{C_{NO3}}{C_{NO3}+K^h_{NO3}}\right)(\mathrm{DO^{sw}})$
14	2.2147	-2.4233		-0.2274		Heterotrophic aerobic utilization of UAP with NO_2^-: $\hat{q}^h_{UAP} X_h \left(\frac{C_{UAP}}{C_{UAP}+K^h_{UAP}}\right)\left(\frac{C_{NO2}}{C_{NO2}+K^h_{NO2}}\right)(\mathrm{DO^{sw}})$
15				-0.9160		Fermenters utilization of UAP with NH_4^+: $\hat{q}^f_{UAP} X_f \left(\frac{C_{UAP}}{C_{UAP}+K^f_{UAP}}\right)(\mathrm{DO^{sw}})(NO_x^{sw})\left(\mathrm{CO_2^{inh}}\right) I_f^{pH}$
16	1.5400			0.3580		Heterotrophic aerobic utilization of BAP with NH_4^+: $\hat{q}^h_{BAP} X_h \left(\frac{C_{BAP}}{C_{BAP}+K^h_{UAP}}\right)\left(\frac{C_{DO}}{C_{DO}+K^h_{DO}}\right)\left(\mathrm{NH_4^{+inh}}\right)$
17	1.7628		-1.6218	0.0641		Heterotrophic aerobic utilization of BAP with NO_3^-: $\hat{q}^h_{BAP} X_h \left(\frac{C_{BAP}}{C_{BAP}+K^h_{UAP}}\right)\left(\frac{C_{NO3}}{C_{NO3}+K^h_{NO3}}\right)(\mathrm{DO^{sw}})$
18	1.8007	-2.7611		0.0608		Heterotrophic aerobic utilization of BAP with NO_2^-: $\hat{q}^h_{BAP} X_h \left(\frac{C_{BAP}}{C_{BAP}+K^h_{UAP}}\right)\left(\frac{C_{NO2}}{C_{NO2}+K^h_{NO2}}\right)(\mathrm{DO^{sw}})$
19				0.6814		Fermenters utilization of BAP with NH_4^+: $\hat{q}^f_{BAP} X_f \left(\frac{C_{BAP}}{C_{BAP}+K^f_{BAP}}\right)(\mathrm{DO^{sw}})(NO_x^{sw})\left(\mathrm{CO_2^{inh}}\right) I_f^{pH}$

203

Table C.3 continued. Stoichiometry matrix for MYAnode bulk liquid reactions.

	Bicarbonate	Nitrite	Nitrate	Ammonium	Ammonia (liquid)	Utilization rate equation
Chemical formula	HCO_3^-	NO_2^-	NO_3^-	NH_4^+	NH_3	
Symbol	C_{HCO3}	C_{NO2}	C_{NO3}	C_{NH4}	C_{NH3}	r_{ut}
20						PCOD hydrolysis: $k_{hyd}X_{PCOD}$
21	0.2000			0.0400		Heterotrophic aerobic endogenous decay: $b_h X_h \left(\frac{C_{DO}}{C_{DO}+K_{DO}^h}\right)$
22	0.2000		-0.1600	0.0400		Heterotrophic anoxic endogenous decay with NO_3^-: $b_h X_h \left(\frac{C_{NO3}}{C_{NO3}+K_{NO3}^h}\right)$
23	0.2000	-0.2667		0.0400		Heterotrophic anoxic endogenous decay with NO_2^-: $b_h X_h \left(\frac{C_{NO2}}{C_{NO2}+K_{NO2}^h}\right)$
24	0.2000			0.0400		AOB endogenous decay: $b_{AOB} X_{AOB} \left(\frac{C_{DO}}{C_{DO}+K_{DO}^h}\right)$
25	0.2000			0.0400		NOB endogenous decay: $b_{NOB} X_{NOB} \left(\frac{C_{DO}}{C_{DO}+K_{DO}^h}\right)$
26				0.0400		Fermenters endogenous decay: $b_f X_f (\mathrm{DO^{sw}})(NO_x^{sw})(\mathrm{CO_2^{inh}})$
27	0.1000			0.0400		Methanogens endogenous decay: $b_m X_m (\mathrm{DO^{sw}})(NO_x^{sw})$

Table C.3 continued. Stoichiometry matrix for MYAnode bulk liquid reactions.

	Bicarbonate	Nitrite	Nitrate	Ammonium	Ammonia (liquid)	Utilization rate equation
Chemical formula	HCO_3^-	NO_2^-	NO_3^-	NH_4^+	NH_3	
Symbol	C_{HCO3}	C_{NO2}	C_{NO3}	C_{NH4}	C_{NH3}	r_{ut}
28						EPS hydrolysis: $k_{hydEPS}X_{EPS}$
29	0.0500			0.0300		AOB biomass hydrolysis: $k_{hyd}X_{AOB}(\mathrm{DO^{sw}})(NO_x^{sw})$
30	0.0500			0.0300		NOB biomass hydrolysis: $k_{hyd}X_{NOB}(\mathrm{DO^{sw}})(NO_x^{sw})$
31						Gas/liquid phase partitioning of CH_4: $\left(\frac{V_l}{V_g}\right)K_La\left(C_{CH4}-H_{CH4}C_{CH4}^gRT\right)$
32						Gas/liquid phase partitioning of CO_2: $\left(\frac{V_l}{V_g}\right)K_La\left(C_{H2CO3}-H_{CO2}C_{CO2}^gRT\right)$
33					-1	Gas/liquid phase partitioning of NH_3: $\left(\frac{V_l}{V_g}\right)K_La\left(C_{NH3}-H_{NH3}C_{NH3}^gRT\right)$
34						Gas/liquid phase partitioning of N_2: $\left(\frac{V_l}{V_g}\right)K_La\left(C_{N2}-H_{N2}C_{N2}^gRT\right)$

Species only present in chemical speciation calculations are omitted (i.e., $CO3_2^-$, HNO_2).

205

Table C.3 continued. Stoichiometry matrix for MYAnode bulk liquid reactions.

	Dissolved oxygen	Methane (liquid)	Nitrogen (liquid phase)	Protons	Water	Utilization rate equation
Chemical formula	O_2	CH_4	N_2	H^+	H_2O	
Symbol	C_{DO}	C_{CH4}	C_{N2}	C_{H+}	C_{H2O}	r_{ut}
1	-3.8500			1.9550	2.8150	Heterotrophic aerobic utilization of domestic wastewater with NH_4^+: $\hat{q}_S^h X_h \left(\frac{C_S}{C_S + K_S^h}\right)\left(\frac{C_{DO}}{C_{DO} + K_{DO}^h}\right)\left(\mathrm{NH_4^{+inh}}\right)$
2			2.1537	-1.1505	3.9452	Heterotrophic aerobic utilization of domestic wastewater with NO_3^-: $\hat{q}_S^h X_h \left(\frac{C_S}{C_S + K_S^h}\right)\left(\frac{C_{NO3}}{C_{NO3} + K_{NO3}^h}\right)(\mathrm{DO^{sw}})$
3			3.4968	-3.9780	5.3314	Heterotrophic aerobic utilization of domestic wastewater with NO_2^-: $\hat{q}_S^h X_h \left(\frac{C_S}{C_S + K_S^h}\right)\left(\frac{C_{NO2}}{C_{NO2} + K_{NO2}^h}\right)(\mathrm{DO^{sw}})$
4				0.0200	-0.1100	Heterotrophic biomass hydrolysis: $k_{hyd} X_h (\mathrm{DO^{sw}})(NO_x^{sw})$
5				1.2428	0.3895	Fermenters utilization of domestic wastewater with NH_4^+: $\hat{q}_S^f X_f \left(\frac{C_S}{C_S + K_S^f}\right)(\mathrm{DO^{sw}})(NO_x^{sw})\left(\mathrm{CO_2^{inh}}\right) I_f^{pH}$
6	-0.3445			-0.1318	0.0655	NOB utilization of NO_2^-: $\hat{q}^{NOB} X_{NOB} \left(\frac{C_{NO2}}{C_{NO2} + K_{NO2}^{NOB}}\right)\left(\frac{C_{DO}}{C_{DO} + K_{DO}^{NOB}}\right)\mathrm{CO_2^{inh}}$

206

Table C.3 continued. Stoichiometry matrix for MYAnode bulk liquid reactions.

	Dissolved oxygen	Methane (liquid)	Nitrogen (liquid phase)	Protons	Water	Utilization rate equation
Chemical formula	O_2	CH_4	N_2	H^+	H_2O	
Symbol	C_{DO}	C_{CH4}	C_{N2}	C_{H+}	C_{H2O}	r_{ut}
7	-0.9144			1.4541	1.1590	AOB utilization of NH_4^+: $\hat{q}^{AOB} X_{AOB} \left(\frac{C_{NH4}}{C_{NH4} + K_{NH4}^{NOB}}\right)\left(\frac{C_{DO}}{C_{DO} + K_{DO}^{AOB}}\right) \mathrm{CO}_2^{\mathrm{inh}}$
8	-0.6160			-0.1272	0.7704	Heterotrophic aerobic utilization of acetate with NH_4^+: $\hat{q}_{ace}^{h} X_h \left(\frac{C_{ace}}{C_{ace} + K_{ace}^{h}}\right)\left(\frac{C_{DO}}{C_{DO} + K_{DO}^{h}}\right) \left(\mathrm{NH}_4^{+\mathrm{inh}}\right)$
9			0.3080	-0.6640	0.7440	Heterotrophic aerobic utilization of domestic wastewater with NO_3^-: $\hat{q}_{ace}^{h} X_h \left(\frac{C_{ace}}{C_{ace} + K_{ace}^{h}}\right)\left(\frac{C_{NO3}}{C_{NO3} + K_{NO3}^{h}}\right) (\mathrm{DO}^{\mathrm{sw}})$
10			0.5133	-1.1254	0.9663	Heterotrophic aerobic utilization of domestic wastewater with NO_2^-: $\hat{q}_{ace}^{h} X_h \left(\frac{C_{ace}}{C_{ace} + K_{ace}^{h}}\right)\left(\frac{C_{NO2}}{C_{NO2} + K_{NO2}^{h}}\right) (\mathrm{DO}^{\mathrm{sw}})$
11		0.7315		-0.1811	-0.4693	Methanogens utilization of acetate: $\hat{q}^{m} X_m \left(\frac{C_{ace}}{C_{ace} + K^{m}}\right) (\mathrm{DO}^{\mathrm{sw}})(NO_x^{sw})\left(\mathrm{NH}_4^{+\mathrm{inh}}\right) I_m^{pH}$

207

Table C.3 continued. Stoichiometry matrix for MYAnode bulk liquid reactions.

	Dissolved oxygen	Methane (liquid)	Nitrogen (liquid phase)	Protons	Water	Utilization rate equation
Chemical formula	O_2	CH_4	N_2	H^+	H_2O	
Symbol	C_{DO}	C_{CH4}	C_{N2}	C_{H+}	C_{H2O}	r_{ut}
12	-1.4202			2.3362	2.7479	Heterotrophic aerobic utilization of UAP with NH_4^+: $\hat{q}^h_{UAP} X_h \left(\frac{C_{UAP}}{C_{UAP}+K^h_{UAP}}\right)\left(\frac{C_{DO}}{C_{DO}+K^h_{DO}}\right)\left(\mathrm{NH_4^{+inh}}\right)$
13			0.5681	1.0033	2.2339	Heterotrophic aerobic utilization of UAP with NO_3^-: $\hat{q}^h_{UAP} X_h \left(\frac{C_{UAP}}{C_{UAP}+K^h_{UAP}}\right)\left(\frac{C_{NO3}}{C_{NO3}+K^h_{NO3}}\right)(\mathrm{DO^{sw}})$
14			0.9468	0.01889	2.6883	Heterotrophic aerobic utilization of UAP with NO_2^-: $\hat{q}^h_{UAP} X_h \left(\frac{C_{UAP}}{C_{UAP}+K^h_{UAP}}\right)\left(\frac{C_{NO2}}{C_{NO2}+K^h_{NO2}}\right)(\mathrm{DO^{sw}})$
15				1.6261	2.7479	Fermenters utilization of UAP with NH_4^+: $\hat{q}^f_{UAP} X_f \left(\frac{C_{UAP}}{C_{UAP}+K^f_{UAP}}\right)(\mathrm{DO^{sw}})(NO_x^{sw})\left(\mathrm{CO_2^{inh}}\right) I_f^{pH}$
16	-1.5400			1.182	-1.074	Heterotrophic aerobic utilization of BAP with NH_4^+: $\hat{q}^h_{BAP} X_h \left(\frac{C_{BAP}}{C_{BAP}+K^h_{UAP}}\right)\left(\frac{C_{DO}}{C_{DO}+K^h_{DO}}\right)\left(\mathrm{NH_4^{+inh}}\right)$
17			0.9872	0.0769	0.0897	Heterotrophic aerobic utilization of BAP with NO_3^-: $\hat{q}^h_{BAP} X_h \left(\frac{C_{BAP}}{C_{BAP}+K^h_{UAP}}\right)\left(\frac{C_{NO3}}{C_{NO3}+K^h_{NO3}}\right)(\mathrm{DO^{sw}})$

208

Table C.3 continued. Stoichiometry matrix for MYAnode bulk liquid reactions.

	Dissolved oxygen	Methane (liquid)	Nitrogen (liquid phase)	Protons	Water	Utilization rate equation
Chemical formula	O_2	CH_4	N_2	H^+	H_2O	
Symbol	C_{DO}	C_{CH4}	C_{N2}	C_{H+}	C_{H2O}	r_{ut}
18			1.5606	-1.0212	0.6579	Heterotrophic aerobic utilization of BAP with NO_2^-: $\hat{q}^h_{BAP} X_h \left(\frac{C_{BAP}}{C_{BAP} + K^h_{UAP}}\right)\left(\frac{C_{NO2}}{C_{NO2} + K^h_{NO2}}\right)(\mathrm{DO^{sw}})$
19				0.8971	-2.0442	Fermenters utilization of BAP with NH_4^+: $\hat{q}^f_{BAP} X_f \left(\frac{C_{BAP}}{C_{BAP} + K^f_{BAP}}\right)(\mathrm{DO^{sw}})(NO_x^{sw})\left(\mathrm{CO_2^{inh}}\right) I_f^{pH}$
20						PCOD hydrolysis: $k_{hyd} X_{PCOD}$
21	-0.2000			0.1600	-0.1200	Heterotrophic aerobic endogenous decay: $b_h X_h \left(\frac{C_{DO}}{C_{DO} + K^h_{DO}}\right)$
22			0.0800	2.22E-16	-0.0400	Heterotrophic anoxic endogenous decay with NO_3^-: $b_h X_h \left(\frac{C_{NO3}}{C_{NO3} + K^h_{NO3}}\right)$
23			0.1333	-0.1067	0.0133	Heterotrophic anoxic endogenous decay with NO_2^-: $b_h X_h \left(\frac{C_{NO2}}{C_{NO2} + K^h_{NO2}}\right)$
24	-0.2000			0.1600	-0.1200	AOB endogenous decay: $b_{AOB} X_{AOB} \left(\frac{C_{DO}}{C_{DO} + K^h_{DO}}\right)$

209

Table C.3 continued. Stoichiometry matrix for MYAnode bulk liquid reactions.

	Dissolved oxygen	Methane (liquid)	Nitrogen (liquid phase)	Protons	Water	Utilization rate equation
Chemical formula	O_2	CH_4	N_2	H^+	H_2O	
Symbol	C_{DO}	C_{CH4}	C_{N2}	C_{H+}	C_{H2O}	r_{ut}
25	-0.2000			0.1600	-0.1200	NOB endogenous decay: $b_{NOB}X_{NOB}\left(\frac{C_{DO}}{C_{DO}+K_{DO}^{h}}\right)$
26				0.0600	-0.1200	Fermenters endogenous decay: $b_f X_f(\mathrm{DO^{sw}})(NO_x^{sw})(\mathrm{CO_2^{inh}})$
27		0.1000		0.0600	-0.2200	Methanogens endogenous decay: $b_m X_m(\mathrm{DO^{sw}})(NO_x^{sw})$
28						EPS hydrolysis: $k_{hydEPS}X_{EPS}$
29				0.0200	-0.1100	AOB biomass hydrolysis: $k_{hyd}X_{AOB}(\mathrm{DO^{sw}})(NO_x^{sw})$
30				0.0200	-0.1100	NOB biomass hydrolysis: $k_{hyd}X_{NOB}(\mathrm{DO^{sw}})(NO_x^{sw})$
31		-1				Gas/liquid phase partitioning of CH_4: $\left(\frac{V_l}{V_g}\right)K_L a\left(C_{CH4}-H_{CH4}C_{CH4}^{g}RT\right)$
32						Gas/liquid phase partitioning of CO_2: $\left(\frac{V_l}{V_g}\right)K_L a\left(C_{H2CO3}-H_{CO2}C_{CO2}^{g}RT\right)$

210

Table C.3 continued. Stoichiometry matrix for MYAnode bulk liquid reactions.

	Dissolved oxygen	Methane (liquid)	Nitrogen (liquid phase)	Protons	Water	Utilization rate equation
Chemical formula	O_2	CH_4	N_2	H^+	H_2O	
Symbol	C_{DO}	C_{CH4}	C_{N2}	C_{H+}	C_{H2O}	r_{ut}
33						Gas/liquid phase partitioning of NH_3: $\left(\frac{V_l}{V_g}\right) K_L a\left(C_{NH3} - H_{NH3} C_{NH3}^g RT\right)$
34			-1			Gas/liquid phase partitioning of N_2: $\left(\frac{V_l}{V_g}\right) K_L a\left(C_{N2} - H_{N2} C_{N2}^g RT\right)$

Species only present in chemical speciation calculations are omitted (i.e., $CO3_2^-$, HNO_2).

211

Table C.3 continued. Stoichiometry matrix for MYAnode bulk liquid reactions.

	Carbon dioxide (gas)	Ammonia (gas)	Methane (gas)	Nitrogen gas	Utilization rate equation
Chemical formula	CO_2	NH3	CH_4	N_2	
Symbol	C^{g}_{CO2}	C^{g}_{NH3}	C^{g}_{CH4}	C^{g}_{N2}	r_{ut}
1					Heterotrophic aerobic utilization of domestic wastewater with NH_4^+: $\hat{q}^{h}_{S} X_h \left(\frac{C_S}{C_S + K^{h}_{S}}\right)\left(\frac{C_{DO}}{C_{DO} + K^{h}_{DO}}\right)\left(NH_4^{+inh}\right)$
2					Heterotrophic aerobic utilization of domestic wastewater with NO_3^-: $\hat{q}^{h}_{S} X_h \left(\frac{C_S}{C_S + K^{h}_{S}}\right)\left(\frac{C_{NO3}}{C_{NO3} + K^{h}_{NO3}}\right)(DO^{sw})$
3					Heterotrophic aerobic utilization of domestic wastewater with NO_2^-: $\hat{q}^{h}_{S} X_h \left(\frac{C_S}{C_S + K^{h}_{S}}\right)\left(\frac{C_{NO2}}{C_{NO2} + K^{h}_{NO2}}\right)(DO^{sw})$
4					Heterotrophic biomass hydrolysis: $k_{hyd} X_h (DO^{sw})(NO_x^{sw})$
5					Fermenters utilization of domestic wastewater with NH_4^+: $\hat{q}^{f}_{S} X_f \left(\frac{C_S}{C_S + K^{f}_{S}}\right)(DO^{sw})(NO_x^{sw})\left(CO_2^{inh}\right) I_f^{pH}$
6					NOB utilization of NO_2^-: $\hat{q}^{NOB} X_{NOB} \left(\frac{C_{NO2}}{C_{NO2} + K^{NOB}_{NO2}}\right)\left(\frac{C_{DO}}{C_{DO} + K^{NOB}_{DO}}\right) CO_2^{inh}$

212

Table C.3 continued. Stoichiometry matrix for MYAnode bulk liquid reactions.

	Carbon dioxide (gas)	Ammonia (gas)	Methane (gas)	Nitrogen gas	Utilization rate equation
Chemical formula	CO_2	NH3	CH_4	N_2	
Symbol	C^g_{CO2}	C^g_{NH3}	C^g_{CH4}	C^g_{N2}	r_{ut}
7					AOB utilization of NH_4^+: $\hat{q}^{AOB} X_{AOB} \left(\frac{C_{NH4}}{C_{NH4} + K^{NOB}_{NH4}}\right)\left(\frac{C_{DO}}{C_{DO} + K^{AOB}_{DO}}\right) CO_2^{inh}$
8					Heterotrophic aerobic utilization of acetate with NH_4^+: $\hat{q}^h_{ace} X_h \left(\frac{C_{ace}}{C_{ace} + K^h_{ace}}\right)\left(\frac{C_{DO}}{C_{DO} + K^h_{DO}}\right)\left(NH_4^{+inh}\right)$
9					Heterotrophic aerobic utilization of domestic wastewater with NO_3^-: $\hat{q}^h_{ace} X_h \left(\frac{C_{ace}}{C_{ace} + K^h_{ace}}\right)\left(\frac{C_{NO3}}{C_{NO3} + K^h_{NO3}}\right)(DO^{sw})$
10					Heterotrophic aerobic utilization of domestic wastewater with NO_2^-: $\hat{q}^h_{ace} X_h \left(\frac{C_{ace}}{C_{ace} + K^h_{ace}}\right)\left(\frac{C_{NO2}}{C_{NO2} + K^h_{NO2}}\right)(DO^{sw})$
11					Methanogens utilization of acetate: $\hat{q}^m X_m \left(\frac{C_{ace}}{C_{ace} + K^m}\right)(DO^{sw})(NO_x^{sw})\left(NH_4^{+inh}\right) I_m^{pH}$

Table C.3 continued. Stoichiometry matrix for MYAnode bulk liquid reactions.

	Carbon dioxide (gas)	Ammonia (gas)	Methane (gas)	Nitrogen gas	Utilization rate equation
Chemical formula	CO_2	NH3	CH_4	N_2	
Symbol	C^{g}_{CO2}	C^{g}_{NH3}	C^{g}_{CH4}	C^{g}_{N2}	r_{ut}
12					Heterotrophic aerobic utilization of UAP with NH_4^+: $\hat{q}^{h}_{UAP} X_h \left(\frac{C_{UAP}}{C_{UAP} + K^{h}_{UAP}}\right)\left(\frac{C_{DO}}{C_{DO} + K^{h}_{DO}}\right)\left(NH_4^{+inh}\right)$
13					Heterotrophic aerobic utilization of UAP with NO_3^-: $\hat{q}^{h}_{UAP} X_h \left(\frac{C_{UAP}}{C_{UAP} + K^{h}_{UAP}}\right)\left(\frac{C_{NO3}}{C_{NO3} + K^{h}_{NO3}}\right)(DO^{sw})$
14					Heterotrophic aerobic utilization of UAP with NO_2^-: $\hat{q}^{h}_{UAP} X_h \left(\frac{C_{UAP}}{C_{UAP} + K^{h}_{UAP}}\right)\left(\frac{C_{NO2}}{C_{NO2} + K^{h}_{NO2}}\right)(DO^{sw})$
15					Fermenters utilization of UAP with NH_4^+: $\hat{q}^{f}_{UAP} X_f \left(\frac{C_{UAP}}{C_{UAP} + K^{f}_{UAP}}\right)(DO^{sw})(NO_x^{sw})\left(CO_2^{inh}\right) I_f^{pH}$
16					Heterotrophic aerobic utilization of BAP with NH_4^+: $\hat{q}^{h}_{BAP} X_h \left(\frac{C_{BAP}}{C_{BAP} + K^{h}_{UAP}}\right)\left(\frac{C_{DO}}{C_{DO} + K^{h}_{DO}}\right)\left(NH_4^{+inh}\right)$

214

Table C.3 continued. Stoichiometry matrix for MYAnode bulk liquid reactions.

	Carbon dioxide (gas)	Ammonia (gas)	Methane (gas)	Nitrogen gas	Utilization rate equation
Chemical formula	CO_2	NH3	CH_4	N_2	
Symbol	C^g_{CO2}	C^g_{NH3}	C^g_{CH4}	C^g_{N2}	r_{ut}
17					Heterotrophic aerobic utilization of BAP with NO_3^-: $\hat{q}^h_{BAP} X_h \left(\frac{C_{BAP}}{C_{BAP} + K^h_{UAP}}\right)\left(\frac{C_{NO3}}{C_{NO3} + K^h_{NO3}}\right)(DO^{sw})$
18					Heterotrophic aerobic utilization of BAP with NO_2^-: $\hat{q}^h_{BAP} X_h \left(\frac{C_{BAP}}{C_{BAP} + K^h_{UAP}}\right)\left(\frac{C_{NO2}}{C_{NO2} + K^h_{NO2}}\right)(DO^{sw})$
19					Fermenters utilization of BAP with NH_4^+: $\hat{q}^f_{BAP} X_f \left(\frac{C_{BAP}}{C_{BAP} + K^f_{BAP}}\right)(DO^{sw})(NO_x^{sw})(CO_2^{inh})I_f^{pH}$
20					PCOD hydrolysis: $k_{hyd} X_{PCOD}$
21					Heterotrophic aerobic endogenous decay: $b_h X_h \left(\frac{C_{DO}}{C_{DO} + K^h_{DO}}\right)$
22					Heterotrophic anoxic endogenous decay with NO_3^-: $b_h X_h \left(\frac{C_{NO3}}{C_{NO3} + K^h_{NO3}}\right)$

Table C.3 continued. Stoichiometry matrix for MYAnode bulk liquid reactions.

	Carbon dioxide (gas)	Ammonia (gas)	Methane (gas)	Nitrogen gas	Utilization rate equation
Chemical formula	CO_2	NH3	CH_4	N_2	
Symbol	C^{g}_{CO2}	C^{g}_{NH3}	C^{g}_{CH4}	C^{g}_{N2}	r_{ut}
23					Heterotrophic anoxic endogenous decay with NO_2^-: $b_h X_h \left(\frac{C_{NO2}}{C_{NO2} + K^h_{NO2}}\right)$
24					AOB endogenous decay: $b_{AOB} X_{AOB} \left(\frac{C_{DO}}{C_{DO} + K^h_{DO}}\right)$
25					NOB endogenous decay: $b_{NOB} X_{NOB} \left(\frac{C_{DO}}{C_{DO} + K^h_{DO}}\right)$
26					Fermenters endogenous decay: $b_f X_f (DO^{sw})(NO_x^{sw})(CO_2^{inh})$
27					Methanogens endogenous decay: $b_m X_m (DO^{sw})(NO_x^{sw})$
28					EPS hydrolysis: $k_{hydEPS} X_{EPS}$
29					AOB biomass hydrolysis: $k_{hyd} X_{AOB} (DO^{sw})(NO_x^{sw})$
30					NOB biomass hydrolysis: $k_{hyd} X_{NOB} (DO^{sw})(NO_x^{sw})$

216

Table C.3 continued. Stoichiometry matrix for MYAnode bulk liquid reactions.

	Carbon dioxide (gas)	Ammonia (gas)	Methane (gas)	Nitrogen gas	Utilization rate equation
Chemical formula	CO_2	NH3	CH_4	N_2	
Symbol	C^{g}_{CO2}	C^{g}_{NH3}	C^{g}_{CH4}	C^{g}_{N2}	r_{ut}
31			1		Gas/liquid phase partitioning of CH_4: $\left(\frac{V_l}{V_g}\right) K_L a\left(C_{CH4} - H_{CH4} C^{g}_{CH4} RT\right)$
32	1				Gas/liquid phase partitioning of CO_2: $\left(\frac{V_l}{V_g}\right) K_L a\left(C_{H2CO3} - H_{CO2} C^{g}_{CO2} RT\right)$
33		1			Gas/liquid phase partitioning of NH_3: $\left(\frac{V_l}{V_g}\right) K_L a\left(C_{NH3} - H_{NH3} C^{g}_{NH3} RT\right)$
34				1	Gas/liquid phase partitioning of N_2: $\left(\frac{V_l}{V_g}\right) K_L a\left(C_{N2} - H_{N2} C^{g}_{N2} RT\right)$

Species only present in chemical speciation calculations are omitted (i.e., $CO3_2^-$, HNO_2).

217

APPENDIX D

SUPPLEMENTAL INFORMATION FOR CHAPTER 5

D.1 Supplemental Graphs

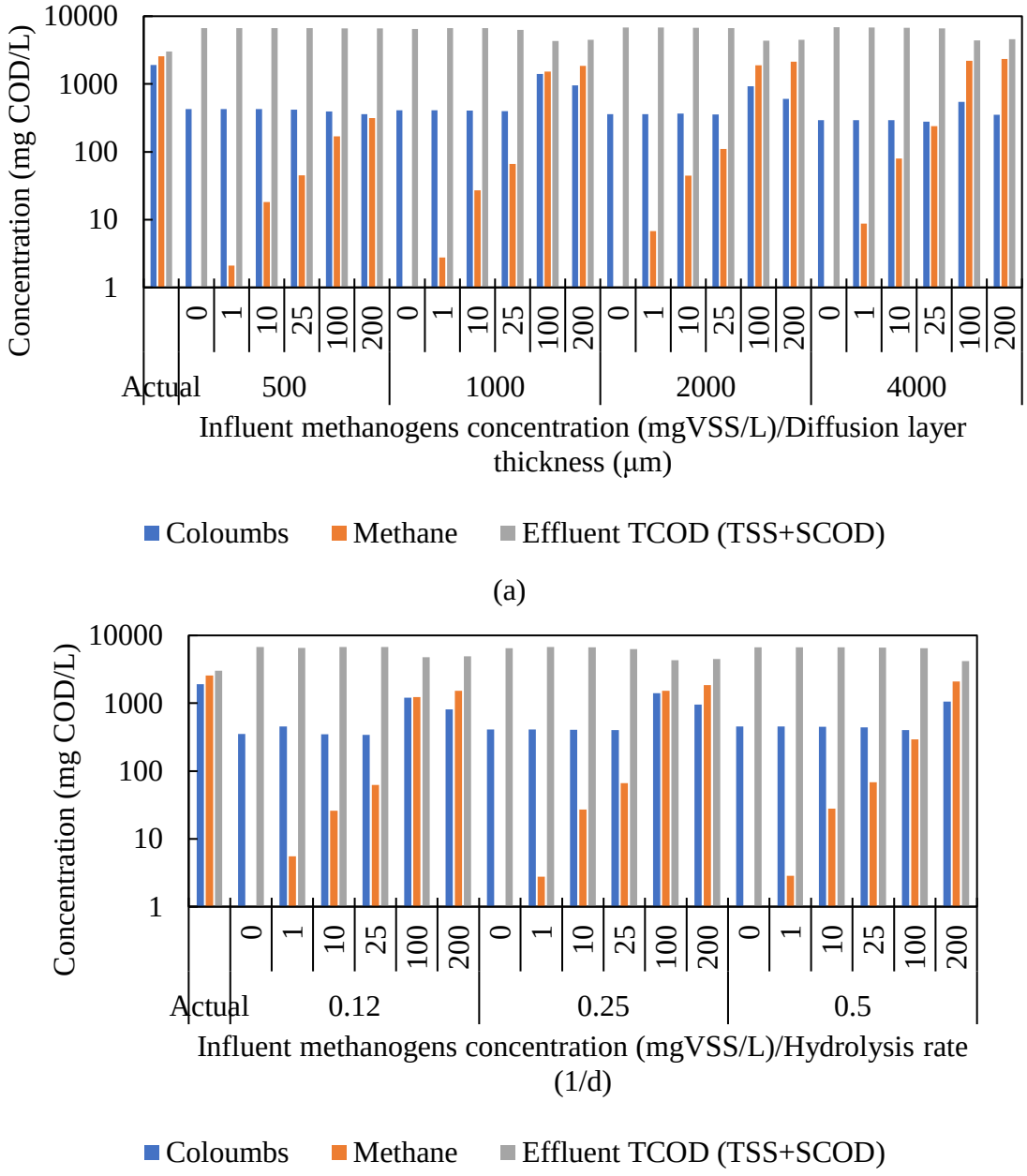

Figure D.1. Effluent composition at a 12-d anode chamber HRT and 0-200 mg VSS/L influent methanogens concentrations (a) with varying diffusion layer thickness at a 0.25/d PCOD hydrolysis rate and (b) with varying hydrolysis rate at a 1000 μm diffusion layer thickness. Experimental data was obtained from Ki et al. (2017a).

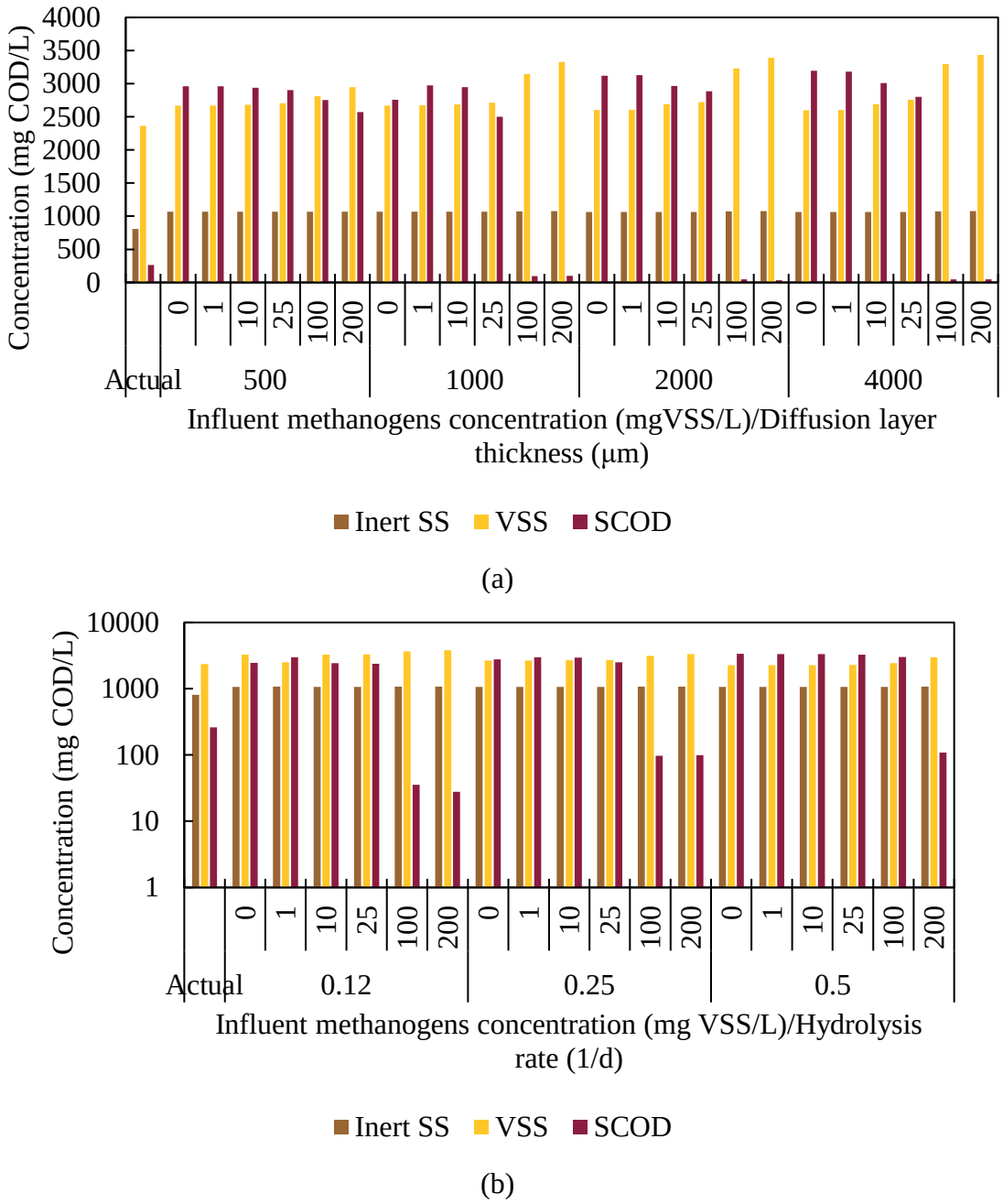

Figure D.2. Effluent TCOD composition at a 12-d anode chamber HRT and 0-200 mg VSS/L influent methanogens concentrations (a) with varying diffusion layer thickness at a 0.25/d PCOD hydrolysis rate and (b) with varying hydrolysis rate at a 1000 μm diffusion layer thickness. Experimental data was obtained from Ki et al. (2017a).

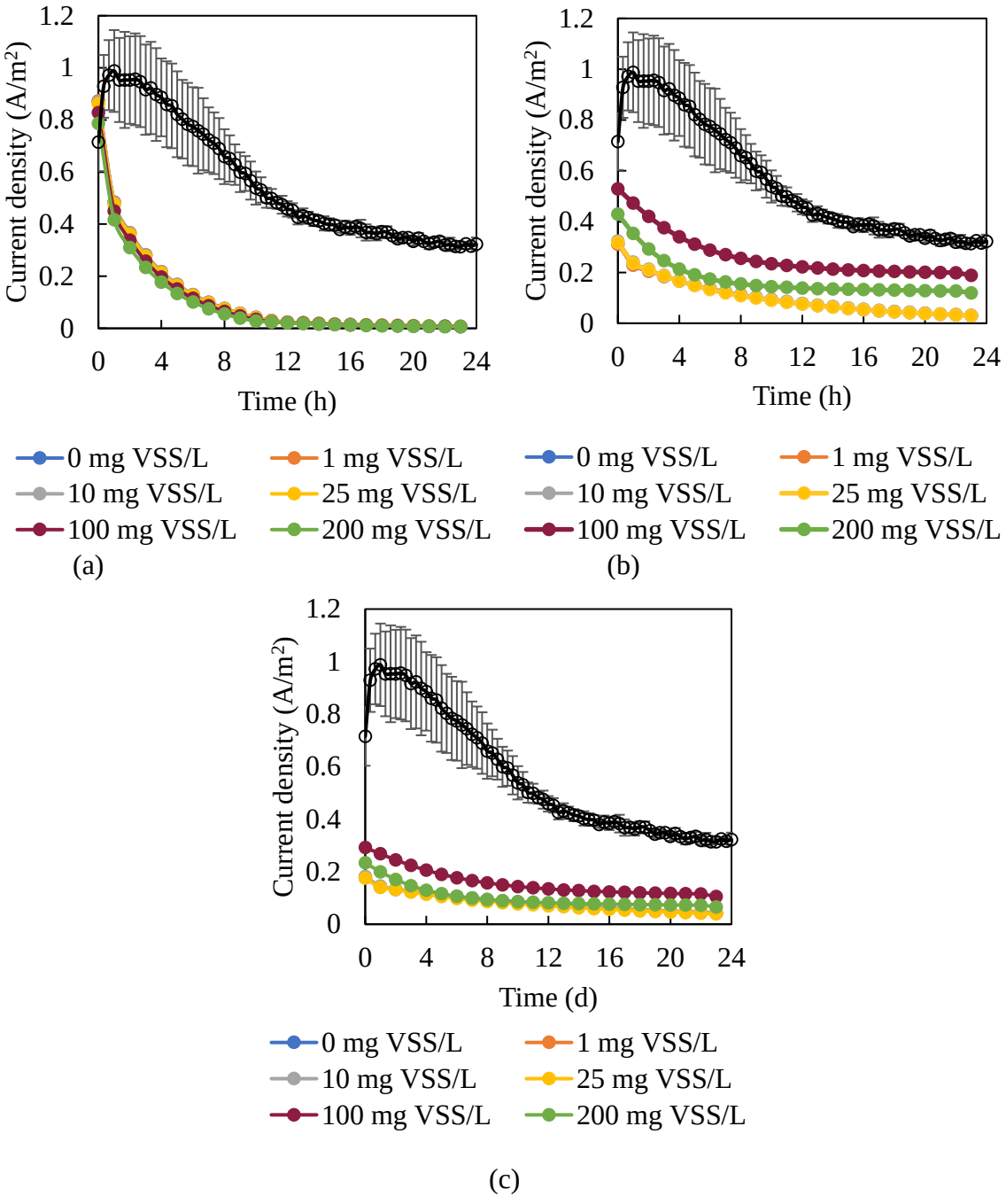

Figure D.3. Daily current densities at a 12-d anode chamber HRT, 0.25/d PCOD hydrolysis rate, and 0-200 mg VSS/L influent methanogens concentrations with varying diffusion layer thicknesses: (a) 500 μm, (b) 2000 μm, and (c) 4000 μm. The 1000 μm data is presented in Appendix C. Experimental data was obtained from Ki et al. (2017a).

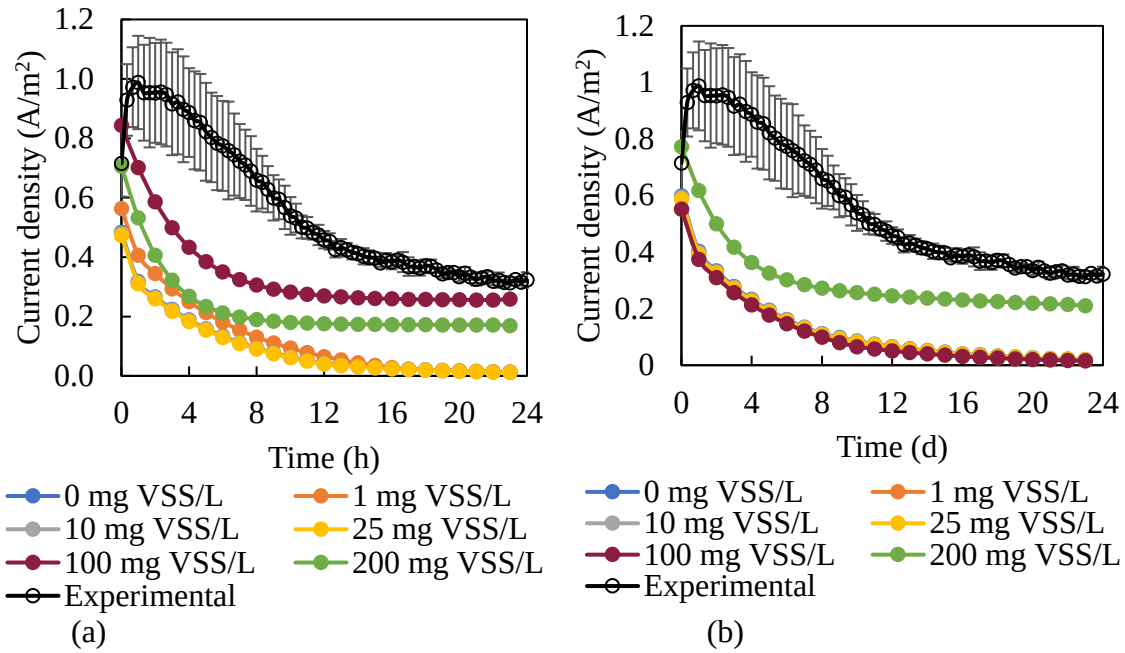

Figure D.4. Daily current densities at a 12-d anode chamber HRT, 1000 μm diffusion layer thickness, and 0-200 mg VSS/L influent methanogens concentrations at hydrolysis rates of (a) 0.12/d and (b) 0.5/d. The 1000 μm data is presented in Appendix C. Experimental data was obtained from Ki et al. (2017a).

APPENDIX E

SUPPLEMENTAL INFORMATION FOR CHAPTER 6

E.1 Supplemental Graphs

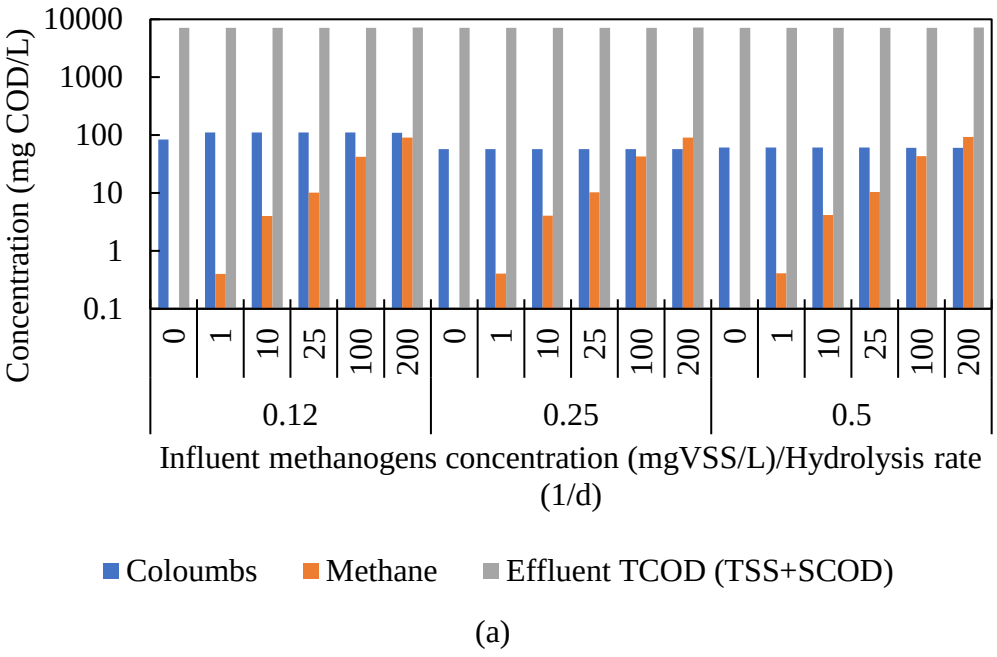

(a)

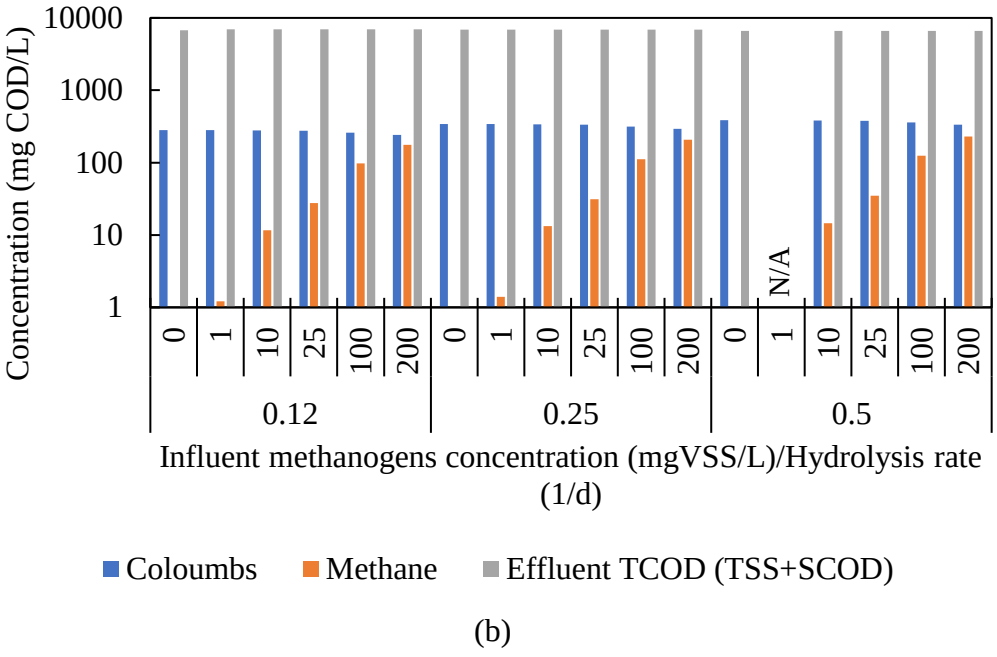

(b)

Figure E.1. Effluent composition at different anode HRTs: (a) 6 d, (b) 9 d, and (c) 15 d. The 12-d HRT data is included in Appendices C and D. The influent methanogens composition ranges from 0-200 mg VSS/L, and the hydrolysis rate varies from 0.12-0.5/d.

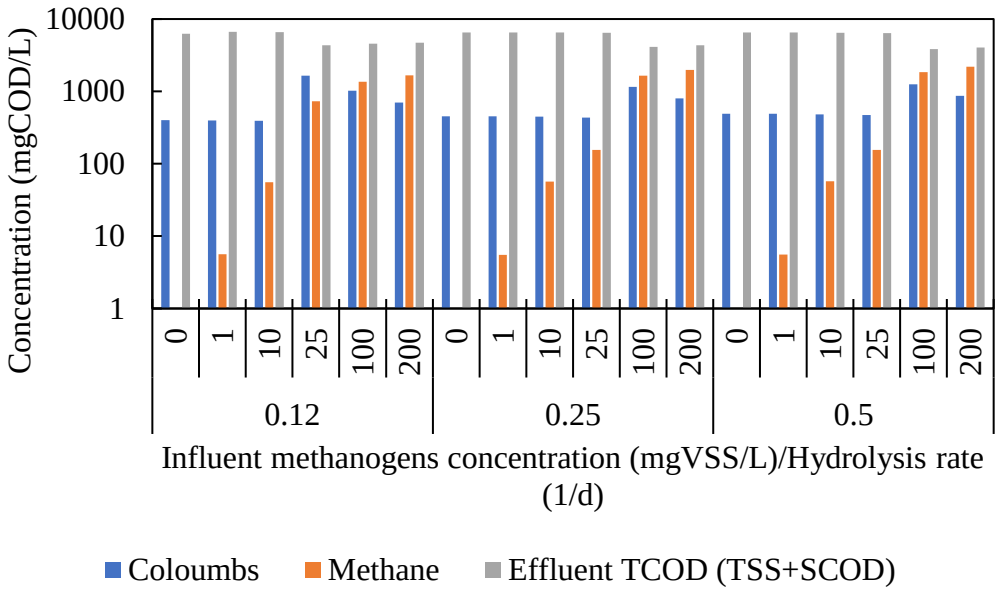

(c)

Figure E.1 continued. Effluent composition at different anode HRTs: (a) 6 d, (b) 9 d, and (c) 15 d. The 12-d HRT data is included in Appendices C and D. The influent methanogens composition ranges from 0-200 mg VSS/L, and the hydrolysis rate varies from 0.12-0.5/d.

-

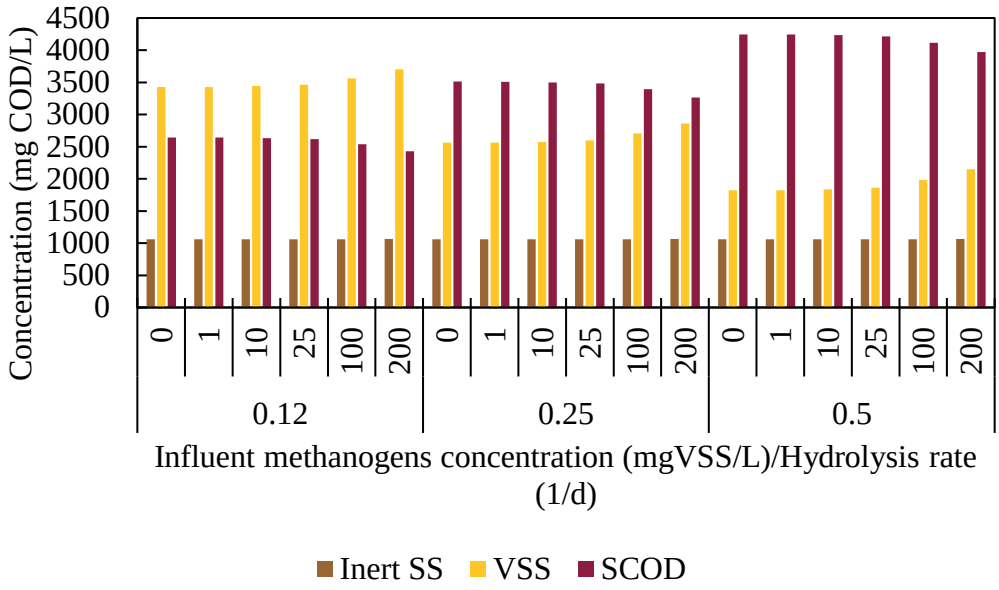

(a)

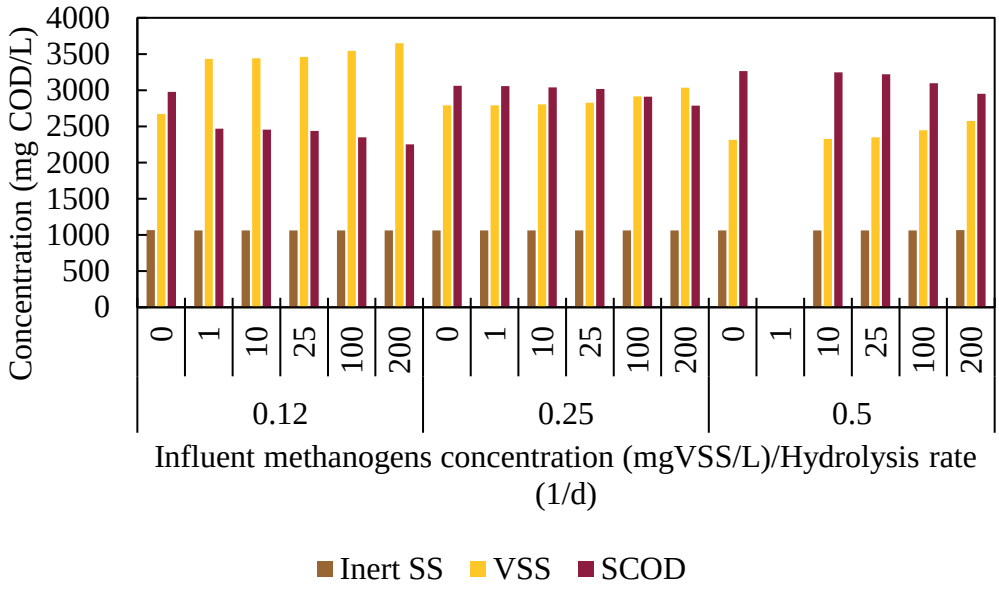

(b)

Figure E.2. Effluent TCOD composition at different anode HRTs: (a) 6 d, (b) 9 d, and (c) 15 d. The 12-d HRT data is included in Appendices C and D. The influent methanogens composition ranges from 0-200 mg VSS/L, and the hydrolysis rate varies from 0.12-0.5/d.

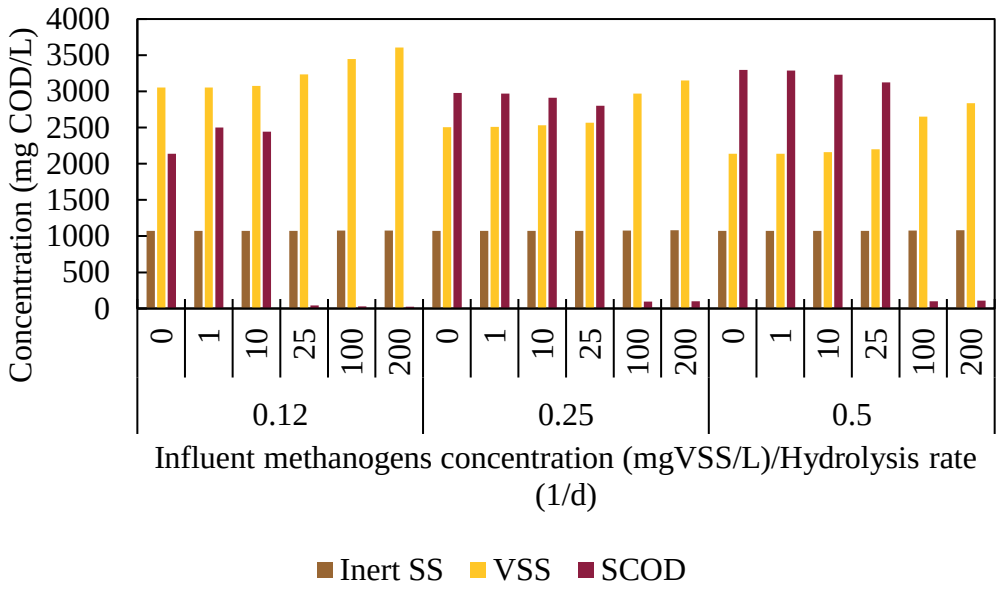

(c)

Figure E.2 continued. Effluent TCOD composition at different anode HRTs: (a) 6 d, (b) 9 d, and (c) 15 d. The 12-d HRT data is included in Appendices C and D. The influent methanogens composition ranges from 0-200 mg VSS/L, and the hydrolysis rate varies from 0.12-0.5/d.

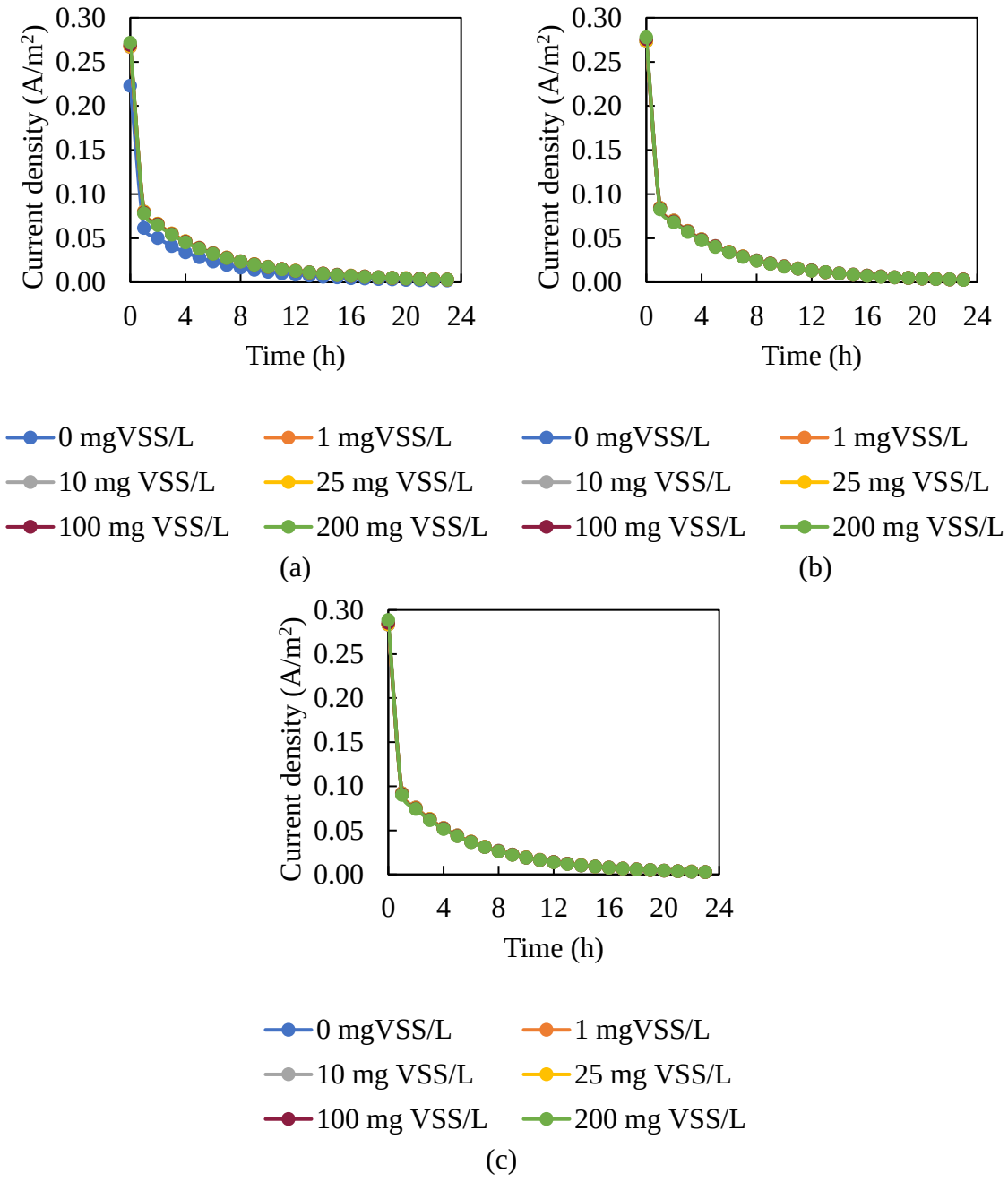

Figure E.3. Daily current densities at a 6 d HRT and (a) 0.12/d, (b) 0.25/d, and (c) 0.5/d hydrolysis rates. The influent methanogens composition ranges from 0-200 mg VSS/L. The 12-d HRT data is included in Appendices C and D.

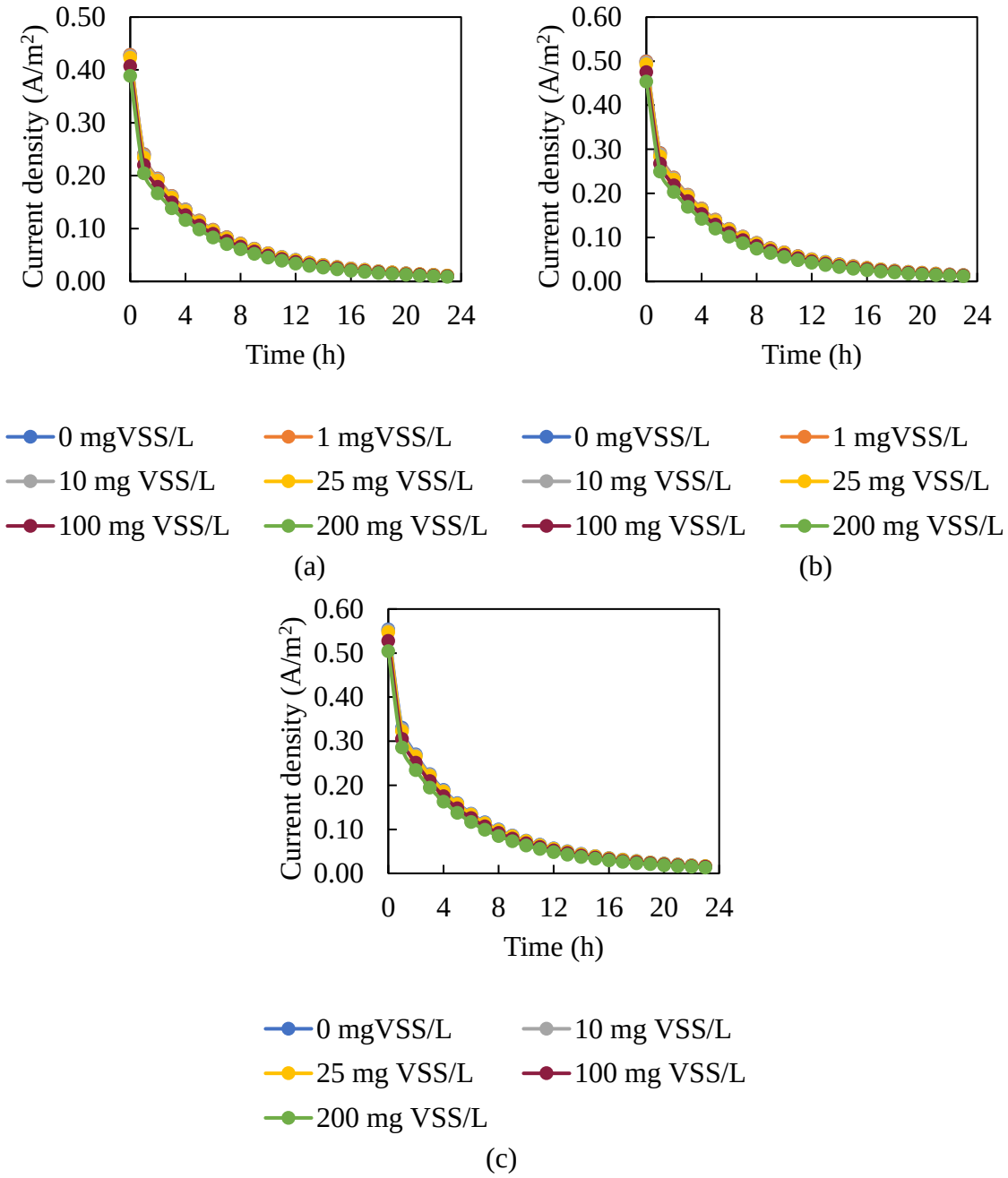

Figure E.4. Daily current densities at a 9 d HRT and (a) 0.12/d, (b) 0.25/d, and (c) 0.5/d hydrolysis rates. The influent methanogens composition ranges from 0-200 mg VSS/L. The 12-d HRT data is included in Appendices C and D.

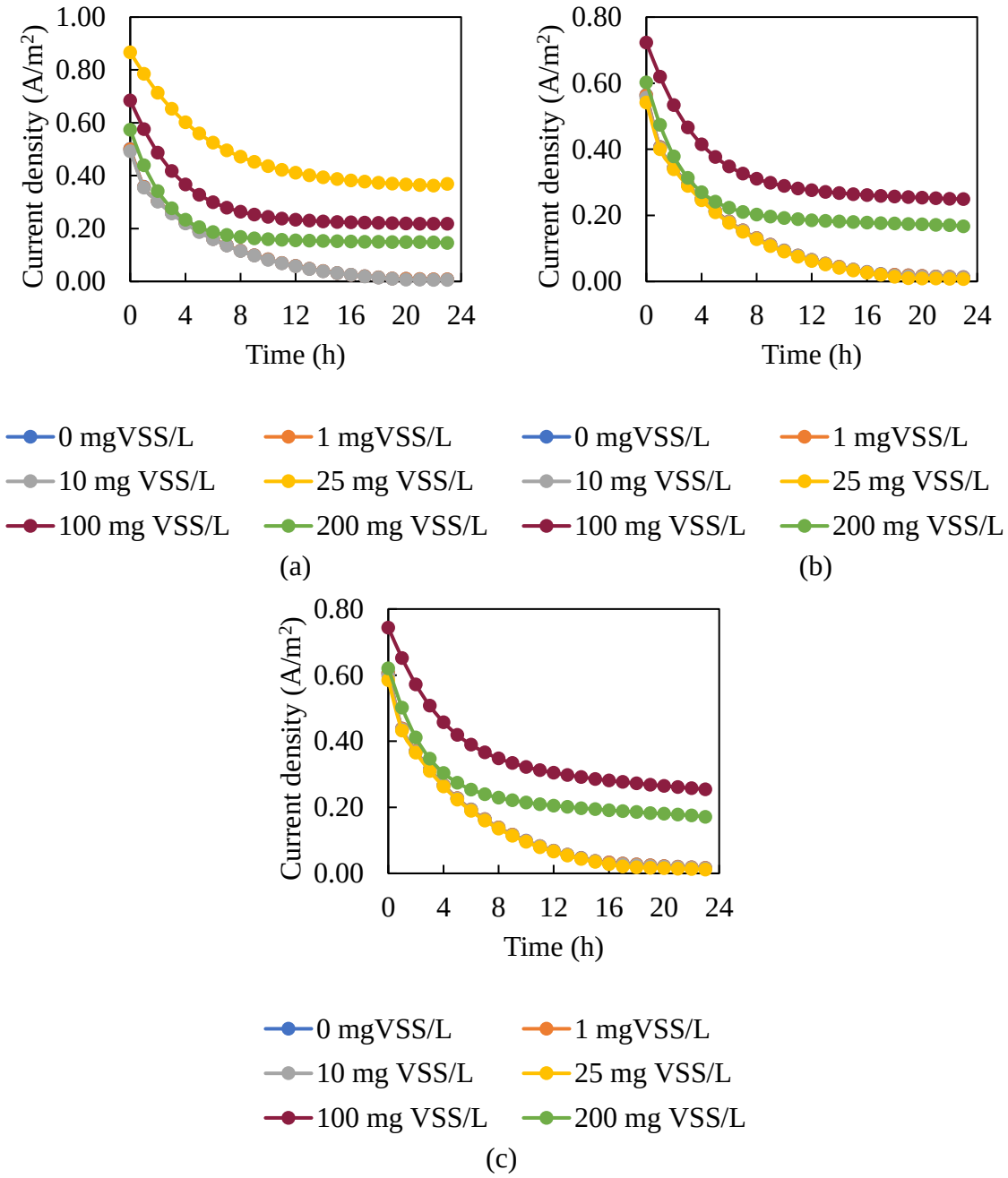

Figure E.5. Daily current densities at a 15 d HRT and (a) 0.12/d, (b) 0.25/d, and (c) 0.5/d hydrolysis rates. The influent methanogens composition ranges from 0-200 mg VSS/L. The 12-d HRT data is included in Appendices C and D.

APPENDIX F

PERMISSIONS TO USE PREVIOUSLY PUBLISHED WORKS

F.1 Permission to reproduce the articles from publishers

ELSEVIER LICENSE
TERMS AND CONDITIONS

Apr 21, 2017

This Agreement between Michelle Young ("You") and Elsevier ("Elsevier") consists of your license details and the terms and conditions provided by Elsevier and Copyright Clearance Center.

License Number	4093690576490
License date	
Licensed Content Publisher	Elsevier
Licensed Content Publication	Journal of Power Sources
Licensed Content Title	Understanding the impact of operational conditions on performance of microbial peroxide producing cells
Licensed Content Author	Michelle N. Young,Nadrat Chowdhury,Emily Garver,Patrick J. Evans,Sudeep C. Popat,Bruce E. Rittmann,César I. Torres
Licensed Content Date	Available online 12 April 2017
Licensed Content Volume	n/a
Licensed Content Issue	n/a
Licensed Content Pages	1
Start Page	
End Page	
Type of Use	reuse in a thesis/dissertation
Intended publisher of new work	other
Portion	full article
Format	both print and electronic
Are you the author of this Elsevier article?	Yes
Will you be translating?	No
Order reference number	
Title of your thesis/dissertation	Understanding the Mechanisms and Potential of Microbial Peroxide-Producing Cells (MPPCs)
Expected completion date	Jul 2017
Estimated size (number of pages)	200
Elsevier VAT number	GB 494 6272 12
Requestor Location	Michelle Young 1001 S McAllister Ave TEMPE, AZ 85287 United States Attn: Michelle Young
Publisher Tax ID	98-0397604
Billing Type	Invoice

Billing Address	Michelle Young 1001 S McAllister Ave TEMPE, AZ 85287 United States Attn: Michelle Young
Total	0.00 USD

Terms and Conditions

9/4/2018 RightsLink Printable License

JOHN WILEY AND SONS LICENSE TERMS AND CONDITIONS

Aug 16, 2018

This Agreement between Michelle Young ("You") and John Wiley and Sons ("John Wiley and Sons") consists of your license details and the terms and conditions provided by John Wiley and Sons and Copyright Clearance Center.

License Number	4410990408123
License date	Aug 16, 2018
Licensed Content Publisher	John Wiley and Sons
Licensed Content Publication	ChemSusChem
Licensed Content Title	Tailoring Microbial Electrochemical Cells for Production of Hydrogen Peroxide at High Concentrations and Efficiencies
Licensed Content Author	Michelle N. Young, Mikaela J. Links, Sudeep C. Popat, et al
Licensed Content Date	Nov 10, 2016
Licensed Content Volume	9
Licensed Content Issue	23
Licensed Content Pages	8
Type of use	Dissertation/Thesis
Requestor type	Author of this Wiley article
Format	Print and electronic
Portion	Full article
Will you be translating?	No
Title of your thesis / dissertation	Understanding the Mechanisms and Potential of Microbial Peroxide-Producing Cells (MPPCs)
Expected completion date	Dec 2018
Expected size (number of pages)	200
Requestor Location	Michelle Young 1001 S McAllister Ave TEMPE, AZ 85287 United States Attn: Michelle Young
Publisher Tax ID	EU826007151
Total	0.00 USD

F.2 Permission to use articles from co-authors.

May you find this as silly and heartwarming as I did.

Michelle Young <aumny@asu.edu>

URGENT -- Permission to use article in my dissertation
29 messages

Michelle Young <aumny@asu.edu> Thu, Aug 16, 2018 at 2:34 PM
To: Nadrat Chowdhury <nadrat.chowdhury@gmail.com>, Mikaela Stadie <Mikaela.Stadie@asu.edu>, Emily Garver <Emily.Garver@asu.edu>, Sudeep Popat <spopat@clemson.edu>, Pat Evans <evanspj@cdmsmith.com>, "César I. Torres" <cit@asu.edu>, Bruce Rittmann <Rittmann@asu.edu>

Hi all!

You are all my coauthors on both of or either

- "Tailoring Microbial Electrochemical Cells for Production of Hydrogen Peroxide at High Concentrations and Efficiencies" in ChemSusChem (https://onlinelibrary.wiley.com/doi/10.1002/cssc.201601182)

and/or

- "Understanding the impact of operational conditions on performance of microbial peroxide producing cells" published in Journal of Power Sources (https://www.sciencedirect.com/science/article/pii/S0378775317304135?via%3Dihub).

I am elated to report that I'm getting ready to defend my dissertation. (Sign of the apocalypse?!). As my coauthors, Arizona State University requires that you provide me permission to use these articles in my dissertation (see the details here: https://graduate.asu.edu/sites/default/files/policy-on-using-previously-published-work.pdf). **Can you please reply to this email stating that I have your permission to use these articles as part of my dissertation no later than August 31, 2018?**

Since you're all basically family, I will keep you updated as I schedule the defense date, which is likely the second week of September. While you may not be able to be here in person, I'd love for you to join via YouTube. Thanks in advance for your help!

Michelle Young
Graduate Research Assistant, Environmental Engineering
Biodesign Swette Center for Environmental Biotechnology
Arizona State University
1001 S. McAllister Ave.
Tempe, AZ 85281-5701
(303) 263-4702

Bruce Rittmann <Rittmann@asu.edu> Thu, Aug 16, 2018 at 2:36 PM
To: Michelle Young <aumny@asu.edu>, Nadrat Chowdhury <nadrat.chowdhury@gmail.com>, Mikaela Stadie <Mikaela.Stadie@asu.edu>, Emily Garver <Emily.Garver@asu.edu>, Sudeep Popat <spopat@clemson.edu>, Pat Evans <evanspj@cdmsmith.com>, Cesar Torres <cit@asu.edu>

You certainly have permission from me.

Bruce

From: Michelle Young <aumny@asu.edu>
Date: Thursday, August 16, 2018 at 2:35 PM
To: Nadrat Chowdhury <nadrat.chowdhury@gmail.com>, Mikaela Stadie <Mikaela.Stadie@asu.edu>, Emily Garver <Emily.Garver@asu.edu>, Sudeep Popat <spopat@clemson.edu>, Pat Evans <evanspj@cdmsmith.com>, Cesar Torres <cit@asu.edu>,

Bruce Rittmann <Rittmann@asu.edu>
Subject: URGENT -- Permission to use article in my dissertation

[Quoted text hidden]

Michelle Young <aumny@asu.edu> Thu, Aug 16, 2018 at 2:37 PM
To: Bruce Rittmann <Rittmann@asu.edu>

LOL -- thought so :)

Michelle Young
Graduate Research Assistant, Environmental Engineering
Biodesign Swette Center for Environmental Biotechnology
Arizona State University
1001 S. McAllister Ave.
Tempe, AZ 85281-5701
(303) 263-4702

[Quoted text hidden]

Bruce Rittmann <Rittmann@asu.edu> Thu, Aug 16, 2018 at 2:38 PM
To: Michelle Young <aumny@asu.edu>

Trying to set a good example!

From: Michelle Young <aumny@asu.edu>
Date: Thursday, August 16, 2018 at 2:37 PM
To: Bruce Rittmann <Rittmann@asu.edu>
Subject: Re: URGENT -- Permission to use article in my dissertation

[Quoted text hidden]

Michelle Young <aumny@asu.edu> Thu, Aug 16, 2018 at 2:38 PM
To: Bruce Rittmann <Rittmann@asu.edu>

You're always a good example. You even like Monty Python!

Michelle Young
Graduate Research Assistant, Environmental Engineering
Biodesign Swette Center for Environmental Biotechnology
Arizona State University
1001 S. McAllister Ave.
Tempe, AZ 85281-5701
(303) 263-4702

[Quoted text hidden]

Bruce Rittmann <Rittmann@asu.edu> Thu, Aug 16, 2018 at 2:45 PM
To: Michelle Young <aumny@asu.edu>

Killer rabbit!

From: Michelle Young <aumny@asu.edu>
Date: Thursday, August 16, 2018 at 2:39 PM

[Quoted text hidden]

[Quoted text hidden]

Mikaela Links <mikaela.j.links@gmail.com> Thu, Aug 16, 2018 at 3:13 PM
To: Bruce Rittmann <Rittmann@asu.edu>
Cc: Michelle Young <aumny@asu.edu>, Nadrat Chowdhury <nadrat.chowdhury@gmail.com>, Mikaela Stadie <Mikaela.Stadie@asu.edu>, Emily Garver <Emily.Garver@asu.edu>, Sudeep Popat <spopat@clemson.edu>, Pat Evans <evanspj@cdmsmith.com>, Cesar Torres <cit@asu.edu>

How exciting, Michelle! You have my permission to use these articles as part of your dissertation.

Wishing you all the best :)

-Mikaela Links

Sent from my iPhone
[Quoted text hidden]

Michelle Young <aumny@asu.edu> Thu, Aug 16, 2018 at 5:32 PM
To: mikaela.j.links@gmail.com

Thanks chica! I hope you and Alex are doing well in Flag!

Michelle Young
Graduate Research Assistant, Environmental Engineering
Biodesign Swette Center for Environmental Biotechnology
Arizona State University
1001 S. McAllister Ave.
Tempe, AZ 85281-5701
(303) 263-4702

[Quoted text hidden]

Evans, Patrick J. <EvansPJ@cdmsmith.com> Thu, Aug 16, 2018 at 6:59 PM
To: Bruce Rittmann <Rittmann@asu.edu>
Cc: Michelle Young <aumny@asu.edu>, Nadrat Chowdhury <nadrat.chowdhury@gmail.com>, Mikaela Stadie <Mikaela.Stadie@asu.edu>, Emily Garver <Emily.Garver@asu.edu>, Sudeep Popat <spopat@clemson.edu>, Cesar Torres <cit@asu.edu>

Mine too. Good luck!

Pat

On Aug 16, 2018, at 2:36 PM, Bruce Rittmann <Rittmann@asu.edu> wrote:

[Quoted text hidden]

Michelle Young <aumny@asu.edu> Thu, Aug 16, 2018 at 7:06 PM
To: Pat Evans <EvansPJ@cdmsmith.com>

Thanks Pat! When's the retirement official?

Michelle Young
Graduate Research Assistant, Environmental Engineering
Biodesign Swette Center for Environmental Biotechnology
Arizona State University

1001 S. McAllister Ave.
Tempe, AZ 85281-5701
(303) 263-4702

[Quoted text hidden]

Evans, Patrick J. <EvansPJ@cdmsmith.com> Thu, Aug 16, 2018 at 7:15 PM
To: Michelle Young <aumny@asu.edu>

You're welcome. Right after the SERDP conference

Pat
[Quoted text hidden]

Mikaela Links <mikaela.j.links@gmail.com> Thu, Aug 16, 2018 at 7:44 PM
To: Michelle Young <aumny@asu.edu>

Thanks, everything is good here in Flagstaff! Hope all is well with you too :) Let me know if you're ever up here—I miss you!

-Mikaela

Sent from my iPhone
[Quoted text hidden]

Sudeep Popat <spopat@clemson.edu> Thu, Aug 16, 2018 at 9:33 PM
To: Michelle Young <aumny@asu.edu>
Cc: Nadrat Chowdhury <nadrat.chowdhury@gmail.com>, Mikaela Stadie <Mikaela.Stadie@asu.edu>, Emily Garver <Emily.Garver@asu.edu>, Pat Evans <evanspj@cdmsmith.com>, "César I. Torres" <cit@asu.edu>, Bruce Rittmann <Rittmann@asu.edu>

Hi Michelle,

You have my permission. I'll be sure to tune in on YouTube! All the best.

Sudeep
[Quoted text hidden]

Cesar Torres <cit@asu.edu> Thu, Aug 16, 2018 at 9:34 PM
To: Sudeep Popat <spopat@clemson.edu>, Michelle Young <aumny@asu.edu>
Cc: Nadrat Chowdhury <nadrat.chowdhury@gmail.com>, Mikaela Stadie <Mikaela.Stadie@asu.edu>, Emily Garver <Emily.Garver@asu.edu>, Pat Evans <evanspj@cdmsmith.com>, Bruce Rittmann <Rittmann@asu.edu>

You have my permission as well!

cit

César I. Torres
Associate Professor, Chemical Engineering
School for Engineering of Matter, Transport and Energy
Biodesign Swette Center for Environmental Biotechnology

Arizona State University
(480)727-9689 Phone
(480)727-0889 Fax

http://torres.environmentalbiotechnology.org

From: Sudeep Popat <spopat@clemson.edu>
Sent: Thursday, August 16, 2018 9:34 PM
To: Michelle Young <aumny@asu.edu>
Cc: Nadrat Chowdhury <nadrat.chowdhury@gmail.com>; Mikaela Stadie <Mikaela.Stadie@asu.edu>; Emily Garver <Emily.Garver@asu.edu>; Pat Evans <evanspj@cdmsmith.com>; Cesar Torres <cit@asu.edu>; Bruce Rittmann <Rittmann@asu.edu>
Subject: Re: URGENT -- Permission to use article in my dissertation

[Quoted text hidden]

Emily Garver <egarver@asu.edu> Fri, Aug 17, 2018 at 8:56 AM
To: Cesar Torres <cit@asu.edu>
Cc: Sudeep Popat <spopat@clemson.edu>, Michelle Young <aumny@asu.edu>, Nadrat Chowdhury <nadrat.chowdhury@gmail.com>, Mikaela Stadie <Mikaela.Stadie@asu.edu>, Emily Garver <Emily.Garver@asu.edu>, Pat Evans <evanspj@cdmsmith.com>, Bruce Rittmann <Rittmann@asu.edu>

That's so exciting! You have my permission.

Emily
[Quoted text hidden]

Michelle Young <aumny@asu.edu> Fri, Aug 17, 2018 at 12:15 PM
To: Emily Garver <egarver@asu.edu>

Thanks honey! How are you (and the kids and the guy) doing?

Please excuse my brevity--this is coming from my smartphone.
[Quoted text hidden]

Nadrat Chowdhury <nadrat.chowdhury@gmail.com> Fri, Aug 17, 2018 at 3:40 PM
To: Emily Garver <egarver@asu.edu>
Cc: Cesar Torres <cit@asu.edu>, Sudeep Popat <spopat@clemson.edu>, Michelle Young <aumny@asu.edu>, Mikaela Stadie <Mikaela.Stadie@asu.edu>, Emily Garver <Emily.Garver@asu.edu>, Pat Evans <evanspj@cdmsmith.com>, Bruce Rittmann <Rittmann@asu.edu>

You have my permission of course! I'm so excited for you! I'd love to tune in.

Nadrat

Sent from my iPhone
[Quoted text hidden]

Emily Garver <egarver@asu.edu> Fri, Aug 17, 2018 at 4:35 PM
To: Michelle Young <aumny@asu.edu>

I miss you! I'm doing ok. My Happy actually got bloat and passed away yesterday despite having emergency surgery, so I've definitely been better. But my other bunnies are doing good, I only have four right now. My old man Pepsi is going strong almost a year and a half after being diagnosed with cancer, and he's bonded with Frost now. I'm working on getting my vet school applications submitted this week, so that's exciting. How are you and Jim and all of your buns doing? (:
[Quoted text hidden]

Michelle Young <aumny@asu.edu> Fri, Aug 17, 2018 at 6:08 PM
To: egarver@asu.edu

I'm so sorry to hear about Mr. Happy. We're down to 7 buns. We lost Bingley in January -- out of the blue, no warning -- and it still haunts me. Louise isn't interested in another mate, and she's just finally coming to terms with being alone -- she doesn't seem as lonely now, which is good. And she's letting us love her more. Moose contracted e. cuniculi in his spine. We've been fighting that since December. He likely has permanent semi-paralysis in his back legs. We're in physical therapy now to try and help him out.

I'm so glad to hear Pepsi's doing OK. I'm sure he and Frost make an adorable couple.

We're OK. The PhD has been brutal for the last year. A lot of trying to come to common ground with my advisors. I hear that, luckily for you, MDs don't usually have that same problem.

IF YOU NEED ANYTHING FOR YOUR VET SCHOOL APPS, PLEASE CONTACT ME! Jim and I still love you to death, Em, and miss you and your dad dearly. You're the little sister I'd like to see kick ass in medical school! Maybe when the defense is done, we can grab lunch.

Michelle Young
Graduate Research Assistant, Environmental Engineering
Biodesign Swette Center for Environmental Biotechnology
Arizona State University
1001 S. McAllister Ave.
Tempe, AZ 85281-5701
(303) 263-4702

[Quoted text hidden]

Michelle Young <aumny@asu.edu> Fri, Aug 17, 2018 at 6:09 PM
To: Nadrat Chowdhury <nadrat.chowdhury@gmail.com>

Thanks chica! How's beautiful North Carolina treating you? I bet you're up to your neck in research responsibilities by now. :)

Michelle Young
Graduate Research Assistant, Environmental Engineering
Biodesign Swette Center for Environmental Biotechnology
Arizona State University
1001 S. McAllister Ave.
Tempe, AZ 85281-5701
(303) 263-4702

[Quoted text hidden]

Michelle Young <aumny@asu.edu> Fri, Aug 17, 2018 at 6:11 PM
To: Sudeep Popat <spopat@clemson.edu>

Hey Sudeep!

Thanks man! I'll keep you informed on the YouTube -- you and Prathap are the really the only reasons I'm doing it. I've gotta have my 2 big mentors there, even if it's over the internet!

Things seem to be going well for you at Clemson. You've been getting some amazing grants....and you've expanded the family! ;) (BTW, congrats!) So glad to see you and Megha doing well. Are you going to Ismet?

Michelle Young
Graduate Research Assistant, Environmental Engineering
Biodesign Swette Center for Environmental Biotechnology
Arizona State University
1001 S. McAllister Ave.
Tempe, AZ 85281-5701
(303) 263-4702

[Quoted text hidden]

Michelle Young <aumny@asu.edu> Fri, Aug 17, 2018 at 6:15 PM
To: Pat Evans <EvansPJ@cdmsmith.com>

Pat, it's been such a wonderful experience working with you on SERDP. You have such an amazing understanding of the water and wastewater fields. You're my professional idol. My husband still brings up how cool and genuine you are after meeting you at Residuals and Biosolids in DC a couple of years ago. I hope you really get to enjoy retirement and have fun. Don't be a stranger!

Michelle Young
Graduate Research Assistant, Environmental Engineering
Biodesign Swette Center for Environmental Biotechnology
Arizona State University
1001 S. McAllister Ave.
Tempe, AZ 85281-5701
(303) 263-4702

[Quoted text hidden]

Michelle Young <aumny@asu.edu> Fri, Aug 17, 2018 at 6:17 PM
To: "César I. Torres" <cit@asu.edu>

Are you sure?!?! LOL! None of it would've been possible without you!

Michelle Young
Graduate Research Assistant, Environmental Engineering
Biodesign Swette Center for Environmental Biotechnology
Arizona State University
1001 S. McAllister Ave.
Tempe, AZ 85281-5701
(303) 263-4702

[Quoted text hidden]

Evans, Patrick J. <EvansPJ@cdmsmith.com> Mon, Aug 20, 2018 at 8:51 AM
To: Michelle Young <aumny@asu.edu>

Hi Michelle,

What a nice email! Thank you very much! I had fun working with you too and wish you the best of luck. What are your plans (assuming you pass your defense of course!)

Pat

From: Michelle Young <aumny@asu.edu>
Sent: Friday, August 17, 2018 6:16 PM
To: Evans, Patrick J. <EvansPJ@cdmsmith.com>
Subject: Re: URGENT -- Permission to use article in my dissertation

[Quoted text hidden]

Sudeep Popat <spopat@clemson.edu> Tue, Aug 21, 2018 at 4:16 AM
To: Michelle Young <aumny@asu.edu>

Hi Michelle,

Yes, looking forward to it. Let me know the details of how to join via YouTube.

Michelle Young <aumny@asu.edu> Mon, Aug 27, 2018 at 2:38 PM
To: Sudeep Popat <spopat@clemson.edu>

Wow -- your group is growing pretty damn quickly, and you already have MS graduates! You've got some intriguing grants for FOG and AnMBRs that I look forward to reading more about. (Yes, I check out your website regularly.) I will be presenting at ISMET this year -- cross the ol' fingers!

Michelle Young
Graduate Research Assistant, Environmental Engineering
Biodesign Swette Center for Environmental Biotechnology
Arizona State University
1001 S. McAllister Ave.
Tempe, AZ 85281-5701
(303) 263-4702

[Quoted text hidden]